IN VITRO CHARACTERISATION OF STENT DEPLOYMENT AND LOCAL ARTERIAL STRAINS

Iwona Zwierzak

School of Medicine and Biomedical Sciences

Department of Cardiovascular Science

Medical Physics Group

Submitted for the degree of PhD

Submission Date

August 2014

ABSTRACT

Cardiovascular disease causes approximately half of all deaths in Europe, with atherosclerosis one of the most common forms, resulting in stenosis of the coronary arteries. Balloon angioplasty with stenting is a common interventional procedure to treat stenotic arteries, but a significant problem is the biological response to stent placement, leading to in-stent restenosis of the vascular lesion.

This thesis presents an investigation of stent expansion using a non-contact optical method, aimed at providing high-accuracy measurements of local strain during stent deployment. The hypothesis of this research is that *in vitro* 3D measurement of the local deformation of an unconstrained stent, and of vessel wall strain following stent implantation, will provide a better understanding of vessel wall injury. The interaction of the stent with the vessel wall has hitherto been poorly examined *in vitro,* and improvements in current knowledge are sorely needed to validate computational findings.

The experimental system requires precise camera calibration to provide accurate 3D reconstruction of the stent/vessel surface. To obtain robust results, stent geometry characterisation was validated with micro-computed-tomography and error in strain was computed using zero-strain tests. Differences between optical and micro-CT measurement of 3D geometry were less than 2%, confirming the robustness and accuracy of the optical technique. During stent expansion tests within a vessel

analogue high local strains were measured at both the distal and proximal ends of the analogue, reaching 17% in the semi-deployed phase and 31% under full balloon inflation. Zero-strain tests reported a maximum strain error of <1%.

This experimental work has led to improved understanding of stent behaviour in 3D and insight into the relationship between stent expansion and vessel wall strain. Interpretation of these results in the context of vessel injury and the resulting neointimal hyperplasia which causes in-stent restenosis may contribute to a reduction in restenosis rates.

ACKNOWLEDGEMENTS

Few years ago, on a cold winter day with streets full of snow I arrived in Sheffield to start my journey in Cardiovascular Science and my time here has passed in a nice atmosphere thanks to everyone who was part of my journey.

I would like to take this opportunity to thank my supervisors, Dr Andrew Narracott and Dr John Fenner, for their help and inspirational guidance throughout the research study. My gratitude is extended especially towards Dr Andrew Narracott for hours of discussions about creative ideas, help, as well as his enthusiasm and encouragement.

I would also like to thank our group leaders: Prof Patricia Lawford and Prof Rodney Hose for a warm welcome to Medical Physics, their support and for bikes, with which I discovered the fabulous Peak District.

My lab friends and colleagues, it was great to have you around during these years: Claudia, e' stato bello fare tutti i viaggi per le conferenze con te, ridere e chiacchierare. Angela (floare), it was nice to have those long chats with you. There are so many other colleagues from I/O floor (you know who you are) I would like to thank for the: international lunches, coffees/teas, good laughs, deep chats and social events. All this will stay in my mind as a fantastic experience with good memories. The Medical Physics group were a better dream team than I could have asked for.

Margaret and Steve, thank you for your help in organising trips and supplying me with necessary resources.

Dziękuję za rozmowy, wiarę we mnie i dużo miłości, które zawsze otrzymuję od Was Mamo i Tato oraz za bycie takim fantastycznym rodzeństwem Piotrze, Tadeuszu i Alu.

Mój Błażeju, dziekuję Ci za cierpliwość i przypominanie mi, że mogę góry (nawet Mount Everest) przeskoczyć. Cieszę się, że jesteś.

I want to acknowledge that staying in Sheffield would not have proven possible without many other wonderful people that I met here, who made me feel welcome everywhere and every time.

"A scientist in his laboratory is not a mere technician: he is also a child confronting natural phenomena that impress him as though they were fairy tales" Maria Skłodowska-Curie

Table of Contents

Chapter 3

Chapter 4

Chapter 7

List of Figures

LIST OF TABLES

AIM OF RESEARCH

This thesis is focused on stent deployment characteristics. An optical system is applied to examine three dimensional objects through reconstruction of the surface observed by a pair of digital cameras. The aim is to evaluate stent expansion behaviour and determine the deformation of a vessel analogue after stent implantation.

It is important to understand the mechanical behaviour of stents and potential sources of vessel wall injury, because this leads to neointimal tissue growth and, ultimately, in-stent restenosis [1-3]. In cases where endovascular implants expand asymmetrically local extreme deformations of the vessel wall may result [1, 4, 5]. Optical tracking of the deformation of the external surface of the artery during stent deployment can provide useful information regarding stent/vessel interactions. *In vitro* and *ex vivo* methods for analysing vessel wall strain will provide valuable insight of in-stent restenosis and may lead to improvements in stent design.

Project objectives:

a) Design and characterise an optical system to allow imaging at coronary artery length scales.

b) Develop a satisfactory geometric reconstruction technique with well characterised error margins.

c) Apply the 3D optical reconstruction technique to balloon expandable stent geometric characterisation (validated against micro-CT technique).

d) Characterise changes in stent geometry during expansion in 3D to determine the cause of local extreme deformations of the vessel wall.

e) Quantify the local strain imposed by the stent on the vessel analogue surface during the deployment process.

In summary, this study aims to develop and characterise an experimental technique which can be applied to validate numerical simulation and measure coronary stent deployment *in vitro*.

CHAPTER 1

INTRODUCTION AND LITERATURE REVIEW

Chapter 1 presents an overview of the atherosclerosis process and therapeutic approaches for coronary artery disease (CAD) with a particular focus on percutaneous coronary intervention (PCI): balloon angioplasty and coronary stenting. This chapter also reviews the literature relating to in-stent restenosis and the links between the biological response of the vessel wall and its mechanical environment. Changes in vascular stress and strain during stent expansion are discussed, including the implications for strain measurement and optimisation of stent expansion. A summary of the research undertaken to improve the understanding of vessel deformation during and following stent implantation is presented including experimental work and numerical modelling carried out by several research groups and the implications of this research in terms of the development of in-stent restenosis.

1. CARDIOVASCULAR DISEASES AND ATHEROSCLEROSIS

Cardiovascular disease (CVD) is the leading cause of human mortality in Europe [6]. Atherosclerosis is one of the most common forms of CVD, leading to clinical endpoints including angina, heart attack and ischemic stroke, insidiously developing throughout life. Atherosclerosis occurs mostly in the coronary arteries and the arteries leading to the legs and brain [7] with symptoms rarely reported until vessel occlusion is greater than 50%. From this point ischemia may start to present.

This thesis focuses on the coronary arteries which supply blood to the heart; atherosclerosis in these vessels contributes to almost half of all CVD deaths. Percutaneous coronary intervention (PCI) can restore blood flow to relieve ischemia, with stent implantation commonly used in such procedures [8]. However, in-stent restenosis (ISR) affects 20-30% of patients [9]. ISR occurs as a result of vessel wall injury caused by stent implantation and the resulting neointimal tissue growth. Drug-eluting stents (DES) have been shown to reduce the rate of ISR to less than 10% of treated cases [10]. However, mechanical vascular injury is not eliminated by DES use.

The first part of this review provides an overview of normal coronary anatomy, atherogenesis, clinical manifestations of CAD and interventional approaches (particularly balloon angioplasty and coronary stenting) used to treat the disease. The second part describes coronary stent characteristics, the phenomenon of in-stent restenosis and the outcomes of research studies (experimental and numerical) aimed to reduce restenosis and improve long-term vessel patency.

1.1. CORONARY ARTERY ANATOMY AND CONSTITUTION

The coronary arteries are the vessels which carry oxygen and nutrient-rich blood to the myocardium. *Figure 1-1* illustrates the anatomy of the heart and the coronary arteries.
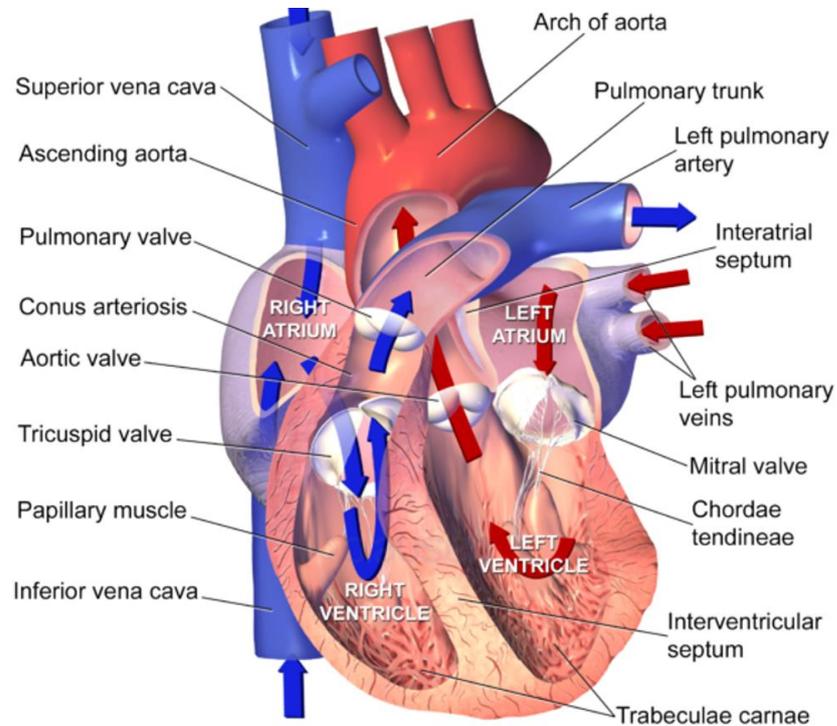
Figure 1-1: Sectional anatomy of the heart.* License: *This file is licensed under Creative Commons Attribution 3.0 Generic (CC BY 3.0).

The right coronary artery supplies the right atrium, right ventricle and apex of the left ventricle with oxygen-rich blood. The left main coronary artery divides into the left anterior descending artery (LAD) which perfuses the left atrium and the lateral and posterior part of the left ventricle [11].

Coronary arteries are composed of three layers: the tunica intima, the tunica media and the tunica adventitia (*Figure 1-2*). The intima is the innermost layer, in contact with the blood, and is composed of a monolayer of endothelial cells (ECs) [12], which prevents blood adhering to the luminal surface [13]. In the healthy artery ECs are

aligned in the direction of the flow and have a flat, elongated shape. Below the EC monolayer is a sheath of highly extensible material called the internal elastic lamina [14].
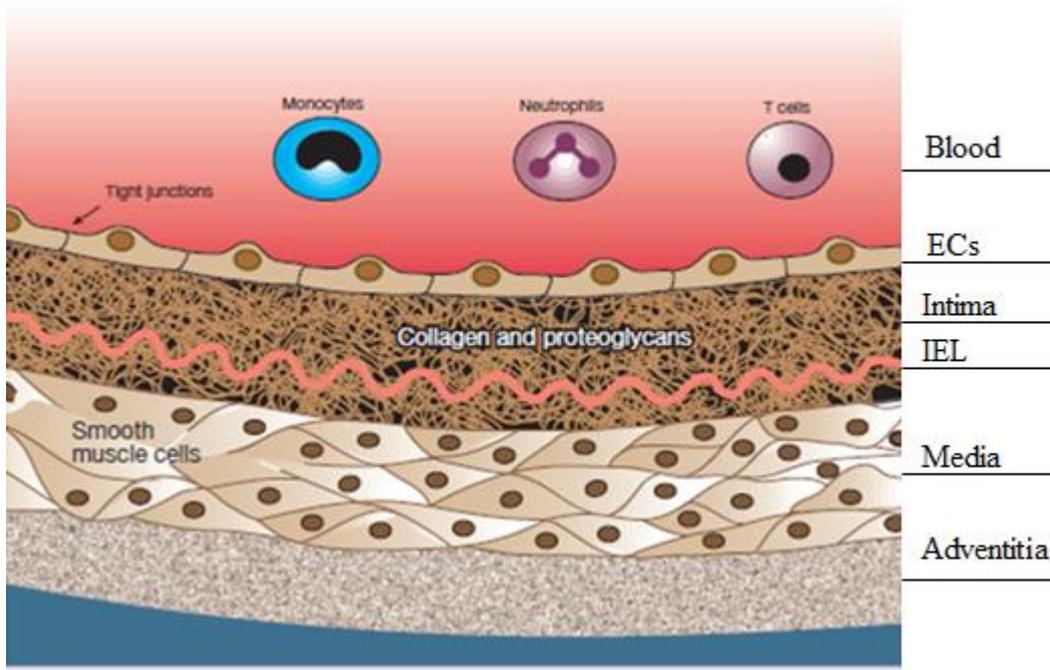
Figure 1-2: Scheme of a healthy coronary artery adapted with permission from Lusis [14].

The media is the middle and the thickest layer of the vessel wall. It consists largely of spindle-shaped smooth muscle cells (SMCs), elastin, type I, III and V collagen, and proteoglycans [13]. Moreover, is dynamic in nature, contracting or relaxing in response to the prevailing physiological signals [15] and has the greatest influence on the mechanical properties of the artery [13]. The task of the SMCs is to maintain vessel structure and function [16]. They are responsible for producing extracellular matrix (ECM) proteins including collagen and proteoglycans. If the endothelial cell layer is damaged, the SMCs respond to cytokines secreted by damaged ECs and proliferate and migrate to the intima. The ECM regulates many cellular functions of the artery wall. This matrix consists of fibrous proteins, which provide mechanical support. The

major component of the ECM is collagen. Cell function regulation by the ECM is achieved through interaction between cell receptors and matrix proteins [16].

The adventitia is the outer layer that contains small blood vessels which nourish the cells in the thick media. It tethers the vessel loosely to the surrounding tissue. It is composed mainly of collagen and elastin, which are responsible for maintaining the structural integrity of the vessel [17].

1.1.1. RESPONSE OF ARTERIAL CONSTITUENTS TO MECHANICAL LOADING

The vessel wall is permanently subjected to mechanical loads as a result of the beating of the heart. The endothelial cells (ECs) are subject to dynamic loading conditions because of pulsatile changes in blood flow and pressure [17]. Cyclic strain of the endothelium occurs as a result of vessel wall distension due to blood pressure oscillation and changes in shear stress on the endothelium caused by the pulsatile flow. The smooth muscle cells (SMCs) within the media are also exposed to the cyclic stretch from pulsatile changes in blood pressure [18].

Changes in the mechanical loading of the artery, due to high blood pressure, have been linked to disease processes. Abnormal mechanical loading can alter the function of SMCs leading to changes in extracellular matrix (ECM) composition and the development of atherosclerosis [16]. In addition, atherosclerotic lesions have also been shown to occur in regions where blood flow is disturbed [19], for example at vessel branches and at sites of high curvature. The distribution of wall shear stress in these locations is non-uniform and irregular.

An understanding of the anatomy of healthy arteries and their constituents is important because it gives context to changes which arise during the progression of atherosclerosis. The next section considers the process of disease progression.

1.1.2. ATHEROSCLEROSIS

Atherosclerosis consists of an accumulation of lipid-rich cells, connective tissue, cell debris and macrophages within the wall of an artery vessel [14]. In time this forms an atherosclerotic plaque, which may cause stenosis (narrowing of the arterial lumen), of the arteries that supply blood to the myocardium [20, 21]. Early atherosclerotic lesions (associated with sub-endothelial accumulation of macrophages which contain cholesterol- so called 'foam cells') can be found in the aorta as early as in the first decade of life, the coronary arteries in the second decade and in the cerebral arteries from the third and fourth decade [14]. An idealised example of diseased coronary artery is shown in *Figure 1-3*.
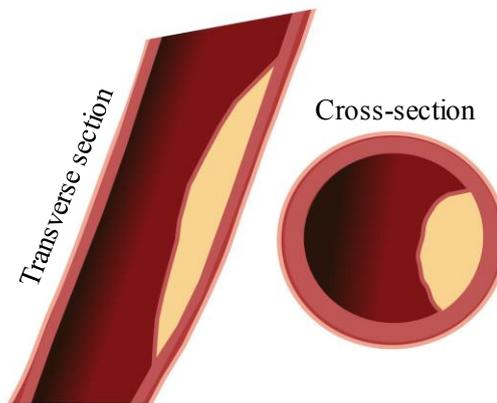
Figure 1-3: Representation schema of the atherosclerotic plaque in a coronary artery.

Atherosclerosis often occurs in side branches, bifurcations and at locations of arterial curvature, due to multidirectional and disturbed blood flow in these regions [22]. DeBakey *et al* [23] characterised the distribution of atherosclerosis-related disease into

four major categories. As illustrated in *Figure 1-4*, atherosclerosis was more commonly reported in the arterial branches of the abdominal aorta (category III). This thesis considers disease in the coronary arteries, depicted by category I.
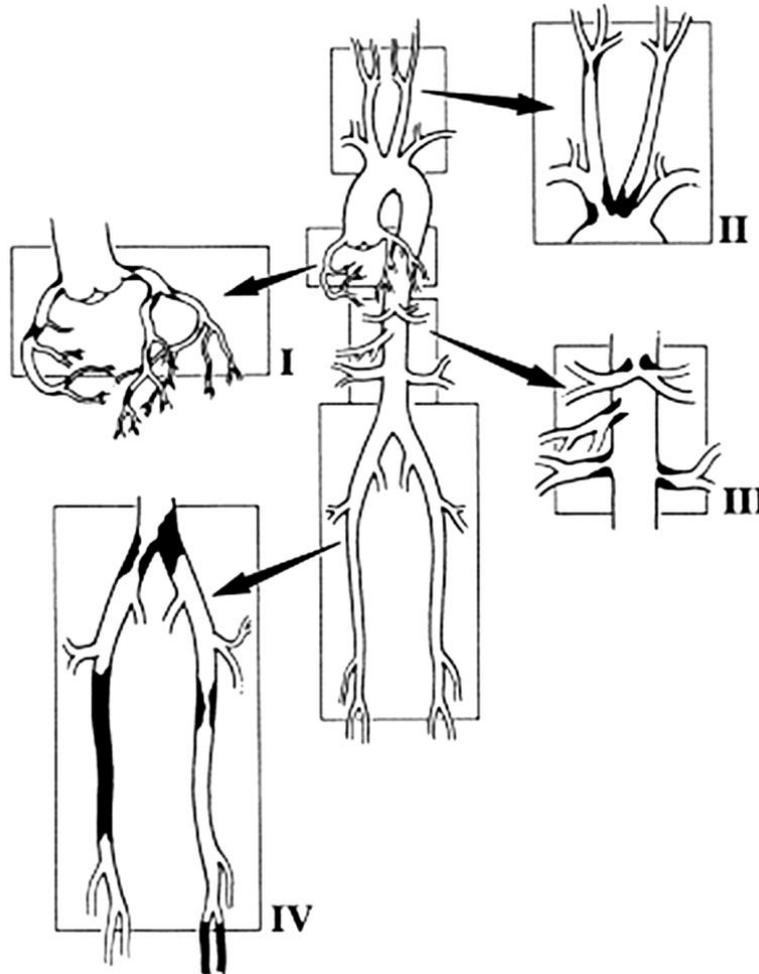
Figure 1-4: The distribution of atherosclerotic plaques within human arteries: I-coronary artery bed, II- major branches of aortic arch, III- visceral arteries of abdominal aorta, IV- terminal abdominal aorta, adapted with permission from Debakey et al. [23].

The steady progression of atherosclerotic plaque development over a lifetime can result in death from CVD [24]. Atherosclerotic plaque [14] is stiffer than the native arterial wall. Lesions become increasingly complex with calcification and ulceration at the luminal surface. Lipid-rich plaques are more vulnerable to rupture [25]. Thrombosis can occur as a result of plaque rupture [26] or erosion of the plaque at its

weakest point. This occurs where the fibrous cap is thinnest, and in regions filled with foam cells [14], as a result of stresses caused by forces affecting the vessel wall [27]. Exposure of underlying tissue factors precipitate clot formation. If plaque grows sufficiently to impair blood flow, this may result in occlusion and myocardial infarction [28]. Restriction of blood flow to the myocardium impairs normal cardiac function.

In summary, atherosclerosis is caused by the accumulation of lipids, fibrous tissue, calcium deposits and blood products within the sub-endothelial space. This accumulation leads to thickening and hardening of the arteries, in some cases also reducing the vessel lumen and causing a stenosis. A stenosis is considered significant (requiring intervention) when more than a 75% reduction in the luminal diameter is observed [29]. Different interventional approaches such as coronary artery bypass grafting (CABG) surgery, angioplasty and stenting have been developed to treat coronary artery disease. The following section describes these approaches in more detail.

1.2. INTERVENTIONAL APPROACHES

This section describes surgical techniques which have been applied to treat coronary artery stenosis. Severe narrowing or blockage of the main coronary artery may require open heart bypass surgery [30]. Less invasive methods include Percutaneous Coronary Intervention (PCI). PCI methods include both balloon angioplasty and stent implantation.

1.2.1. BYPASS SURGERY

Coronary artery bypass surgery is usually considered for patients with severe narrowing or occlusion in multiple coronary arteries. There is recent evidence (from 2011) that annually about 800,000 patients worldwide with multiple coronary artery disease undergo CABG [31]. In this procedure blocked coronary arteries are bypassed by a portion of a healthy vessel (artery or vein) harvested from the arm (the radial artery), leg (the saphenous vein) or chest (the internal mammary artery). The bypass length depends on severity and distribution of disease [32]. Most patients receive between 1 and 5 grafts. During the operation a pump maintains the circulation artificially by adding oxygen to the blood and circulating the blood through the body.

1.2.2. BALLOON ANGIOPLASTY

Percutaneous Transluminal Coronary Angioplasty (PTCA) is a technique in which a balloon is inflated to dilate the arterial lumen. In 1977, PTCA was the first percutaneous therapy to be used [33]. To perform angioplasty the radial or femoral artery is accessed and a catheter is inserted using a guide wire. X-ray angiography is used to visualise the blood vessels and help the clinician position the catheter correctly at the site of coronary lesion by injecting a radio-opaque dye (contrast medium) into the vessel from the catheter [34]. A collapsed balloon, attached to the tip of the catheter, is passed into the artery through the blockage and aligned with the atherosclerotic plaque. The balloon is inflated with a handheld syringe pump using a mixture of saline and contrast medium to visualise balloon inflation and the inflation pressure is increased gradually. The balloon presses the plaque against the artery wall dilating the stenosis and restoring blood flow [35]. After angioplasty, the lumen of the blood vessel is wider and hence blood flow is increased.

A limitation of balloon angioplasty is restenosis. This occurs in around 40 - 50% of cases [35, 36]. Studies have shown that narrowing after angioplasty is caused by a number of factors including elastic recoil of the overstretched segment [7], vascular remodelling and neointimal proliferation [36, 37].

Elastic recoil is an acute response of the vessel occurring immediately after balloon deflation. As the artery wall is elastic, it may return close to the original diameter when the balloon is removed [7]. Arterial *remodelling* is defined as a structural change in the arterial wall responsible for late lumen loss [38, 39] and occurs in response to balloon-induced injury [37, 40]. Remodelling can increase lumen narrowing, resulting in further shrinkage of the vessel lumen because there is nothing to support the vessel. *Neointimal hyperplasia* is the abnormal growth of new intimal tissue. This is a vascular repair process initiated by vascular injury and driven by the smooth muscle cell response [37].

In response to these complications the introduction of stent insertion has been shown to be superior to balloon angioplasty alone, although there are some circumstances where the latter may be used such as: when dual antiplatelet therapy may be detrimental to the patient; in small side branches where stenting is not practical; or as a temporary measure prior to CABG [41].

1.2.3. BALLOON ANGIOPLASTY WITH STENTING

Balloon angioplasty may be supplemented by deploying a stent mounted on the balloon. As the balloon is inflated, the stent expands to form a permanent internal scaffold thus maintaining vessel patency [37]. Coronary stent implantation is the most used commonly procedure to treat stenosed coronary arteries.

The market for research and design is constantly developing and expanding. In 2011 the global market for coronary stent devices reached $7.1 billion (more than $2.5M in Europe). It is expected that by 2016, the total market value will reach $10.6 billion, with an estimated annual growth rate of 8.3% [42].

Stents are small metallic tubular scaffolds placed in the arteries to relieve stenosis and maintain the flow of blood [43]. Balloon expandable stents were invented in 1987 by Palmaz *et al* [44] to reduce the rate of restenosis following angioplasty and have been embraced worldwide by cardiologists as a highly effective tool [45]. Previous clinical studies have shown that stenting reduces restenosis from 40% to 20% [2, 35, 46, 47]. When the balloon is removed, the stent remains permanently in place and acts as a scaffold for the artery to eliminate elastic recoil and maintain patency (*Figure 1-5*).
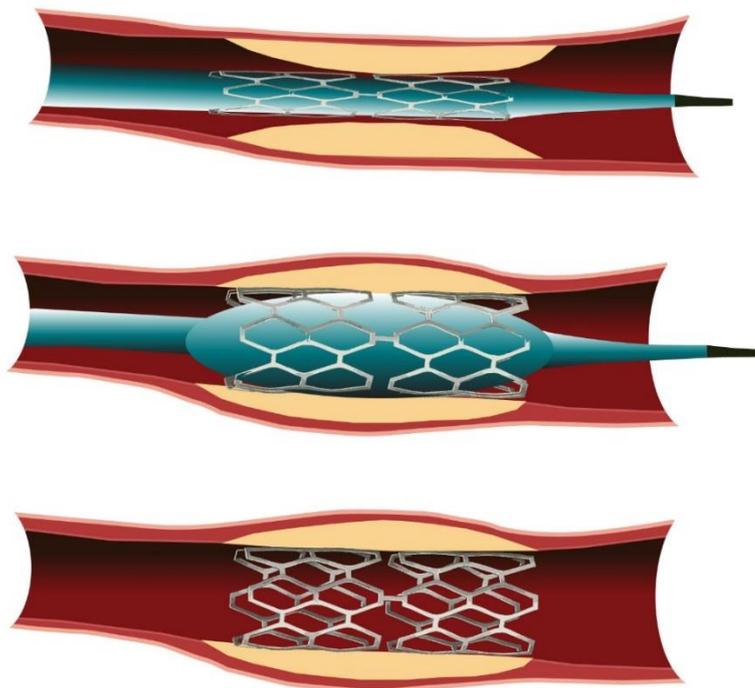
Figure 1-5: Representative schema of implanted stent in the atherosclerotic artery to keep it open and restore blood flow to the heart.

Whilst stenting is more successful than balloon angioplasty alone, early enthusiasm for stent technology was reduced due to the problem of in-stent restenosis.

From section 1.4 of this review describes the characteristics of coronary stents, the phenomenon of in-stent restenosis and the outcomes of research studies aimed at improving stent performance.

1.3. CORONARY STENTS

Coronary stents can be self-expanding or balloon-expandable. A self-expandable stent is compressed by a protective sheath on a catheter, expanding by itself when the sheath is retracted [48]. The present study focuses on balloon-expandable stents which are mounted on a balloon catheter in a collapsed or "crimped" state. The stent expands as the balloon is inflated and is left as a permanent implant after the balloon is deflated and removed. *Figure 1-6* illustrates a fully deployed balloon expandable coronary stent (Taxus Express made of 316L stainless steel).
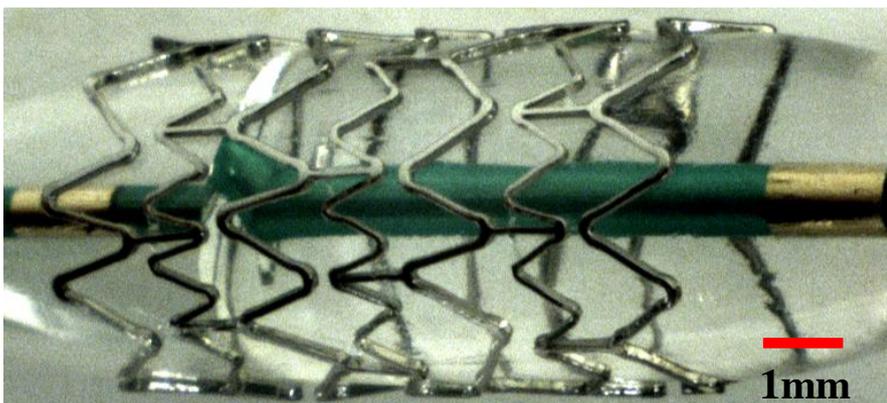
Figure 1-6: Balloon expandable 316L stainless steel Taxus Express coronary artery stent (Boston Scientific, 8mm length) fully expanded to 3.5mm diameter using an angioplasty balloon. Image taken with camera Flea2 (FL2G-13S2C-C, Point Grey, Canada).

1.3.1. STENT DESIGN CONSIDERATIONS

Different stent designs have different expansion and recoil characteristics [49]. From a structural design perspective an ideal stent should:

- have a low profile, be flexible and trackable, to ensure ease of delivery,

- be composed of biocompatible materials to ensure no negative biological reaction after implantation,

- have a low radial and longitudinal recoil with excellent radial strength to maintain vessel patency after expansion,

- expand symmetrically to avoid high local strains [45].

These characteristics are determined by stent material and geometry [49, 50]. Stainless steel 316L has been used for many stent designs [49]. It has satisfactory physical properties and an acceptable level of radio-opacity [51]. However, this material is not fully biocompatible, which contributes to the formation of restenosis and thrombosis. Other commonly used, more biocompatible, materials include metal alloys such as cobalt-chromium (Co-Cr alloy), nitinol and polymers. These elicit a less vigorous vessel response than stainless steel [49]. Thicker struts give better radio-visibility and arterial wall support, but may cause more vascular injury [52]. Stents with thinner struts have a lower risk of restenosis so are often used for high risk lesions [50].

Clinically, stent choice is determined by several vessel /lesion related factors such as: lesion length, reference vessel diameter, lesion calcification and vessel tortuosity. The diameter and length can be judged by using the guiding catheter or pre-dilation angioplasty balloon (with known dimensions) as a reference [53]. Choice between bare metal stents (BMS), drug eluting stents (DES) or simple medical therapy is determined

by lesion position, length, diameter, along with patient factors such as compliance with medication (dual antiplatelet therapy is mandatory for 6 weeks following BMS and for 12 months post DES implantation).

Research to improve stent design is focussed on the reduction of vascular injury and improvement of clinical outcomes [51].

1.4.   IN-STENT RESTENOSIS

In-stent restenosis (ISR) is the reoccurrence of stenosis after stent placement. It remains an important, not completely resolved clinical problem. Usually it occurs secondary to vessel wall injury associated with neointimal tissue growth [7, 37]. This section describes the biological factors associated with development of ISR and the mechanical factors that contribute to the arterial injury, stimulating the ISR response.

1.4.1.   BIOLOGICAL RESPONSE TO STENTING

The biological mechanisms which occur post stent implantation are described by the four-phase process shown in *Figure 1-7*:

▪   The primary reaction to stenting is ***thrombosis***. A layer of blood thrombus forms following denudation of the thromboresistant layer of endothelial cells (ECs) [7, 54]. Thrombus accumulates in the region of the partially denuded endothelium and adheres around the stent struts. Thrombus deposition occurs on a timescale of days (from day 1).

▪   An ***inflammatory reaction***, which includes adherence of monocytes to the artery wall, occurs within the first day of stenting [7, 55].   Inflammatory cell

recruitment starts close to the stented region [37]. Stent struts cause focal disruption of the artery wall leading to prolonged, chronic damage [54].

- The main factor for restenosis is the migration and ***proliferation of SMCs.*** SMCs migrate towards the lumen in response to the arterial injury. These cells produce extracellular matrix proteins, which form a ***neointima*** [46]. SMCs and monocytes proliferate and contribute to the architectural framework of the hyperplastic lesion.
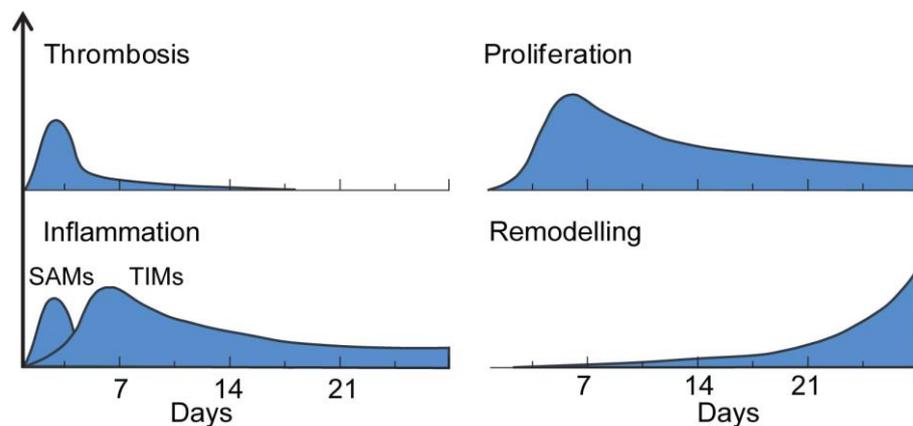
Figure 1-7: Intensity of responses versus time; the inflammation stage includes the activity level of surface-adherent monocytes (SAMs) and tissue infiltrating monocytes (TIMs)，(data adapted from Duraiswamy [7]，permission was not required).

- Stent insertion limits recoil, but it does not reduce ***remodelling***. The dynamic and responsive nature of the artery adapts to a new environment and strains imposed by the stent via remodelling [7]. Remodelling is caused by increased collagen deposition, elastin destruction and persistent inflammation [54].

- Neointimal tissue formation is influenced by the force of a foreign body, the stent, against the arterial wall causing changes in stress and strain distribution [28, 56]. In 50% of cases, ISR occurs within three to six months after the stenting procedure [46, 57]. The image below (*Figure 1-8*) presents cross-section of a porcine coronary

artery 28 days after stenting (image courtesy of Dr Julian Gunn). The original lumen and decrease in luminal area due to intimal hyperplasia are highlighted with the red dashed line and using the arrow respectively.

To understand the ISR response, it is important to investigate the mechanical basis of arterial injury, which can occur during catheter insertion, stent expansion or as a chronic effect as described below.
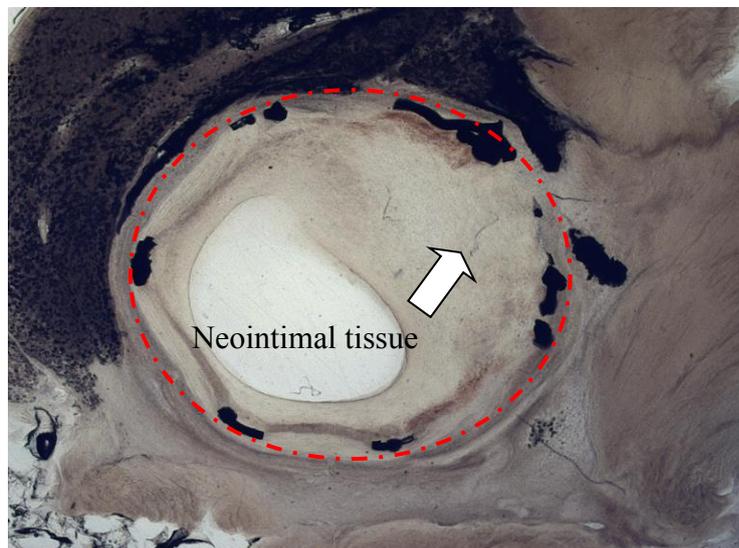
Figure 1-8: Porcine coronary artery 28 days after stenting (image courtesy of Dr Julian Gunn).

1.4.1.1. STENT INSERTION

On rare occasions, if there are several occlusions, the coronary artery can be injured by the insertion of the catheter. The guide wire can create a false lumen within the plaque, which may subsequently delaminate and occlude blood flow [58].

1.4.1.2. STENT EXPANSION

Asymmetrical stent expansion can cause deep vascular injury [59] due to penetration of the arterial wall by the stent struts. Uneven deployment of the stent struts or rotation

of the balloon catheter can scrape or lacerate the vessel wall. Previous studies reveal partial or complete endothelium denudation as an outcome of stent deployment which can be related to foreshortening of the stent during deployment [60, 61]. This may initiate SMC migration, which is proportional to the degree of arterial injury [62, 63].

It has been shown that the greatest neointimal tissue growth occurs at the proximal and distal regions of the stent. This may be due to the first contact of the implant with the artery as a result of the "dog-boning" effect [2, 64]. Manufactured balloons are longer than the stent to prevent slippage of the stent relative to the balloon that may occur during travel of the device through the vasculature. This is related to the "dog bone" geometry which occurs at the proximal and distal ends in the first stage of the angioplasty balloon inflation (*Figure 1-9*).
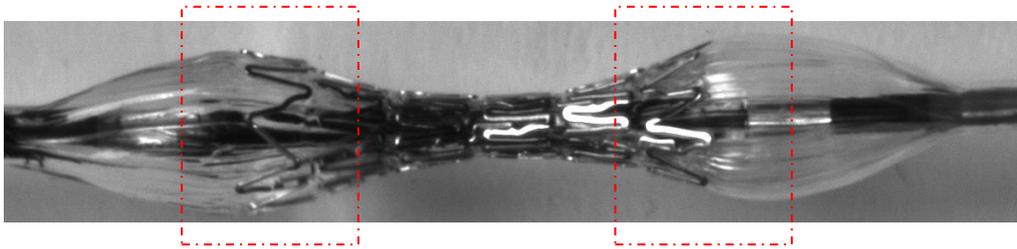
Figure 1-9: Dog-boning effect: distal and proximal part of the stent expands before the central.

Uneven local strut deformation has been shown to be dependent on the nature of balloon folding through characterisation of stent deployment in 3D [65]. This may have implications for the local vessel wall injury generated during contact of the stent with the vessel wall [66].

1.4.1.3. CHRONIC INJURY

The biomechanical interaction of the stent and the vessel wall is important to the long-term success of the procedure. Deep injury of the media triggers SMCs migration and proliferation [47] as a process of vessel healing along with establishment of a new endothelial monolayer. Chronic restenosis is related linearly to the degree of vessel wall damage [67, 68]. Given the link between the mechanical injury caused by stent implantation and the biological response, it is not surprising that there has been significant research focussed on the understanding of these effects.

The remaining sections of this Chapter present the state-of-the-art understanding of the correlation between stent design, ISR and the mechanical environment of the vessel through *in vivo*, *in vitro* and numerical studies.

1.5. STATE-OF-ART OF STENT ANALYSIS

This section reviews the state-of-the-art in the study of stent mechanical properties and stent/vessel wall interactions, and their potential to influence future stent design modifications. These studies include *in vivo* human clinical studies and animal models aimed at improving understanding of the biological response to stenting. The section concludes with a discussion of the approaches used to replicate the behaviour of arteries during experimental studies.

1.5.1. *IN VIVO* STUDIES

Intravascular ultrasound data confirm that most of the luminal narrowing seen in humans takes place within the first six months following stent implantation [69] due to strains which the stent imposes on the artery wall. The extent of neointimal hyperplasia was found to be strongly related to stent design [57]. The area occupied

by neointimal tissue ranged from 20% to 50% of the lumen diameter (depending on the stent type). Stent design plays an important role in neointimal tissue hyperplasia. This suggests that different stent types may have different interactions with the arterial wall.

The pathobiological responses of the coronary arteries to stent insertion have been examined in numerous animal investigations [2, 59, 70]. Schulz *et* al [59] used a sheep coronary model to examine stent performance on a strut-by-strut basis and determined that local strain is an important factor in neointimal tissue formation. The relationship between permanent strain on the vessel wall and neointimal tissue growth was confirmed by this study. The porcine coronary model has been suggested to be the best candidate for the study of in-stent restenosis [2, 70] as the porcine inflammatory and thrombotic response has been shown to be similar to that observed in human coronary arteries [55]. Arterial stretch and over expansion of the stent was studied to examine development of neointimal tissue caused by deep vascular injury [70]. It was found that even stretch without an injury can lead to neointimal tissue growth. In addition Timmins *et* al [2] measured the pathobiological response in a porcine model following deployment of two distinct stent designs in order to understand if neointimal tissue volume depends upon stent design. This study demonstrated that the implanted stents imposed different strains on the arterial wall with higher strains resulting in a higher degree of neointimal tissue growth. A higher rate of restenosis was observed at the proximal and distal regions of the stent in agreement with clinical observations [57]. It is suggested that this is related to the dog-boning effect during stent expansion which causes increased arterial injury at the stent edges. Animal models indicate that stent design has a significant impact on

vessel trauma and the amount of subsequent intimal hyperplasia [59]. The limitation of studying restenosis in sheep and pig coronary arteries is that these are healthy, non-atherosclerotic vessels, not diseased human arteries.

1.5.2. *IN SILICO* MODELS

Computational modelling and simulations are often used to characterise stent behaviour following implantation. *In silico* analyses include different stent designs [71, 72], contact conditions of the stent with the artery [73], stent deployment in curved vessels [74], influence of strut thickness on the strains in the coronary wall [1, 52] and local luminal flow of the blood [5, 7, 75]. Numerical modelling techniques are effective and have been found to be efficient for understanding mechanical properties of stents and arterial stresses induced by stents. The combination of *in silico* techniques and *in vivo* analysis provides insight into the links between biomechanical variations generated by the stent with quantitative *in vivo* evidence of neointimal hyperplasia [2].

Lally *et* al [71] used the finite element method (FEM) to study the behaviour of two different stent designs in order to quantify arterial stresses as a measure of the level of vascular injury. Interaction of the stent with the atherosclerotic artery was examined with the hypothesis that restenosis was strongly related to stent design. An analysis of the arterial wall stresses indicated that a less rigid stent causes lower stress. Further studies confirmed that stress and strain can vary in the arterial wall depending on stent design [46]. Gijsen *et* al [1] examined the influence of the same stent design with two different strut thicknesses on the strains in the vessel wall with the hypothesis that thicker and thinner struts will produce different arterial responses. It was found that

thicker struts cause more damage to the arterial wall through higher stresses. This hypothesis is supported by clinical evidence from the implantation of stents with differing strut thickness [76]. It was found that thinner stent struts elicits less neointimal tissue growth. The results also showed that stresses in the arterial wall are high where the wall is thin and in the area behind the stent struts (near the connectors between the struts).

Zahedmanesh *et* al [52] also reported that strut thickness is an important predictor of restenosis. Lower stresses cause less injury to the vessel wall and therefore reduce the likelihood of restenosis. However, a stent with thinner struts may recoil more than those with thicker ones due to greater flexibility and compliance. In his recent study [77] he analysed response of the artery interaction with the struts of the stent expanded to a diameter of 4.3, 4.7 and 5.1 mm, representing cases with mild, medium and deep strut penetration respectively (*Figure 1-10*). Two strut thicknesses, of 0.085 and 0.17 mm, were compared. It was found that the maximum SMCs and neointimal tissue growth occurred after deploying the stent struts to the larger diameter.
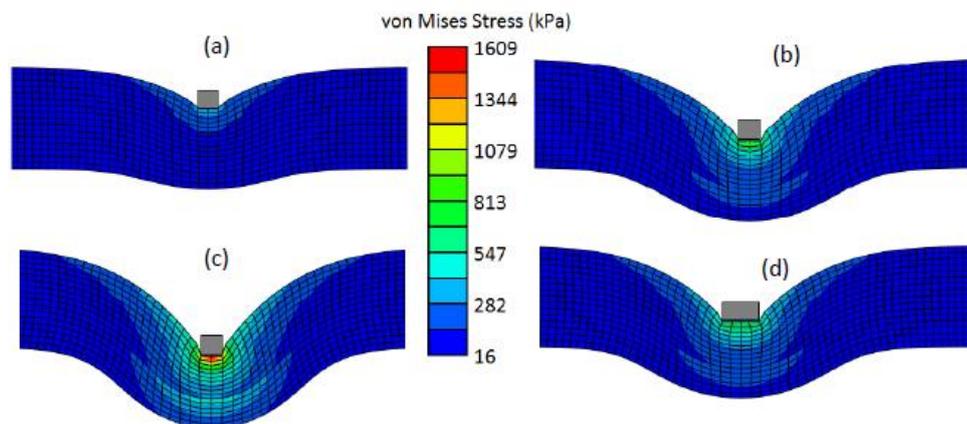
Figure 1-10: The representation of the artery behaviour due to stent struts interaction with the internal artery wall. The thin stent strut (0.085 mm) deployed to a diameter of: a) 4.3 mm, b) 4.7 mm, c) 5.1 mm and with thick stent strut (0.17 mm) deployed to d) 4.7 mm diameter; adapted with permission from Zahedmanesh et al. [77].

De Beule *et* al [78] reported that an asymmetric stent design caused less dog-boning than a symmetric design and that the unfolding of the balloon determines the way the stent expands [10]. Pericevic *et* al [79] investigated how different types of plaques and various inflation pressures influence arterial wall stresses. They suggested that an appropriate pressure should be applied depending on plaque composition, i.e. high pressures should be used for calcified plaques, but not for the softer plaque. They believe that this approach may reduce occurrence of in-stent restenosis.

The level of detail provided in computational studies of such complicated problems can be challenging to reproduce in clinical or experimental studies. Numerical models are excellent research tools, especially when physical models are difficult to create, but rely upon a number of assumptions. The principal advantage of numerical models is that it is easy to investigate specific parameters, different materials and loading conditions, but the influence of underlying assumptions mean that it is necessary to carry out experimental work to validate the results [80].

1.5.3. *IN VITRO* MODELS

To investigate the deformation of the coronary arteries and stent deployment, non-contact imaging systems are desirable due to the small scales involved and the delicate nature of the stent structure. Non-contact methods can characterise complete full-field surface displacements [81, 82]. It is desirable to measure the response of sample over the full geometry, as variations in the response of the material between local regions can be significant in the characterisation of non-homogenous materials such as coronary arteries [83]. Even if stent cell design is symmetrical and high precision manufacturing is possible, in practice, stents can expand in an eccentric manner.

Asymmetric expansion may result in excessive strain on the vessel wall resulting in increased vascular injury leading to higher restenosis rates [84].

Previous experimental studies have used a single camera to characterise stent expansion in a rigid transparent pipe in two dimensions (2D). These studies focussed on changes in stent diameter and length with applied balloon pressure [80, 85]. The increase in stent diameter was found to be non-linear with the applied pressure load in the balloon [85]. Kiousis *et* al [86] reported 2D experimental measurement of free expansion of six vascular stents to investigate the deformation mechanisms and provided comparisons with a computational model. They described three components (foreshortening, maximum dog-boning and elastic recoil) of the expansion process. In addition, the mechanical behaviour of the angioplasty balloons alone was examined. This study proposed improved stent design to enhance uniform deployment during balloon inflation. No interaction of the implant with the vascular wall was included. Takashima *et al*. [73] characterised in 2D the contact area of the stent with cylindrical vessel analogues, both with and without a silicone lesion. Stents with differing numbers of cells and links were considered. It was found that stents containing more cells have a larger contact area with the vessel wall and stresses are distributed over a larger surface. This may decrease the subsequent stimulus for neointimal tissue growth.

Deformation of the arterial surface after stent expansion *in vitro* in the bovine coronary arteries and *ex vivo* in femoral rabbit arteries was examined by Squire *et* al [81]. An irregular pattern was applied to the arterial surface using ink from a printer cartridge in order to examine the strain by tracking deformation vectors of the pattern. Stainless steel stents of 3 mm final diameter were deployed until a maximum balloon inflation

pressure load of 8 atmospheres (in 2 atm steps) was achieved. A single camera was used to capture the whole inflation processes. Accuracy of the strain measurement was determined by inflating a large scale artery analogue with a manually marked grid. This resulted in a 4.1% error of the system. 2D images of deformed markers on the vessel wall were used to back-project onto a 3D cylindrical model for strain analysis. Large errors (standard error of *in vivo* strain measurements of 4%) were reported due to the limited resolution of the cameras and the back-projection process.

Optical tracking of stent deployment *in vitro* in atherosclerotic human arteries was carried by Horny and co-workers [87]. Deformation was computed as a ratio between the deformed and undeformed state to assess changes due to interaction of the stent with the occluded artery. Edge detection algorithms were used to plot changes in the artery's diameter. They found significant deformation in the diseased part of the vessel. This study was limited to arterial contour detection only and use of a single camera could not provide full 3D displacement field of the deformed artery.

To the author's knowledge there have been only a small number of experimental studies which report 3D characterisation of stent expansion or vessel wall deformation. Narracott *et* al [88] published experimental data of free stent expansion in 3D using two different balloon folding patterns. Balloons with 'C' shape folding resulted in greater non-uniform stent expansion than balloons with an 'S' shape. This study confirmed the hypothesis that the folding pattern of the balloon influences significantly the symmetry of the deployment and demonstrated robustness of the optical reconstruction method. Connolley *et al* [89] used micro-CT scanning to image 3D stent behaviour at various stages of balloon inflation. Coronary stent was deployed in

mock silicone artery with a simulated occlusion of 30% (length of 8.6 mm, width of 3.7 mm with maximum thickness of 1 mm). The results obtained showed stent shortening during deployment (from 13 mm length in the initial stage to 12.6 mm at a pressure of 8 atm). The dog-boning effect was also observed before the stent was fully deployed. It was found that micro-CT provides high resolution data (5.3 µm x 5.3 µm x 5.3 µm) of the metallic stent geometry. Furthermore, Mori *et al.* [4] used micro-CT for 3D observation of the behaviour of unconstrained stent expansion and the elastic recoil of each stent cell after balloon deflation. It was found that elastic recoil varies along the stent length (from 2.5% in the distal part to 6.7% in the proximal part). This study highlighted the value of 3D qualitative and quantitative results for understanding vessel wall damage following stent deployment. Micro-CT has been shown to provide excellent 3D models of the stents; unfortunately data acquisition takes several minutes, whereas stent deployment occurs over a few seconds.

Sutton *et al.* [82] used a digital image correlation (DIC) method to demonstrate that measurement of deformation of mouse arteries in 3D is feasible and strains on the vessel wall can be characterised through surface marker displacement tracking. However, this study did not report stent/vessel wall interactions. Moreover, the high magnification of the microscope gave a shallow depth of field and hence a loss of focus at the edges of the carotid surface.

The goal of the present study is to characterise the strain at the contact area between the stent and the artery through experimental measurement. In a preliminary report Horny *et al.* [90] presented the application of digital image correlation (DIC) to provide information about stent/vessel interaction in the presence of atherosclerosis in

a human coronary artery harvested during autopsy. Displacements of a small number of reference points on the vessel wall were described. Supra-physiological circumferential deformation was found where the stent was in contact with the vessel wall (0.5mm/mm at the peak value). 3D DIC was found to be a suitable candidate to evaluate *ex vivo* stent implantation. Moreover, Zhao [91] quantified strain on a stented latex straight tube using 3D DIC and developed a computational model to recapture the stenting experiment. However, the diameter and thickness of the vessel analogue investigated in this study was two times greater (6.32 mm) and five times thicker (1.55 mm) than the typical dimensions of a coronary artery. Anyway this study provided basic understanding of the artery deformation. An advantage in this study was the validation of the experimental outcome with the computational model.

1.5.4. EXPERIMENTAL MODELS FOR ARTERIES

The use of mock arteries/coronaries analogues in experimental investigations is increasing. They can be adopted as a replacement for animal tissue, reducing cost and ethical concerns [89]. Latex and silicone mock arteries used in experimental studies of stent expansion allow researchers to understand stent behaviour and evaluate the complex mechanics related to variations in stent design [89].

Walker *et al*. [92] studied a blood vessel analogue which was fabricated from layered latex. A plastic rod was covered with uniform coats of latex using a fine brush to create a latex tube. This was used for compliance and pulse wave velocity measurements. The results demonstrated that a vessel analogue can achieve similar mechanical properties to these results of human arteries observed *in vivo* (Young's modulus of 0.61-1MPa).

The use of mock arteries also provides the possibility of lesion building. Connolley *et al.* [89] used silicone foam to represent the plaque. For experimental use latex or silicone mock arteries require radial compliance, radius and wall thickness dimensions similar to real arteries [92-94]. The table below presents the dimensions, internal diameter (ID) and wall thickness (t), of the mock arteries used in previous studies.

Table 1: Internal diameter (ID) and wall thickness (t) of the vessel mock arteries used in the previous studies.

	Mock arteries				
	Toner [95]	Rajesh [94]	Conolley [89]	Colombo [96]	Zhao [91]
ID [mm]	3.0	3.0	3.0	3.0	6.0
t [mm]	0.5	0.34, 0.35, 0.36	1.0	0.8	1.5

SUMMARY

Coronary restenosis following stent deployment remains an important and unresolved clinical problem [28, 59]. The amount of neointimal tissue growth in response to stent deployment has been shown to be related to the magnitude of the stresses and strains caused during stent implantation [1, 70, 71, 97]. ISR is reduced from 20-30% to 10% of treated patients by drug eluting stents [10], but these mechanical bases of injury due to non-uniform stent deployment still remains an issue. There is a need for high quality validation data to confirm the results of numerical models of vessel deformation during stent expansion. The application of non-contact, optical methods to the study of stent-vessel interaction yields such data at an appropriate resolution to describe the local variation of strain within the vessel wall. A detailed understanding of 3D stent geometry and dynamic variation may provide useful information for engineers and clinicians in terms of optimising stent design. It is acknowledged that improvements in stent design can reduce neointimal tissue growth and that restenosis varies with stent design [76].

It is suggested that the examination of non-uniform local strain distribution on the artery wall following stent implantation can deliver improvements in future stent design. Stent-induced local strain concentrations in the vessel wall may lead to tissue injury, which initiates neointimal tissue growth. Whilst experimental techniques are starting to be applied to the study of this problem, only two experimental studies report

the vessel wall strain during stent expansion in three dimensions. Digital image correlation (DIC) is applied to track surface deformation. However, this brief technical note [90] and stent expansion in the latex vessel [91] does not include detailed local strain results.

This thesis describes the development and application of non-contact methods for optical imaging of stent expansion. Chapter 2 reviews optical imaging methods which have been applied to measure object geometry and deformation. The mathematical basis of stereo photogrammetry is described; cameras are calibrated to assess the accuracy of the Bouguet Calibration Toolbox. Additionally, a preliminary deformation test of an elastic material is reported to determine the feasibility of using this technique to measure strain. In Chapter 3 an optical system is characterised at three different length scales with focus on the assessment of coronary artery stent performance. Chapter 4 explains the challenges associated with the accurate assessment of 3D device geometry using imaging techniques. Quantitative comparison of a volumetric 3D technique and biplanar 2D technique is reported for two distinct clinical applications encompassing differing length scales. Chapter 5 outlines application of the 3D optical reconstruction method to examine stent deployment, characterising the change in geometry locally and globally during balloon inflation. Discussion of these results considers the specific mechanisms of expansion which may cause maladaptive chronic vascular responses. Chapter 6 focuses on the stent together with vessel analogue wall interaction and the local strains induced following stent deployment. Image registration methods are applied to quantify local strain. Chapter 7 summarises the results of the thesis and describes opportunities for further research.

A highly characterised and validated optical system is developed throughout this project to obtain results of sufficient accuracy to determine strain fields in vessel analogues and in the future in coronary arteries *ex vivo,* underpinned by rigorous calibration and quality assurance assessment. This study also reports the validation of optical reconstruction results with micro-CT.

CHAPTER 2

3D OBJECT RECONSTRUCTION FROM 2D IMAGES

Stereo-photogrammetry, an optical non-contact method, was used to characterise the geometry and deformation of stents in three dimensions (3D). This method uses stereo image pairs to compute 3D world coordinates by triangulation of selected markers/landmarks and requires a rigorous experimental procedure to provide camera calibration and compute intrinsic and extrinsic camera parameters. 3D surface reconstruction is accomplished by triangulation, performed through projections of rays from right and left camera origins through matched pixel pairs in the right and left images.

This chapter initially reviews optical imaging methods which have been applied to measure object geometry and deformation. This is followed by a description of the mathematical basis of stereo photogrammetry and a discussion of methods for camera calibration and calibration/reconstruction accuracy assessment in an experimental camera system. Finally, a preliminary test is reported to demonstrate the feasibility of using this technique to measure strain in a deforming elastic material.

2.   INTRODUCTION

This study uses stereo-photogrammetric optical reconstruction methods to characterise the geometry and deformation of the objects in three dimensions (3D), particularly the examination of stent expansion behaviour and interaction with vessel analogue. As described in Chapter 1, quantification of strain following stent implantation can aid understanding of the mechanical injury to the vessel wall during stent expansion with implications for stent design and deployment techniques.

Stereo-photogrammetry for reconstruction of three dimensional (3D) geometry using pairs of two dimensional (2D) images is a non-contact technique used for quantitative measurement of surface geometry from optical digital images. The fundamental principle used to determine 3D geometry and provide depth from 2D images is triangulation.   Stereoscopically positioned cameras are used to capture object deformation and the triangulation process determines surface 3D coordinates which can be used to determine strain as the object deforms. A high contrast pattern which deforms along with the object surface is necessary to provide correspondence points for triangulation to quantify the deformation.

Before describing the mathematical basis of stereo photogrammetry in further detail a review of optical imaging methods which have been applied to measure object geometry and deformation is provided.

2.1. OPTICAL METHODS FOR MEASUREMENT OF 3D GEOMETRY AND DEFORMATION

To examine stent expansion it is important to avoid any contact and perturbation of the device, so sensors such as strain gauges are far from ideal to determine strain variation during stent deployment [98]. In any case, electrical resistance strain gauges are unable to provide a full-field map of the strain distribution on a deformed object and are not small enough for coronary stent application. In principle, optical imaging techniques have the advantage of giving direct, unambiguous and quantitative depth information. At sufficient frame rates, digital cameras can freeze object movement to provide a record of the object deformation [99] supported by software to control the image capture process [100]. Other non-contact methods include use of Moiré patterns, which require two identical patterns of closely spaced straight lines which are overlaid while displaced or rotated a small amount from one another. This technique is unsuitable for use in the current study due to the complexity of projecting the grating accurately onto vessel analogue wall and the lack of spatial resolution for the small length scales involved [101]. Moreover, it cannot be applied to quantify large deformations. Photoelasticity methods require application of a photoelastic coating to the object surface which is likely to be difficult for both the stents and coronary artery analogue, since local reinforcement and material stiffening can occur [101].

Several optical methods that have previously been used to examine object surface deformation are reported in *Table 2*.

Table 2: Experimental techniques used for strain measurement. OP- optical reconstruction; IR- image registration.

Method	Large deformation	Full-field measure	Local measure	Out-of-plane displacement	Application method
Strain gauges	No	No	Yes	Sensitive	On the surface
Photoelasticity	Yes	Yes	Yes	Sensitive	Coating
Moire	No	Yes	Yes	Sensitive	Grating
OP	Yes	Yes	Yes	Sensitive	Landmarks
IR	Yes	Yes	Yes	Sensitive	Speckle pattern

Hence, this project focuses on the optical photogrammetry (OP) reconstruction method using both structured and unstructured marker patterns to determine deformation using image registration (IR) techniques. The remainder of this chapter describes the mathematical basis and experimental implementation of an OP technique using manual methods to define correspondence for triangulation. Further discussion of image registration techniques is provided in Chapter 6.

2.2. PHOTOGRAMMETRY

Photogrammetry provides a three dimensional (3D) description of surface geometry using two dimensional (2D) images from a pair or more of calibrated cameras [99, 102]. This has been shown to give reliable information about object surface properties [103]. The photogrammetric technique can be applied to measure both rigid-body and elastic object behaviour. Large rigid body motions can also be examined, and these should not influence data accuracy. Complex deformations (such as stent deployment) can be measured as well as those of simple systems (such as elastic material or ideal cylinders). Where the deformation takes place over short timescales, the two independent cameras need to be synchronised to freeze the investigated object at each stage of deformation. A marked pattern on the object

surface provides landmarks which are imaged before and during deformation using an ordinary light source. The 2D images obtained from each of the two stereoscopically positioned cameras are used to compute 3D world coordinates of the landmark points using triangulation [104].

Stereo-photogrammetry has been demonstrated as a good solution for measuring deformation of objects at a range of scales in three dimensions [65, 102, 105]. This includes stent length scales using high magnification lenses [65, 106]. The fundamental approach used by this technique is triangulation [107]. By taking an image from at least two cameras in different locations, 3D coordinates of the points of interest are obtained mathematically [104, 108].
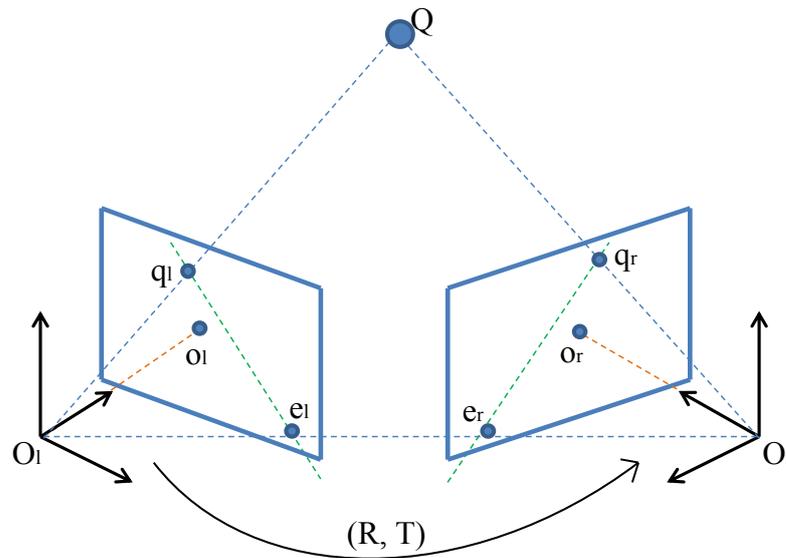
Figure 2.2-1: The epipolar plane consists of the 3D position of a point (Q) and the optical centres of left (Ol) and right (Or) cameras. The epipolar lines correspond to the intersection of this plane with the image sensors of the left and right cameras. Projection of the 3D point in each camera image should lie along the epipolar line; ql and qr are the pixel locations of Q in left and right images. R and T represent the rotation matrix and translation vector between the left and right cameras.

Triangulation of a selected point in three dimensional space can be visualised by intersection of epipolar lines from two cameras as shown in *Figure 2.2-1*, where Q is the 3D position of a landmark point and ql and qr are the positions of this landmark in each of the left and right camera images. Triangulation of a set of points requires knowledge of the camera position and orientation, acquired through a calibration process, which is a rigorous experimental procedure (further detail is provided in section 2.2.3). The accuracy of the photogrammetric measurement depends on several factors, including: camera sensor resolution, the size of the object within the camera field of view, the number of images used to produce the calibration data and the geometric layout of the cameras relative to the object [99]. To obtain high accuracy 3D data the images need to be of high quality as each camera captures the 3D scene as a flat 2D image. During this mapping information on depth is lost and is recovered through triangulation and 3D reconstruction.

2.2.1. TECHNICAL PRINCIPLES AND MATHEMATICAL BACKGROUND

Camera calibration needs to be carried out to characterise the imaging system, so that interpretation of the point in the image can be related to its position in the real world. Typically this involves an experimental calibration protocol that computes camera parameters, which can be used, along with correspondence points in the stereo image pair to carry out 3D optical reconstruction. To be familiar with the camera calibration method it is important to understand how real world objects are projected onto the image sensor inside the camera. A pinhole camera model is used to describe the basic geometry of projecting rays. This simple model can then be expanded by adding lens distortion terms.

2.2.1.1. THE PINHOLE CAMERA MODEL

The classical geometric model for a camera is a pinhole camera model which describes the mathematical relationship between the 3D real world and its projection onto the 2D image plane [109]. All light rays are assumed to pass through the optical centre and no lenses are considered. Geometric distortion and blurring are not included in this system [104]. The distance from the pinhole aperture to the image plane (P) is the focal length f (*Figure 2.2-2*). Perspective projection is used to describe the relationship between the 3D real world coordinates and the coordinates of its projection [110].
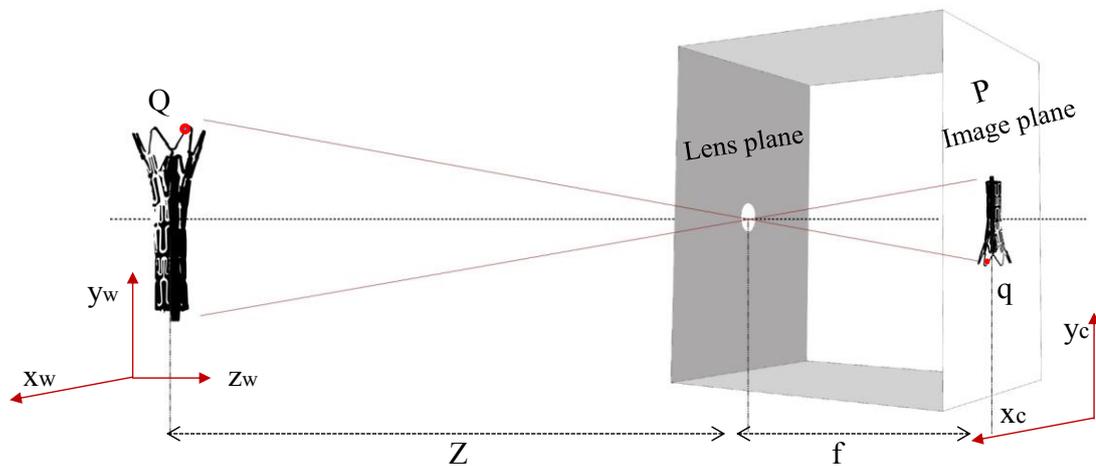
Figure 2.2-2: Pinhole camera geometry showing the projection of stent geometry. The point q on the imaging plane is the projection of the real world point Q.

The principle of similar triangles is applied to calculate the projection of point $Q=(X_w, Y_w, Z_w)$ onto the image at point $q=(x,y)$, given by equation 2-1.

$$x = f\, X_w / Z_w \qquad\qquad y = f\, Y_w / Z_w \qquad\qquad \text{2-1}$$

Modifications are required if this model is applied to a physical camera containing lenses. To represent the aspect ratio of the camera sensor s_x, s_y is defined as the sensor

size in horizontal and vertical directions respectively [111]. This gives a new measure of focal length:

$$f_x = f \ s_x \qquad\qquad f_y = f \ s_y \qquad\qquad\qquad \text{2-2}$$

As the centre of the sensor may not lie on the optical axis, possible displacement of the optical centre can be defined using parameters c_x and c_y (x and y coordinate of principal point determined in pixels) [109]. The parameters f_x, f_y, c_x and c_y are known as intrinsic parameters. Including these additional parameters to the camera model relates the coordinates of point $Q(X_w, Y_w, Z_w)$ to the pixel coordinates of point q(x, y):

$$x = f_x(X_w/Y_w) + c_x$$

$$y = f_y(Y_w/Z_w) + c_y \qquad\qquad\qquad \text{2-3}$$

The depth information in a stereo rig is computed through information about the relative position of the two cameras. If we consider an undistorted, aligned stereo rig the Z coordinate of the object is computed from the magnitude of the translation vector (T), as shown in *Figure 2.2-3*, where:

$$Z = fT/(qlx - qrx) \qquad\qquad\qquad \text{2-4}$$
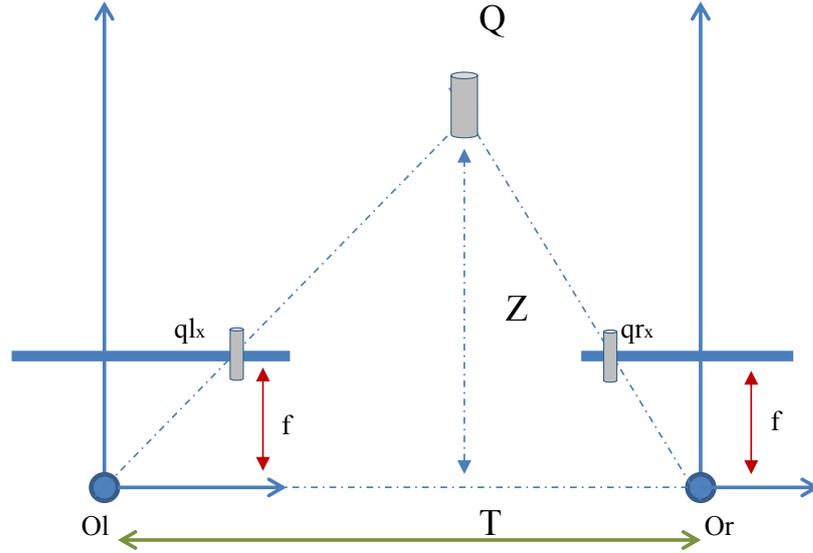
Figure 2.2-3: Undistorted, aligned stereo rig demonstrating the relationship between depth coordinate (Z) and magnitude of translation vector between camera pair; qlx and qrx are the x coordinates of the Q target in the left and right image respectively.

Experimental camera rigs often include a rotation (R) between the viewing planes of each camera. The rigid body transformation from the 3D world, $Q(X_w, Y_w, Z_w)$, to the coordinate system of each camera, $c(x_c, y_c, z_c)$, can be described by a 3 x 3 rotation matrix and translation vector [112].

$$\begin{bmatrix} x_c \\ y_c \\ z_c \end{bmatrix} = R \begin{bmatrix} X_w \\ Y_w \\ Z_w \end{bmatrix} + T, \qquad \text{2-5}$$

$$\text{where } R = \begin{bmatrix} r_1 & r_2 & r_3 \\ r_4 & r_5 & r_6 \\ r_7 & r_8 & r_9 \end{bmatrix} \text{ and } \qquad T = \begin{bmatrix} T_x \\ T_y \\ T_z \end{bmatrix} \qquad \text{2-6}$$

3D rotation can be decomposed into a 2D rotation around each axis. The products of rotation around the axes are the rotation matrices. As an example a two-dimensional rotation around the axis Z is presented below.
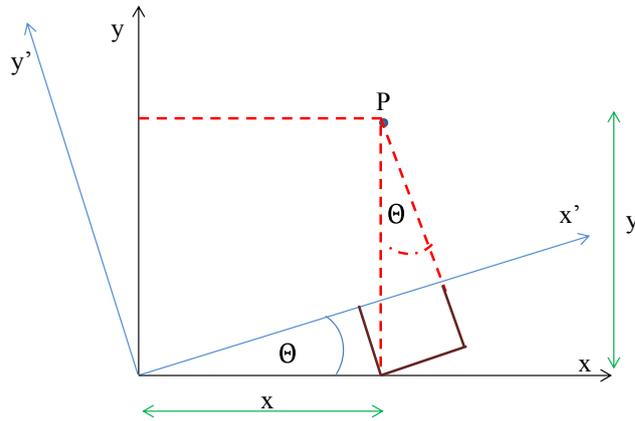
Figure 2.2-4: Rotating point

$$\begin{bmatrix} x' \\ y' \end{bmatrix} = R_z(\Theta) \begin{bmatrix} x \\ y \end{bmatrix} = \begin{bmatrix} cos\Theta & sin\Theta \\ -sin\Theta & cos\Theta \end{bmatrix} \begin{bmatrix} x \\ y \end{bmatrix}$$

These rotation matrix and translation vectors are extrinsic parameters provided by stereo calibration, as discussed later, and are a prerequisite for carrying out 3D geometry reconstruction.

2.2.2.2. LENS DISTORTION

Theoretically it is possible to define a lens that introduces no distortion. However, lenses in physical cameras are not perfect and as a result the images may include lens distortion effects which represent the deviation from the image produced by a perfect lens. In a real system lenses may not be fixed perfectly parallel to the sensor plane [111]. Radial and tangential distortion may result from the lens shape and assembly process of the camera respectively [113]. Fryer [114] defined radial distortion in terms of three parameters: k1, k2 and k3 and determined tangential distortion by two additional parameters p1 and p2. The same distortion model was applied in Bouguet Calibration Toolbox.

$$x_{corrected} = x(1 + k_1 \ r^2 + k_2 \ r^4 + k_3 \ r^6)$$

$$y_{corrected} = y(1 + k_1 \ r^2 + k_2 \ r^4 + k_3 \ r^6)$$

$$x_{corrected} = x + \left(2 \ p_1 \ y + \ p_2 \ (r^2 + \ 2x^2)\right)$$

$$y_{corrected} = y + (p_1 \ (r^2 + \ 2y^2) + \ 2p_2 \ x) \qquad \text{2-7}$$

where *r* is the distance of a point on the image plane from the optical centre. In a radial distortion plot, distortion is zero at the centre of the image and increases with distance from the optical centre due to bending of the rays further from the lens centre (*Figure 2.2-5a*). This behaviour is often observed in real cameras where the image can become noticeably distorted in pixels near the edges of the sensor [111]. $x_{corrected}$ and $y_{corrected}$ are new locations of *x* and *y* corrected for lens distortion (equation 2-7). *Figure 2.2-5a* and *b* shows the radial and tangential components of the distortion model computed during camera calibration of an experimental system at the coronary artery length scale described in Chapter 4.

Note that more peripheral points are increasingly displaced. The arrows represent the effective displacement of a pixel induced by the lens distortion. Note that points at the corners of the image are displaced by as much as 15 pixels for radial distortion. The second figure shows the impact of the tangential component of distortion. On this plot, the maximum induced displacement is 1.4 pixel. The cross on the figure indicates the centre of the image, and the circle the location of the principal point.

Pixel error	= [0.7954, 0.9826]	
Focal Length	= (14340.5, 14405.8)	+/- [1747, 1986]
Principal Point	= (562.543, 428.24)	+/- [50.39, 54.46]
Skew	= 0	+/- 0
Radial coefficients	= (-17.68, 8700, 0)	+/- [10.32, 7038, 0]
Tangential coefficients	= (0.01447, -0.007154)	+/- [0.02557, 0.02846]
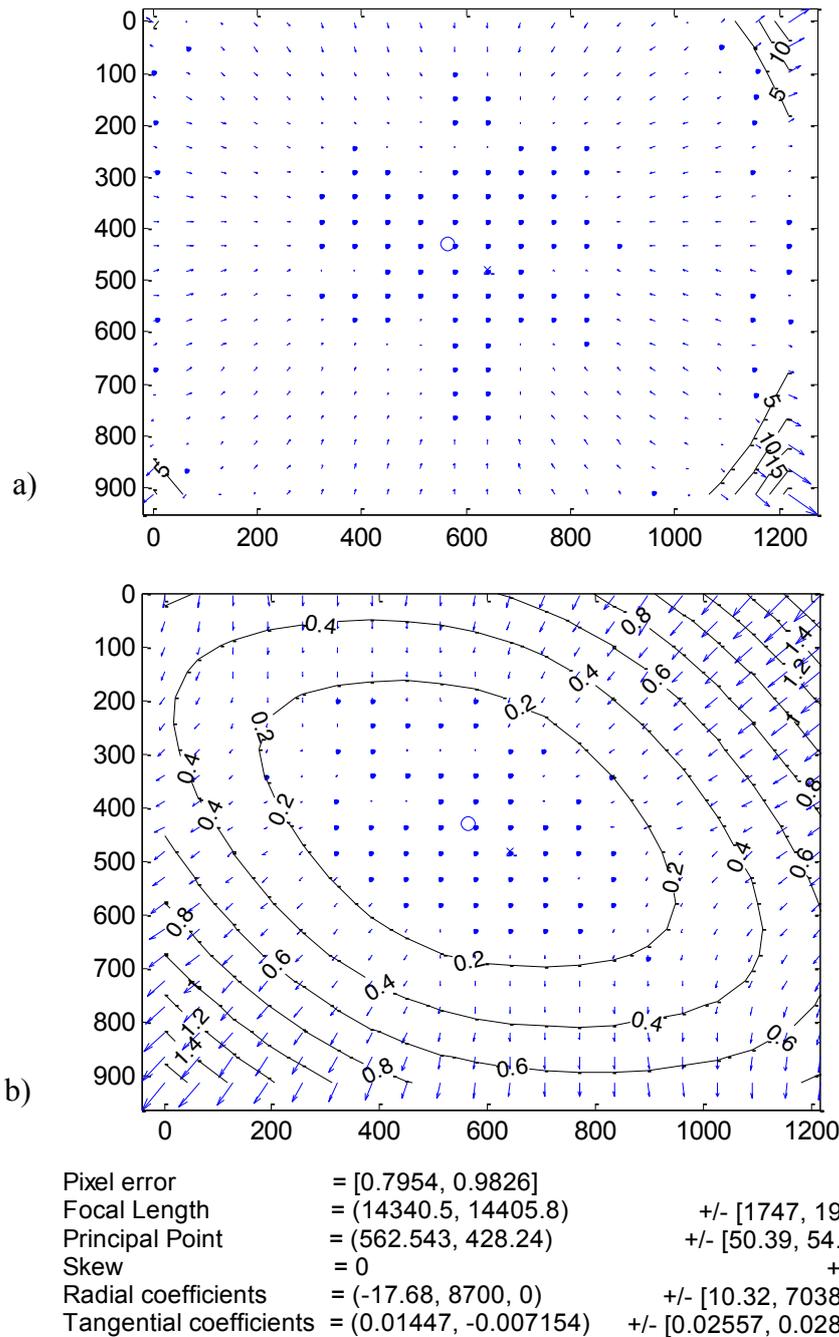
Figure 2.2-5: a) Radial and b) tangential distortion plots made in Matlab using the Bouguet Calibration Toolbox [115] for a calibration image obtained with a Flea2 camera with a 31.5mm focal length lens. The arrows on the rectangular grid show pixel displacements induced by the lens distortion.

2.2.2. CAMERA CALIBRATION

Accurate camera calibration is a prerequisite in 3D reconstruction in order to extract precise quantitative measurements from 2D images [116]. The calibration process is

used to compute intrinsic and extrinsic parameters of the cameras, which are used in reconstruction [104, 109]. The intrinsic parameters determine the inherent properties of the optics, whereas the extrinsic parameters inform us about camera position and orientation with respect to the coordinate system.

Accurate calibration procedures have been developed over many years [115-117]. A Matlab toolbox for camera calibration was used in this study. The toolbox is based on the work of Zhang [116] and Bouguet [115]. The main advantage of this toolbox is use of a flat calibration object with a checkerboard grid pattern, which can be printed using high resolution laser printers. This Bouguet Calibration Toolbox for Matlab has been used in previous studies [118, 119] and has demonstrated point extraction to sub-pixel accuracy [120]. Calibration is achieved using a checkerboard grid pattern of accurately known dimensions, chosen depending on the required magnification. The grid is captured in a number of orientations in order to calibrate each camera. *Figure 2.2-6* illustrates camera calibration output: checkerboard grid pattern (36 x 36mm) captured in 11 various orientations.
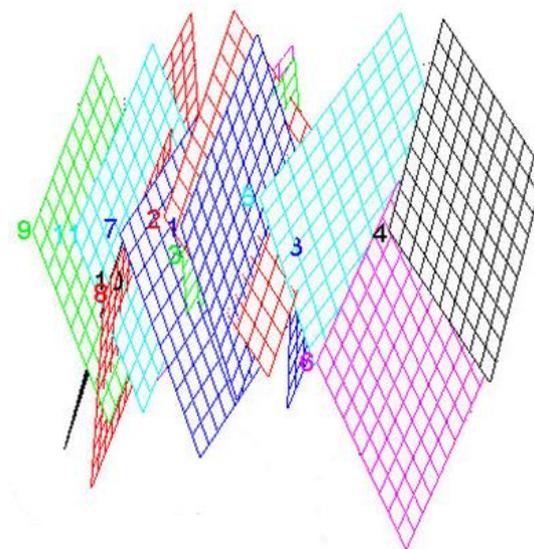
Figure 2.2-6: Grid position plotted in Matlab captured in 11 different orientations during the experimental calibration test.

The 3D stereo rig geometry is determined by stereo camera calibration, providing the extrinsic parameters which describe the grid orientations in relation to both cameras. The accuracy of stereo calibration can be assessed by comparison between the calculated extrinsic parameters and the physical stereo system distances measured manually (see section 2.4.2, *Figure 2.2-15*). To assess calibration accuracy a control object of known size is imaged and the stereo calibration data is used to reconstruct the object geometry through triangulation (see section 2.4).

2.2.2.1. SINGLE CAMERA CALIBRATION

To carry out single camera calibration, images from the right or left cameras are captured for various positions of the checkerboard grid and loaded into Matlab (The MathWorks Inc., Natick, MA, 2000). In the figure below, *Figure 2.2-7*, two grids imaged in six orientations are presented.

a)   b)
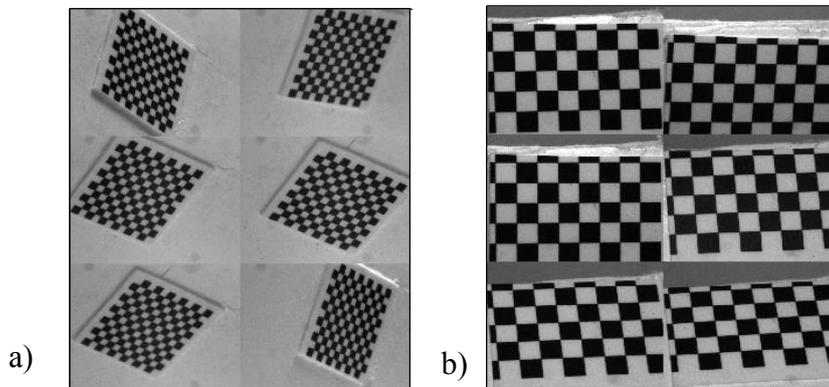
Figure 2.2-7: Calibration images obtained with a Flea2 camera, single image size 1288x964. a) A 10 x 10 checkerboard captured in 6 positions with internal grid size 0.5x0.5mm prior to a stent deployment experiment (Chapter 4, Coronary stents). b) A 6 x 4 checkerboard captured in 6 positions with internal grid size 2x2mm (Chapter 5, coronary stents).

Initially both cameras are calibrated separately. The corners of the grid are extracted in all images. Corner extraction requires the user to manually define four extreme corners on the checkerboard pattern and confirm the size of each grid square in the *x*

and *y* directions (dX and dY). It is important to be aware that dX and dY determine

the calibration scaling i.e. the lengths dX and dY need to be determined before cameras

can be accurately calibrated [115].
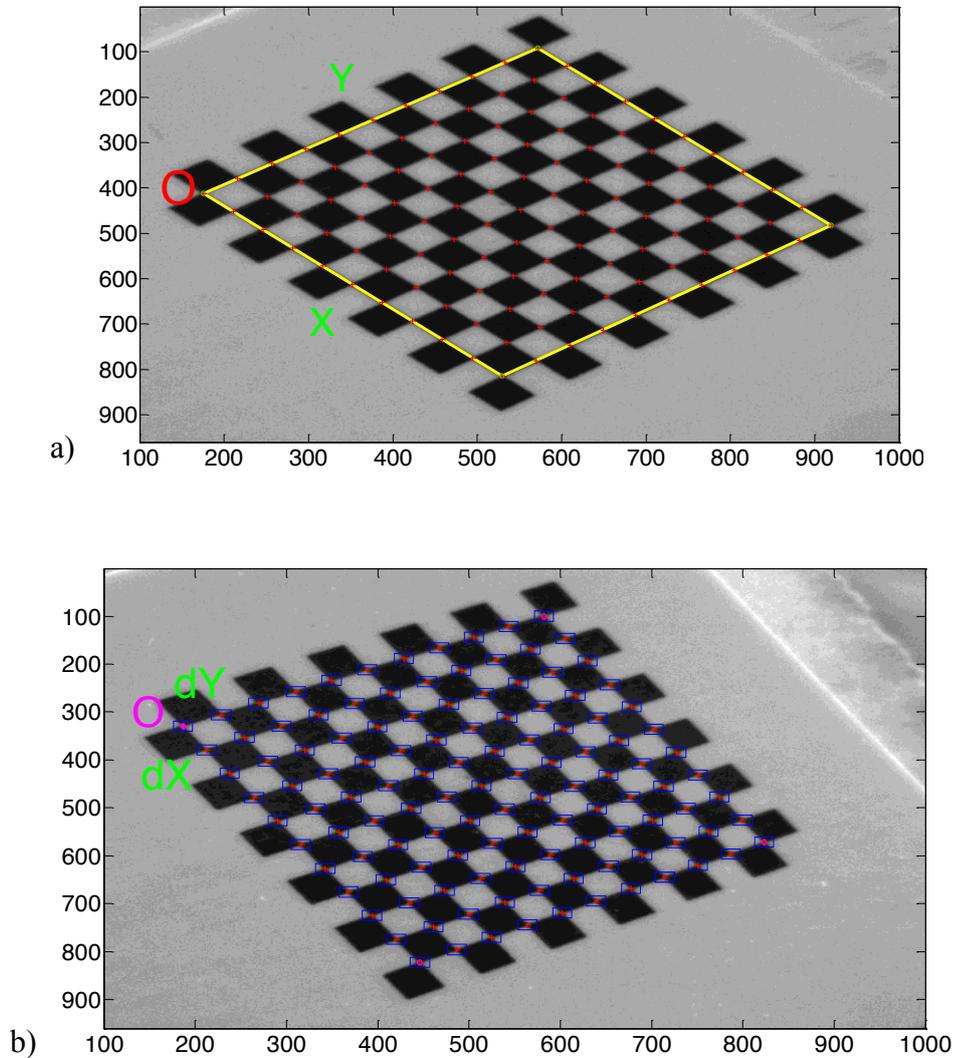
Figure 2.2-8: a) The boundary of the calibration grid with the origin point of the reference frame attached to the grid. b) Blue squares around the corner points depict the limits of the corner finder window.

The same set of points must be selected in each grid image with consistent selection

of the first clicked corner to define the origin point (O), i.e. upper left hand corner of

the checkerboard grid pattern (*Figure 2.2-8a*), where row and column directions are

defined along the *x* and *y* axis respectively. The corner extraction automatically identifies all other corners and determines the number of squares in the pattern. When the extracted grid corners (red crosses in *Figure 2.2-8*a) are close to the grid corners in the image this indicates absence of noise and aberrations. The blue squares around the corner, *Figure 2.2-8b* represent the limit of the corner finder window. The toolbox requires typing the size of the window to detect the corners.

If image distortion is extreme the Bouguet Calibration Toolbox may struggle to predict the correct number of squares and it may be necessary to repeat the image acquisition and calibration process. Consistent identification of origin location is important if more than one camera from the same setup is investigated (in this case to compute the relative position of the stereo camera pair in space) [108] to guarantee an identical pattern reference frame. Bouguet demonstrated that the Calibration Toolbox can extract the grid corners resulting in reprojection error of 0.1 pixels [115] using 300 mm x 300 mm grid (30 mm x 30 mm internal grid size). The reprojection error (for examples see *Figure 2.2-10*) is a geometric error corresponding to the distance in an image (hence, measured in pixels) between a projected point and a measured one. This error is calculated by projecting the checkerboard points from world coordinates into image coordinates. The comparison between reprojected and detected points gives the distances in pixels which present the error. When this error is small, the corners have been extracted well. A larger error often occurs when the images are distorted and it is harder to find the corners. Reprojection errors are considered to be non-significant if less than one pixel (Computer Vision System Toolbox, MathWorks). During this study the reprojection error varied from 0.5 pixels for a 30 mm x 30 mm grid (3 mm x

3 mm internal grid size) to a maximum of 0.9 pixels for a 6 mm x 6 mm grid (0.5 mm x 0.5 mm internal grid size).

Following identification of the grid corners, the camera calibration is obtained in two steps:

- initialisation (not including any lens distortion),
- optimisation (a non-linear optimisation step minimises the total reprojection error (in the least squares sense) over all the calibration parameters), including lens distortion terms,

Single camera calibration provides the intrinsic camera parameters:

- focal length (f_x, f_y), the distance from the middle of the lens to its focal point, calculated in pixels and stored in the 2 x 1 vector, fc,

- principal point (c_x, c_y), the intersection of the optical axis and the image plane, calculated in pixels and stored in the 2 x 1 vector, cc,

- skew coefficient (the image axes skew), the angle defined between the x and y pixel axes, calculated in degrees (for the perfect sensors axes are perpendicular to each other, 90°) and stored as a scalar, alpha_c,

- lens distortion (k_c), radial and tangential distortion coefficients, stored in the 5x1 vector, kc,

- pixel error (err_x, err_y), defined as 3x the standard deviation of all the reprojection errors, stored as 2 x 1 vector, err.

2.2.2.2. STEREO CAMERA CALIBRATION

To obtain stereo calibration with multiple cameras, the simultaneous capture of every grid orientation by both right and left cameras is required in order to generate a consistent set of stereo data. The stereo calibration algorithm starts from parameters for both cameras obtained from their single camera calibrations. The stereo calibration produces two sets of updated intrinsic parameters (one for each camera), and allows computation of the extrinsic parameters which describe relative 3D camera position and orientation [117]. The relative geometry of two or more cameras in the 3D world is modelled as a single rigid body transformation [108], as described in equation 2-5 and 2-6:

▪ rotation matrix (R), the rotation between the coordinate system of the camera (u, v, w axes) and coordinate system of the calibration object (x, y, z axes), stored as a 3 x 3 matrix

▪ translation vector (T), the vector of the origin of the grid pattern in the camera reference frame [115], stored as a 3 x 1 vector.

2.2.2.3. STEREO CAMERA RIG SEPARATION ANGLE

Cameras in a stereo rig need to be placed at a certain angle in order to image the stent. The image of the device needs to be sharp and, ideally, no reflection should occur. To ensure that the geometric layout of the cameras to the object and angle of the stereo rig would not influence final results, calibration and reconstruction accuracy was studied for three angles.

2.2.2.3.1. METHODS

The analysis of experimental camera calibration was undertaken to check differences in results for different angle between two cameras. It was important to check how much the angle between cameras influenced reconstruction accuracy. A stereo rig was used to capture checkerboard grid patterns in number of orientations for calibration and 3D reconstruction accuracy assessment. The calibration protocol was repeated using a stereo rig with camera separation angle 30º, 60º and 90º, shown graphically in *Figure 2.2-9*.
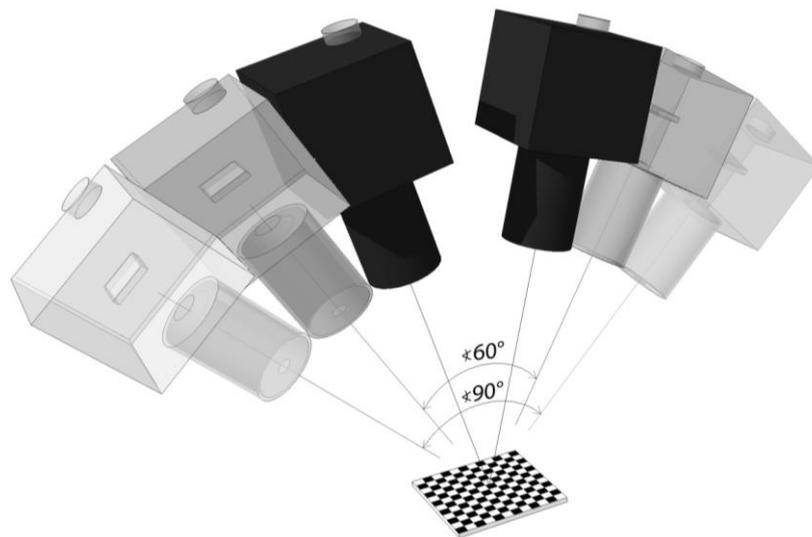
Figure 2.2-9: Angle separation to capture the calibration grid: 30, 60 and 90 degree respectively.

The calibration images (6 for each angle) were used to check reconstruction accuracy. The distance between 10 internal grids (2 x 2 mm each) was measured for five translations to control the variation.

2.2.2.3.2. RESULTS

The pixel reprojection errors for right and left camera calibrations are presented in *Table 3, Figure 2.2-10*.

Table 3: The average of the reprojection errors presented in Figure 2.2-10.

	Mean reprojection error			
	Left		right	
degree	x	y	x	y
30	0.85	0.60	0.72	0.60
60	0.85	0.57	0.71	0.57
90	0.86	0.58	0.73	0.61
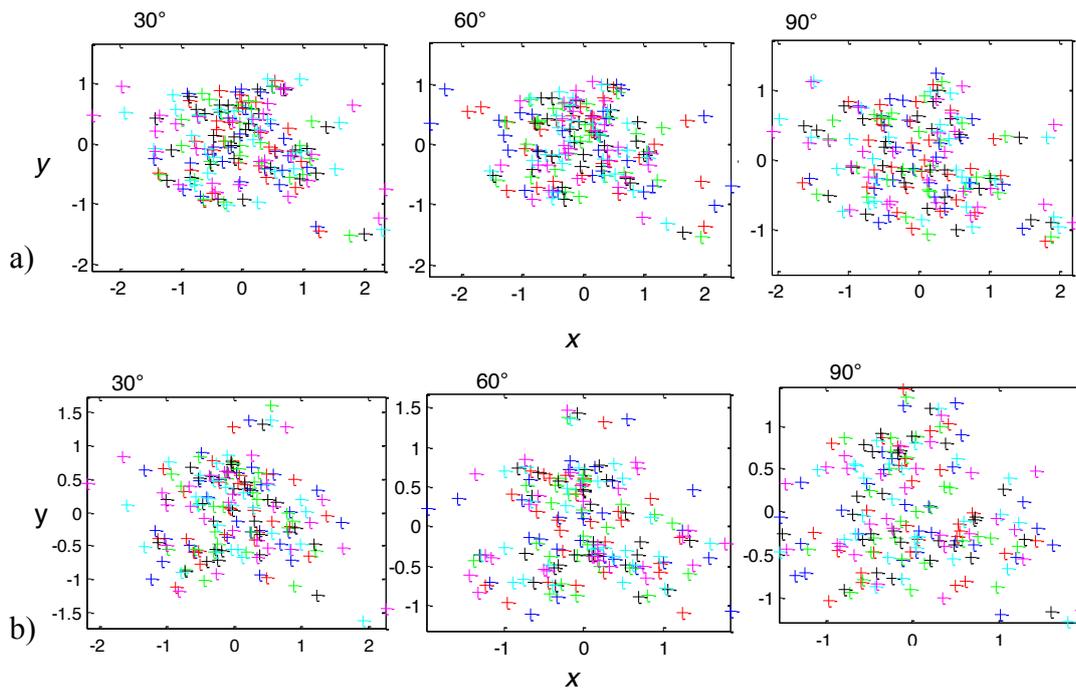
Figure 2.2-10: Pixel (reprojection) errors for a) left and b) right camera calibration for three separations of the camera

3D reconstruction accuracy assessment results are presented in table below.

Table 4: The output data from the 3D accuracy assessment test for the stereo rig set at different angles between cameras.

Degree [°]	Difference [μm]			STDEV [μm]
	max	average	min	
30	55	22	3.0	15
60	52	23	2.3	16
90	41	14	1.8	12

2.2.2.3.3.   DISCUSSION

There is no significant difference between the reprojection errors obtained for the three stereo rigs. These results show that the angle between cameras can be set between 30 and 90 degrees. In the previous study for the *in vitro* measurement stent expansion in 3D [88] the separation angle of 60 degree was used. Lujan *et al*. [121] set different angles between cameras to measure the strain on the knee joint. He found that the strain measurement was more accurate in the x direction when the camera angle was largest and least accurate when the angle was at its minimum; the opposite results occurred in the z direction. In the stereo rig design manuals a larger stereo-angle is advised to use to improve out-of-plane results.

2.3.   3D OBJECT RECONSTRUCTION FROM 2D IMAGES

Following calibration of the stereo camera pair, stereo-photogrammetry can be applied to determine 3D geometry (Chapter 4) and deformation (Chapter 5 and Chapter 6). The reconstruction method requires that distinct landmarks/markers on the object surface are visible to both cameras, and that the cameras do not move during the collection of a single stereo image pair.

The depth of the object can be recovered from each stereo image pair through reconstruction using triangulation [122]. The 3D position of a point in space is computed from the pixel locations of the point in both 2D images and the camera calibration parameters. If the point location is first identified in a single image, knowledge of relative camera geometry from calibration allows selection of a corresponding landmark/marker in the second image aided by a geometric epipolar constraint. In the other words once a landmark point is identified in one image, if the

same point lies on the epipolar line in the other image determined from the calibration data, this indicates robust camera calibration [108, 109]. If the landmark does not lie on the epipolar line this points to poor calibration, that images from left or right cameras were taken at different stages of object deformation or that there are other significant errors due to noise during the experiment. To provide the 3D coordinates of the points of interest [122] as presented in *Figure 2.2-1*, epipolar lines are mathematically intersected.

Figure 2.2-11 shows an image of the checkerboard grid pattern and the speckle pattern sprayed on elastic material and coronary stent from the experimental geometry reconstruction.
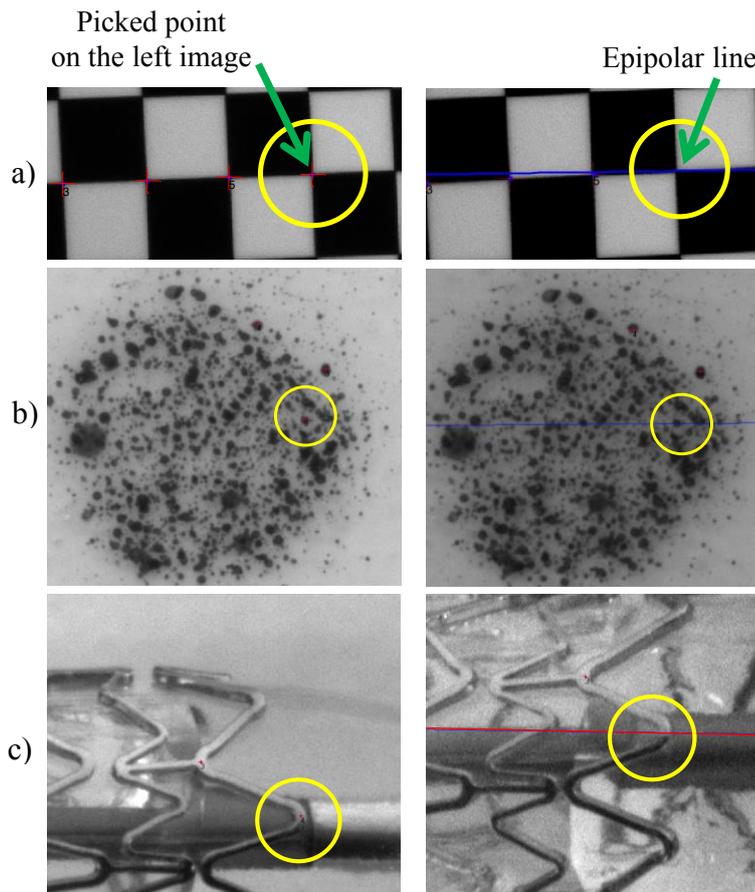
Figure 2.2-11: a) checkerboard grid pattern used to assess calibration and reconstruction accuracy; b)characterisation of the scattered pattern sprayed on elastic material and c) characterisation of the geometry of fully expanded stent on the angioplasty balloon.

Points have been selected in the left-hand (*Figure 2.2-11*) and the epipolar line indicates the correspondence points on the right-hand images, demonstrating robust calibration (images were taken during the experiments described in Chapter 5 and Chapter 6 with a Flea2 stereo camera rig).

In summary, the 3D position of a point in space is obtained by recording its 2D projections as reported by two independent cameras, placed at different locations [88]. Identification of the same points in stereo image pairs enables localisation of the point in the 3D coordinate space of the camera rig using triangulation.

Stereo triangulation [115] computes the 3D location of a set of points given their left and right image projections. If the point qlx and qrx are known, their projection lines are also known. If the two image points correspond to the same 3D point Q the projection lines must intersect precisely at Q. This means that Q can be calculated from the coordinates of the two image points; a process called triangulation.

Section 2.2 outlined the mathematical basis of camera calibration and described application of the Bouguet camera calibration Toolbox [115]. Section 2.3 describes an experimental stereo camera system used to examine a simple tensile test of elastic material undergoing large deformations. This experiment aims to demonstrate the feasibility of using photogrammetry for strain measurement through 3D reconstruction and assess the robustness of the camera calibration and reconstruction process.

2.4. EXPERIMENTAL ASSESSMENT OF CAMERA CALIBRATION AND APPLICATION TO STRAIN MEASUREMENT

Using the techniques described in section 2.3 an experimental system using Canon Powershot A40 cameras (CP-A40) was established to explore and to understand stereo-photogrammetry, and to establish a robust protocol for camera calibration, 3D reconstruction and strain measurement.

2.4.1.1. METHODS

The stereo camera pair was mounted on tripods to ensure setup stability and separated by approximately 70 degrees (*Figure 2.2-12*).
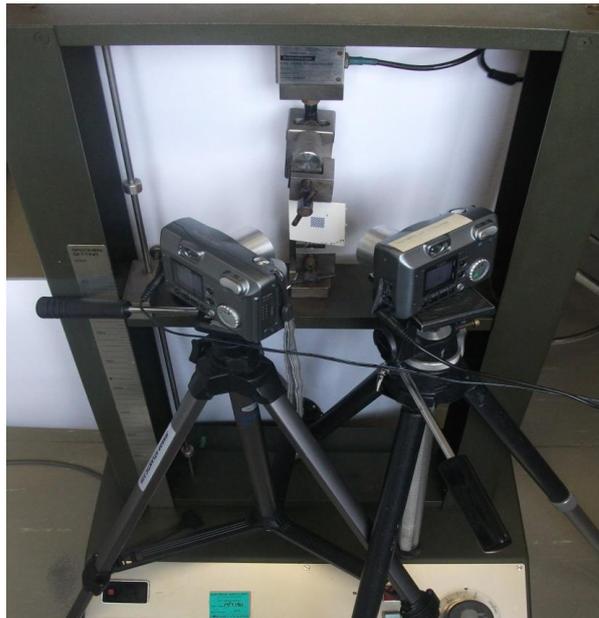
Figure 2.2-12: Experimental setup; stereo rig with two Canon Powershot A40 cameras.

A calibration checkerboard grid 12 x 12 squares (1 x 1 mm each) was imaged in six orientations with both cameras. As mentioned previously, in order to ensure precision of the calibration routine, accuracy assessments were carried out with a control object of known size (30 mm x 30 mm) with printed dots (*Figure 2.2-16*) separated by a

known distance (3 mm). This was translated using a travelling microscope (rigid body motion) through 2.5 mm in increments of 0.5 mm.

Following camera calibration, the feasibility of deriving strain measurements from reconstructed 3D geometry was assessed by imaging the deformation of a sheet of elastic material during a tensile test using a GOODBRAND GBX (Rakuten, Taiwan) testing machine. 2D image pairs were used to carry out 3D reconstruction of an elastic material marked with reference points separated approximately by 2 mm to allow strain calculation (*Figure 2.2-13*). Markers were applied manually using a Pilot fine point SW-DR5-B drawing pen. The sample was fixed in grips and stretched uniaxially at a strain rate of 0.167 mm/s to produce a total displacement of 10 mm over 60 seconds.
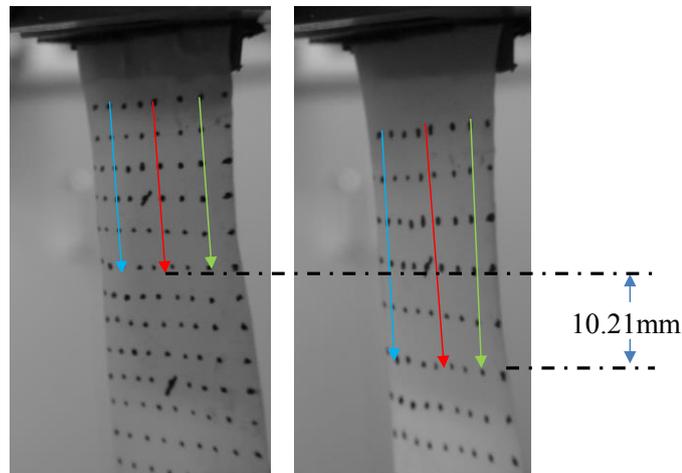
Figure 2.2-13: The elastic material with the far (blue), central (red) and near (green) investigated lines.

To capture images the shutter button from left and right camera had to be pressed manually, so the tensile machine was stopped every 5s ± 1s and a stereo image pair was captured (12 image pairs in total) after 10 seconds to allow stress-relaxation and

ensure consistent images from both cameras. The image pairs were used to carry out 3D reconstruction of the deformed material and derive measures of strain.

Strain measurement required tracking and reconstruction of consistent marker points on the deforming object. Engineering strain (ε), which is the ratio of deformation to the initial dimension, was computed as the change in length (ΔL) per unit of the original length (L_0) between reference points, L- length after deformation (2-7a). Average values of strain (equation 2-7b, *Figure 2.2-14*) were calculated for the three lines presented with blue, red and green in *Figure 2.2-13* and compared with the total strain (ε_T) measurement.

$$\varepsilon = \frac{L - L_0}{L_0} = \frac{\Delta L}{L} \qquad \text{a)}$$

$$\varepsilon_{av} = \frac{\left(\sum_i^n \varepsilon_i\right)}{n} \qquad \text{b)}$$

$$\text{2-7}$$
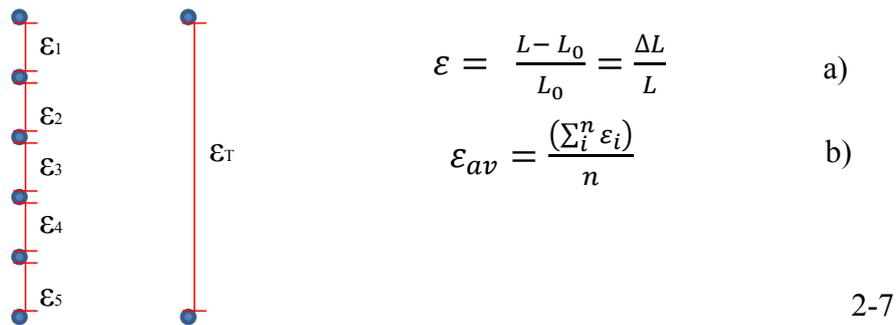
Figure 2.2-14: Diagram presenting strain characterisation.

The use of a 'centre of gravity' algorithm written by J. Hughes [123] was applied to locate the centre of each marker. This algorithm calculates the centre of mass of the closest dot to a manually selected location.

2.4.2. RESULTS

Single and stereo calibration was performed as described in subsections 2.2.3.1 and 2.2.3.2 respectively. The camera separation and distance from the grid derived from

camera calibration was shown to be in good agreement with manual measurements from the camera lens to the grid (97% ± 0.5%) made with a ruler, *Figure 2.2-15*.

Reconstruction of twenty printed dots on the surface of the cylinder indicated an uncertainty of dot separation of the order 30 μm, with inter-point distance of 3 mm ± 0.02 mm (*Figure 2.2-16*).
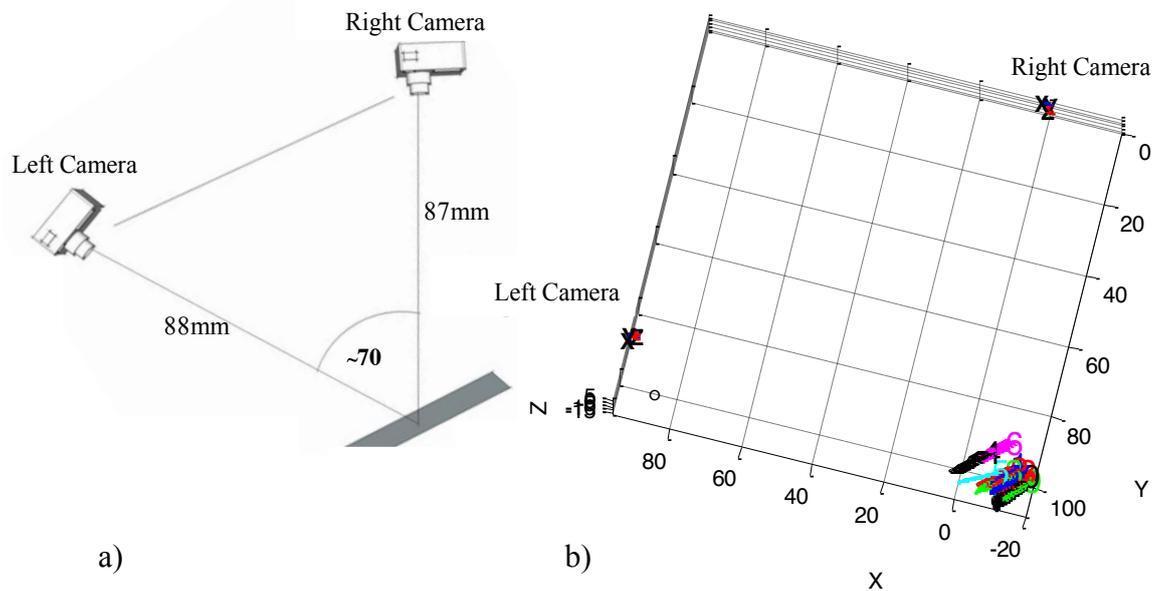
Figure 2.2-15: Accurate calibration (stereo 3D rig, b) is confirmed by accurate representation of the physical stereo system (a). Here the calibration result agrees with the manual measurements to within 97% ± 0.5%.
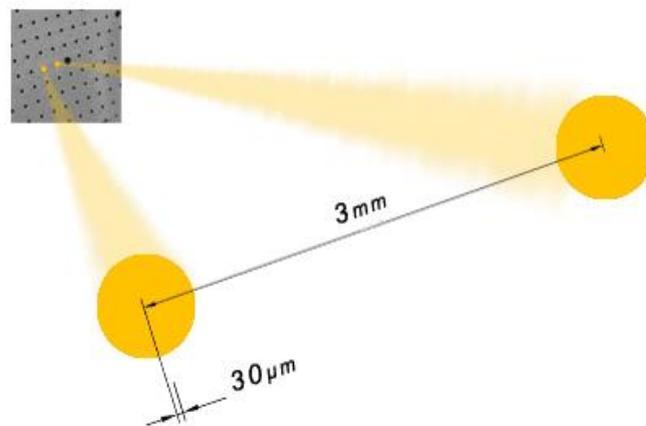
Figure 2.2-16: Control object used in accuracy assessment test. Magnified distance between points (3 mm ± 0.02 mm) to emphasize reconstruction accuracy (30 μm).

Total strain results computed from the 3D reconstruction for three regions of the elastic material (*Figure 2.2-13*) agreed to within 98% ± 0.7% of a manual caliper measurement of initial and final length. Average values of strain (equation 2-7) calculated for the three lines presented with blue, red and green in *Figure 2.2-13* differ slightly (0.5% ± 0.2%) from the total strain (ε_T) measurement (*Table 5*).

Table 5: The final strain results, ε_{av}- average value of $\varepsilon_{i's}$- εi, ε_T- the total strain between the first and last point, ε_i — the strain between neighbouring points.

Strain between markers [%]		
Area	$\boldsymbol{\varepsilon_{av}}$	$\boldsymbol{\varepsilon_T}$
First line	43.3	43.0
Central line	48.2	47.8
Last line	51.4	50.7

2.4.3. DISCUSSION

This simple experiment of deformation of a sheet of elastic material demonstrates the robustness and accuracy of the calibration and reconstruction techniques at these length scales. The length scale of the elastic material used was 3 times larger than a typical coronary stent length (field of view > 30 mm), due to limits of the magnification possible with the Canon Powershot cameras for this reconstruction test, even with use of an additional 16D macro lens. These limitations result in low resolution of the captured object on the output image due to low magnification.

The standard deviation in reconstruction accuracy of 30 μm may be associated with a number of factors: performance of the centre gravity algorithm used to determine the centre of each marker, marker size and separation, quality of the camera optics (which cannot be controlled in compact cameras). Even though the cameras were firmly

mounted on the tripods, clicking the shutter button may introduce a slight motion and cause un-intentional errors which could be improved by remote capture techniques.

All strain values reported were positive as strain was only determined in the *y* direction. These results indicate a variation of 8% in the strain values reported over the strip region. The material underwent greater deformation on the right than on the left side of the image. This is related to the geometry of the strip and fixation conditions and was noticeable in the output images. Although the surface of the strip was observed to deform out-of-plane during application of strain the method applied includes out-of-plane deformation due to stereo calibration.

A manual marking method using a Pilot fine point SW-DR5-B drawing pen was effective for this idealised test material and simple application of strain, but the marking method adopted must also be successful for higher magnification imaging and for different types of material including soft tissues (described in more detail in Chapter 6).

In conclusion, this initial test provided a sound understanding of the principles of the optical 3D reconstruction method. Improvement of the camera system to provide high resolution, high magnification imaging is discussed in the next Chapter.

SUMMARY

Optical measurement methods are promising tools for the experimental analysis of stent behaviour during deployment and to measure strains induced on the vessel wall [87, 90]. To work with compliant materials, soft tissues and fragile implants such as stents, a non-contact measurement technique has a major advantage; it minimises any mechanical interference. Optical reconstruction can be applied to full field measurements or can focus on the local variations of strains on the surface of specimen [124]. This is perfect when non-homogenous materials such as biological soft tissues (arteries) are tested. Of course, the accuracy of the calculated strain depends on the quality of the imaging system and a robust calibration process. To extract precise 3D information from the images obtained, calibration needs to be accurate. Cameras are calibrated if intrinsic and extrinsic parameters are derived and if the computed positions of cameras and the reconstructed object agrees with the real experimental conditions. The Toolbox used to perform calibration in this study was the "Bouguet Toolbox in MatLab" [115]. This has been shown to provide accurate calibration results [120].

The simple experiment of deformation of a sheet of elastic material using consumer cameras demonstrates acceptable resolution and magnification at these length scales (30-40 mm). It highlights the challenges of stent characterisation, requiring increased optical magnification and camera resolution. Moreover, these consumer cameras had

manual shutters. This introduces instability in camera position, resulting in noise and larger 3D reconstruction error, as experienced in the current study. To address these issues prior to the measurement of 3D stent geometry in Chapter 4, an appropriate design of an optical system for imaging at coronary artery length scales was required. This is presented in Chapter 3.

CHAPTER 3

DESIGN AND EXPERIMENTAL TESTING OF AN OPTICAL SYSTEM TO ALLOW IMAGING AT CORONARY ARTERY LENGTH SCALES

Application of stereo-photogrammetry to characterise the geometry and deformation of coronary stents requires a high resolution and high magnification system to obtain accurate results. This project explored the use of different types of camera, providing experience with a range of optical systems and an understanding of their influence on reconstruction quality, including the consumer camera system described in the previous chapter. Chapter 3 details the use of a custom lens approach which allows design of the optics to suit the application length scale. The design of the system is based on simple optics theory with appropriate experimental testing.

The design of the optical system described here is applied in later chapters to allow investigation of *in vitro* stent deployment and examine local strains on the surface of a vessel analogue. This chapter details the challenges of applying the stereo-photogrammetric technique at such small length scales (approximately 10 mm), balancing the requirements for high magnification whilst maintaining a sufficient depth of field to capture stent deformation.

3.   INTRODUCTION

Chapter 2 introduced stereo-photogrammetry, camera calibration and 3D reconstruction approaches. The reconstruction of a planar 3D geometry and measurement of strain were reported using consumer cameras at a length scale of the order of 30 mm. Application of the technique at smaller length scales presents challenges as a high magnification is required, whilst maintaining a sufficient depth of field.

This chapter outlines the design of an appropriate optical system to determine stent expansion *in vitro* over a range of length scales, with a primary focus on the coronary artery length scale (~10 mm), since coronary stent deployment and interaction with the vessel wall is the main focus of this thesis. However, a sound understanding of the principles associated with optical design of such systems has allowed consideration of other applications during the course of this research, including the assessment of larger scale stent devices (Chapter 4) and imaging of the whole heart (Future work).

It is hypothesised that high resolution cameras with appropriately designed lenses can capture a stent throughout expansion, whilst maintaining image focus. Examination of the imaging system involves understanding fundamental parameters such as: sensor size (SS), image resolution, working distance (u), lens to sensor distance (v), field of view (FOV), focal length (f), magnification (M) and depth of field (DOF). It is important to appreciate how these parameters are related in order to obtain satisfactory results at a particular length scale. This chapter summarises the expected relationship between these parameters based on simple optical theory and examines the experimental outcomes for a given optical design.

Recommended parameters are provided for optical systems at three different length scales which correspond to the imaging of coronary stents (Chapter 4, 5 and 6), the imaging of valve stents (Chapter 4) and the imaging of the whole heart (Future work). Experimental assessment of the optical system at coronary artery length scales is undertaken to ensure experimental results support the theory. The drawing below illustrates the difference in scale, where the heart has the length of approximately 100 mm, valve stent 34 mm and coronary stent 10 mm.
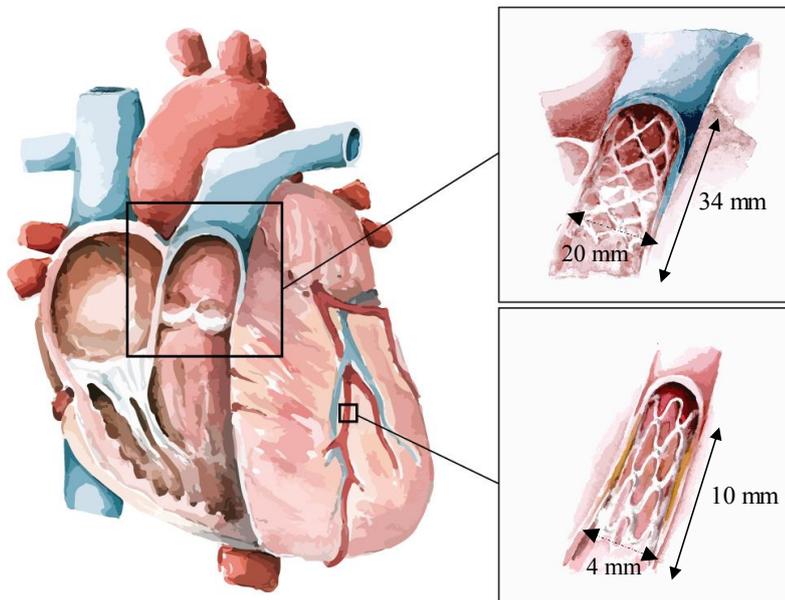
Figure 3-1: ***Representative schema of the increasing challenge in optical design. Small length scale (coronary stent) requires high magnification.***

The following sections describe the fundamental parameters of the optical system. The theoretical relationship between these parameters based on simple theory is described in section 3.2, with experimental measurement of a system at the coronary stent length scale (~10 mm) presented in section 3.3.

3.1.   FUNDAMENTAL PARAMETERS OF AN OPTICAL SYSTEM

To overcome the limitations of consumer camera described in the previous chapter, this project has developed an approach using fire-wire cameras, with a single lens optical system which can be modified for application at different length scales. Black-and-white (FL2G-13S2M-C) and colour (FL2G-13S2C-C) Flea2 cameras (Point Grey, Canada) have been used to create a stereo rig. These cameras were operated via computer using FlyCap2 software (Point Grey, Canada). *Table 6* provides the specification of the Flea2 cameras.

Table 6: Flea2 camera specification

Attribute	Specification
Image Sensor	ICX445 1/3"; dimension 4.6 mm by 3.8 mm
Maximum Resolution	1288 x 964
Pixel size	3.75 x 3.75 μm
Maximum Frame Rate	1288 x 964 at 30 FPS
Power Consumption	power via Vext GPIO pin or 9-pin 1394b interface: 8 to 30 V, less than 2.5 W
Lens Mount	C- mount
Camera Specification	IIDC 1394-based Digital Camera Specification v1.31, compatible with IEEE-1394b and IEEE-1394a interfaces
Dimensions (L x W x H)	9 mm x 29 mm x 30 mm (excluding lens holder, without optics)

The C-mount system allows attachment of a user-defined lens system. To determine the appropriate specification for such a system it is important to consider the fundamental parameters of the lens/camera system relevant to the application in this study, which are described in the following sections.

3.1.1. RESOLUTION

Sensor resolution is the number of columns and rows of charge-coupled device (CCD) pixels in the camera sensor. Cameras with a CCD sensor were chosen in this study as they have lower noise than the CMOS (complementary metal-oxide semiconductor).
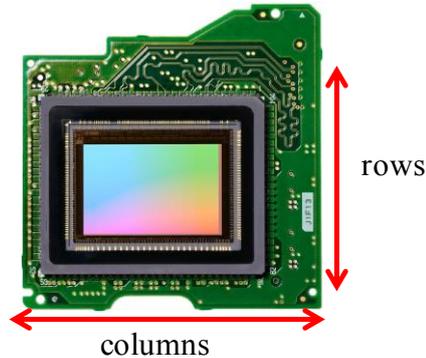
Figure 3-2: CCD sensor.

Spatial resolution dictates the amount of object detail that the imaging system can reproduce; it is determined from the field of view (FOV) size and the camera sensor dimensions. The Canon Powershot A40 cameras (used to capture tensile test of elastic material in the previous chapter) had a sensor resolution of 1600 x 1200 pixels (5.33 mm x 4 mm sensor size, SS). Despite the use of an additional macro 16D lens the highest possible spatial resolution was ~48 μm, limited by the low magnification of the camera optics. This resolution was insufficient to accurately examine coronary stents. During imaging with this system the 12 x 12 mm calibration grid occupied only 1/6 of the image in the horizontal direction. Dividing horizontal sensor size by field of view (approximately 76 mm) provides an indication of the optical magnification (M = 0.07). Despite the lower sensor resolution of the Flea2 cameras the flexibility of a custom C-mount lens system allows higher spatial resolution to be achieved by obtaining a smaller field of view.

3.1.2. IMAGE CONTRAST

Poor image contrast may affect the resolution and accuracy of results obtained using a quantitative optical approach. To determine local strain on the surface of the vessel analogue a high contrast pattern is required as described in Chapter 6. Increased image contrast may improve the performance of image registration using digital images [125]. Image contrast depends on lens quality, shutter speed and illumination. A short camera shutter speed decreases contrast and delivers poor levels of illumination [126]. It is necessary to distinguish in the output image differences between the object of interest and the shades of grey in the background. Real lenses never reproduce a perfect square intensity wave when imaging an object that goes from black to white, as presented in *Figure 3-3*.

Imaging pixels →
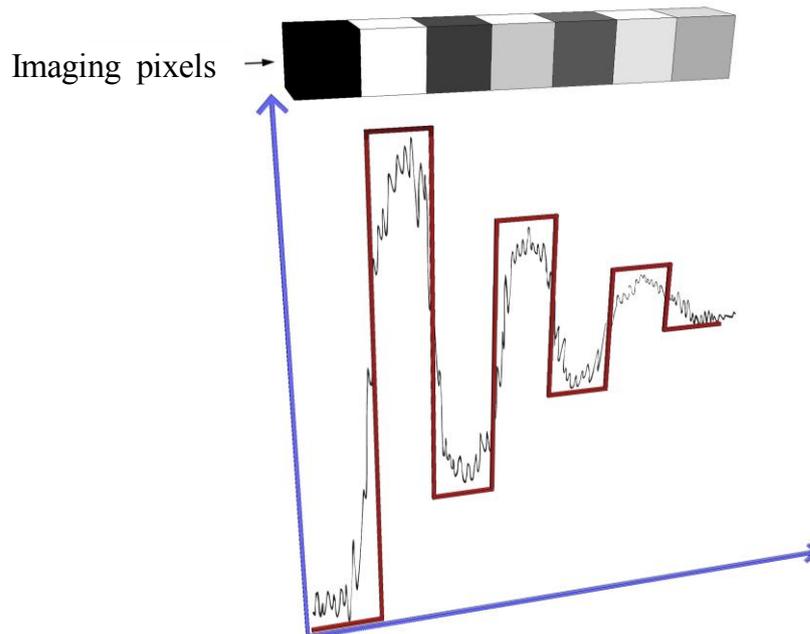
Figure 3-3: Ideal and real presentation of the square wave function of decreasing contrast.

This optical limitation occurs as a result of numerous factors including diffraction or the blur caused by a shallow depth of field. The plot above (*Figure 3-3*) shows an

idealised square intensity wave with decreasing image contrast and the expected real intensity wave for comparison.

Image contrast can be calculated from the image intensities as follows:

$$\%C = \frac{I_{max} - I_{min}}{I_{max} + I_{min}} \; 100 \qquad\qquad 3\text{-}2$$

Imax and *Imin* are the maximum and minimum image intensity values respectively. For an 8 bit image format the maximum intensity value is 255 and the minimum is 0.

3.1.3. MAGNIFICATION

The magnification of the lens system for application at a given length scale, is determined by the ratio between the sensor size and the field of view (SS/FOV) required to fit the object of interest within the image.
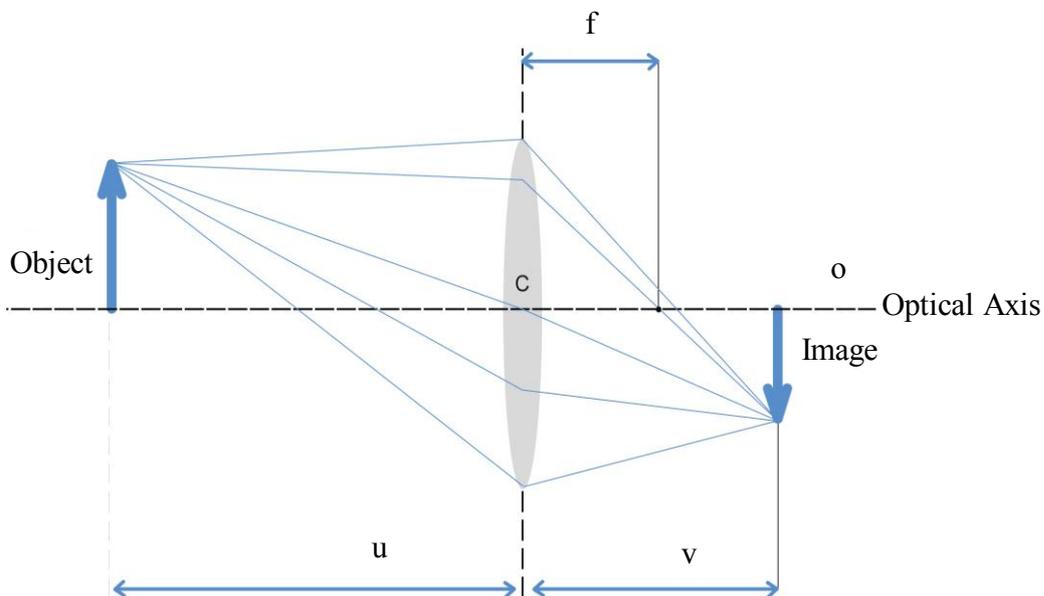
Figure 3-4: Principle of imaging with a lens. u is the object-lens distance, v is the image-lens distance and f is the focal length of the lens.

The physical parameters used to determine the anticipated magnification of a single lens system include the distance between the sensor and lens v, the lens to object distance u and the focal length of the lens f to be used. Analytical characterisation of these parameters for stent application is described in section 3.2.

3.1.4. DEPTH OF FIELD, APERTURE SIZE AND DIFFRACTION

Depth of field (*DOF*) is the maximum object depth that can be maintained entirely in focus [113] as shown in *Figure 3-5*. An ideal optical system would provide infinite depth of field (*DOF*) allowing objects at all distances from the lens to be captured in focus.

In this image *DOF* covers all of the stent geometry when it is imaged in position 2 (in position 1 and 3 the stent is out of focus and appears blurred).
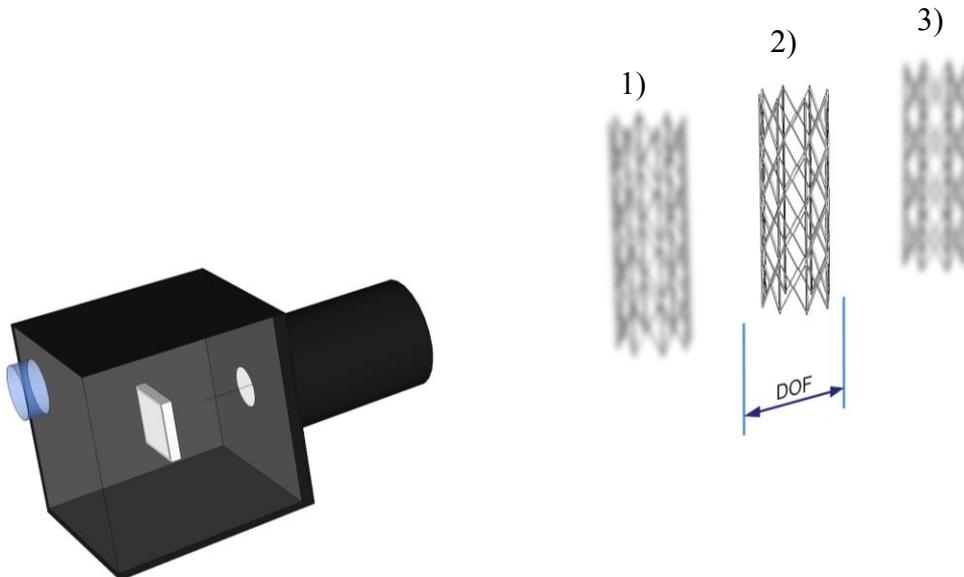
Figure 3-5: The range of the distance when stent appears acceptably sharp.

For the applications in this study, *DOF* needs to be sufficient to image the expanding stent and keep focus throughout the deployment process. It is important to estimate how much the object might move relative to the camera during capturing. The relative

movement includes a decrease in the distance between the stent and the camera as the stent diameter increases, and possible changes in stent position due to motion of the balloon catheter.

Use of a larger aperture and closer focusing distances produce a shallower *DOF*, conversely, decreasing the aperture increases the *DOF*. However, significant decrease in aperture size, and extended exposure times, can cause diffraction and noise in the image respectively, limiting the effective resolution of the image [127, 128] and decreasing image contrast.

The Fraunhofer diffraction pattern generated by a circular aperture is illustrated in *Figure 3-6*. The magnitude of the diffraction effect can be characterised by the diameter of the Airy disk, which is defined as the central bright region shown in *Figure 3-6*. If we assume that our lens is perfect, the Airy disk will depend only on the diameter of the aperture, the wavelength of the light and lens to sensor distance (sub-section 3.2.1, equation 3-6).
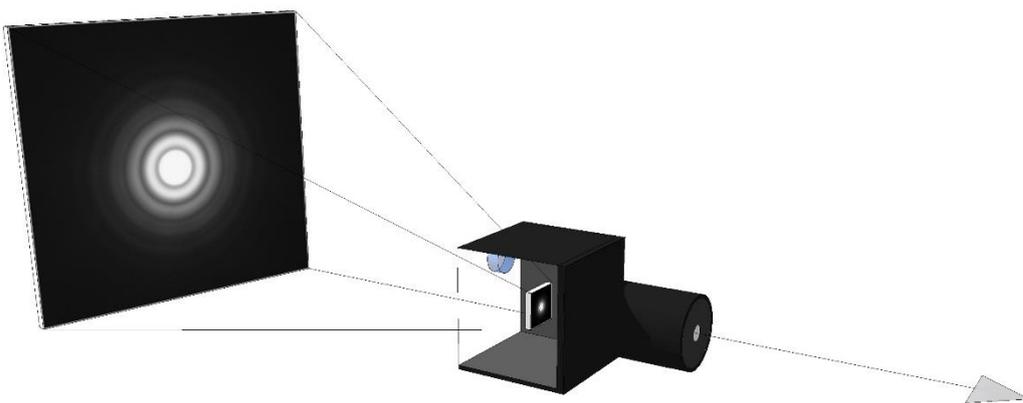
Figure 3-6: Diffraction effect due to camera capture using lens of small diameter aperture. Presentation of the central bright spot (Airy disc) and fringes.

3.1.5. DISCUSSION

The fundamental properties of the lens/camera system have been described above. Important parameters for consideration in this study are the depth of field (*DOF*) and the magnification (M). At coronary artery/stent length scales high magnification (M) is required to investigate local areas of the stent. This can be achieved, either by moving closer to the subject or using a lens of greater focal length, decreasing the DOF.

As the stent expands it will increase in diameter, so sufficient DOF is required to maintain focus throughout the experiment. However, by decreasing aperture size to increase DOF, light passing through the aperture may generate notable diffraction [99, 113, 128] so that, even if the DOF is sufficient, the sharpness of the image may be reduced as a result of diffraction blur. As a result the acceptable level of diffraction in the image limits the maximum resolution that can be obtained.

An optimal system would provide maximum resolution (due to high magnification, M) and maximum depth of field, without introducing significant diffraction. Under some conditions this may not be possible requiring compromise. In section 3.2 theoretical relationships between these parameters are used to estimate the appropriate parameters for an optical system at the three length scales described previously, in section 3.3 the theory is experimentally validated for the coronary length scale.

3.2. ANALYTICAL CHARACTERISATION OF THE OPTICAL SYSTEM

This section considers the design of an optical system suitable for the Flea2 cameras at each investigated length scale, defined in terms of the object diameter and length

(field of view) in *Table 7*. The method is described below for the coronary stent application, with results reported for the other length scales in section 3.2.2.

Table 7: Length scales at which the optical system has been applied.

	Diameter [mm]	Length [mm]
Heart	-	80
Valve stent	20	34
Coronary stent	4	8-10

3.2.1. METHODS

The horizontal size of the camera Flea2 sensor is 4.6 mm (*Figure 3-7*).
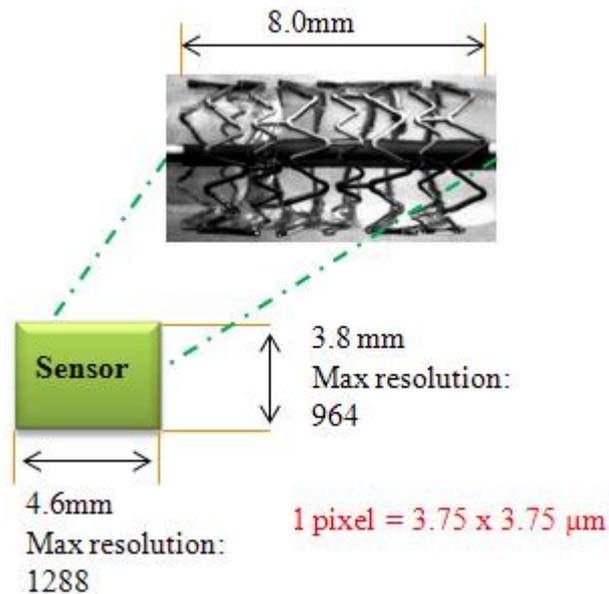
Figure 3-7: Flea2 image sensor size and fully expanded coronary stent.

To image a coronary stent of length 8-10 mm it is necessary to achieve a magnification of approximately 0.4 (4.6 divided by 10 plus consideration of the proximal and distal part of the inflation balloon, approximately 1+1 mm).

As most of the investigated stents have a diameter of 1 mm before and 4 mm after expansion, their radius will change by 1.5 mm. As rigid body movement of the catheter during stent deployment might occur, it would be appropriate to design the system to provide a DOF of 4 mm, to be completely sure that expanding stent is in focus all the time as presented below (*Figure 3-8*).

Initial radius (0.5mm)

Final radius (2mm)

DOF(4mm)
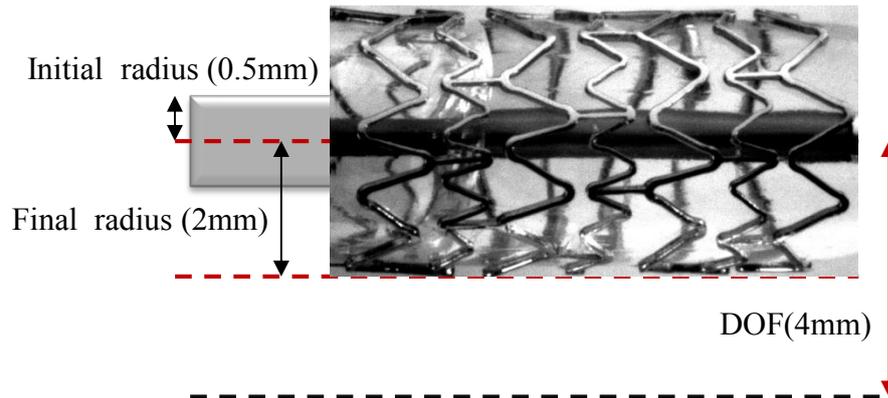
Figure 3-8: Appropriate DOF for stent expansion characterisation, considering a final stent radius of 2 mm.

The optical system is analytically characterised by equations 3-3 to 3-6 [113, 127, 128], with the relationship between the parameters shown in *Figure 3-9*. These equations characterise the lens/camera system in terms of the lens to object distance *u*, the lens to sensor distance *v*, lens focal length *f* and image magnification *M*. The latter is equivalent to the ratio of v to u (from the similar triangles theorem) [99], whereas the depth of field *DOF* depends on both v and u and the acceptable size of the blur spot due to the object moving out of focus *c*.
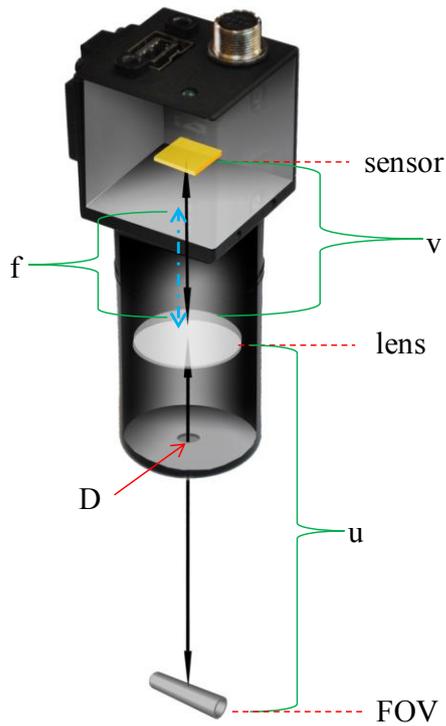
$$\frac{1}{f} = \frac{1}{v} + \frac{1}{u} \qquad\qquad \text{3-3}$$

$$M = \frac{v}{u} \qquad\qquad \text{3-4}$$

$$DOF = \frac{2\frac{v}{D}cf^2u^2}{f^2-\left(\frac{v}{D}\right)^2 c^2u^2} \qquad\qquad \text{3-5}$$

$$Diff = 2.44\,\lambda\,\frac{v}{D} \qquad\qquad \text{3-6}$$

Figure 3-9: Presentation of working distance (u), lens to sensor distance (v) and aperture diameter (D).

Four lenses (Planoconvex lens, Comar Optics, 10 mm diameter each) of focal length (f) 20, 25, 31.5 and 40 mm, and three apertures of diameter (D) 0.8, 2.0 and 3.0 mm were available for experimental testing. For each value of focal length the v, u, DOF and Diff values were computed for all aperture sizes to provide the desired magnification of 0.4.

3.2.2. RESULTS & DISCUSSION

Results of analytical characterisation of the optical system are presented in the *Table 8* below.

Table 8: The performance of an optical system at length scales relevant to coronary stent expansion; M - magnification, f - focal length, v - sensor to lens distance, u - lens to object distance, D - aperture diameter, DOF - depth of field, Diff - diffraction. Theoretical output data.

M	f [mm]	v [mm]	u [mm]	D [mm]	DOF [mm]	Diff [μm]
0.4	20	28	70	0.8	17.7	47
				2.0	1.9	18.6
				3.0	0.7	12.6
	25	35	87.5	0.8	18	58
				2.0	2.9	23.3
				3.0	1.2	15.8
	31.5	45	105	0.8	26	75
				2.0	4.3	29
				3.0	1.9	15
	40	56	134	0.8	30	108
				2.0	7.0	43
				3.0	2.5	25.3

To provide the required magnification (M = 0.4), the computed values of *v* and *u* for each value of *f* are presented in the third and fourth column respectively. This magnification results in a field of view of 11.0 mm x 9.0 mm and a spatial resolution of approximately 8 μm. Note that for each focal length, depth of field increases as the aperture diameter is decreased (3 > 2 > 0.8 mm).

At these small length scales sufficient DOF was computed for two focal lengths of lens (31.5 mm and 40 mm). However, the computed diffraction effect is reduced for *f* = 31.5 mm. The analytical investigation suggests an appropriate optical system with focal length 31.5 mm, sensor to lens distance (v) 45 mm and aperture diameter (D) of 2 mm to examine coronary artery stent deployment. The computed DOF (4.3 mm) is reasonable for these parameters but the predicted diffraction blur of 29 μm is much

larger than a single image pixel. However, this findings need to be validated experimentally.

The challenge of designing optics to obtain high magnification whilst maintaining a sufficient depth of field can be seen by plotting calculated change in both *DOF* and Diff parameters with aperture diameter D (x axes) as shown in Figure 3-10. These data are plotted for the optics with focal length of 31.5 mm and magnification of 0.4.
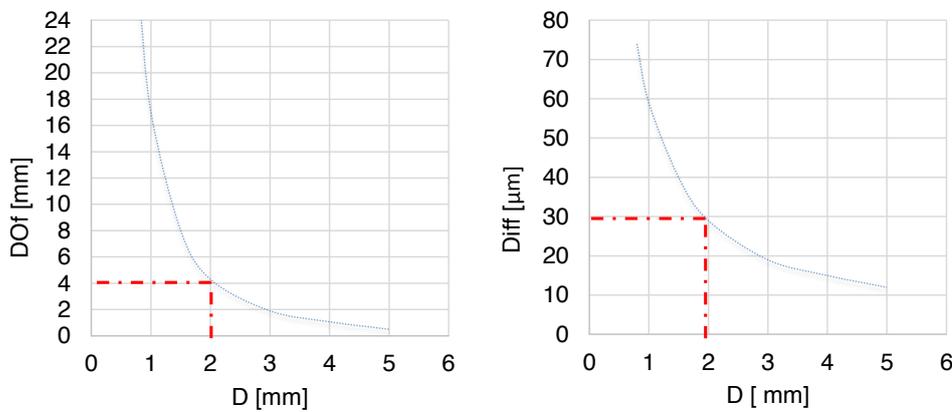
Figure 3-10: DOF and Diff plots; output from analytical results; dashes presents DOF and Diff values for D=2 mm.

To provide the required magnification for the valve stent and the heart length scale (0.15, 0.07 respectively), the computed values of *v* and *u* for required value of *f* are presented in the *Table 9*.

Table 9: The parameters of the optical system at higher length scales.

Object	M	f [mm]	v [mm]	u [mm]	D [mm]	DOF [mm]	Diff [μm]
Valve stent	0.1	31.5	35	315	2	23	23
		40	44	440	3.0	20	19
Heart	0.07	40	43	570	3.0	42	19
		100	107	1528	6	75	23

As the length scale of the object increases whilst using the same lens focal length (31.5 mm), the sensor to lens distance decreases to obtain lower magnification, resulting in a larger lens to object distance. The outcome of this scaling is a larger DOF due to lower magnification and reduced diffraction due to short lens to sensor distance. The reason the diffraction is lower is that the magnitude of the diffraction pattern scales with the v distance (as shown in the equation 3-6).

If a larger distance from the camera to the object is required for practical reasons (e.g. rig set-up environment), the lens focal length can be increased (e.g. to 40 mm) along with the aperture diameter (to 3 mm diameter) to suppress the evident diffraction of the light (*Table 9*).

3.3.   EXPERIMENTAL CHARACTERISATION OF THE OPTICAL SYSTEM

The values computed in section 3.2 for a coronary stent length scale (*Table 8*) were compared with experimental assessment of an optical system consisting of a Flea2 camera (Point Grey) with a single lens system (Comar Optics, UK) controlled using FlyCap2 capture software (Point Grey, Canada). The experimental tests are described in the following sections and include assessment of image contrast with lenses of two focal lengths (f = 31.5 mm and f = 40 mm) and depth of field assessment for a lens with f = 31.5 mm with various aperture diameters. The significance of diffraction effects in the captured images was evaluated.

3.3.1. METHODS

For both image contrast and depth of field tests a single camera was positioned perpendicular to a test object. To determine the influence of the optics on the accuracy of 3D reconstruction a stereo rig (with angle between cameras of 45 degrees) was built to image rigid body motion of a cylinder at coronary artery length scales.

IMAGE CONTRAST EXAMINATION

Image contrast was assessed by examining the captured image of a checkerboard grid pattern placed perpendicular to the camera Z axis and computing contrast from the intensity plot using equation 3-2. Lenses of focal length 31.5 mm and 40 mm were positioned approximately 45 mm and 56 mm respectively from the camera sensor, both resulting in a magnification of approximately 0.4. The aperture was 2 mm in both cases. Shutter speed and frame rate were set with FlyCap2 software (PointGrey, Canada) to obtain sufficient light and avoid noise. For a 40 mm focal length lens shutter speed was decreased to improve contrast, reducing the frame rate (*Table 10*).

Table 10: different focal lengths used to examine image contrast

Specification		
Focal length [mm]	**31.5**	**40**
Shutter speed [129]	30	83
Frame rate [fps]	30	10

DEPTH OF FIELD TESTING

DOF was assessed using the sharpness of black and white vertical lines placed at an angle of 45° to the camera axis. Optics with f = 31.5 mm, v = 45 mm were used to assess the sharpness of a set of black and white vertical lines placed at an angle of 45°

to the camera axis (*Figure 3-11*). The aperture was varied from 0.8 mm to 5 mm and the image intensity was examined to determine blur due to DOF effects.

Image with D=2mm

Image with D=5mm
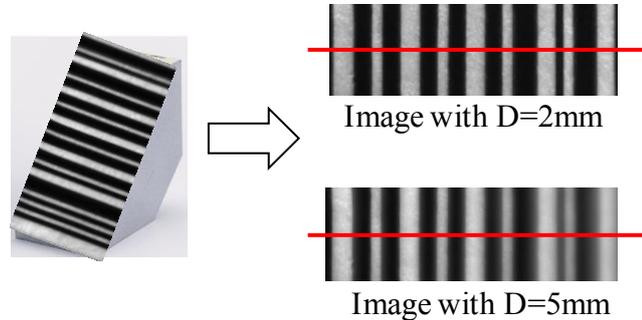
Figure 3-11: Black and white vertical lines placed at an angle of 45°, a) for D=2 mm, b) for D=5 mm

RIGID BODY MOTION TEST / RECONSTRUCTION ACCURACY

Using lenses with focal length 31.5 mm and setting D = 2 mm, to provide sufficient *DOF*, the stereo camera rig was calibrated, as described in Chapter 2 using the Bouguet Calibration Toolbox for Matlab [115] and used to assess the error of the optical reconstruction method. A rigid body motion test was performed with a marked cylindrical control object of known size, which was translated through 2.5 mm in increments of 0.5 mm using a travelling microscope.
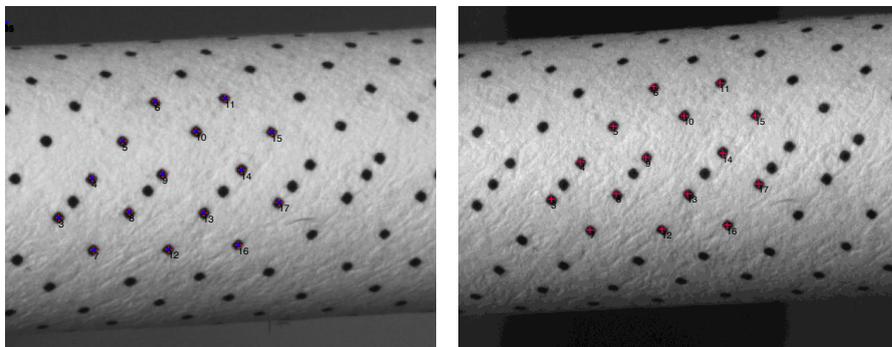
Figure 3-12: Marked cylindrical control object of known size used for rigid body motion test to assess calibration and reconstruction accuracy.

3.3.2. RESULTS

Image contrast and depth of field test results obtained with single camera as well as rigid body motion output from stereo rig are presented below.

IMAGE CONTRAST

Output images to determine image contrast are depicted in *Figure 3-13*. The image intensity along the central row was plotted in Matlab (*Figure 3-14*). An idealised virtual image was created and plotted for comparison.

idealised   f = 31.5 mm   f = 40 mm

600 pixels
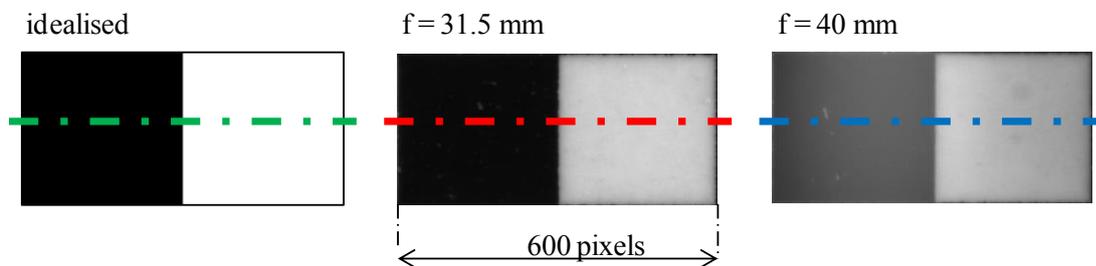
Figure 3-13: Images obtained with focal length of 31.5 mm, gives a contrast of 91% and f=40 mm, which results in poor contrast of 41% (equation 3-2), compared with idealised virtual image with 100% contrast.
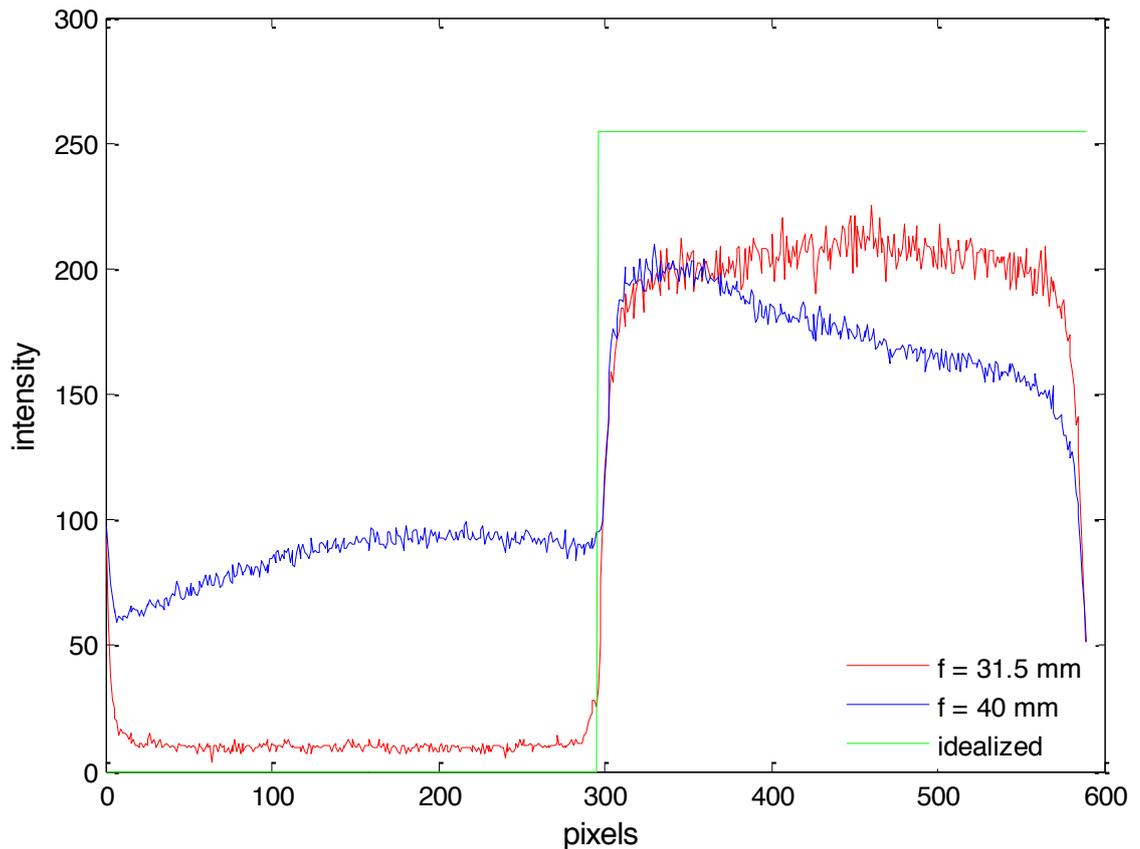
Figure 3-14: *Image intensity of a central row plotted for idealised virtual image, focal length of 31.5 mm and 40 mm using aperture diameter of 2 mm.*

The geometry of the two images were directly comparable due to the same object magnification (*M=0.4*). If a black and white object is examined, black and white details should produce the lowest (close to 0) and highest (close to 250) intensity pixels respectively, with all shades of grey in between accurately imaged. A black line on a white background is an example of 100% contrast (as in an idealised virtual image, *Figure 3-13*, equation 3-2, where max intensity is equal to 255 and minimum intensity is equal 0), which experimentally is impossible to achieve. The diffraction limit of the optical system distorts the square wave expected based on an idealised virtual image, as described earlier [127]. The diffraction effect becomes more significant in the image captured using the custom lens with focal length of 40 mm as shown in *Figure 3-14* and the same aperture diameter (2 mm) as for 31.5 mm focal length lens. *Figure 3-15*

explains this behaviour where the focal length increasing from 31.5 mm to 40 mm requires longer lens to sensor distance- v ($\frac{v}{D}$).

An aperture of 2 mm was used for both custom lenses. The light projected through an aperture still has to travel from the aperture to the sensor. If the distance is greater, less light reaches the sensor, what is confirmed with intensity plot (*Figure 3-14*).
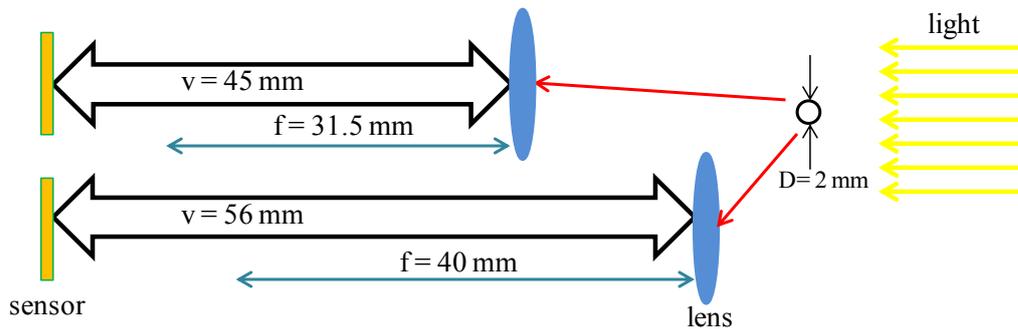
Figure 3-15: Focal length increase requires sensor to lens distance increase.

DEPTH OF FIELD TESTING

The image intensity of the central row of pixels is plotted for five aperture diameters, from 0.8 mm to 5 mm (*Figure 3-16*). Additionally the intensity for aperture of 4 mm and 5mm diameter was plotted to present significant decrease in depth of field.
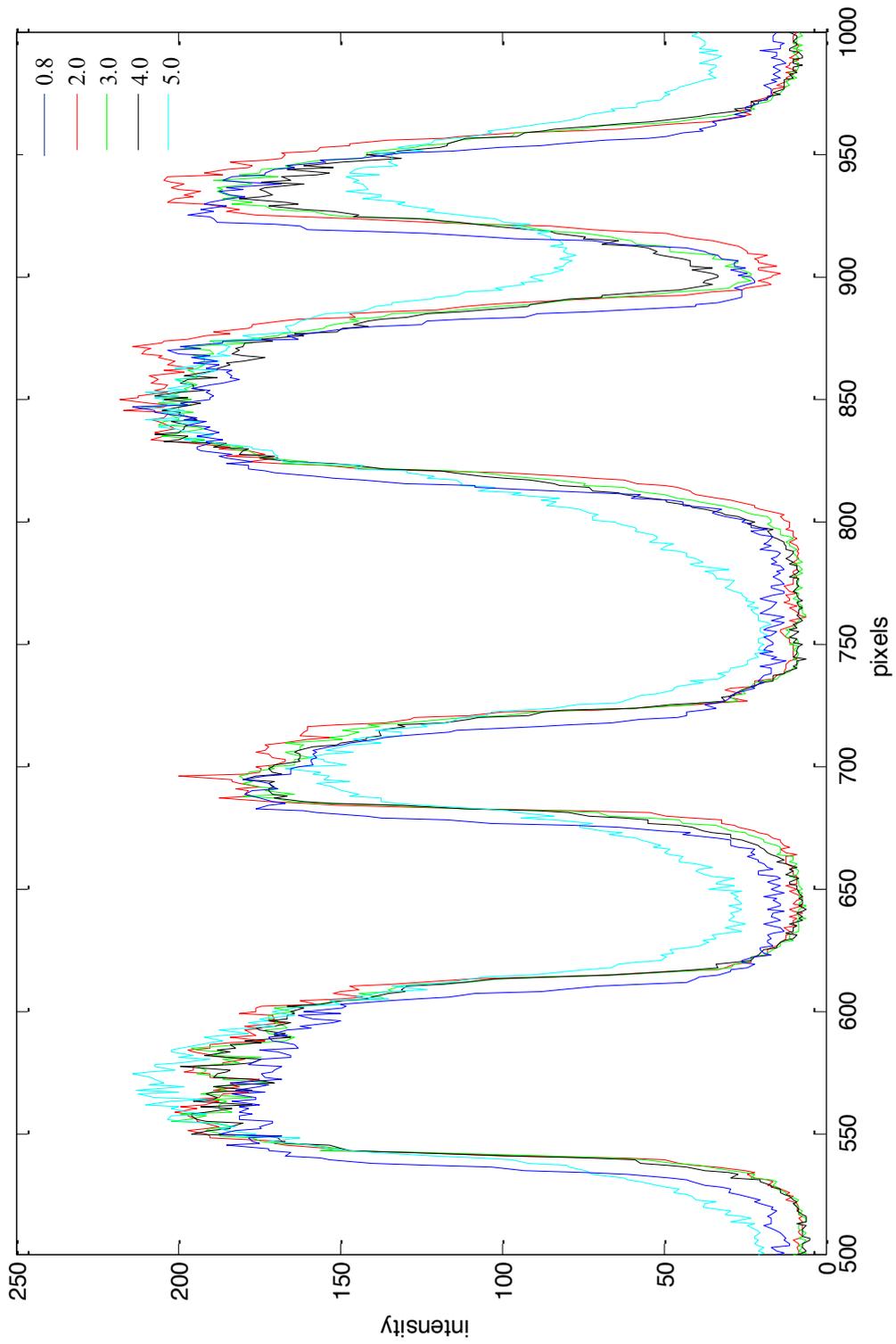
Figure 3-16: Image intensity of a central image row plotted in Matlab for aperture increasing from 0.8 mm to 5 mm diameter aperture.

For a better visualisation only 500 pixels (c = 5.21 mm) are presented in *Figure 3-16*. As the object was placed at an angle of 45° to the camera axis it gives approximately b = 3.7 mm of depth, as calculated using equation 3-7.
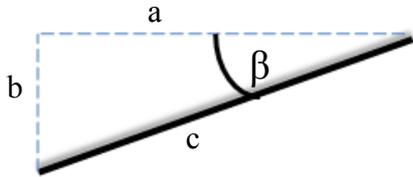
$$a^2 + b^2 = c^2 \; (a = b) \qquad\qquad 3\text{-}8$$

Tests performed with a range of apertures demonstrate significant reduction in the DOF as the aperture, *D*, is increased from 2 mm (*Table 8*, *Figure 3-16*). Reducing *D* to 0.8 mm was observed to result in noticeable diffraction blur.

RIGID BODY MOTION TEST / RECONSTRUCTION ACCURACY

The results from change in the distance between fifteen reconstructed points on the cylindrical object for five successive translations of this object suggest measurement accuracy of the order 14 μm with marker separation of 1 mm.

Table 11: Maximum, average and minimum variation in distance between reconstructed points.

Difference in computed distance [*μm*]			STDEV [*μm*]		
Max	Mean	Min	Max	Mean	Min
40	14	1.2	14	12	11

Calibration results presented as a 3D plot confirmed the analytically calculated and experimentally measured lens to object distance (u) of approximately 105 mm.
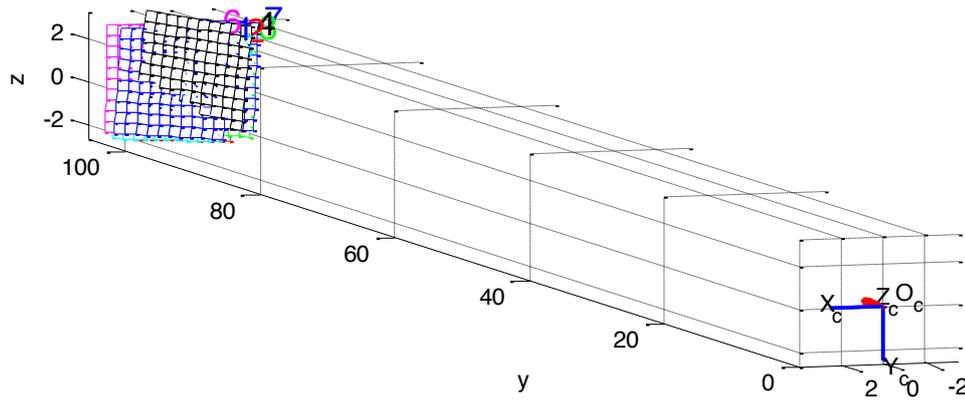
Figure 3-17: 3D plot of extrinsic parameters obtained via calibration showing the distance from the lens to the object (u) confirms computed distance.

3.4. DISCUSSION

A focal length of 31.5 mm and aperture diameter of 2 mm was selected as the most appropriate to image coronary stent deployment, providing M = 0.43 whilst maintaining sufficient DOF (4.3 mm) and not causing significant diffraction. Moreover, this results in good contrast. This is an advantage in tracking deformation with image registration techniques. Additional advantage of this choice (f = 31.5 mm) is the potential to capture dynamic changes due to the high frame rate (15-30 fps) and fast shutter speed (~20-30 ms) which can be used to obtain acceptable image quality. At higher focal lengths (40 mm) the ability to capture dynamic effects is limited due to the longer shutter speeds (>80 ms) and lower frame rates (approximately 10 fps) that are required if illumination is kept constant. However, the most significant difference is in the level of observed diffraction. Rigid body motion tests at this length scale have shown acceptable errors in 3D reconstruction with accuracy of the order 14 μm. This system has been applied to study coronary stents described further in Chapter 4, 5 and 6.

The advantage of using a single lens system is that optics can be reconfigured to image at a range of length scales. The parameters computed in this chapter have been used to design optical systems applied to the imaging of valve stents (Chapter 4) and preliminary imaging at the whole heart length scale (Chapter 7).

SUMMARY

This chapter details the design of an optical system for a stereo rig to measure *in vitro* stent deployment. Fire-wire Flea2 cameras (PointGrey, Canada) have been chosen for the stent application due to fast transfer of data (up to 800 Mbps), high resolution ease of use and low cost. To obtain appropriate magnification and maintain sufficient depth of field a single lens system has been designed for applications over a range of length scales. As the most challenging application is the coronary artery length scale, this was selected for experimental confirmation of the optical theory. The calibration grid and stent can be viewed in real time with the FlyCap2 software (Point Grey, Canada). Stereo images are displayed in a side-by-side format. This help to set proper angle between cameras and fit investigated sample in the field of view of both cameras, to avoid reflection and check the depth of field. The C-mount system allowed attachment of a user-defined lens system.

The appropriately configured optical system will be used to characterise stent geometry (Chapter 4) and for the experimental analysis of stent behaviour during its deployment (Chapter 5) due to obtained high magnification and sufficient depth of field at the coronary length scale.

CHAPTER 4

STENT GEOMETRY CHARACTERISATION TO ASSESS OPTICAL RECONSTRUCTION ACCURACY

This chapter reports methods and results used to assess the accuracy of measurement of 3D device geometry using optical methods and comparison of this technique with other imaging techniques. Quantitative comparison of volumetric and biplanar 3D techniques is reported for two distinct clinical applications, at different length scales, where stent geometry is of interest.

Optical measurement of stent geometry for both applications is undertaken using the optical system described in Chapter 3, tailored to the appropriate length scale. The most important outcome for this study is to confirm the accuracy of the approach at the coronary artery length scale to ensure robust output data is obtained during the stent deployment tests described in Chapter 5.

This chapter reports results which have been published in Medical Engineering and Physics [130].

4. INTRODUCTION

The design process for the stereo camera Flea2 system with custom lenses has been described in Chapter 3 for applications over a range of length scales. This chapter describes use of this system to capture the geometry of fully deployed Percutaneous Pulmonary Valve Implantation (PPVI) stent at low magnification (x0.1) and balloon expandable coronary stents at high magnification (x0.4). The robustness and accuracy of 3D reconstructions from the optical stereo-photogrammetric method is determined through comparison with volumetric methods in both cases. The assessment of valve stent reconstruction involved collaborative work undertaken with University College London (UCL) and compared three additional imaging methods (biplanar fluoroscopy, computed-tomography and micro-computed-tomography) with the optical method.

The coronary stent geometry examined using the optical method was compared with micro-computed tomography, as other imaging techniques were found to have insufficient resolution to characterise the local geometry.

This investigation of the optical method at two length scales demonstrates the effectiveness of biplanar imaging methods at lower magnification before proceeding to the most challenging coronary artery length scale. The reason for stent geometry characterisation using both optical biplanar and volumetric methods was to assess accuracy and check robustness of the methodology before employing this method to examine local regions of a coronary stent during deployment.

4.1. LARGE SCALE-VALVE STENT

The study of the Percutaneous Pulmonary Valve Implantation (PPVI) stent was a collaborative effort with contributions from members of the MeDDiCA Marie Curie Initial Training Network at UCL. The study was designed to provide a quantitative assessment of uncertainty in the 3D reconstruction of stents using available imaging techniques.

A number of imaging techniques were used to assess 3D stent geometry of a deployed Cheatham Platinum (CP) stent with a 6 ring configuration (*Figure 4-1*c), the PPVI device, Melody^{TM} (Medtronic, MN, USA). The stent length was approximately 34 mm and diameter varied from 22 mm, 19 mm and 24 mm in the distal, central and proximal regions respectively. The valve stent is used to implant the pulmonary Melody valve in patients with valve dysfunction.   2D X-ray fluoroscopy and 3D computed tomography are used to control valve stent position and to assess its mechanical performance over time.

4.1.1. METHODS

4.1.1.1. IMAGE ACQUISITION

To mimic the anatomical valve stent implantation site, a right ventricular outflow tract (RVOT) of a PPVI patient, was reconstructed from magnetic resonance images (MRI) using the commercial software Mimics (Materialise, Leuven, Belgium) at UCL (*Figure 4-1a*). A 3D compliant analogue of the obtained volume was produced in a flexible elastomeric material (TangoPlus Full-Cure® 930 compound, Objet Ltd, Rehovot, Israel), *Figure 4-1b*. The CP stent was deployed onto this implantation site model to match the geometry of the underlying vessel. Six metallic spherical markers

(Figure 4-1b, c) were glued with super glue in several positions on the RVOT analogue (around the stent) to provide reference markers for further comparison between all imaging methods.
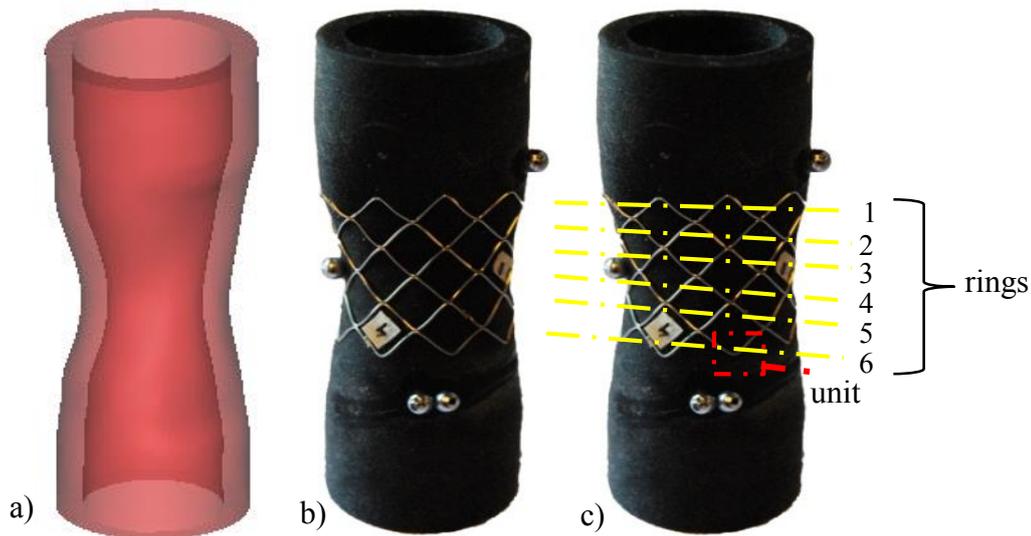
Figure 4-1: a) Right ventricular outflow tract (RVOT) of a PPVI patient reconstructed from magnetic resonance (MR), b) valve stent deployed on the model made from elastomeric material (TangoPlus Full-Cure® 930 compound, Objet Ltd, Rehovot, Israel), courtesy of Daria Cosentino (UCL), c) 6 ring configuration of the deployed valve stent.

The stent was imaged using: a) micro computed tomography (micro-CT), b) conventional CT, c) biplane fluoroscopy and d) optical stereo-photogrammetry techniques. The imaging equipment for each method is presented in the *Figure 4-2*.

To protect the sample during transport a glass cylinder with a wooden rod fixed in the middle was used. All image acquisitions were obtained within a three day period. CT scanning and fluoroscopy were performed at Great Ormond Street Hospital for Children, London, UK. Optical stereo-photogrammetry and micro-CT were completed in our lab and in Mellanby Centre at the Royal Hallamshire Hospital in Sheffield. Images captured using each of these techniques are presented in

*Figure 4-3*a-*b* (for volumetric methods) and *Figure 4-4*a (for biplanar methods), section 4.1.1.1 (*Image post-processing*).
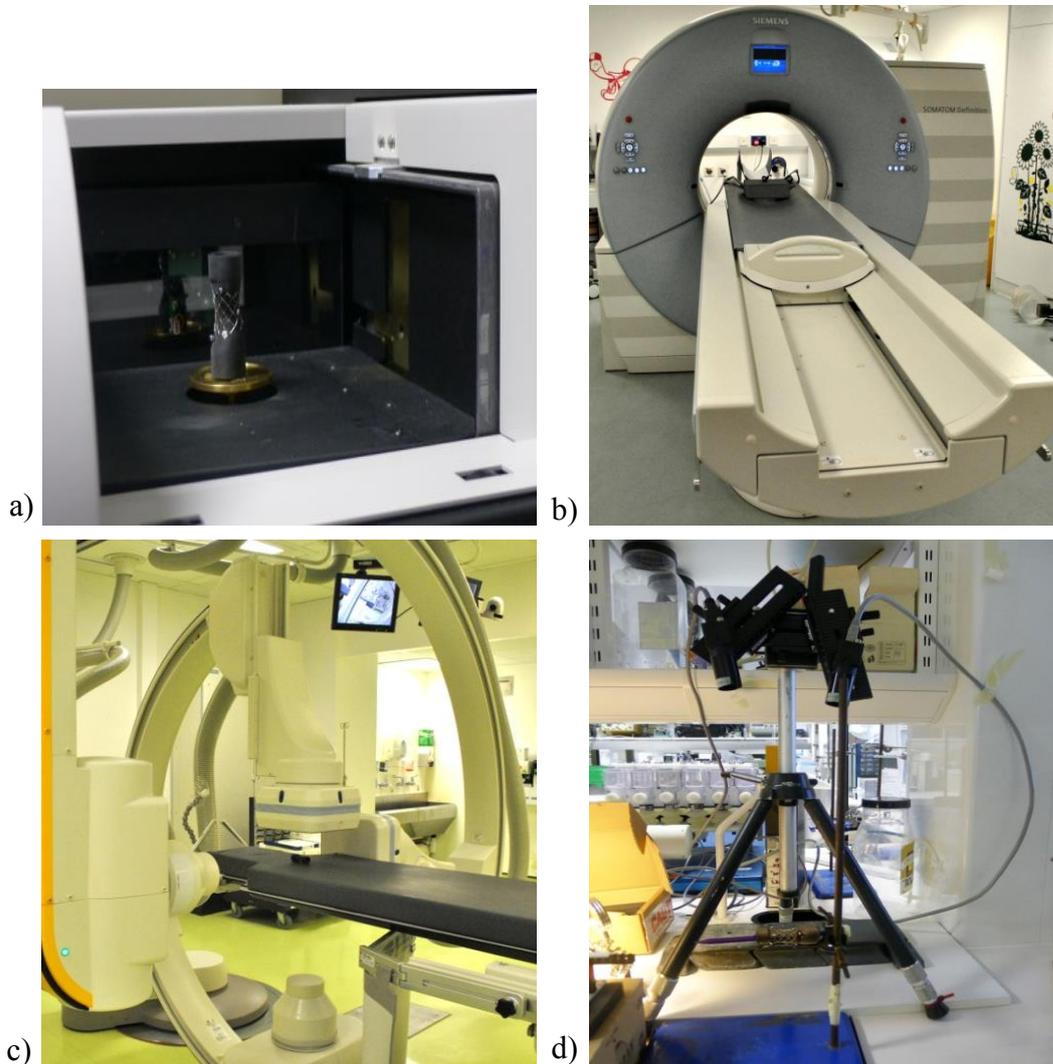
Figure 4-2: Equipment used to image valve stent a) micro-CT scanner Skyscan 1172 ex vivo cone-beam scanner (Bruker, Belgium), b) Conventional CT (SOMATOM Definition, Siemens, Germany), c)Biplane fluoroscopy Axiom Artis Flat Detector system (Siemens, Germany), d) Stereo camera Flea2 rig (Point Grey, Canada).

Micro-CT scan was performed with the Skyscan 1172 *ex vivo* cone-beam scanner (Bruker, Belgium) with spatial resolution of 17 µm. **Conventional CT** was performed using a 64-slice dual-source multidetector system (SOMATOM Definition, Siemens, Germany) with images reconstructed with a pixel size of 127 µm x 127 µm and slice

increment of 299 μm (slice thickness of 600 μm) for the low dose scan (**CT***l*), and with a pixel size of 123 μm x 123 μm and a slice increment of 299 μm (slice thickness of 600 μm) for the high dose scan (**CT***h*).

Fluoroscopy (F) images were acquired in a catheterisation laboratory equipped with Axiom Artis Flat Detector system (Siemens, Germany). The arms of the fluoroscopy system were positioned orthogonally, at the same distance from the deployed stent. Acquisitions with the fluoroscopy scanner resulted in the pixel size of 279 μm x 279 μm.

Optical stereo-photogrammetry was performed using the method described in Chapter 2 to obtain optical image pairs. A pair of Flea2 fire-wire cameras were separated by 45° ± 5° and controlled with FlyCap2 software (Point Grey, Canada). A checkerboard grid pattern containing 7 x 4 squares (2 mm x 2 mm each) was captured in seven different orientations to calibrate the cameras using the Bouguet Calibration Toolbox in Matlab. A large scale checkerboard grid (27 mm x 21 mm) control object was imaged to assess calibration and reconstruction accuracy by reconstructing 3 mm reference distances (defined using a 3 x 3 mm checkerboard grid) captured during three translations. The optical system for the valve stent length scale was designed to provide a field of view of around 34 mm in the maximum image dimension and to ensure adequate depth of field, specified as 20 mm (see section 3.2), allowing focus to be maintained over the full stent geometry. To compare results with the volumetric imaging methods the entire stent geometry was captured by rotating the stent in increments of 45° ± 10° and imaging the stent at each of the eight positions.

The resolution of the optical images was 1288 x 964 pixels with a sensor size of 3.75 µm x 3.75 µm per pixel, as presented in Chapter 3. A lens of focal length 40 mm was used, positioned approximately 46 mm from the camera sensor, resulting in a magnification of 0.1. This magnification results in a field of view of 46 x 38 mm and a spatial resolution of approximately 35 µm. Lens aperture was 3 mm to reduce diffraction effects (Chapter 3, subsection 3.2).

4.1.1.2.   IMAGE POST-PROCESSING

The post-processing applied to the data available from each imaging modality to provide 3D stent geometry is described in this section. The 3D geometry was defined through identification of strut landmark points at the crown location of the stent struts for biplanar and volumetric methods. Comparative measurements (between each method) of the struts length were made assuming strut dimensions are represented by straight lines joining each strut landmark point as shown for micro-CT in *Figure 4-3* and for biplanar methods in *Figure 4-4*.

<u>Volumetric methods</u>

Post-processing of the 3D volumetric image data (micro-CT, *high dose* CT and *low dose* CT) was done using Mimics software at UCL. In *Figure 4-3* a) cross-section and b) 3D reconstructed geometry of the stent obtained from volumetric methods are presented.
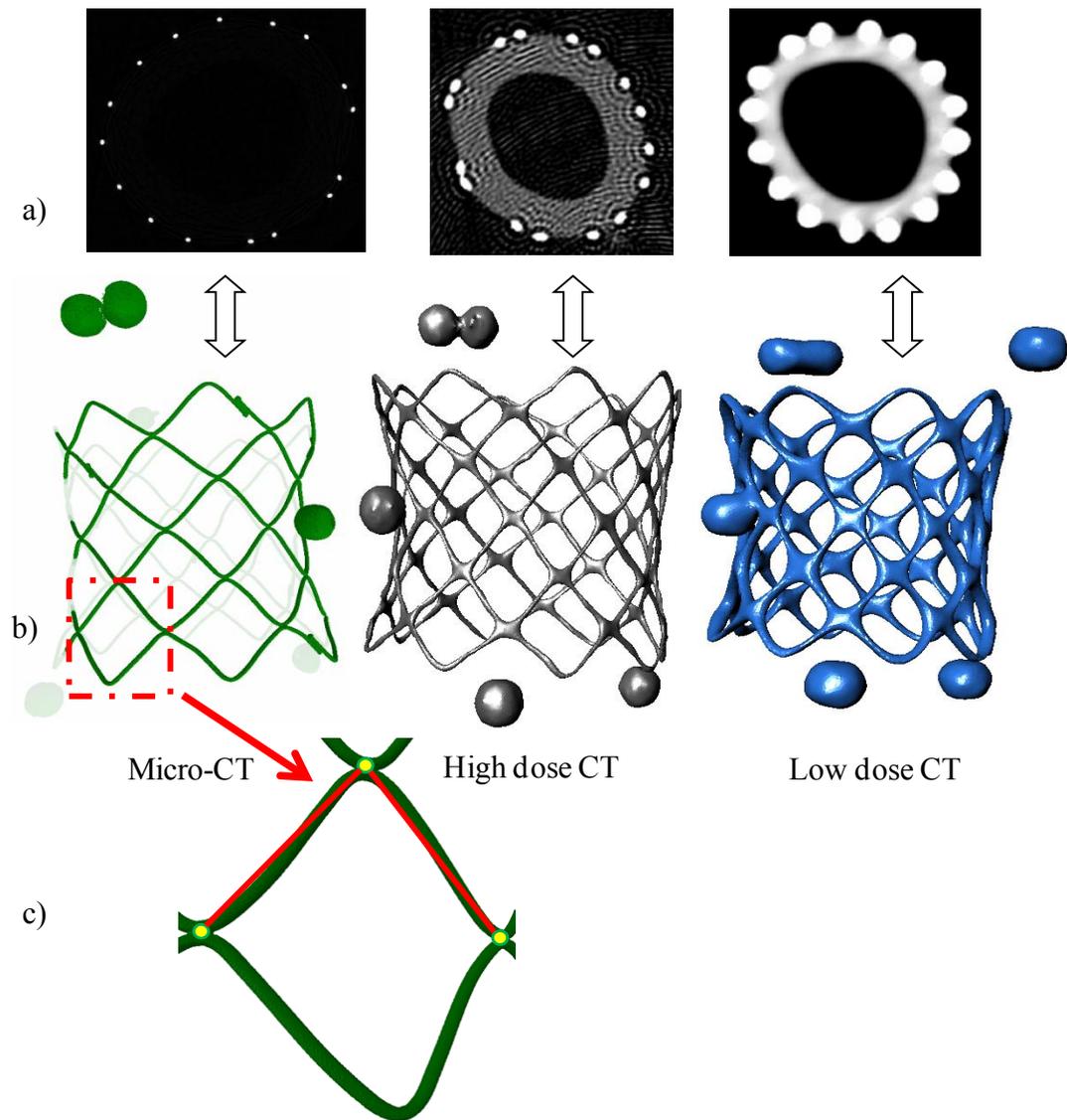
Figure 4-3: a) The orientation of cross-section in the imaging volume; b) reconstructed 3D models obtained from volumetric methods; c) the detail of the micro-CT geometry shown to demonstrate strut landmark points at the crown location of the stent struts and the measurement of strut length, part of image adapted with permission from Cosentino, Zwierzak et al. [130] .

Biplanar methods

Typical images obtained using the two biplanar methods are presented in *Figure 4-4* with the strut dimensions represented by straight lines on the right side and zoomed weld centre area for OP.
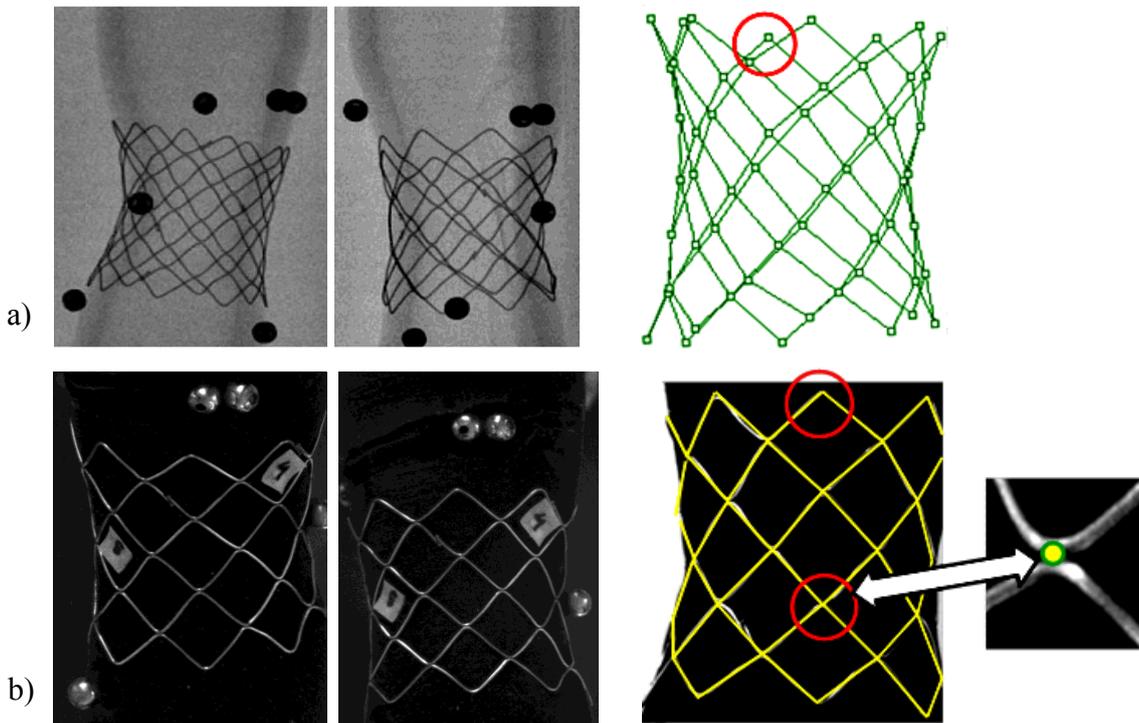
Figure 4-4: Representative images from biplanar imaging techniques a) fluoroscopy, left and right images; b) stereo optical imaging, left and right.

The 2D fluoroscopy image pairs were post-processed to obtain the 3D stent geometry. Landmark points were identified in both fluoroscopy images and back-projected (orthographic projection) into 3D space by tracing parallel rays from the orthogonal projections using CAD software Rhinoceros. The ray intersection determines the position of the strut landmark in 3D space. The calibration was based on the distance measured between reference markers calculated from the micro-CT reconstruction.

For each stent position imaged optically strut landmarks were identified in the left and right 2D camera images. The 3D coordinate of each landmark was obtained by triangulation using the camera calibration data and the 2D position from left and right images [108]. The zoomed region of interest shown in *Figure 4-5* shows the epipolar line in the right image passing through the same landmark in the left image.

Left image   *Epipolar line*   Right image
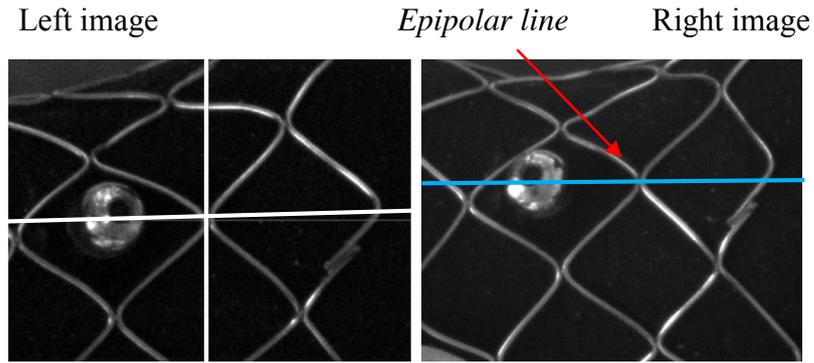
Figure 4-5: Triangulation of a selected point in three dimensional space achieved by intersection of the epipolar lines from two cameras.

For each method the identification of the weld centre was repeated three times using the same image pair to test the repeatability of this process. The average of the three reconstructed points was used to compute stent geometry parameters for comparison with the other imaging methods.

4.1.1.3. MEASURED PARAMETERS

The reconstructed stent geometry obtained from each of the four imaging methods, was used to compute strut length (L), inter-strut angle (β) and circumferential asymmetry (Ca) of each strut unit. The graphical representation of these parameters is presented in *Figure 4-6*. The results obtained using each imaging technique was compared with micro-CT which was assumed to represent the gold standard.

Strut length L (96 struts in total), was defined as the distance between the two landmark points (x_1, y_1, z_1) and (x_2, y_2, z_2) at the end of each strut:

$$L = \sqrt{(x_2 - x_1)^2 + (y_2 - y_1)^2 + (z_2 - z_1)^2} \qquad \text{4-1}$$

Inter-strut angle β (96 angles), was computed using the Law of cosines from the dimensions of the triangle to which the investigated angle belongs:

$$\beta = acos\left(\frac{-b^2+a^2+c^2}{2ac}\right)$$ 4-2

Stent cell asymmetry C_a (40 asymmetries) was calculated as the ratio between the cell

longitudinal (dl) and circumferential (dc) diagonals:

$$C_a = \frac{dl}{dc}$$ 4-3
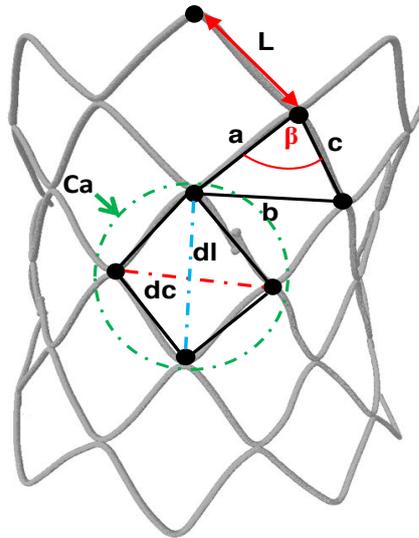
Figure 4-6: Definitions of the parameters measured for comparison: strut length (L), angle (β) and circumferential asymmetry (C_a). Stent 3D model was created using CTan and improved with CTvol.

4.1.1.4. ERROR EXAMINATION

The geometric parameters were calculated from multiple reconstructions of the stent

geometry for each technique. The repeatability error was assessed by calculating the

standard deviation (σ_p) of the parameter values and the maximum percentage

difference (ΔP_{max}) from the average parameter value (P) over all reconstructions, as

defined in equation 4-4.

$$\bar{P} = \sum_{i=1}^{n} \frac{P_i}{n} \qquad \sigma_p = \sqrt{\sum_{i=1}^{n} \frac{(P_i - \bar{P})^2}{n-1}} \qquad \Delta P_{max} = max \left| \frac{(P_i - \bar{P})}{\bar{P}} \right|$$

4-4

This resulted in **n** values of standard deviation and maximum percentage difference for each parameter (96 for strut length, 96 for inter-strut angle and 40 for stent cell asymmetry). For all methods averaging was calculated from three reconstructions (n = 3).

The maximum, mean and average of the *n* values of standard deviation and maximum percentage difference are reported in section 4.1.2. as an estimation of the reconstruction error associated with each imaging technique.

A sensitivity analysis was performed, to define the maximum possible sources of errors for optical reconstruction, which is the main focus of this study. The error in strut angle was evaluated by selecting landmarks away from the centre of each crown weld to assess the potential inaccuracy due to incorrect selection of strut landmarks. The area of interest was chosen randomly for two stent angles. The landmarks were reconstructed three times for chosen struts to assess the variation in angles resulting from inaccurate landmark identification. The diagram below (*Figure 4-7*) illustrates the area within which landmarks were selected.
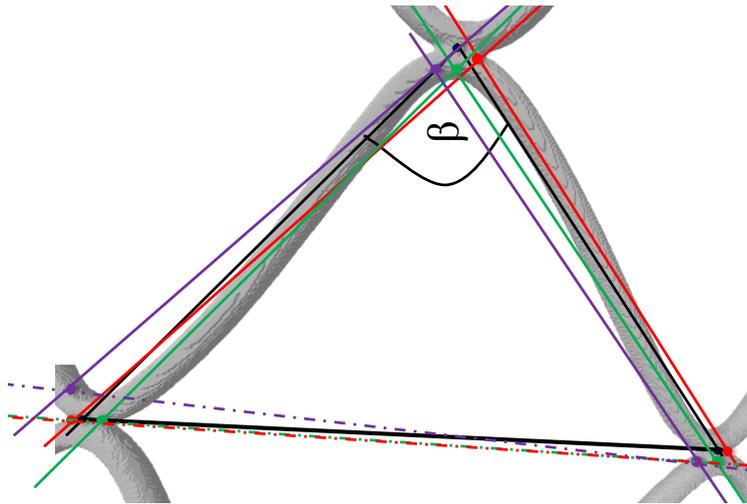
Figure 4-7: Stent strut image reconstructed from micro-CT images. Potential error (uncertainty) area for angle measurement indicated with red green and purple points, where black presents the correct angle.

4.1.1.5. COMPARISON OF IMAGING TECHNIQUES WITH GOLD STANDARD METHOD

Micro-CT measurements of all parameters (L-length, β-inter-strut angle and C_a-circumferential asymmetry) were used as the gold standard for assessment of the error arising from the other imaging techniques. Pearson's correlation coefficient was calculated between the micro-CT data and all other imaging techniques, for all three parameters. Bland-Altman plots were produced for each parameter and for optical reconstruction technique using the micro-CT data as the comparative method.

4.1.2. RESULTS- MEASURED ERROR, DIFFERENCES BETWEEN IMAGING TECHNIQUES

The reconstruction of 25 points in three translation steps for calibration and reconstruction accuracy assessment for the optical method resulted in an average difference of 19 μm (*Table 12*) in computed size of a grid square on the checkerboard.

The variation in the computed parameter values for each technique with repeated reconstruction of the stent geometry is reported in *Table 13*. The calculated values of stent parameters (L, β, Ca) using each imaging technique were correlated with the corresponding values from micro-CT. Pearson's correlation coefficients computed for each parameter are reported in *Table 14*.

The 96 measures of strut length obtained with each imaging method individually are plotted against the micro-CT results in *Figure 4-9*. The length was chosen for the linear regression plot as due to highest variation in the correlation results.

Bland-Altman plots to compare optical reconstruction results with the micro-CT data are shown in *Figure 4-10* for the strut length (L), inter-strut angle (β), and cell asymmetry (Ca), respectively. The percentage error from the comparison of micro-CT with other imaging methods is presented in *Table 15*.

The results from the sensitivity test for the two reconstructed angles for inaccurate landmark identification (as shown in *Figure 4-7*) are presented in *Table 16*. The maximum calculated error of 2.57% was found from the sensitivity test results.

Table 12: Maximum, minimum and standard deviation (STDEV) from all 25 points reconstructed in 3 steps of translation of the control object (Chapter2, section 2.3, Figure 4-8)

Difference in computed distance [μm]			STDEV [μm]
Max	Average	Min	
55	19	0.2	15

Table 13: Maximum and mean standard deviations, and maximum and mean % differences (with respect to average values for each technique presented in the brackets) in the strut lengths (L), strut angles (β) and circumferential asymmetries (Ca) between repeated point selections.

Parameters	STDEV **max and (mean)**	% DIFFERENCE **max and (mean)**
L [mm]		
micro-CT	0.082 (0.021)	2.07 (0.52)
hCT	0.136 (0.042)	3.51 (1.01)
lCT	0.237 (0.068)	6.11 (1.75)
OP	0.065 (0.020)	2.90 (0.35)
F	0.198 (0.063)	3.79 (0.92)
β [º]		
micro-CT	1.175 (0.275)	1.59 (0.43)
hCT	2.048(0.487)	2.71 (0.76)
lCT	3.472 (1.024)	5.57 (1.64)
OP	1.055 (0.356)	1.98 (0.31)
F	2.934 (0.883)	3.60 (0.81)
Ca [-]		
micro-CT	0.009 (0.003)	1.21 (0.44)
hCT	0.017 (0.006)	2.58 (0.85)
lCT	0.047 (0.013)	5.76 (1.77)
OP	0.009 (0.004)	1.18 (0.29)
F	0.024 (0.011)	2.78 (0.71)

Table 14: Results of linear correlation coefficient between values of each parameter calculated using micro-CT and each of the four other imaging techniques.

	*l*CT	*h*CT	**OP**	F
L	0.657	0.542	0.906	0.541
β	0.981	0.993	0.993	0.989
Ca	0.988	0.993	0.995	0.988
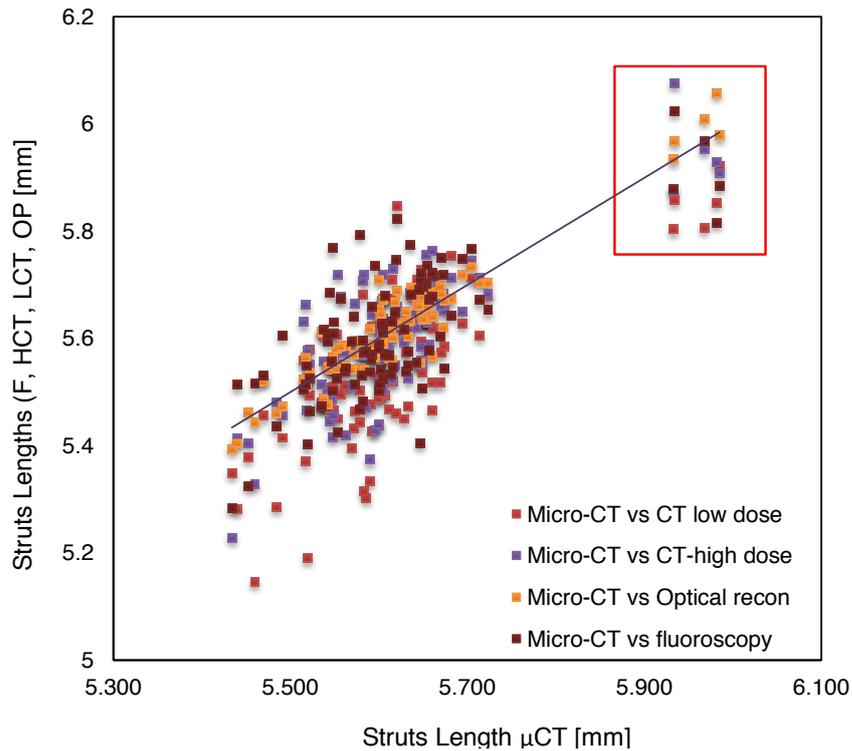
Figure 4-9: *Linear regression plotted for the ideal case to show how close plotted data are correlated against micro-CT*

Table 15: Comparison of hCT, lCT, fluoroscopy and optical stereo-photogrammetry techniques: maximum (mean) % differences of all parameters with respect to micro-CT.

Max (Mean) % Differences	*h*CT	*l*CT	F	OP
L [%]	3.84 (1.04)	5.94 (1.58)	4.26 (1.22)	1.97 (0.18)
β [%]	3.40 (0.96)	5.87 (1.30)	3.07 (0.89)	3.00 (0.89)
Ca [%]	2.32 (0.83)	4.43 (1.30)	4.31 (1.18)	3.02 (1.12)

Table 16: Repeated angle measurement to assess likely maximum error.

	Angle	Measured result [°]	Difference from correct angle [°]	Error [%]
1	1. true	96.97	-	-
	vary 1	96.66	0.31	0.32
	vary 2	97.98	1.01	1.042
	vary 3	94.48	2.49	2.57
2	true	76.61	-	-
	vary 1	75.2	1.41	1.84
	vary 2	77.97	1.36	1.77
	vary 3	77.58	0.97	1.26
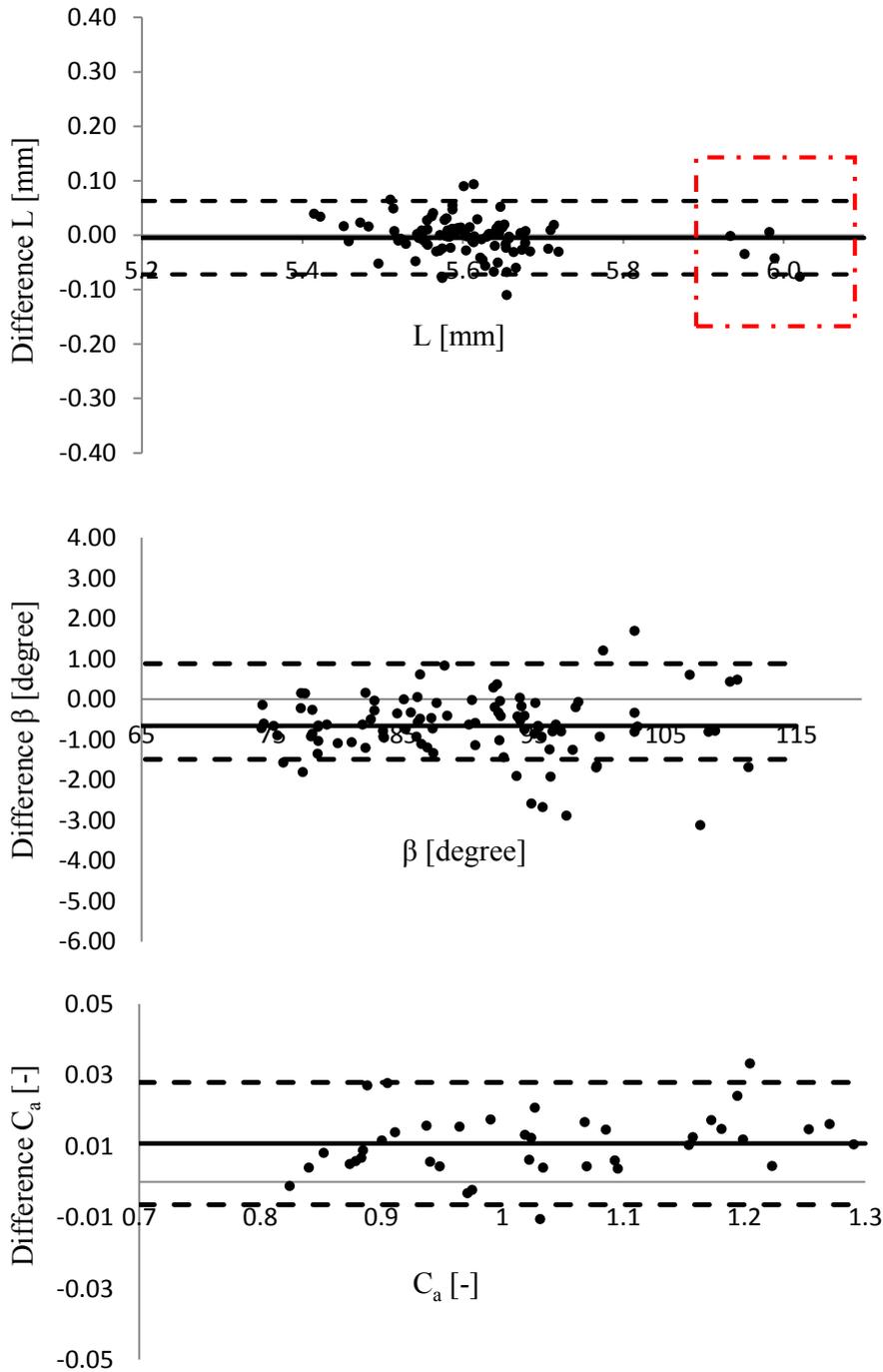
Figure 4-10: *Bland-Altman plots for: a) strut length (L); b) inter strut angles (β); c) circumferential asymmetry (Ca) showing the differences in the values measured with the micro-CT technique and stereo photogrammetry. The thick line represents the mean difference between the value of the parameter measured with each technique and with micro-CT. The dotted lines represent +1.96 and -1.96 standard deviation of the differences between the two methods.*

4.1.3. DISCUSSION

For the volumetric methods the variation in the computation of all parameters with repeated landmark selection increases from micro-CT to hCT to lCT (the transparent arrows in *Table 13* show increasing uncertainty). For the biplanar methods, the variation increases from the optical stereo-photogrammetry to the fluoroscopy (the purple arrows show increasing uncertainty). These results agree with expectations as the micro-CT data are obtained at the highest spatial resolution and low dose CT imaging is expected to be worse than that of the high dose CT. The uncertainty of the optical reconstruction results is of similar magnitude to the micro-CT data, whilst the uncertainty of the biplanar fluoroscopy results is of similar magnitude to that of the high dose CT. This relationship between the results obtained using 2D and 3D methods are in line with the variation in the spatial resolution of each technique. The closest linear correlation with micro-CT measures was obtained using the optical stereo method for all three parameters, as reported in *Table 14* and shown in *Figure 4-9* for the length measure. From *Table 15* it is clear that the optical reconstruction method results in the smallest maximum and mean percentage error values.

These results demonstrate that local 3D PPVI stent geometry can be accurately measured using two biplanar views. Comparison between biplanar fluoroscopy and stereo photogrammetry, demonstrates the improvements in accuracy that can be obtained using high resolution optical systems, which maintain the advantage of high temporal resolution in contrast with volumetric methods.

Whilst biplanar angiography can be applied for *in vivo* imaging the increase in accuracy provided by the optical method is encouraging for *in vitro* application of this

technique at coronary artery length scales, which is the focus of the remainder of this thesis.

4.2. SMALL SCALE-CORONARY STENT

In section 4.1 it has been demonstrated that fluoroscopy can measure the geometry of valve stents *in vivo*. However, this method can be not used to assess the geometry of coronary stents due to their small size, thin struts and the insufficient resolution of the X-Ray equipment to visualise stent details, as it is presented in the image below.

Figure 4-11: Stent implantation in the LAD (Left Anterior Descending Artery); image visualize inflated angioplasty balloon; courtesy of Dr Julian Gunn.

Although optical methods cannot be applied for *in vivo* imaging, the increase in accuracy they provide is encouraging to examine coronary stent performance *in vitro/ex vivo*. From the perspective of design of the optical system, as discussed in Chapter 3, the measurement of 3D coronary stent geometry presents a more significant challenge due to the smaller length scales involved. This section describes extension of the methods applied to the PPVI stent in section 4.1 to compare the accuracy of biplanar optical stereo-photogrammetry and micro-CT for evaluation of 3D coronary stent geometry. Both techniques were used to determine the 3D geometry of one fully deployed (FD) and one semi-deployed (SD) 316L surgical stainless steel Taxus Express™ balloon expandable stent (Boston Scientific) with a 7 ring configuration

(*Figure 4-12*). The TAXUS™ Express^2™ Paclitaxel-Eluting Coronary Stent is an expandable, slotted, stainless steel tube, with a drug (paclitaxel) contained within a thin polymer coating on its surface to reduce neointimal tissue growth (TAXUS™ Express^2™ Manual, Monorail™).
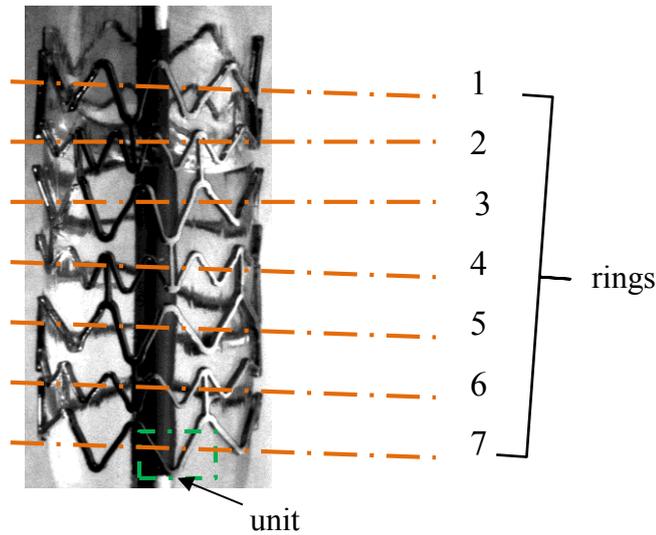
Figure 4-12: Presentation of the 7 ring configuration of the deployed coronary Taxus Express stent on the angioplasty balloon.

Comparison of semi- and fully-deployed stent geometry was undertaken to consider the typical 'dog-boning' effects observed as the stent expands, illustrated schematically in *Figure 4-13*.
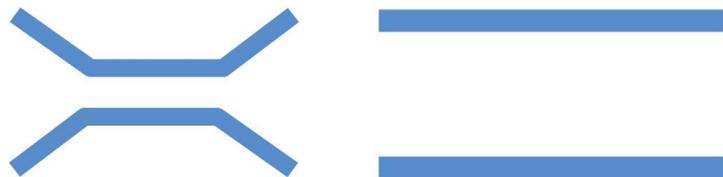
Figure 4-13: Schematic presentation of semi (dog-boning) on the left and fully deployed, on the right, stent configuration.

4.2.1. METHODS

4.2.1.1. IMAGE ACQUISITION

A piece of a metal wire (reference marker) was attached to the balloon catheter used to deploy the stent, to provide a reference position to locate correspondence between the optical and micro-CT imaging methods (*Figure 4-14*).

Reference marker

Figure 4-14: Schematic representation of the reference marker fixed on the catheter.

Optical images were obtained using a stereo camera rig with a pair of Flea2 cameras, separated by 85°, controlled with FlyCap2 software (Point Grey, Canada). The optical system designed in Chapter 3 was used to provide a field of view of around 10 mm along the maximum image dimension and to ensure adequate depth of field of 4 mm to maintain focus over the stent geometry. The optical image resolution was 1288 x 964 with a sensor pixel size of 3.75 µm x 3.75 µm. A lens of focal length 31.5 mm was positioned approximately 44 mm from the camera sensor, resulting in a magnification of 0.4, field of view 10 mm x 8.2 mm and a spatial resolution of approximately 8 µm.

The cameras were calibrated using a small scale checkerboard grid pattern containing 100 squares (0.5 mm x 0.5 mm) with the Bouguet Calibration Toolbox for Matlab [105, 115]. Calibration accuracy was determined through reconstruction of a control checkerboard grid (10 x 6 mm) captured during few translations by reconstructing 2 mm reference distances between single grids.

The stent and catheter were removed from the packaging provided by the manufacturer, clamping the catheter to maintain a horizontal position (*Figure 4-15* and to ensure an appropriate distance (approximately 105 mm) was maintained between the lens and the stent during expansion. This method reduces rigid body motion of the catheter which might move the stent outside the depth of field during balloon inflation, producing blurred images and increasing the error of results. A clinical implantation device (Merit Medical Basix25, Ireland) was connected to the catheter and used to inflate the balloon and to monitor the applied pressure (the setup of the inflation device is in Chapter 5, section 5.1.1). The balloon pressure was incrementally increased in steps of approximately 0.5 atmospheres.

Clamped catheter with stent crimped on the balloon
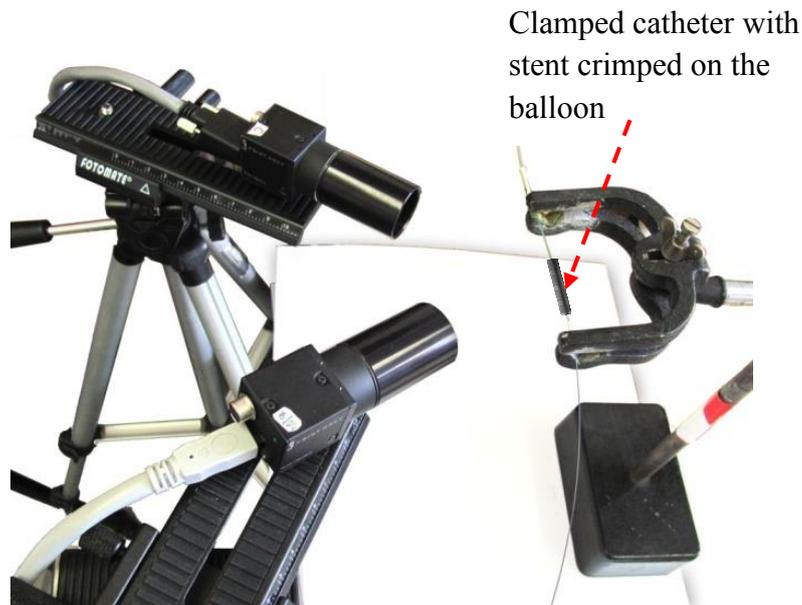
Figure 4-15: Stereo camera rig (pair of Flea2 fire wire cameras) focused on the coronary stent crimped on the balloon.

The first stent with 3.5 mm nominal deployed diameter, 8.0 mm length was semi-deployed (SD), by increasing the balloon pressure to 4 atmospheres until a dog-boning effect was observed and then deflating the balloon. The balloon was not removed to

keep a reference point on the catheter surface. The second stent with 4.0 mm nominal deployed diameter, 8.0 mm length was fully deployed (FD) to the nominal balloon pressure of 9 atmospheres, with the balloon left inflated to avoid stent movement due to balloon deflation and keep the same relationship between the stent and the reference point fixed on the catheter. Micro-CT of the stents was undertaken as a gold standard validation method for comparison with the optical technique. To help and support the stent during scanning, it was placed in the tube made of plastic, which was glued to the scanner plate for the stability purpose. Scans were performed with the Skyscan 1172 *ex vivo* cone-beam scanner (Bruker, Belgium). The voxel size was 6.0 µm x 6.0 µm x 6.0 µm with scanning parameters: 70kV, 141µA, Aluminium/copper filter, and 180° rotation with a 0.7° rotation step resulting in 257 projection images. The stent was scanned as a 3 part oversized scan. Each image acquisition time was 590 ms.

4.2.1.2. IMAGE POST-PROCESSING

Optical images of the coronary stents were analysed using Matlab for the biplanar method, CTan, CTvol (CT data analyser) and Dimension Expert (Dimension Expert, DeskArtes, Finland) for the volumetric methods.

Optical stereo-photogrammetry: Strut landmarks were used to characterise stent geometry, in the same way as for the PPVI stent analysis. Identification of landmarks in the left and right 2D camera images is shown in *Figure 4-16*.

Left camera 2D image   Right camera 2D image
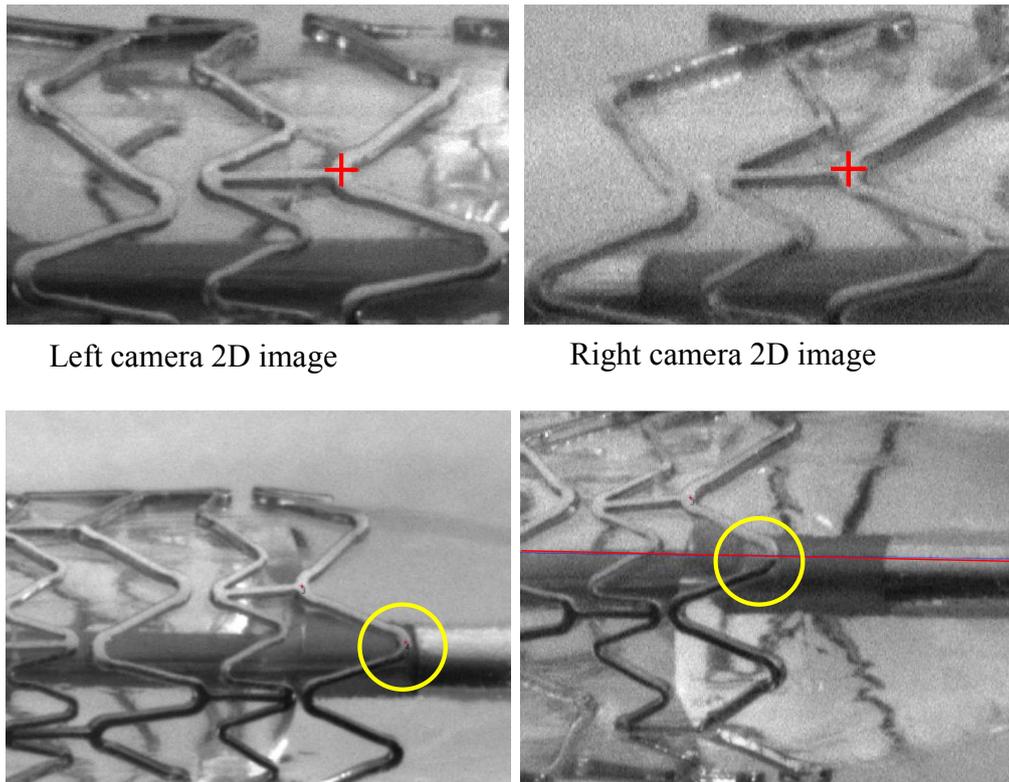
Figure 4-16: Strut landmark in the left and right camera image. Epipolar line indicating correspondence position in the right image.

The 3D coordinate of each weld centre point was obtained by triangulation using the camera calibration data and the 2D position from left and right images [108] as explained in Chapter 2. The accuracy associated with hand picking of strut landmark points was estimated by repeating the measurements 7 times.

Micro-CT: The data was reconstructed using NRecon (Skyscan, Belgium) to provide a 3D volumetric data set for comparison with the stereo optical reconstruction. Regions of interest were selected using CTAn (Skyscan, Belgium) and 3D volumes were created by segmentation, using a binary threshold (105, where maximum intensity is 255). Threshold sensitivity testing demonstrated that a higher binary threshold (>110), caused loss of volume (*Figure 4-17*a), and a lower threshold (<100) resulted in a lot of noise (*Figure 4-17*b).

a)   b)
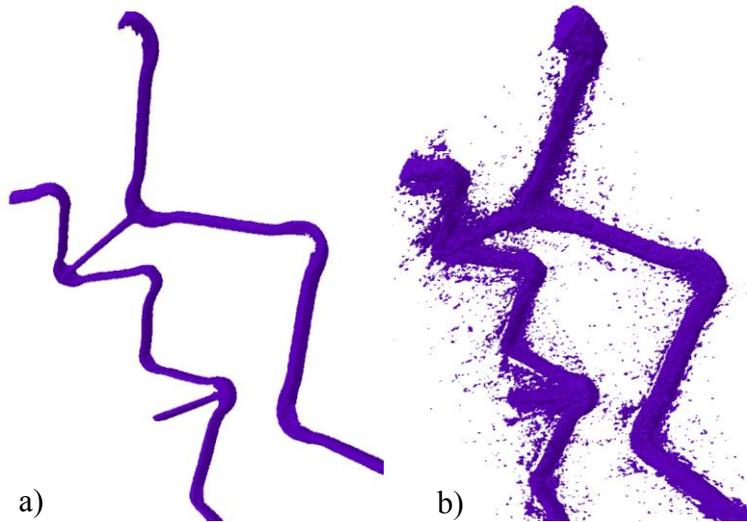
Figure 4-17: 3D models presenting importance of the threshold value.

A standard triangle language (STL) file of the reconstructed stent was exported to Dimension Expert, DeskArtes (*Figure 4-18*), where the 3D data were obtained.

a   d

c
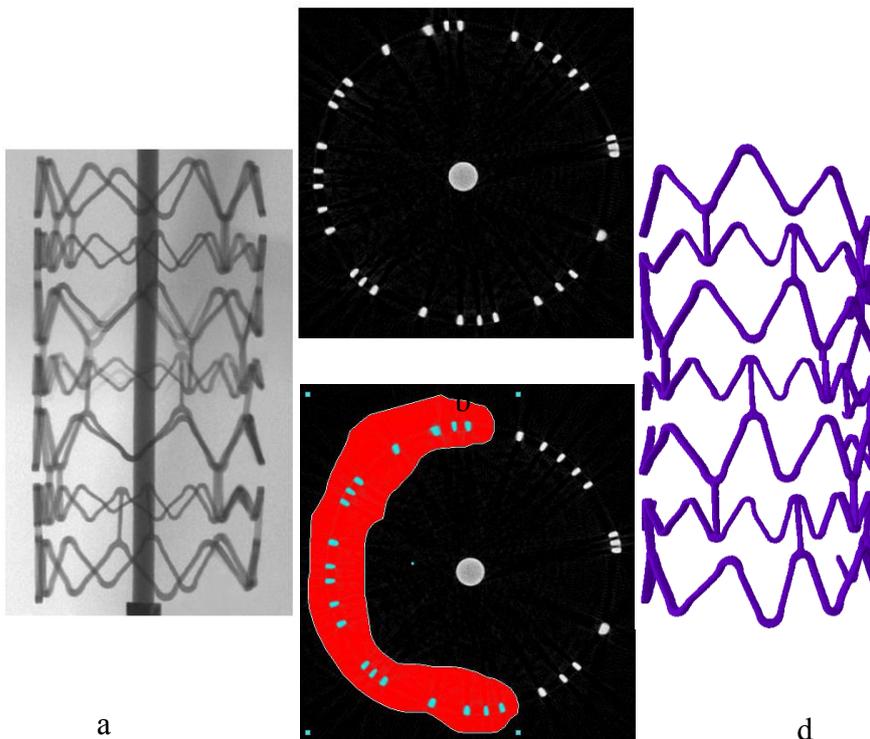
Figure 4-18: Example images of fully-deployed stent, a) Micro-CT scan with selected area for reconstruction; b) stent cross section; c) chosen region of interest; d) 3D model (visualised using Dimension Expert software).

4.2.1.3. MEASURED PARAMETERS

The 3D coordinates of the landmarks derived from each method were used independently to calculate strut length and angle (*Figure 4-19*) using the same equations (4-1) and (4-2) as for the valve stent.

- Strut length L (n = 31 and n = 8 for the FD and SD stents respectively)

- and inter-strut angle β (n = 25 and n = 5 per FD and SD stent respectively)
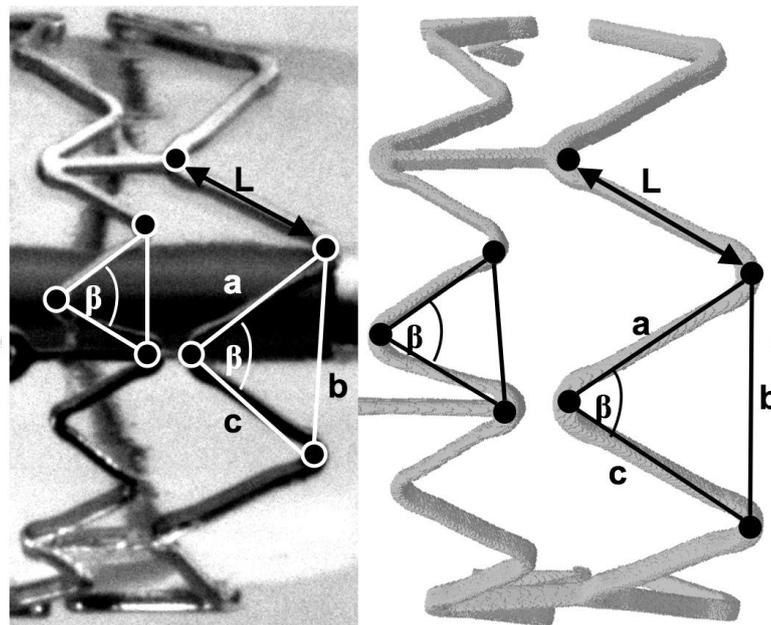
Figure 4-19: Fully deployed (FD) stent geometry: (a) Optical image (b) Segmented surface shown in Desk Alert. Definition of inter-strut angle (β) and strut length (L).

A smaller number of lengths and angles were measured for the SD stent, as it was only deployed at the ends and remained in the undeformed state in the centre.

4.2.1.4. ERROR EVALUATION

The reconstruction was repeated seven times for six landmarks points to assess the repeatability of the measurements. The repeatability error was assessed by calculating

the standard deviation (σ_p) of each parameter value over the seven reconstructions as defined in equation (4-4).

Parameter values (L, β) computed with OP were compared with the micro-CT data gold standard measurement. The maximum percentage difference between the two imaging methods for each parameter was obtained and Pearson's Correlation Coefficient was calculated for a linear fit between the micro-CT data and the optical method. Bland-Altman plots were produced using the micro-CT data as the reference method.

4.2.2. RESULTS

The final geometry of the fully- and semi-deployed stents captured with the left camera is presented in *Figure 4-20*.
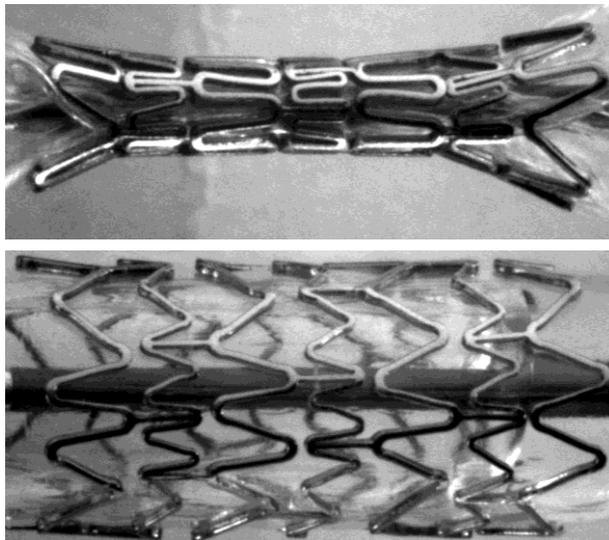
Figure 4-20: Left camera images of semi-deployed Taxus Express 3.5 mm x 8 mm (p= 4.0 atm) and fully-deployed Taxus Express 4x8 mm

Scanned images are presented in *Figure 4-21*, obtained from CTan. The metal wire (reference marker), which was attached to the catheter, is visible in the top of the

image. This marker allowed the same area of the stent to be identified for reconstruction using both imaging methods.
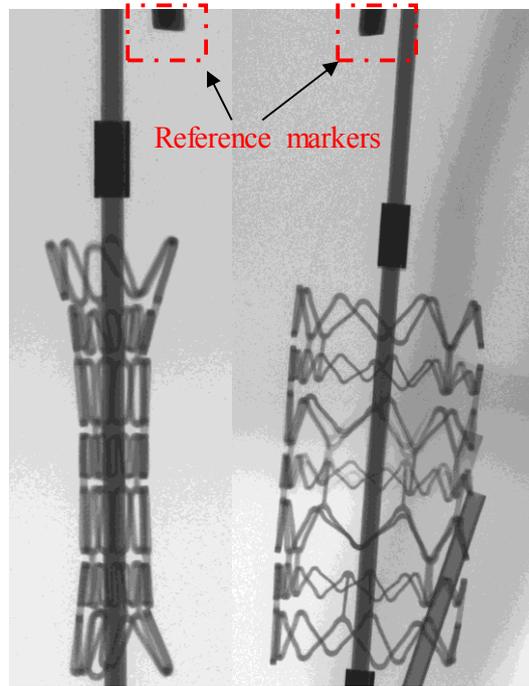
Figure 4-21: Output from the micro-CT scanner; visualisation from CTan.

Control object reconstruction suggested an average measurement accuracy of the order 10 μm for 10 measured differences in distances between points on the grids compared for 5 translations conducted with a travelling microscope, *Table 17*. The accuracy associated with the repeatability of hand picking of strut landmark points is presented together with the calibration accuracy results. A much higher discrepancy occurred when picking the same landmark on the stent surface, rather when picking sharp corner of the checkerboard grids for the calibration accuracy assessment.

Table 17: Maximum, minimum and standard deviation (STDEV) from all 10 points reconstructed in 5 steps of translation of the control object for the calibration accuracy assessment.

Calibration accuracy [μm]				Repeatability accuracy [μm]			
Max	*Mean*	*Min*	*STDEV*	*Max*	*Mean*	*Min*	*STDEV*
24	10	6	10	31	16	6	16

The calculated values of the stent parameters (L, β) measured using OP were correlated with the corresponding values measured using micro-CT. Pearson's Correlation Coefficients values were calculated (FD: R^2=0.9957 for length; R^2=0.9798 for inter strut angle measurement; SD: R^2=0.9988 for length; R^2=0.9629 for angle measurement) demonstrating good linear correlation. Bland-Altman plots comparing OP with micro- CT results for length and angle measurements are shown in *Figure 4-22*.

The OP calculation of strut length agrees to within 98.5 % and inter-strut angle agrees to within 97% of the micro-CT values for FD stent and strut length agrees to within 98% and inter-strut angle agrees to within 96.5% of the micro-CT values for SD stent. A maximum difference of the order 0.03 mm (3.8%) and of the order 3 degrees (4%) was computed for a single strut length and single inter-strut angle respectively.
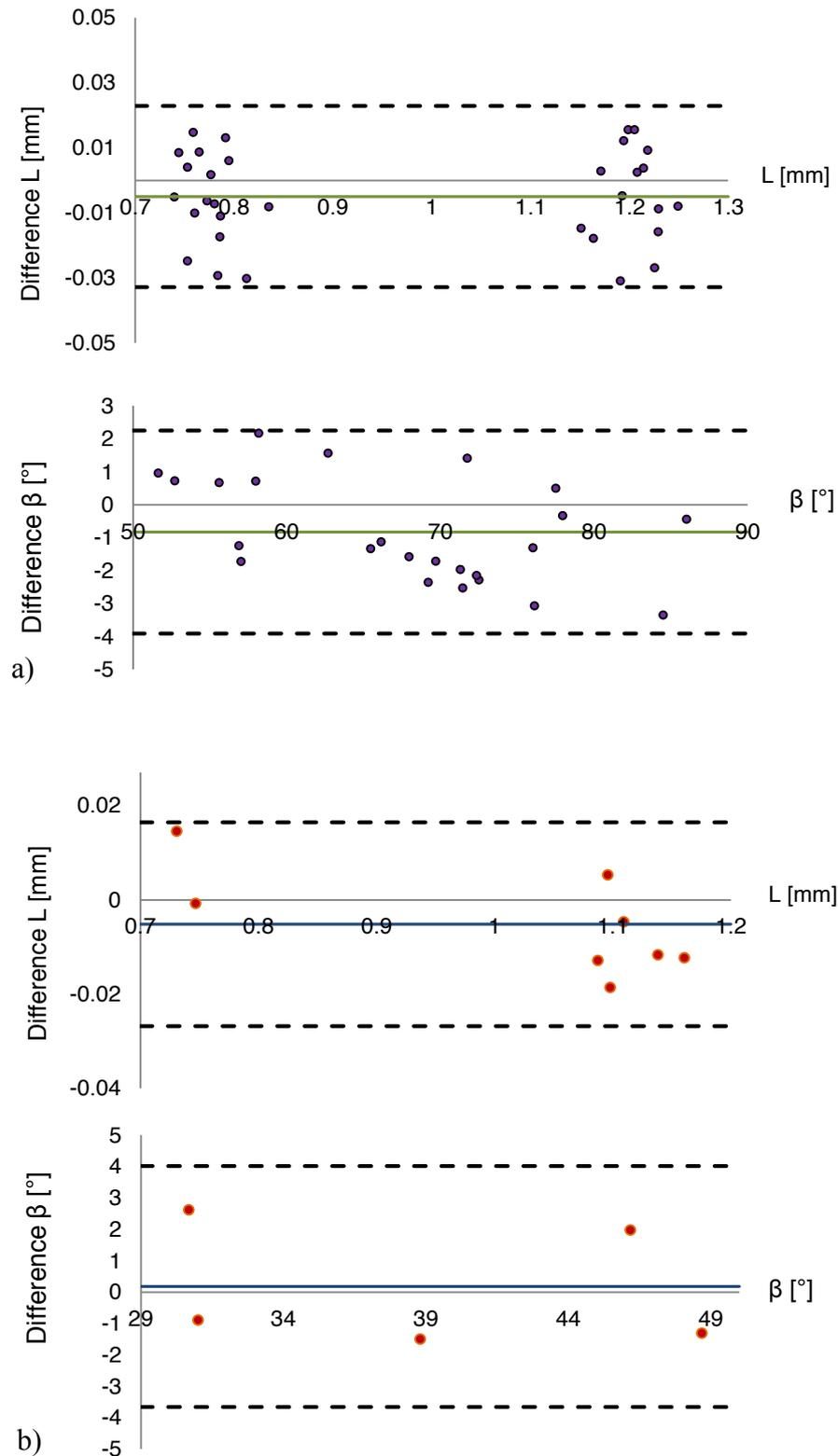
Figure 4-22: a) FD and b) SD stent: Bland-Altman plots for strut length (L) and inter-strut angle (β) (showing the differences in the values measured with the micro-CT and OP technique). The thick line represents the mean difference between the value of the parameter measured with OP and micro-CT. The two dotted lines represent +1.96 and -1.96 standard deviations of the differences between the two considered methods.

4.2.3. DISCUSSION

Local stent geometry (strut lengths, angles between struts) at the smaller length scale of coronary stents was obtained using volumetric micro-CT and biplanar optical stereo-photogrammetry. The optical method reported here has been shown to provide a description of 3D stent geometry which agrees well with volumetric data even at these more challenging length scales.

Both linear regression and Bland-Altman plots confirm good agreement of the optical method with micro-CT data. For the strut length parameter for both stents there is a small negative offset, demonstrating that the stereo method tends to underestimate strut length. However, this offset is significantly less (~ 5 μm) that the mean repeatability error (~ 16 μm) associated with identification of strut landmark points. The offset in angle measurement is not consistent between the two stent reconstructions. The semi-deployed stent had four times less lengths and angles measured due to the reduced number of deployed struts. In general the results demonstrated good agreement between the two techniques.

For *in vitro* measurement, micro-CT provides accurate 3D geometry at high resolution, but cannot capture stent deployment over a realistic timescale of a few seconds. It is possible to obtain micro-CT data for a number of static steps of stent/balloon inflation, as reported by Connolley and colleagues [89], but image acquisition takes 70 min to scan the entire stent at each balloon inflation step (inflation steps were at 0, 8, 12 and 17 atm). The change in stent length and diameter was examined with image analysis software (ImageJ). Another study which focuses on the imaging coronary stent deployment in the micro-CT scanner is presented by Mori [4], who analysed elastic

recoil of the coronary stent after balloon deflation. However, no information regarding experimental accuracy is included in either study.

The advantage of the optical stereo technique is that images of the stent expansion process are collected in the timescales of minutes and have the potential to be acquired dynamically in the way that cannot be achieved using micro-CT scanner. Moreover, our method accuracy is checked each time by testing a control object with known size to obtain informative results.

Whilst optical techniques cannot be employed to evaluate *in vivo* device performance, these techniques may be preferred to assess unconstrained coronary stent deployment [106].

SUMMARY

Accuracy assessment of imaging methods is important to ensure confidence in 3D reconstruction of geometry from biplanar imaging techniques, particularly if strain is to be derived from changes in the geometry during deformation. In this chapter it has been shown that biplanar 3D image techniques can provide accuracy of the same order as 3D volumetric image modalities to assess the geometry of stents at different length scales. To the author's knowledge this is the first time that quantitative measures of local stent geometry have been obtained; the same applies to detailed accuracy assessment of imaging modalities.

The encouraging results support further investigation of the stereo image pairs acquired at a number of inflation steps during unconstrained stent expansion which will be presented in Chapter 5 and stent deployment in a vessel analogue to examine strains on the vessel surface due to stent-vessel interaction, presented in Chapter 6. These subsequent chapters aim to improve our understanding of stent-vessel interactions.

CHAPTER 5

MEASUREMENT OF CHANGES IN LOCAL AND GLOBAL STENT GEOMETRY DURING *IN VITRO* FREE EXPANSION

Chapter 5 describes the application of a 3D optical reconstruction method to examine the free expansion of stents, characterising the change in local (inter-strut angle) and global (dog-boning ratio) geometry during balloon inflation. It is necessary to understand how stents deploy in order to identify potential mechanisms of expansion that may result in adverse vascular responses. This chapter extends the methods described in Chapter 4 to consider incremental changes in stent geometry during expansion and compares pseudo-static expansion with fully dynamic expansion. Dynamic expansion is undertaken over timescales which match those employed clinically.

This chapter reports results which have been published in Journal of Artificial Organs [159].

5.   INTRODUCTION

In Chapter 4 it has been shown that biplanar 3D image techniques can provide accuracy of the same order as 3D volumetric image modalities to assess the geometry of stents at different length scales. The optical stereo-photogrammetry method has been shown to provide a full 3D description of stent geometry which agrees well with volumetric data. The landmarks on the coronary stent were reconstructed in 3D to an accuracy of the order 12 µm. The optical technique has the potential to assess dynamic stent expansion over the same timescales used to clinically deploy the stent.

The methods from Chapter 4 are extended here to assess coronary stent geometry at a number of inflation steps. In a previous study, Kiousis *et al*. [131], reported 2D experimental measurement of free expansion of six vascular stents to investigate the deformation mechanisms and provided comparisons with a computational model. Diameter change, foreshortening, maximum dog-boning, elastic recoil during the deployment process (and stent recoil following balloon deflation) were determined. The balloon pressure ranged between 0 and 12 atmospheres. In this previous study, images of stent deployment were obtained using a single CCD camera with a magnifying lens (details of the camera specification were not provided).   The limitation of this study was the use of single camera. The stent was deployed gradually (in steps) over approximately 17 minutes. This is much greater than the typical timescales for *in vivo* stent deployment which are of the order of seconds. A similar approach was undertaken by Pochrzast [132]. This time a light microscope (no specification provided) was used to image change of stent diameter at distal, central and proximal part. The balloon pressure ranged between 0 and 8 atm.

3D reconstruction adds depth information and the characterisation of 3D stent geometry provides a superior determination of the object surface, which is important for adequate strain analysis. To the author's knowledge, free expansion of the stent in 3D has only been examined previously by Narracott [88] using stereo photogrammetry and Mori [4] using micro-CT.

Narracott used stereo-photogrammetry to characterise stent deployment during inflation of two different balloon folding patterns. This study supported the hypothesis that the folding pattern of the balloon influences the symmetry of the deployment. 3D optical reconstruction techniques offer the potential to determine detailed 3D deformation of the stent during expansion both locally and globally. The limitation of previous work [88] was low camera resolution (640 x 582) and image capture using video data, whereas in current study direct, high resolution pixel data is obtained using a fire-wire connection. An advantage of this current study is validation of the optical method against volumetric micro-CT (Chapter 4). This has not been undertaken previously. Mori *et al*. [4] examined elastic recoil due to balloon deflation using micro-CT scanning. They did not report any errors presenting the results due to high accuracy of volumetric method. However, the timescales of stent expansion in the micro-CT scanner are far from those presented clinically.

This chapter reports an experimental investigation, with a focus on the dilation behaviour of balloon expandable coronary stents in 3D. The aim is to examine the variation between local deformation of individual stent struts and global deformation, as assessed by change in stent diameter. The information describing local stent

deployment during free expansion reported in this chapter will be further discussed in Chapter 6 to inform understanding of distribution of the strain on the vessel analogue.

The stereo rig was used to capture incremental changes in stent geometry during expansion and a single camera captured dynamic expansion undertaken over timescales which match those employed clinically.

5.1. STEREO IMAGING OF PSEUDO-STATIC STENT DEPLOYMENT

5.1.1. METHODS

The stereo camera Flea2 system with custom lenses, described in Chapter 3, was used to capture the free expansion of coronary balloon expandable stents at multiple expansion stages. The same optical configuration was used as described in Chapter 3 to provide a field of view of around 10 mm along the maximum image dimension and to ensure adequate depth of field of 4 mm to maintain focus throughout the process of stent expansion.

Three stents (of two different types) were used to assess stent behaviour in 3D during balloon inflation. Two 316 L surgical stainless steel TAXUS™ Express[2]™ drug eluting balloon expandable stents (Boston Scientific) were chosen for the first experiment and cobalt chromium alloy L-605 Coroflex Blue (B.Braun) stent was chosen for the second experiment. These tests allow comparison of stent behaviour between stent designs during balloon inflation.

The TAXUS™ Express[2]™ Paclitaxel-Eluting Coronary Stent is an expandable, slotted, stainless steel tube, with a drug (paclitaxel) contained within a thin polymer coating on its surface to reduce neointimal tissue growth (TAXUS™ Express[2]™

Manual, Monorail^{TM}). The Coroflex Blue stent is a nine crown design which aims to optimise stent deployment and vessel wall coverage to reduce risk of intimal injury [133]. All stents were full deployed *in vitro* to investigate local and global changes in stent geometry during stent expansion. The stent sizes are presented in *Table 18* and stent designs in *Figure 5-1*.

Table 18: Stent and balloon types used in experimental study

Brand	Short name	Initial D [mm]	Final D [mm]	Length [mm]	Strut thickness [μm]
Taxus Express	TE$_1$		3.0		132
	TE$_2$	1.0	4.0	8.0	
Coroflex Blue	CB$_3$		3.5		65

a)   b)
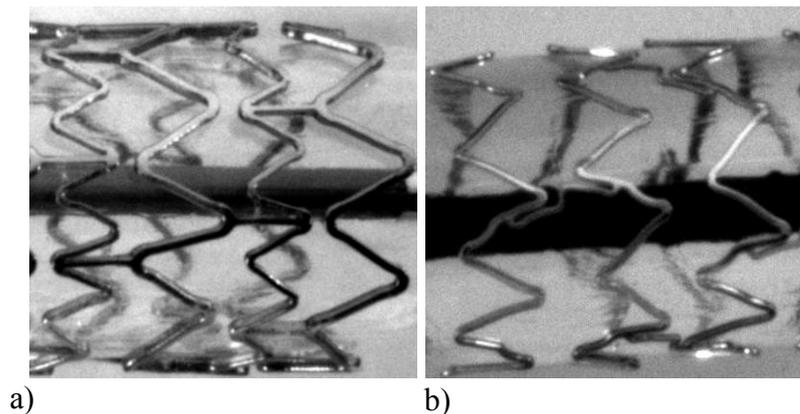
Figure 5-1: Geometry of a)Taxus Express and b) Coroflex Blue coronary stents.

For the TE$_1$ and TE$_2$ stents two cameras were separated as in previous study for the coronary stent by an angle of approximately 85°, for the CB$_3$ stent the angle between cameras was reduced to 55° to be consistent with tests undertaken in Chapter 2 and confirm that camera angle does not change the calibration and reconstruction accuracy results.

The stent catheter was clamped (as presented in Chapter 4, section 4.2.1, *Figure 4.4-5*) to maintain a horizontal position and to ensure an appropriate distance, of approximately 105 mm from the cameras lenses and reduce rigid body motion of the wire during inflation of angioplasty balloon. A diagram presenting lens to stent distance is shown in *Figure 5-2*. Unwanted stent displacement during balloon inflation, outside the depth of field (*DOF*) area, can produce blurred images and increase the error of results as explained in Chapter 3.
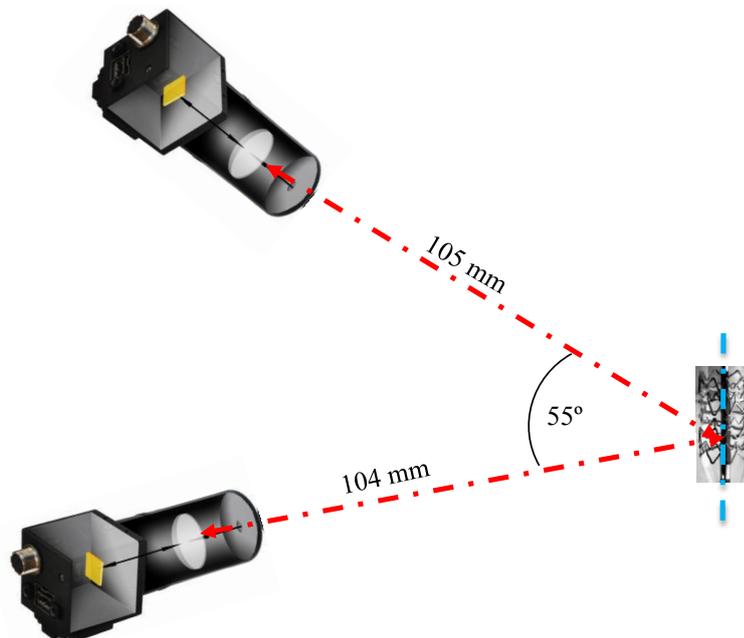
Figure 5-2: Diagram presenting distance from cameras lenses to the CB₃ stent.

Prior to balloon inflation a checkerboard grid pattern was captured in six orientations to calibrate cameras using the Bouguet Calibration Toolbx in Matlab [115], as described in previous Chapters and explained in Chapter 2. Calibration accuracy was determined through reconstruction of a control checkerboard grid with internal grids of size 3 mm x 3 mm. Following calibration assessment the stent was placed within

the field of view of two cameras. *DOF* and correspondence between left and right images was checked using trial images prior to the stent expansion test.

A clinical implantation device (Merit Medical Basix25, Ireland) was connected to the catheter and used to inflate the balloon and to control the applied pressure. Air was removed from the inflation tube and water was used as an inflation medium.
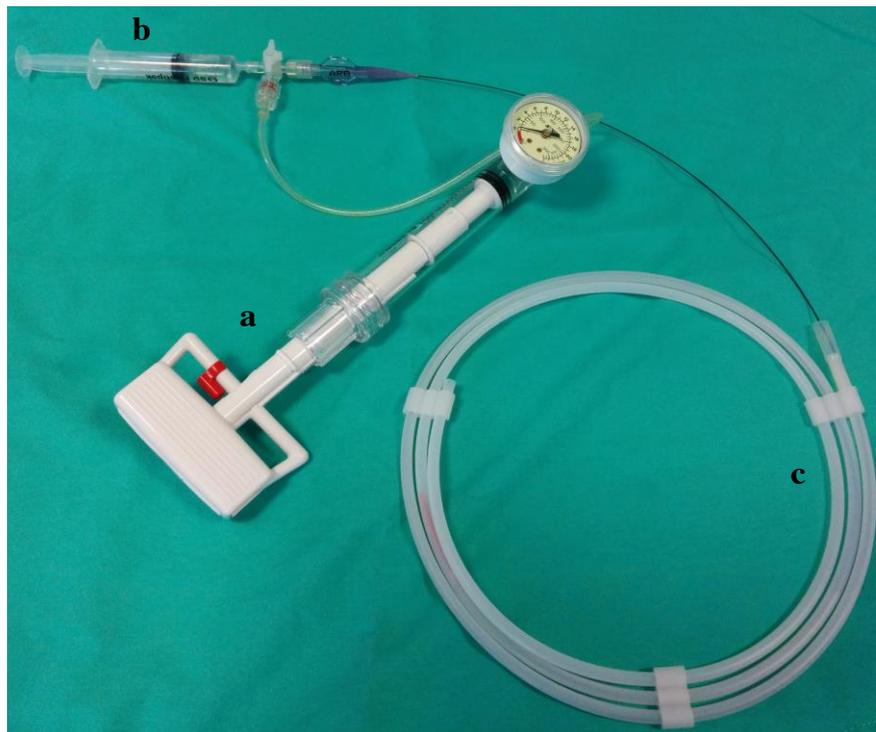
Figure 5-3: The stent delivery system: a) inflation device, b) syringe with 3-way stopcock; c) balloon catheter with crimped stent at its tip.

The pressure was increased to a value of 9 atm (911,92kPa) for both Taxus Express stents, in steps of 1 atm for TE_1 (3.0 mm diameter) in smaller increments of 0.5 atm for TE_2 (4.0 mm diameter). The CB_3 stent (3.5 mm diameter) was inflated to a pressure of 8 atm (810,60kPa) using steps of 1 atm. The stent expansion process was imaged at each pressure increment. To obtain accurate results, few seconds were given to the stent to stabilise, before stereo images were taken.

The stereo optical images were used to characterise stent expansion at each pressure increment as follows:

- Images from each expansion stage were used, along with camera calibration data, to determine the 3D coordinates (x, y, z) of two landmark points on selected stent struts.

- The 3D geometry of the stent struts was reconstructed at each stage of stent expansion.

- The angle (β) between the direction vectors along each strut was calculated as follows:

$$u = [x_u, y_u, z_u] = [x_{p2} - x_{p1}, y_{p2} - y_{p1}, z_{p2} - z_{p1}]$$

$$w = [x_w, y_w, z_w][x_{p4} - x_{p3}, y_{p4} - y_{p3}, z_{p4} - z_{p3}]$$

$$\left|\overrightarrow{u}\right| = \sqrt{(x_{p1} - x_{p2})^2 + (y_{p1} - y_{p2})^2 + (z_{p1} - z_{p2})^2}$$

$$\left|\overrightarrow{w}\right| = \sqrt{(x_{p3} - x_{p4})^2 + (y_{p3} - y_{p4})^2 + (z_{p3} - z_{p4})^2}$$

$$u_{.}w = \cos(\beta)\left|\overrightarrow{u}\right|\left|\overrightarrow{w}\right| \text{ –angle between vectors calculation,} \qquad 5\text{-}1$$

- where $\overrightarrow{u}$ and $\overrightarrow{w}$ are vectors along each strut direction (*Figure 5-4*). This measurement was chosen to provide more meaningful definition of strut angle, particularly at the initial deployment.
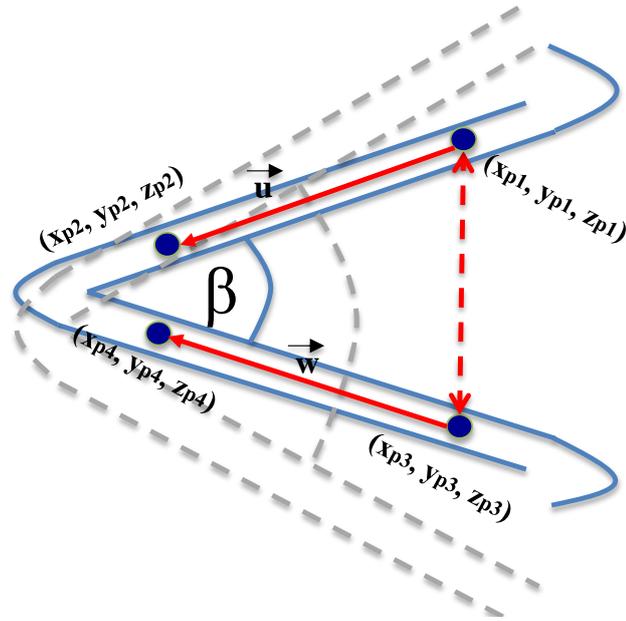
Figure 5-4: Strut length (a, c) and strut separation (b) were used to calculate strut angle. Grey dashes present increase in the angle between struts due to change in pressure load.

In addition, characterisation of global stent deformation in 2D was undertaken by defining the degree of dog-boning between the proximal (DB_p) and distal (DB_d) parts of the stent, relative to the centre, defined as follows (as used by Kiousis [131] and Migliavacca [134]):

$$DB_p = \frac{D_p - D_c}{D_p} \qquad DB_d = \frac{D_d - D_c}{D_d} \qquad\qquad 5\text{-}2$$

D_d represents the distal, D_p-proximal and D_c- central diameter of the stent.

If stent expansion is uniform along the stent length, we would expect stent behaviour similar to that predicted by *in silico* models, as shown in *Figure 5-5*.

a)   b)   c)

Figure 5-5: Presentation of ideal schema of stent deployment, where a) presentation of initial stage, b) semi-deployed stage and c) final stage. Scenario presented during cylindrical balloon inflation, figure adapted with permission from publication of De Beule [10].

Under such conditions the angles of all the units' would expand gradually, in the same way, under increasing pressure and no dog-boning effect would occur. The variation of the measured parameters under these conditions is expected to be as shown in *Figure 5-6a*, which shows the anticipated variations in angle between struts expansion vs pressure. In this case stent expansion results in no dog-boning (*Figure 5-6b*).
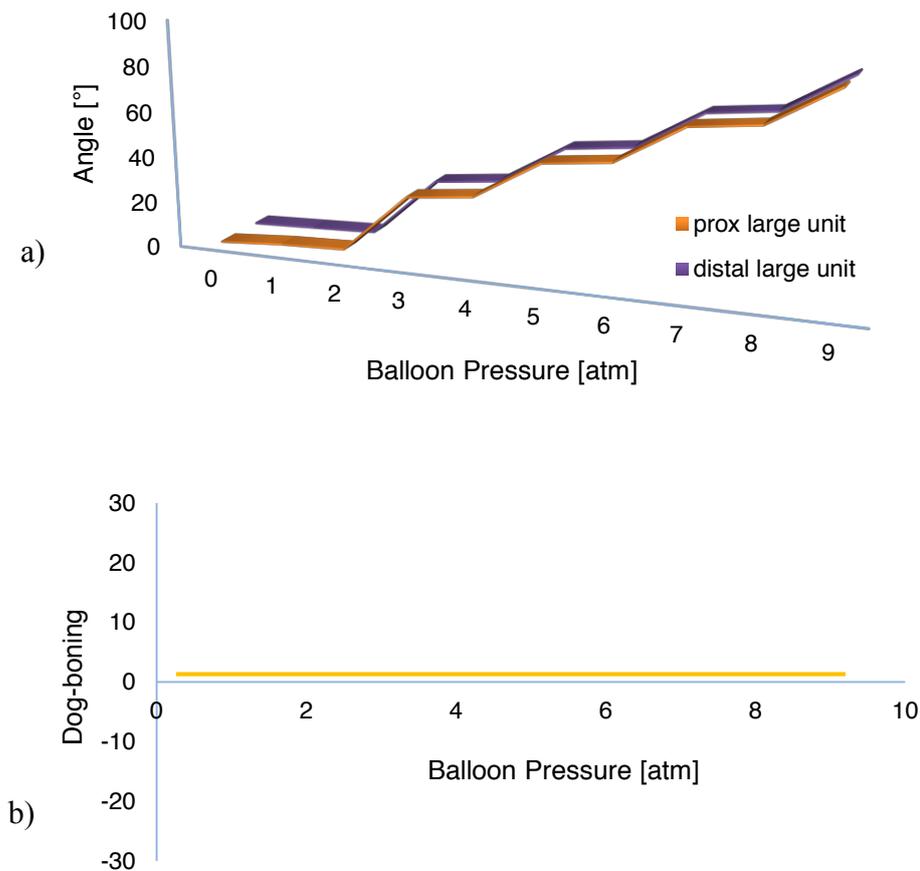
Figure 5-6: Presentation of a) local and b) global expansion of the ideal stent. This plot presents situation in which stent has always the same diameter at distal, central and proximal part during each step of expansion; no dog-boning phase.

Such stent behaviour may be predicted by numerical studies [10], particularly under the assumption that the balloon exerts a uniform pressure on the stent. Under *in vitro* experimental conditions a greater variation in stent deployment is anticipated and has been previously reported [4, 131].

5.1.2. RESULTS

The results from calibration and reconstruction accuracy assessment using a control object for all three tests suggest measurement accuracy of the order 15 μm for both setups. The camera angle did not influence the calibration and reconstruction accuracy results.

Table 19: Maximum, minimum and standard deviation (STDEV) from all 25 points reconstructed in 3 steps of translation of the control object.

Difference in computed distance [μm]			STDEV [μm]
Max	Average	Min	
18	8	6	15

As an example of non-uniform deployment, images of the TE_2 (4 mm) stent geometry at a pressure load of 0 (a), 3.75 (b) and 9 atm (c) are presented in *Figure 5-7*.
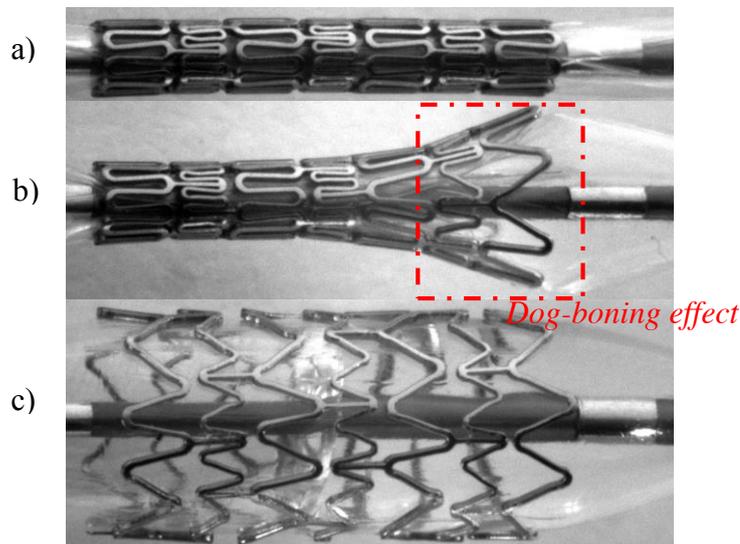
Figure 5-7: Images of the geometry of 4mm diameter stent (a) in the initial configuration (0atm), (b) showing dog-boning effect at 3.75 atm (in the region of the dashed lines) and (c) fully expanded at 9 atm.

The change in inter-strut angle (local strut deformation) and dog-boning measures (global stent deformation) during balloon inflation are shown below (*Figure 5-8* for TE_1, *Figure 5-9* for TE_2 and *Figure 5-10* for CB_3). The struts on the proximal (prox)

and distal (dis) end of the stent, which were in the field of view of both cameras during the whole expansion process, were used to compute inter-strut angles. The error bars represent the maximum error in angle (4%) reported during comparison between optical methods and micro-CT reconstruction of stent geometry from the previous chapter.
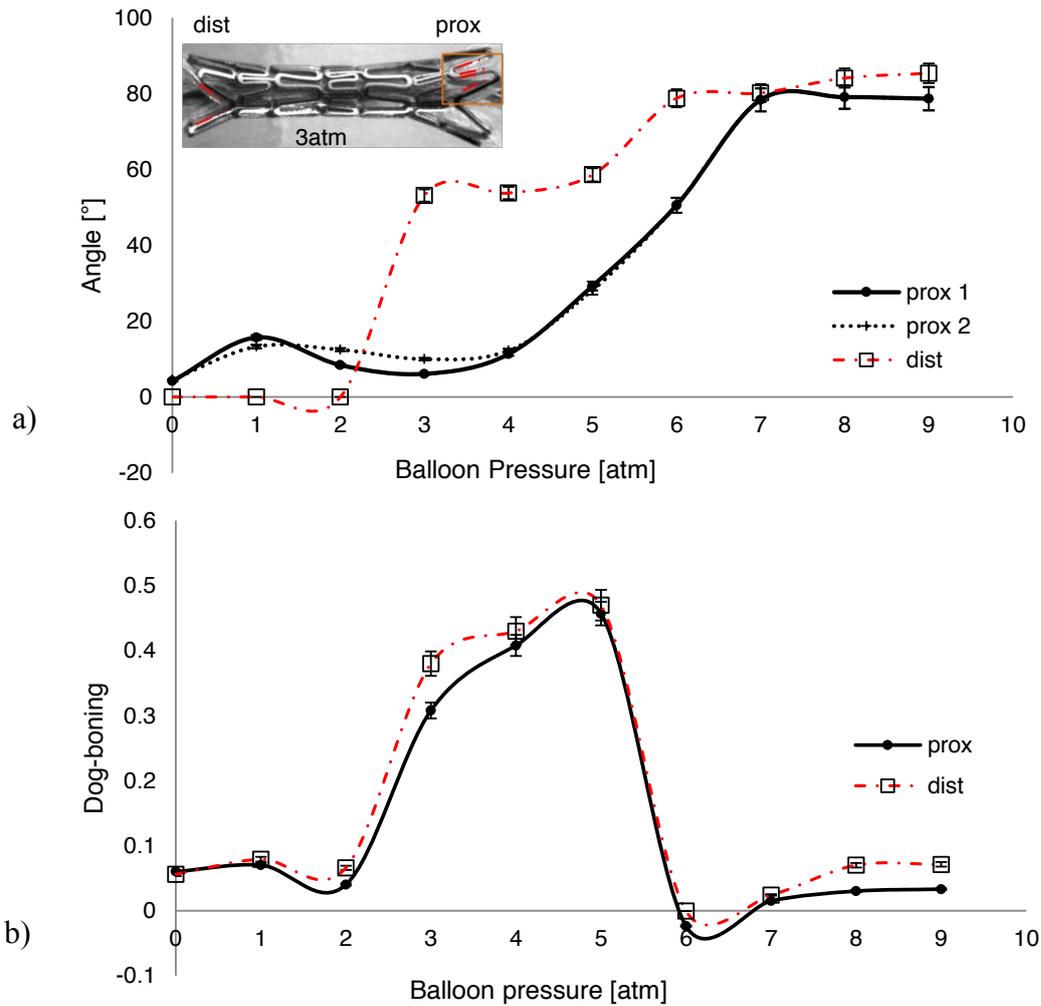
Figure 5-8: TE₁- 3 mm diameter Taxus Express stent: a) variation in strut unit angle with balloon pressure for two units at the proximal end and one at the distal end. b) dog-boning ratio for proximal and distal ends; an image showing locations of the struts using to compute angles is presented at a pressure load of 3 atm.
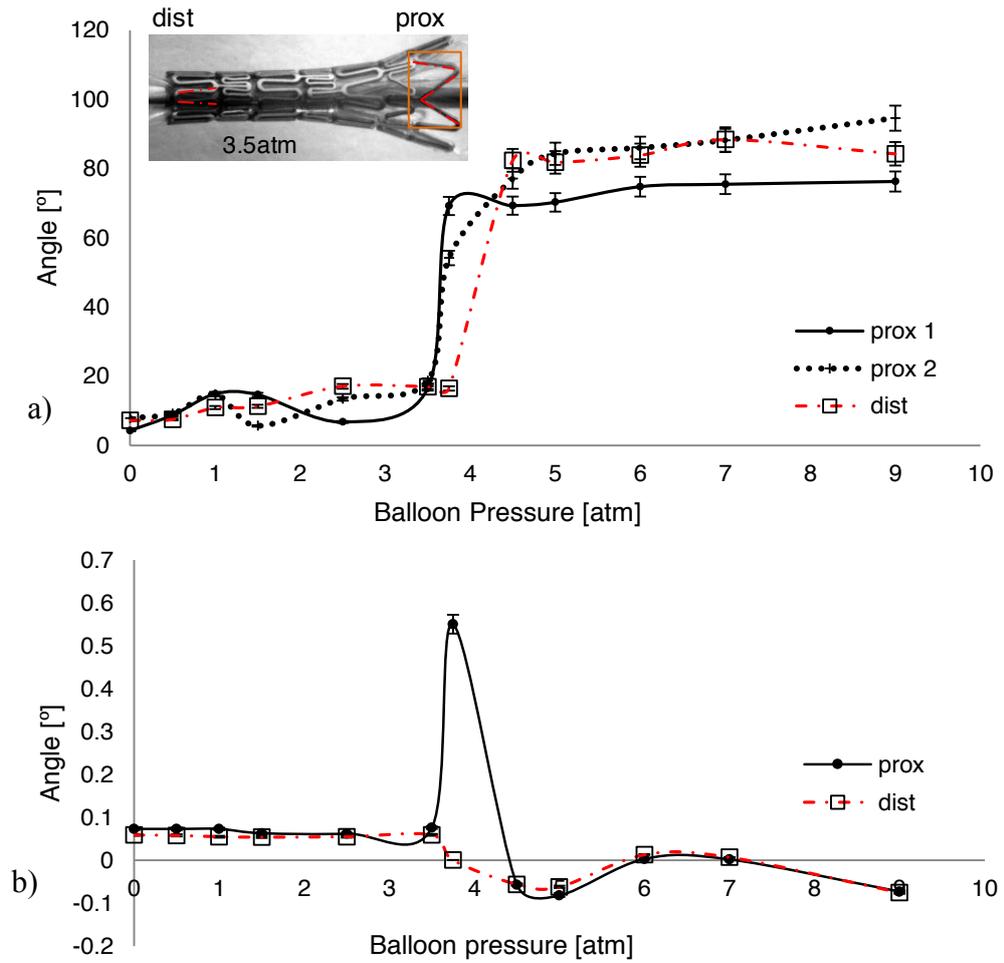
Figure 5-9: TE₂- 4 mm diameter Taxus Express stent: a) dog-boning ratio for proximal and distal ends; b) variation in strut unit angle with balloon pressure for two units at the proximal end and one at the distal end
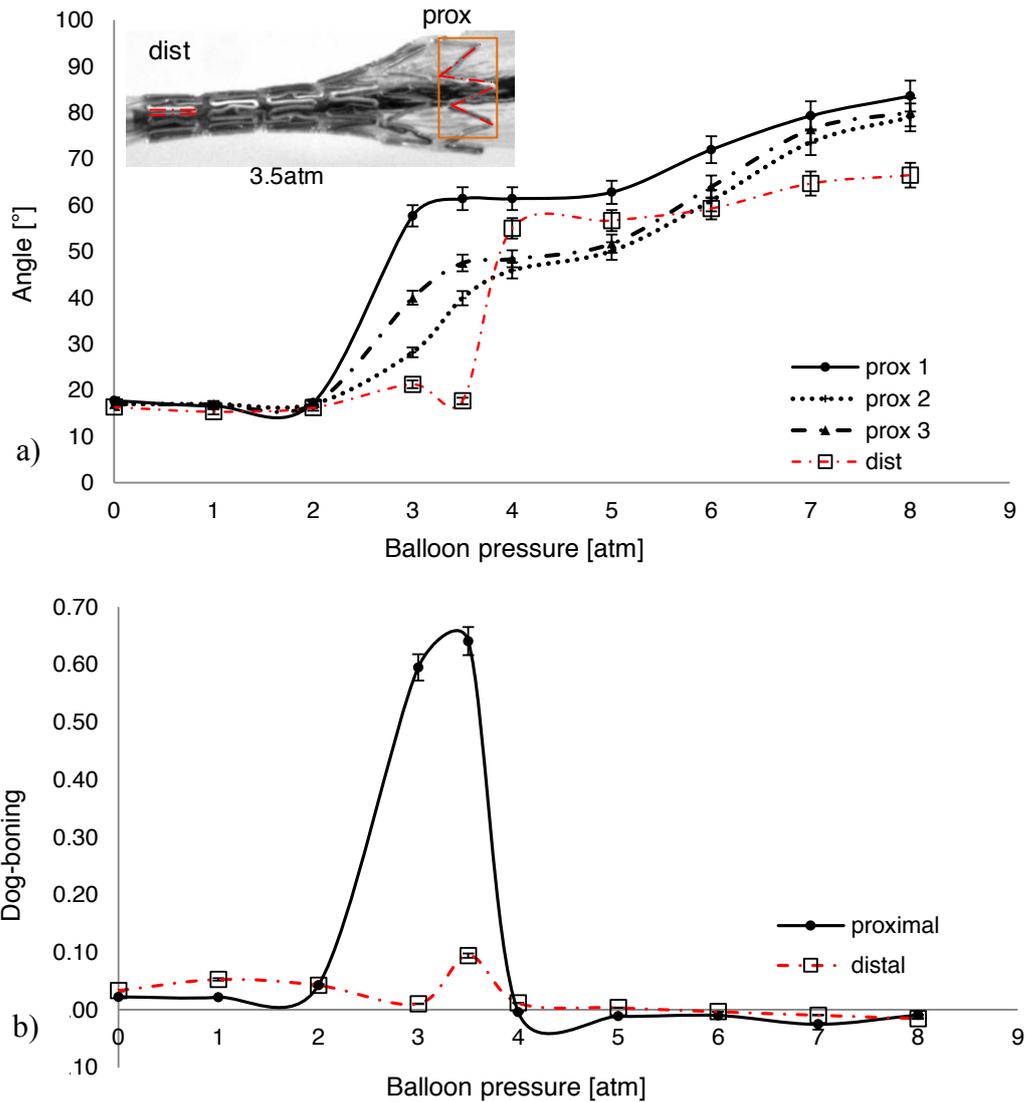
Figure 5-10: CB₃- 3.5 mm diameter Coroflex Blue stent. a) Dog-boning ratio for proximal and distal ends; b) variation in strut unit angle with balloon pressure for two units at the proximal end and one at the distal end.

5.1.3. DISCUSSION

3D reconstruction of stent geometry during balloon inflation allows characterisation

of the local deformation of stent units around the proximal and distal circumference.

In addition, measures used in previous studies [48, 131] employing 2D methods which

provide a more global assessment of changes in stent geometry were also computed

for comparison. Different outcomes of local and global measures of proximal and

distal stent deformation confirm that local strut deformation does not always correlate with changes in stent diameter.

Rotation of the stents was observed during balloon inflation, resulting in the stereo-visibility of a limited number of strut units throughout the expansion process. During increase of balloon inflation pressure to a value of 3 atm for 3 mm (TE_1) and 3.5 mm (CB_3) diameter stents (*Figure 5-8*a and *Figure 5-10*a) and 3.75 atm for the larger, 4 mm (TE_2) diameter stent (*Figure 5-9*a) significant dog-boning of the stent geometry was observed. Changes in the dog-boning ratio during stent expansion demonstrated greater deformation at both the proximal and distal ends within the range 3 to 6 atmospheres. For the TE_1 stent dog-boning occurred at both ends of the stent. However, for the TE_2 and CB_3 stent this effect was only observed at the proximal end. In all cases increase in pressure to 4.5 atmospheres was sufficient to cause full expansion of the stent. Further balloon inflation gradually increased stent diameter. The angular strut separation of the TE_1 stent in the distal region follows the global dog-boning effect whilst the two proximal units expand more gradually (*Figure 5-8*). This variation in the expansion of the proximal units may be due to their smaller initial angular separation. The TE_2 stent results indicate the angle of the unit in the proximal part increased significantly as the pressure increased to 3.75 atm whilst the distal unit remained unexpanded until the pressure increased to 4.5 atm (*Figure 5-9*). This local variation in strut expansion correlates with the global expansion, as shown by the differences in dog-boning effect between the distal and proximal ends of the stent. Expansion behaviour of the CB_3 stent was similar to that of the TE_2. However, the angle of the unit in the proximal part increased significantly at a pressure of 3 atm (*Figure 5-10*) with the distal unit remaining crimped until the pressure reached 4 atm.

For the CB$_3$ stent, the local variation in strut separation correlated with the global behaviour.

Similar behaviour was also observed for the 3D semi-deployed stent geometry obtained from Micro-CT data, examined in Chapter 4 and shown in *Figure 5-11*. The variation in deployment of each stent unit at an applied pressure load of 4 atm was observed in both the distal and proximal regions, as reconstructed using CTan (CT data analyser).
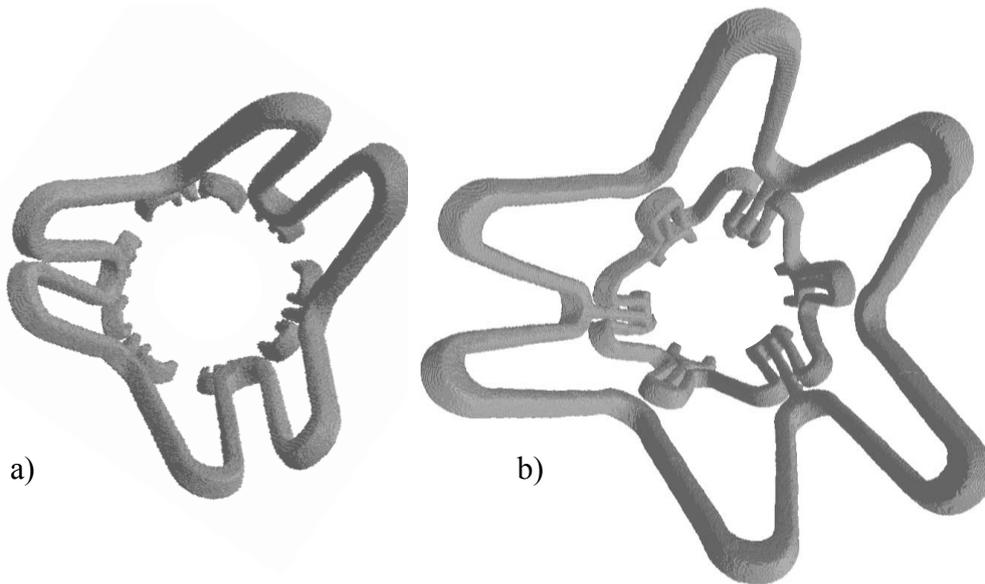
Figure 5-11: 3D model of a) distal and b) proximal part; view from top and bottom of the stent.

The dog-boning behaviour shown in *Figure 5-8b*, *Figure 5-9b* and *Figure 5-10b* was also observed in the study of Kiousis *et*. *al*. [131] and Pochrzast [132]. However a difference was reported in terms of the pressure loads which cause the dog-boning: these were 2.5 atm in [131, 132] and 3-3.75 atm in current study. For both stent designs used in the current study it is clear that the local deformation of individual stent units does not always directly correspond to changes in stent diameter. It was also evident that both stents (TE$_2$ and CB$_3$) deployed in similar way. It proved impossible to assess

all stent units due to the limited field of view and stent rotation relative to the camera during balloon inflation. *Figure 5-8b, Figure 5-9b* shows the expansion of two proximal and one distal units and *Figure 5-10b* shows the expansion of 3 proximal (it should be noted that two of these are measured from the time when applied pressure was 3 atm onwards) and one distal unit. To the author's knowledge no previous study has explored the detail of the local deformation of the stent in 3D. The focus in previous studies was mainly on the stent diameter and length change with applied pressure load.

5.2. DYNAMIC STENT EXPANSION AND DYNAMIC INFLATION OF BALLOON CATHETERS

To determine if dynamic stent deployment corresponds to the behaviour observed during pseudo-static stent expansion tests a single camera, Flea2, was used at 30 frames per second (fps) to capture the free expansion of a Coroflex Blue (B.Braun) stent. Expansion was performed by a clinician using an identical protocol to that employed during a clinical intervention. 30 fps was chosen as it is the maximum frame rate available for full-frame capture with the Flea2 camera. This experiment was designed to assess whether dog-boning occurs to the same extent during dynamic deployment.

In previous studies researchers [85, 131, 132] have used a single camera to image gradual expansion of the coronary stents and characterise changes in the external diameter of the stent. The analysis of the results showed that the increase in stent diameter was not proportional to the pressure load applied in the balloon. A sudden expansion of the stent occurred after applying a certain value of pressure (approximately 3-4 atmospheres). This was supported by the pseudo-static test results

reported in section 5.1.2. To the author's knowledge no studies have examined dynamic expansion of an unconstrained stent in the same timescales as it occurs in a real clinical scenario.

Following expansion of the stent, the balloon was detached from the plastically deformed, fully deployed stent, to examine qualitatively balloon inflation alone.

5.2.1. MATERIAL AND METHODS

The standard protocol for stent expansion was applied as described in previous sections of this chapter. The stent size was 4.0 mm (diameter) by 8 mm (length). The air was removed from the catheter using additional syringe (as presented in the *Figure 5-3*, page 132). The stent expansion process took 8.5 seconds (225 frames), the balloon was left fully inflated for approximately 13 seconds (403 frames) and was then deflated. A total of 628 frames were saved.

The deployment of the stent was characterised through the change in stent diameter and the elastic recoil (ER) of each ring (*Figure 5-13*) measured from 2D images using the VIEW software [135] for selected frames. The diameter of each ring (circumferential interconnection of units creates ring) of the stent was measured manually. The VIEW software was calibrated using known size of stent initial diameter. To assess the reproducibility of the manual measurement, the same area on the stent was measured 21 times.

ER of each ring was measured and calculated using an equation already introduced by Mori [4]:

$$ER = \frac{D_{inflated} - D_{deflated}}{D_{provided}} \qquad \text{5-3}$$

where $D_{inflated}$ is the maximum diameter measured at the final inflation stage, $D_{deflated}$ is the diameter measured after balloon deflation and $D_{provided}$ is the value of diameter of the fully inflated stent provided by the stent manufacturer.

Changes in balloon folding were recorded during the dynamic increase of balloon pressure. The balloon was fully inflated over approximately 6 seconds, yielding 180 frames. This experiment provides additional insight into the complex deformation mechanism of the balloon, which may be associated with the rotation observed during unconstrained stent expansion.

5.2.2. RESULTS

The VIEW software accuracy assessment for the manual measurement resulted in a standard deviation of 16 μm. *Figure 5-12* shows expansion behaviour at: a) initial stage, b) 0.7s c) 0.93s, d) 1.16s, e) 2.53s, f) 5.06 seconds and g) after balloon deflation. *Figure 5-13* shows each ring of the stent, identified by number and colour. The change in diameter of each ring is plotted in *Figure 5-14*. Elastic recoil which occurred after balloon deflation was noticeable by eye as shown in *Figure 5-15*. To express the elastic recoil visually two images were overlaid in Matlab *Figure 5-15c*. The blended overlay image was created using red for the image with fully deployed stent and green for the image with a recoiled stent. The yellow presents the areas of similar intensity between the two images. The change in diameter for each ring, between full balloon inflation and deflation, is plotted in *Figure 5-16* and the difference in stent diameter

between inflated and deflated balloon stages, along with the percentage of elastic recoil, are presented in *Table 20*.
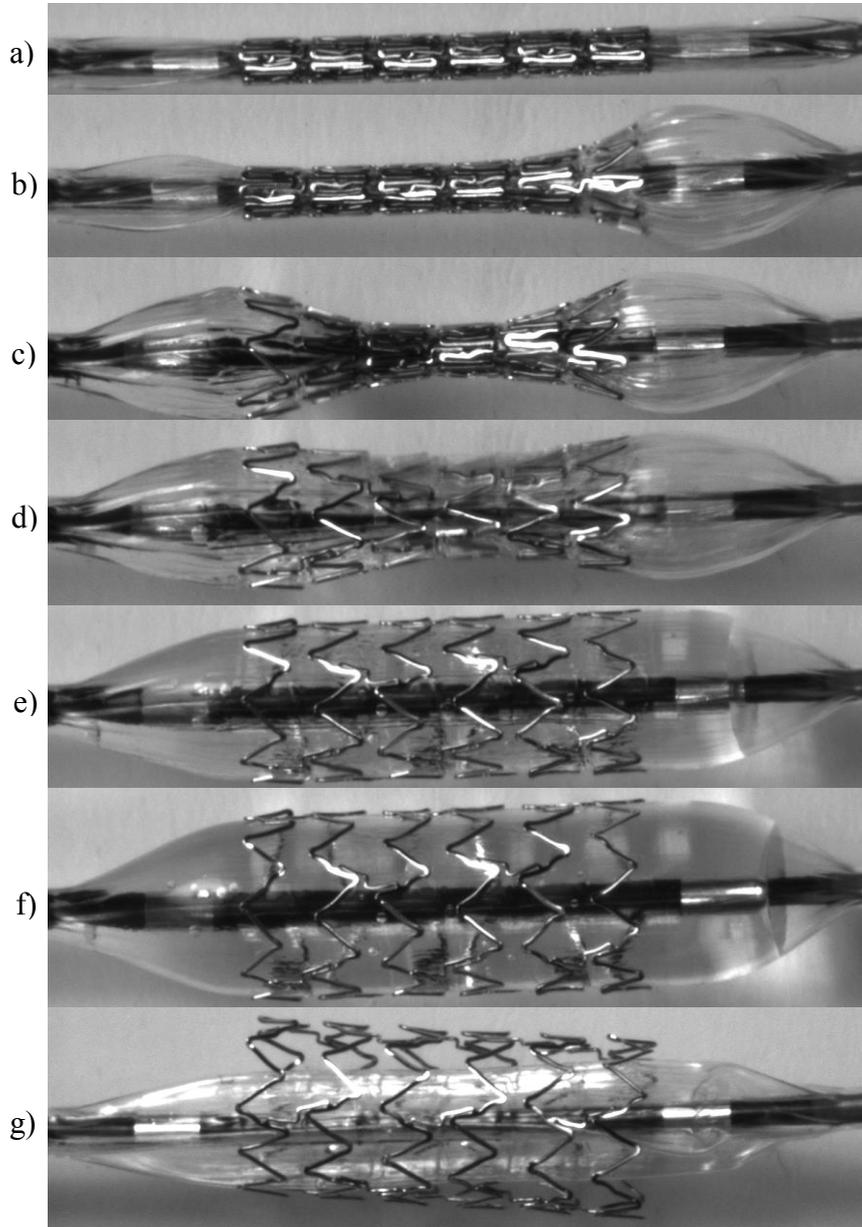
Figure 5-12: Example images from several stages during the stent expansion process.
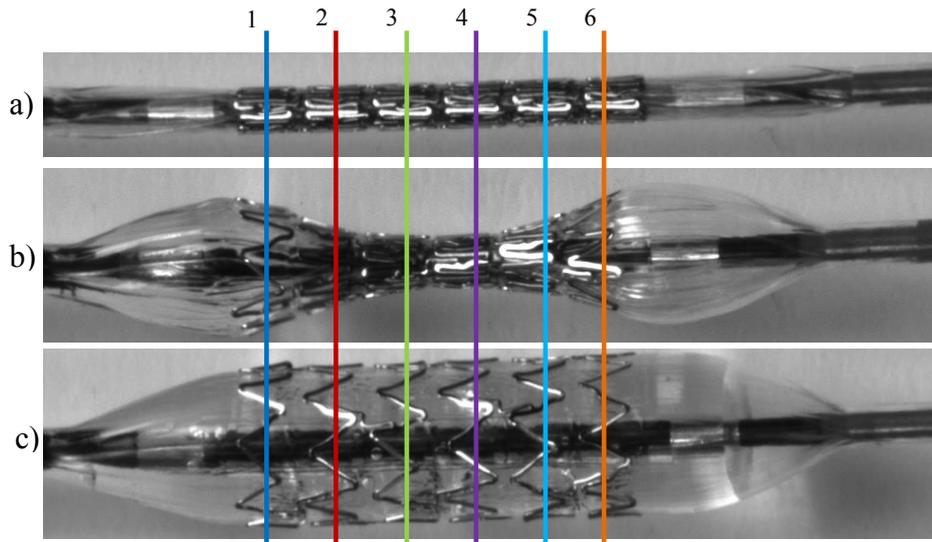
Figure 5-13: Three steps of expansion; each colour correspond to each ring of the stent: a) 0 sec, b) 0.93 sec, c) 2.53 sec.
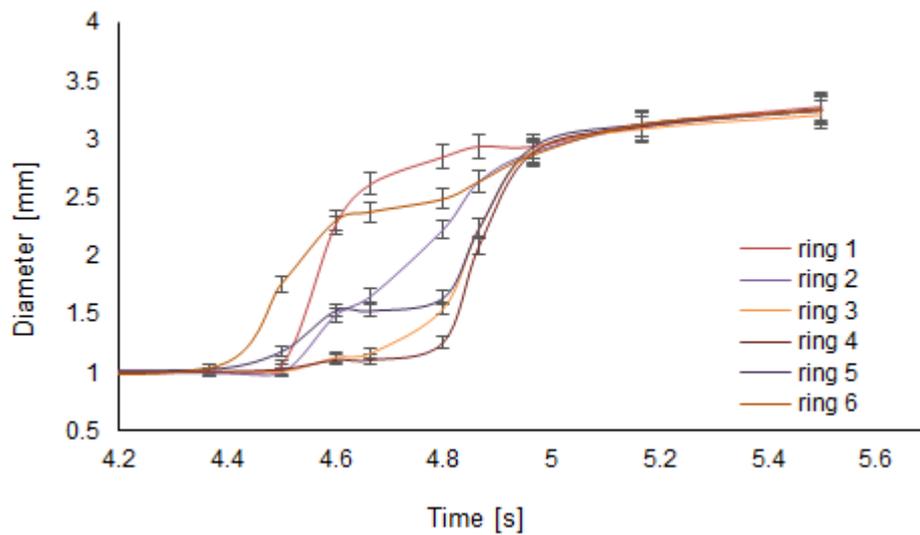
Figure 5-14: Change in diameter due to applied pressure of each ring depending on time; only 1.4 seconds are plotted. The same stent behaviour is observed as in Figure 5-8 for pseudo-static stent expansion.
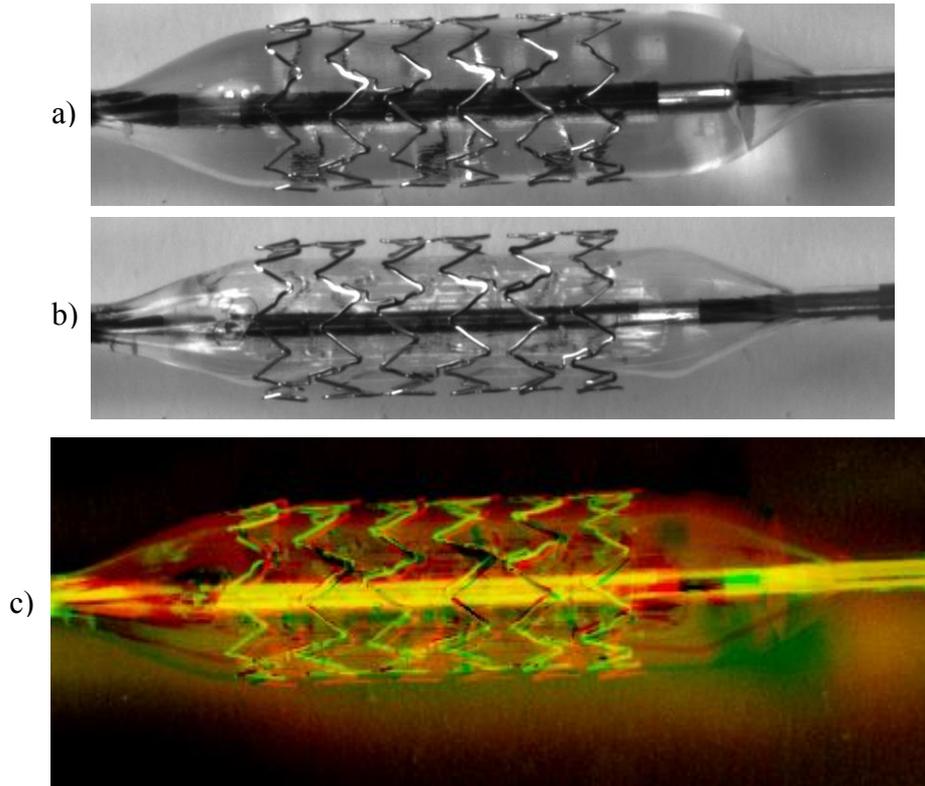
Figure 5-15: Stent presented in two stages a) fully inflated at 8atm and b) deflated balloon; c) overlay of the image with the stent with the fully inflated and the deflated balloon. The blended overlay image was created using red for the image with fully deployed stent and green for the image with a recoiled stent. The yellow presents the areas of similar intensity between the two images.
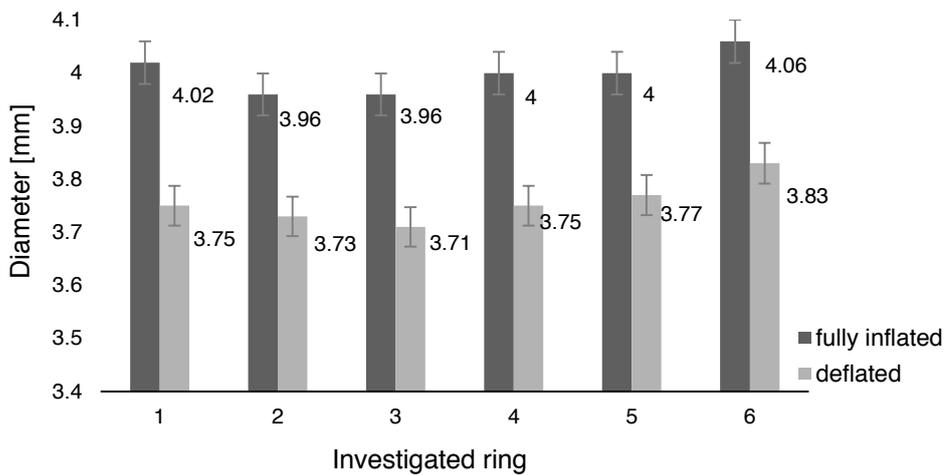
Figure 5-16: Recoil of each ring of the stent following balloon deflation.

Table 20: The results of elastic recoil.

Difference in diameter [mm] between stent with fully inflated and deflated balloon					
0.27	0.23	0.25	0.25	0.23	0.23
Elastic recoil [%]					
6.75	5.75	6.25	6.25	5.75	5.75

Figure 5-17 shows the angioplasty balloon in three configurations: a) deflated, b) semi-inflated and c) fully inflated.

a)

b)

c)
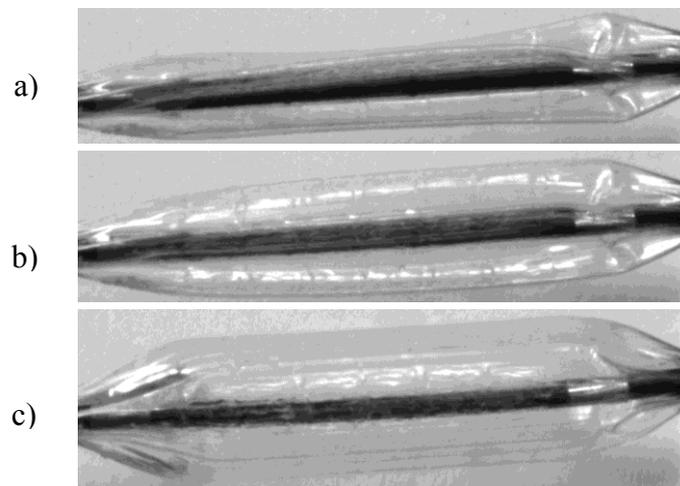
Figure 5-17: Quad folding pattern of the angioplasty balloon; Inflation captured in a) initial stage, b) after 3 seconds, c) after 8 seconds.

5.2.3. DISCUSSION

Due to bandwidth limitations and technical issues with dynamic synchronisation of the stereo camera pair, it was not possible to undertake high resolution imaging of stent expansion at 30fps with the current stereo rig. Examination of 3D fully dynamic stent deployment is not currently possible, but dynamic imaging with a single camera provides quantitative data for the change in diameter of each ring of stent struts during deployment. Single camera dynamic testing can be directly compared with previous experimental pseudo-static stent expansion studies for 2D stent geometry

characterisation [85, 131, 132] to assess potential variation in stent deployment characteristics over timescales typical for *in vivo* deployment.

In the fully dynamic results it was observed that the first and sixth rings expanded significantly faster than other rings. This is clearly visible in *Figure 5-12* above. Significant stent recoil occurs due to balloon deflation. Despite the fact that each ring has the same structure, in current test elastic recoil ranged from 5.75% to 6.75% (0.23 and 0.27 mm) in proximal and distal parts respectively. These results are comparable to results of Mori [4], where the elastic recoil ranged from 4.7 % to 6.7 % in proximal and distal end. This stent behaviour could result in a significant strain reduction due a reduction of stretch in the vessel wall.

In summary, the same dog-boning behaviour was found during free expansion of a stent under dynamic and pseudo-static conditions. De Beule [10] demonstrated (in a numerical study) that unfolding of the balloon during inflation process causes this phenomenon. In the current study, analysis of the 180 frames obtained during balloon inflation only confirms the process of unfolding of the balloon. It is not surprising that the stent rotates during free expansion, as the balloon unfolding process demonstrates similar behaviour without a mounted stent. Moreover, it is not surprising that the stent may deploy non-uniformly.

The variation in local strut unit expansion in both proximal and distal parts of the stent, despite in the similarity of structure, occurred during both pseudo-static and dynamic tests.

SUMMARY

It is suggested that the non-uniform expansion of the stent globally and locally may result in local variation in strain within the vessel wall. The results of the experiments reported in this chapter may provide information on the damage induced by the stent struts if stent deformation is linked to deformation of the arterial wall or an appropriate vessel analogue. Clinical studies [2, 70] have reported strong associations between the asymmetry of stent deployment and the resulting degree of restenosis. This study has demonstrated that local stent strut deformation does not always correlate with change in stent diameter. This behaviour of the stent during the deployment may have implications for local strains generated during contact of the stent with the vessel wall and the resulting vascular injury. There are limitations in the interpretation of the results of free stent expansion experiments in the context of stent/artery interactions which will be addressed in following chapter since the results presented here did not consider the interaction of the stent with the vessel wall.

CHAPTER 6

STENT DEPLOYMENT IN THE CORONARY ANALOGUE TO DETERMINE LOCAL STRAINS

The goal of this chapter is the characterisation of interactions between a stent and a vessel analogue following stent expansion. This *in vitro* study was designed to determine the distribution of strain on the wall of a silicone vessel analogue which is used to mimic a coronary artery. The optical stereo-photogrammetry method described in previous chapters has been used, along with image registration methods employing ShIRT (Sheffield Image Registration Toolkit) and VIC-2D (Correlated Solutions) to examine local surface deformation.

Assessment of various marking methods has been undertaken to determine the most effective high contrast pattern to track surface deformations. To quantify uncertainty in strain measured by ShIRT and VIC-2D, a rigid body motion (RBM), zero strain test was carried out. Following this, the experimental conditions were adapted to gradually move towards a more realistic condition considering first a tensile test and then vessel analogue deformation due to stent deployment. The aim was to compare the variations in strain that occur when moving from the simpler test to the more complex case. It is important to examine the strain distribution due to interaction of the stent with the vessel wall in the context of the results from free stent expansion presented in Chapter

5, to determine whether localised strains are due to strut interaction with the vessel wall. Analysis of these results can be used to suggest the likely distribution of vessel wall injury following stent deployment.

6.   INTRODUCTION

In Chapters 2, 3, 4 and 5 markers/landmarks on the specimen surface were selected manually for 3D reconstruction. A point of interest was chosen on the left image and (as long as the calibration of the cameras was robust) the epipolar line indicated the same point on the corresponding right image.   Subsequently, reconstruction (triangulation) of a common point was performed to obtain 3D (x, y, z) coordinates. This manual process was repeated at each deformation stage for the same points of interest.

The manual procedure has been shown to provide accurate results for stent geometry characterisation (Chapter 4) and stent expansion (Chapter 5) examination, as well as for strain measurement in large scale specimens marked with a regular pattern (Chapter 2). In order to assess local strain distributions over smaller areas, a speckle/random pattern provides a method to obtain detailed, localised output data. Automatic methods are more effective with irregular markers as it is challenging and time consuming to distinguish corresponding markers on pairs of images visually.

To examine local strains on the surface of an object undergoing large deformations, image registration methods have been explored. Image registration methods employ registration and correlation techniques for accurate 2D or 3D measurements of object deformation through the use of 2D or 3D image data. These methods can be used to determine deformation, displacement as well as strain and are frequently employed in many areas of engineering and science [136-138]. In this study the Sheffield Image Registration Toolkit (ShIRT) and the commercial digital image correlation software

VIC-2D (Correlated Solutions) have been used to determine the deformation of a surface in 3D over a number of deformation steps.

In the current chapter, the background to the registration methods is outlined in Section 6.1. It should be noted that the aim of this study was not to develop or investigate novel image registration algorithms, but rather to apply developed algorithms to examine stent/vessel analogue interaction during stent deployment. Hence a detailed discussion of the algorithms used by ShIRT and VIC-2D is not included. Section 6.2 focuses on the marking methods applied to the vessel analogues and to real tissue. Section 6.3 determines mechanical properties of the silicone used to mimic coronary arteries. Sections 6.4 – 6.5 describe experimental tests undertaken to assess the variation of strain under increasingly complex conditions. Section 6.5.2 compares these results and places them in the context of the results observed during free stent expansion, reported in Chapter 5.

6.1.   IMAGE REGISTRATION PRINCIPLE

Image registration/correlation techniques have been used widely in medical imaging, computer vision and remote sensing [139] and have become increasingly popular for strain measurement in deformed objects [140, 141]. The concept of image registration is to find the optimum mapping of displacement between two images. Image registration can be used to find the mapping between images of the same scene, captured at different times (e.g. for 2D characterisation), or from different viewpoints (using more than one camera for 3D characterisation) [138]. Methods developed for experimental mechanics to examine hard/rigid material and structures [142, 143] have been expanded to examine strain in soft biological materials [82, 144]. These optical

methods involve tracking an applied random speckle pattern on the surface of a test specimen during an experiment.

In this study the Sheffield Image Registration Toolkit (ShIRT) [145], developed at the University of Sheffield, and VIC-2D (digital image correlation, Correlated Solutions) were explored for stent application.

6.1.1. SHEFFIELD IMAGE REGISTRATION TOOLKIT

Sheffield image registration toolkit (ShIRT) was developed by Barber and Hose, with the intention of medical images registration. Detail of the algorithms used in ShIRT has been previously published [145]. The following section provides an overview of the key concepts underlying this image registration technique. The fundamental process is to relate corresponding points in two images. In registration the initial image is referred to as the fixed image and the second image is referred to as the moved image. The output of the algorithm is the displacement required to move every point in the moved image to a corresponding point in the fixed image.

If the coordinates of a point in one image are (x, y) and the coordinates of the same point in the second image are (x', y'), a mapping function can be defined to retrieve the coordinates of the second point from the coordinates of the first point. The relation between the coordinates in each image can be written as:

$$x' = u(x, y) + \ x$$

$$y' = v(x, y) + \ y$$

The aim of the image registration algorithm is to compute the mapping functions (u, v) for every point of the image (x, y). In ShIRT the mapping function is defined at discrete points (nodes) in *x* and *y*.

A visual representation of the registration process is shown in *Figure 6-1*. To assess the registration output the fixed image intensities are displayed as green and the moved image intensities are overlaid in red. A successful registration results in an image coloured yellow, as shown in *Figure 6-1c*. If the registration is unsuccessful the output image may show red or green features as shown in *Figure 6-2*.

In *Figure 6-1* Image 1 presents a regular grid on a chosen area of interest with coordinates (x, y). Image 2 presents the same grid, with the coordinates (x', y') determined from the coordinates in Image 1 and the registration mapping function. Detailed inspection of the location of grid points and the corresponding speckle patterns can also be used to assess the success of the registration between images as shown in *Figure 6-3*.
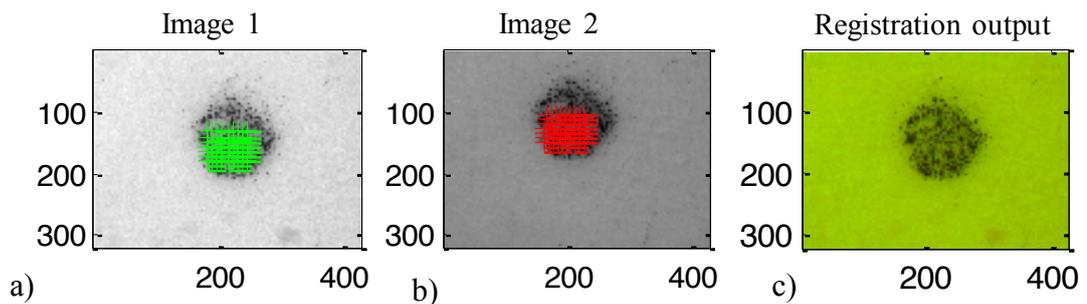
Figure 6-1: The example of two registered images. On the registration output we can notice effective computed mapping.
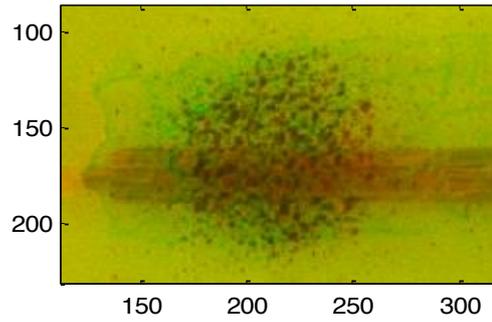
Figure 6-2: An example of failed registration; stent deployed in the transparent elastic material.
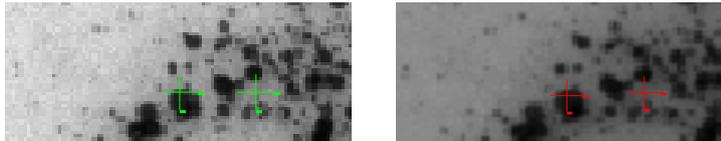
Figure 6-3: Zoomed image to show good correspondence of the landmarks in image1 (green crosses) and image2 (red crosses) image.

Image registration can fail if the displacement between the two images is too large as presented in *Figure 6-4*. This figure shows a checkerboard grid with the grid in the right image rotated through an angle of 60º from the grid in the left image.
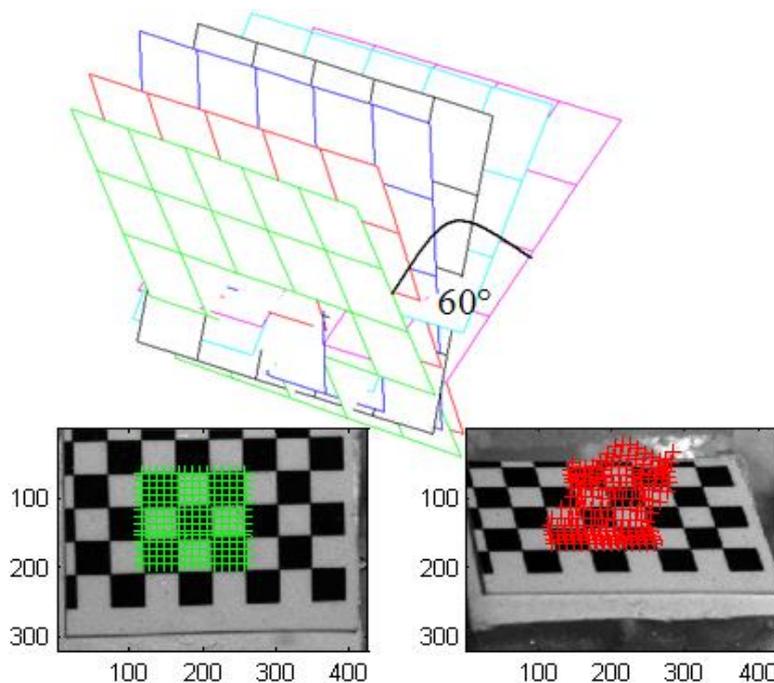
Figure 6-4: Unsuccessful registration due to large rotation angle (approximately 60°) during rigid body motion test.

6.1.2. VIC-2D

VIC-2D (Correlated Solutions) is commercial Digital Image Correlation (DIC) software which uses optimised correlation algorithms to provide full-field displacement data for mechanical testing. This software requires the application of a random speckle pattern on the tested object surface. An example of the technique is shown in *Figure 6-5*. To track the deformation relative to a reference image a region of interest (ROI) is defined in the reference image (shown by the red area).
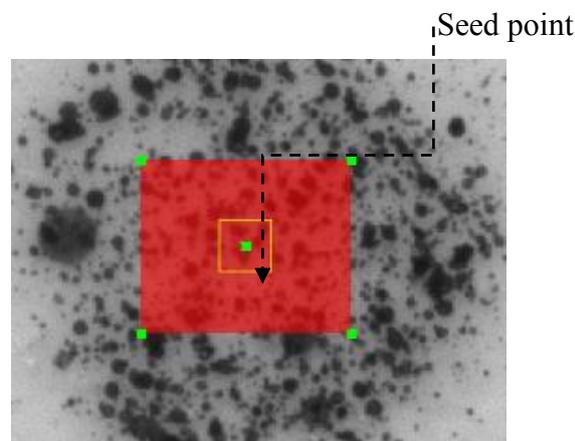
Figure 6-5: Region of interest selected on the left image.

The DIC algorithm divides this ROI into a virtual grid. The target of the software is the same as for ShIRT: to match each point in the grid of the reference image to a corresponding point in the deformed image. Parameters associated with the algorithm include the subset size and step size, which are selected after the ROI is defined. The subset size controls the area of the image that is used to track the displacement between images. It has to be large enough to ensure that there is a sufficiently distinctive pattern contained in the area used for correlation [146]. The step size controls how many pixels are analysed during correlation, e.g. a step size of 5, means that correlation will be carried out at every fifth pixel in both the horizontal and vertical direction. Another important parameter is the seed point, which is defined in the reference image to

determine the starting point for the correlation. It is recommended that this point should be placed in the area of the image that undergoes the smallest amount of motion/deformation during the experiment (VIC-2D [147]). To effectively track grey scale intensities between two images using DIC algorithms, the pattern on the object needs to be random, for example as a speckle pattern created with sprayed paint. A regular, repeating form is not well suited to use with DIC and can introduce large errors [148]. This is a significant difference between VIC-2D and ShIRT.

6.2. MARKING METHODS FOR DEFORMATION TRACKING IN ELASTIC MATERIALS

Noncontact deformation measurement of a surface of uniform colour requires the application of markers/speckle pattern to allow quantification of strain [81, 82, 90, 136, 149]. To accurately assess strain, the applied pattern must deform along with the object and should not alter the response of the material.

Previous investigators have used a range of marking approaches. Squire *et al*. [81] reports marking of bovine and rabbit femoral arteries using ink from a printer cartridge to quantify the strain from the displacement of 40 reference points. Sutton *et al*. coated the surface of a mouse carotid artery with white Enamel spray before applying a pattern using toner powder [82]. Enamel spray (white and black) was also used by Horny *et al*. [90] to mark a human coronary artery. Meunier *et al*. [149] marked silicone rubber with a pattern made of small speckles (the exact method was not defined) to measure local strain fields during bulge and tensile tests.

It is important to use a marker size suitable for the scale at which the specimen is imaged [146]. In this study several random and regular marking patterns were investigated depending on the scale. Use of a permanent Pentel pen for manual marking provided an appropriate reference pattern when undertaking experimental work at low spatial resolutions (see section 2.3) due to the lower magnification and reduced emphasis on small features. Preliminary testing was undertaken to examine the characterisation of cardiac motion with scattered markers shown in *Figure 6-6a*. Improvement in the marking methods was necessary for higher magnifications. The manually applied Pentel pen marker appeared blurred and the square geometry of the scattered markers becomes significant, as shown in *Figure 6-6b*. For assessment of strain in vessel analogues, marker quality was improved using quick drying enamel paint, as shown in *Figure 6-7a*. For application to porcine coronary arteries, graphite powder was applied using a strainer, as shown in *Figure 6-7b*. This method shows promise but it requires improvement to reduce the marker size.

Speckle pattern

a)   b)
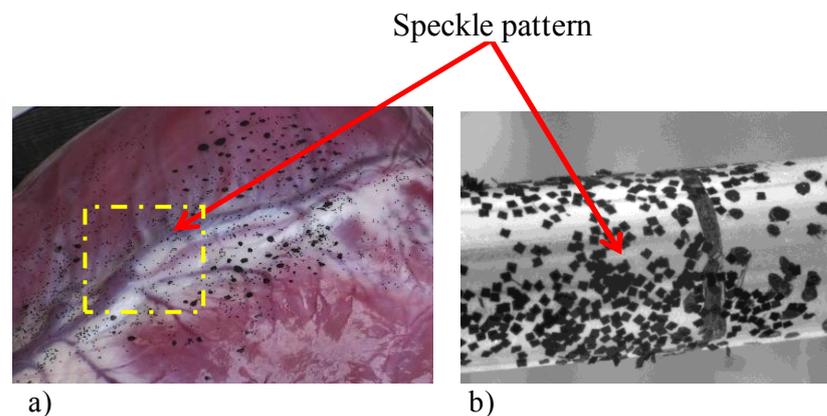
Figure 6-6: Examples of the same markers imaged at different magnification, M. a) M=0.09 surface of a porcine heart (field of view- FOV approximately 200 mm) (Hemolab, Eindhoven), b) M = 0.4 image of a vessel analogue (FOV=10 mm).
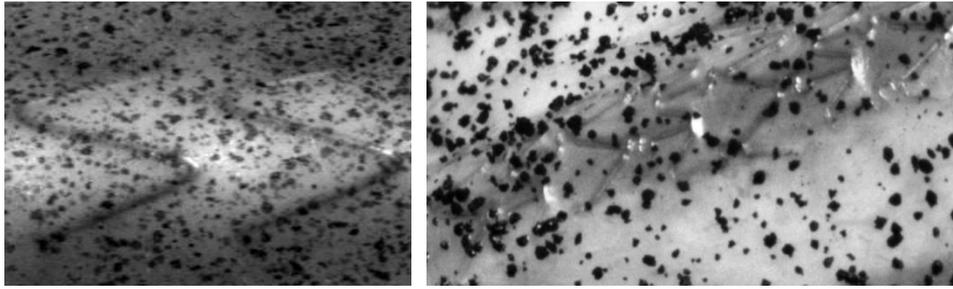
Figure 6-7: a) Stent expanded in the vessel analogue marked using enamel spray; b) Stent expanded in the pig coronary artery ex vivo marked with graphite powder.

The tests reported in this chapter involve the use of a transparent elastic material as a vessel analogue. To improve the contrast between the black markers and the super clear, transparent analogue, and to avoid changes in intensity due to motion of the stent struts within the image, a thin layer of flexible white paint (Stretchi paint, Creative Resources Distribution, Propbuilder) was applied to the surface of the silicone material. To the author's knowledge this is a novel method which has not been considered in previous studies. The advantage of using Stretchi paint is the lack of cracking which occurs at high strain using other paint types. An example of the silicone vessel analogue coated with Stretchi paint and marked with an irregular pattern is shown in *Figure 6-8*.
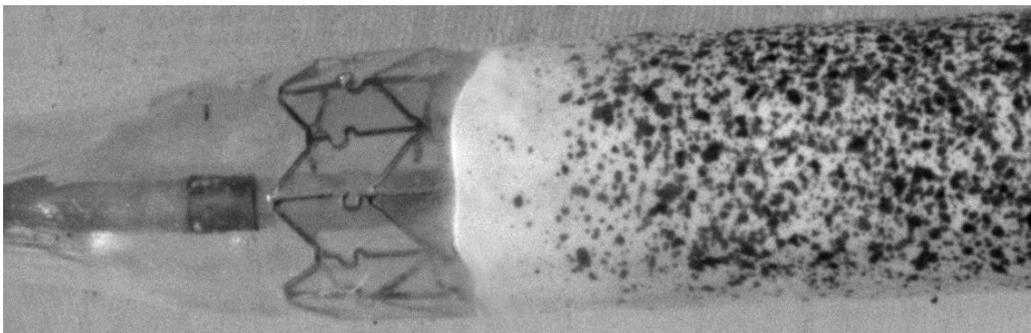
Figure 6-8: Stent deployed in the vessel analogue. A region of the silicone is covered with Stretchi paint with an applied speckle pattern and the other region is left clear, in its original state.

In the example shown in *Figure 6-8* one half of the vessel analogue was covered in paint, the other half remained transparent. The elastic paint dries quickly and adheres well to the surface and is specially formulated to allow bonding to the silicone and deformation without cracking or peeling.

The next section outlines the mechanical properties of the silicone material used to mimic coronary arteries.

6.3.   MATERIAL TO MIMIC VESSEL ANALOGUE TESTING

For medical and engineering research on artificial *in vitro* arteries, it is important to use materials as close as possible to the mechanical properties of the arterial wall. A review of the literature on previous studies using mock arteries is presented in section 1.6.5. The model needs to be sufficiently compliant to expand significantly under typical balloon inflation pressures (~10 atm).

6.3.1. METHODS

To obtain realistic reference geometry for the vessel analogue, a section of porcine heart was dissected perpendicular to the coronary artery axis and the vessel, roughly separated from the rest of the organ, was captured using a single camera positioned perpendicular to the arterial cross-section. Comparative images were obtained for a sheet of silicone material (SILEX limited, Hampshire, UK) with similar thickness to the wall of the porcine arteries. The thickness (t) of both the vessel and the latex sheet was measured using VIEW software [135] using a caliper scale as a calibration reference. The thickness was measured in seven different regions.

The most crucial parameter was the Young's modulus (E). To obtain this information a uniaxial tensile test was performed at the Politechnico di Milano, Milan, Italy. Three samples with length and width presented in *Table 21* were prepared for testing.

Table 21: Dimensions of the sample, where W=width, L₀=initial length and t=thickness.

	W [mm]	L0 [mm]	t [mm]
sample 1	6.50	19.83	
sample 2	6.80	20.53	0.25
sample 3	6.62	19.64	

A dynamometer MTS® Synergie 200H testing machine with load cell F_max of 1kN full scale was used for the tensile test. The control channel during the test was displacement with the maximum Linear Variable Differential Transformers (LVDT) of 1000 mm. Before the principal tensile test, a small tensile pre-load of 0.3N was applied to each silicone sample (to ensure that sample was firmly fixed within the machine clamps). The test velocity was 1 mm/s. Force was applied to each specimen until failure occurred. The maximum stress, strain and Young Modulus were computed.

To create the coronary artery analogue for the stent expansion tests described in Section 6.5.3, the superclear silicone sheet was cut to obtain a sample of 40 mm x 20 mm and covered with Stretchi white paint (Propbuilder, UK) to obtain a good contrast with the fast dry black enamel spray (Plasti-kote, USA) used to create a speckle pattern. To produce an artery analogue with internal diameter of 3 mm, the required circumference (approximately 9.5 mm) of the artificial vessel was

measured with caliper and the silicone sheet was fixed between two blocks to create the artificial coronary artery, *Figure 6-9* and *Figure 6-32*, section 6.5.2.

Figure 6-9: The silicone sheet fixed between two blocks to mimic coronary artery.

An inner diameter of 3 mm, wall thickness of 0.25 mm and length of 40 mm was adopted to mimic a straight section of coronary artery.

6.3.2. RESULTS

The *Figure 6-10a* presents a section of porcine heart dissected perpendicular to the vessel axis with the vessel roughly separated from the rest of the organ and *Figure 6-10b* shows the silicone material (SILEX limited, Hampshire, UK) used to mimic the coronary artery.   The average measured thickness of the silicone was 0.25 mm (standard deviation of 8 μm), while the coronary artery thickness was 0.26 mm (standard deviation of 20 μm). The larger variation in thickness reported for porcine artery is not surprising as it has been reported that the arterial wall adjacent to the myocardium is thicker than the other part of the wall [150].

a)   b)
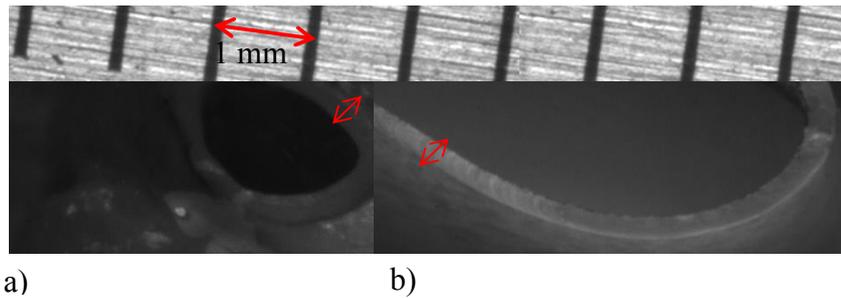
Figure 6-10: Section of the heart tissue with coronary artery in situ;
b- vessel analogue.

The tensile test results for three samples (S1, S2, S3) are presented in *Figure 6-11*
which shows the three stress/strain curves.
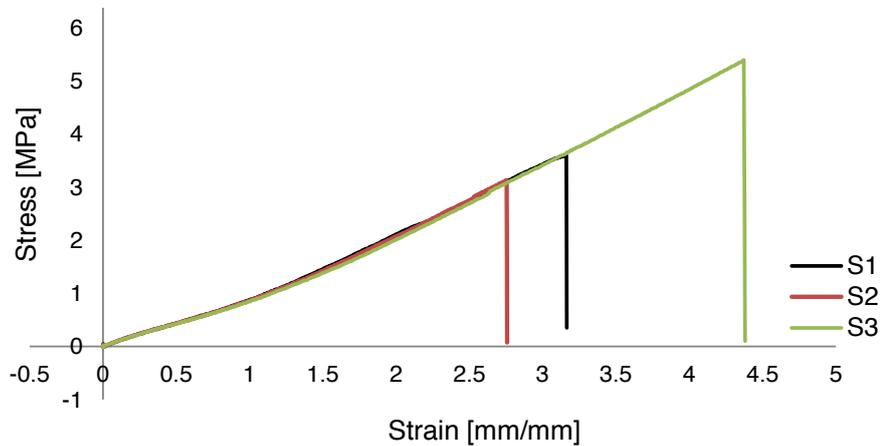
Figure 6-11: Stress/strain plot from three separate tests; result of the tensile test of the
super clear silicone specimen.

The Young Modulus ($E = \sigma/\varepsilon$) was found to be 0.98MPa for S1, 1.03MPa for S2 and
1.1MPa for S3 using the linear part of the stress/strain curve between strain
= 0 and 1.

6.3.3. DISCUSSION

Latex and silicone mock arteries used in experimental studies of stent expansion allow
controlled testing of stent behaviour and evaluation of the mechanical effects related
to stent design [89]. In the current study a silicone sample was shown to have

mechanical properties closely matching the real coronary arteries as the values of Young's Modulus obtained during tensile testing are within the range reported by Karimi *et.al* [151] for healthy human coronaries. The artificially created silicone material is homogenous whereas the natural arteries are highly inhomogeneous (composed of different layers as mentioned in Chapter 1) and anisotropic (have a different behaviour in each direction). Additional variation in material properties of the artery can occur in the presence of the disease (i.e. stiffening due to plaque formation), the presence of atherosclerosis may increase significantly the stiffness of the arteries [151].

Future work could extend the use of artificial vessels to experimentally model disease as discussed in Chapter 7 to increase the complexity of the process.

The next section describes the combination of stereo-photogrammetry and image registration to determine surface deformation in 3D.

6.4. STEREO-PHOTOGRAMMETRY AND IMAGE REGISTRATION TO DETERMINE SURFACE DEFORMATION IN 3D

3D reconstruction using triangulation has been described in previous chapters. As discussed in the introduction to this chapter, to obtain strain over the whole surface of the deformed object the 2D coordinates from left and right image used for 3D reconstruction are derived using image registration (ShIRT and VIC-2D), instead of manual point selection. This section describes the process used to obtain this data.

6.4.1. GENERAL APPROACH

The stereo rig was setup as described previously. The camera angle between 30 and 90 degree was chosen to avoid reflection of the sample and enable the same region of interest to be captured with both cameras. The process undertaken to obtain 3D information of specimen deformation was as follows:

- Calibration (as before) to determine camera parameters.
- Manual reconstruction of a few markers to assess calibration and reconstruction accuracy.

Definition of geometry in 3D requires identification of correspondence points as shown in *Figure 6-12*. The following steps were taken to obtain correspondence points using image registration:

1. Instead of manual identification a grid of points was defined on the left image (pxl). The correspondence points on the right image (pxr) were obtained using the registration mapping between left and right images (from ShIRT/VIC-2D). If the points in the left and right images corresponded well (by visual inspection), step 2 could be undertaken.

2. Changes in position of the left correspondence points (pxl) were tracked using the registration mapping between position $3D_0$ and each new position ($3D_1$, $3D_2$ etc.) (ShIRT/ VIC-2D).
   Output: 2D data for each translation/deformation stage (pxl).

3. Changes in position of the right correspondence points were ttacked in the same way (ShIRT/ VIC-2D)

Output: 2D data for each translation/deformation stage (pxr).

4. The updated 2D point position (pxl and pxr) from each step of translation/deformation was used to recover 3D surface geometry via triangulation (reconstruction).

5. Displacements/strains were computed in 3D from the change in 3D surface.

Figure 6-12 graphically illustrates this process for points 1, 2, 3 and 4.
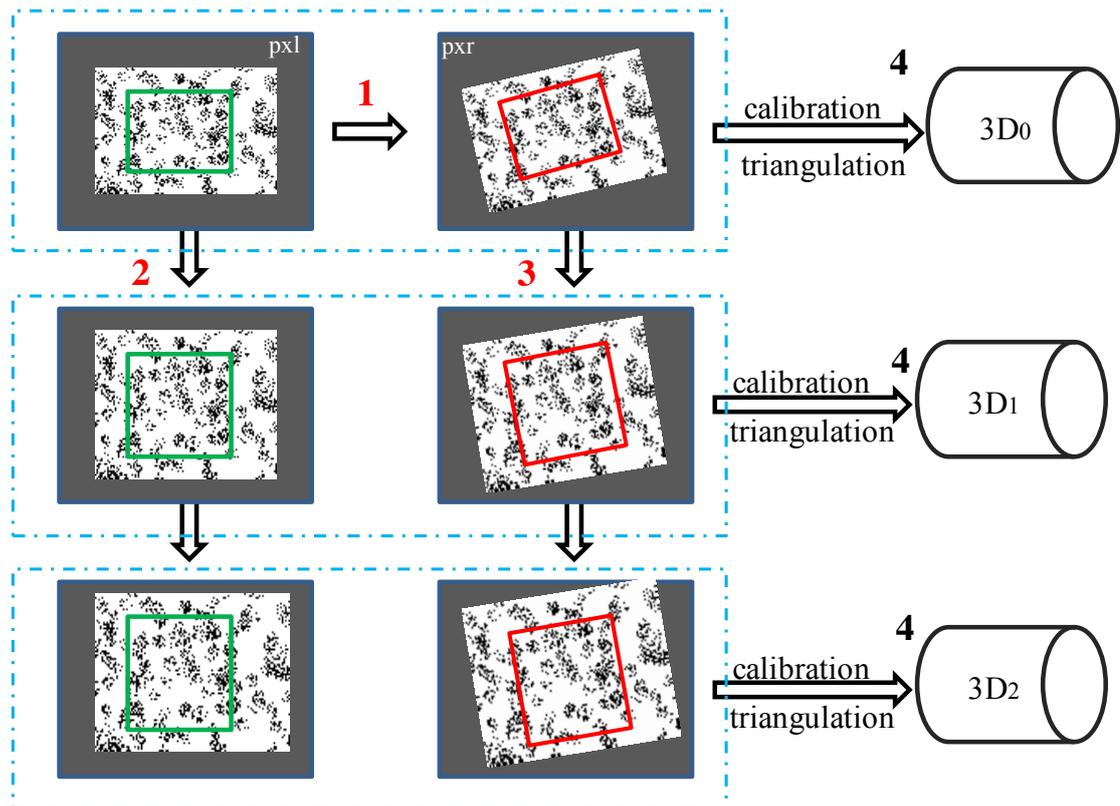
Figure 6-12: Diagram presenting registration of two initial, right and left images; registration of all left images to initial left and the same for right images; 3D reconstruction from pairs of 2D data (pxl, pxr).

6.4.2. POST-PROCESSING SURFACE DEFORMATION TO RECOVER STRAIN

Quantification of surface deformation is based on tracking of markers affixed to the surface, with surface strain used as an outcome measure. A large number of markers are required to allow computation of strain at a local level. Strain can be characterised from the relative displacements of reference points on the object surface. The displacement of the marked pattern on the object surface is computed using either ShIRT or VIC-2D registration, as described in 6.4.1. The 3D coordinates (x, y, z) of the surface at each stage of deformation are provided using stereo triangulation and camera calibration data.

For the rigid body motion tests described in 6.5.1 the 3D coordinates obtained from triangulation were used to compute the strain between pairs of surface points, as shown in *Figure 6-13*.
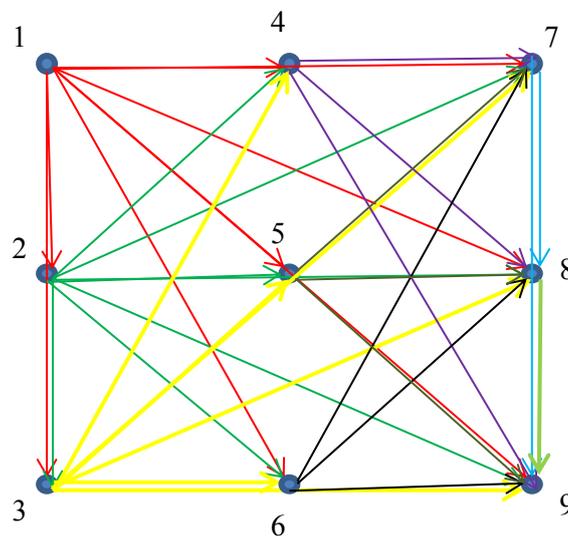
Figure 6-13: Graphical presentation of strain calculation for a local region of 9 surface points.

To assess how the reported strain varies with change in resolution, all combinations of point pairs were used to assess measures of strain. For N points this results in $\sum_{n=1}^{N} n - 1$ measures of strain. For these small strains, engineering strain is computed using the change in distance between points on the undeformed, L_0, and the deformed surface, L.

$$\Delta L = L - L_0 \qquad \varepsilon = \frac{\Delta L}{L} = \frac{L - L_0}{L_0} \qquad\qquad \text{6-1}$$

For large deformations using manual measurements between individual reference points, as described in section 6.1.1 for the elastic tensile test, the Green-Lagrange strain is calculated from the change in length between reference points, as follows:

$$E = \frac{L^2 - L_0^2}{2L_0^2} \qquad\qquad \text{6-2}$$

To provide the strain distribution over the deformed surface under non-zero strain conditions, the Green-Lagrange strain tensor was computed, following the approach described by Genovese *et al*. [136]. To compute the Green-Lagrange tensor the surface is defined using triangles between reconstructed 3D points. An example of single undeformed and deformed triangle is shown in *Figure 6-14*.
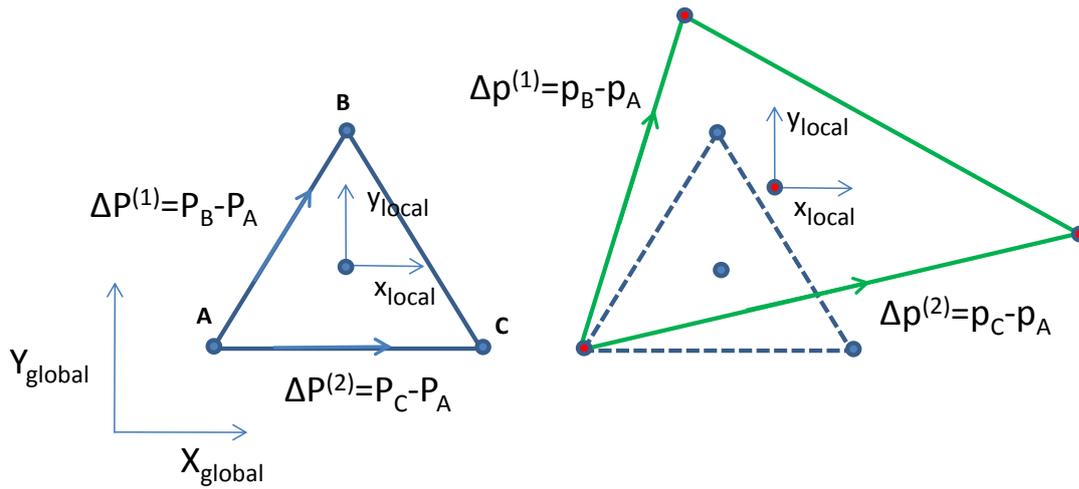
Figure 6-14: An example of single undeformed and deformed triangle.

The Green strain:

$$E = \frac{1}{2}\left(F^T F - I\right) \qquad\qquad 6\text{-}3$$

is calculated locally for each triangular element after computing the deformation gradient tensor F. The triplets of points (e.g. A, B, C) are used to obtain the components of the tensor by computing change from vectors in undeformed configuration: $\Delta P^{(1)} = P_B - P_A$ and $\Delta P^{(2)} = P_C - P_A$ to the deformed configuration: $\Delta p^{(1)} = p_B - p_A$ and $\Delta p^{(2)} = p_C - p_A$. The assumption is that surface deformation in the small triangle region of interest is homogenous $\Delta p = F\,\Delta P$. The strain was measured in longitudinal (Ex) and transversal (Ey) directions relative to the camera. The deformation gradient F is determined from the following equations:

$$\begin{bmatrix} \Delta p_x^{(1)} \\ \Delta p_y^{(1)} \end{bmatrix} = \begin{bmatrix} F_x & F_{xy} \\ F_{yx} & F_y \end{bmatrix} \begin{bmatrix} \Delta P_x^{(1)} \\ \Delta P_y^{(1)} \end{bmatrix}$$

$$\begin{bmatrix} \Delta p_x^{(2)} \\ \Delta p_y^{(2)} \end{bmatrix} = \begin{bmatrix} F_x & F_{xy} \\ F_{yx} & F_y \end{bmatrix} \begin{bmatrix} \Delta P_x^{(2)} \\ \Delta P_y^{(2)} \end{bmatrix} \qquad \text{6-4}$$

F_x, F_y, $F_{xy\ (yx)}$ are the deformation gradients denoted as deformation in x direction, y direction and shear, respectively.

6.5. EXPERIMENTAL PROTOCOL TO ASSESS EFFECTIVENESS

The remainder of this chapter describes experimental tests undertaken to assess the effectiveness of image registration methods in providing measures of surface deformation and to examine the variation of strain under increasingly complex experimental conditions. Experimental tests were undertaken under three sets of conditions demonstrated schematically in *Figure 6-15* . The first condition (*Figure 6-15a* and *b*) involves rigid body motions including rotation and translation; the second condition involves a planar tensile test (c); the third condition (d) involves deployment of a stent within the vessel analogue by balloon inflation.
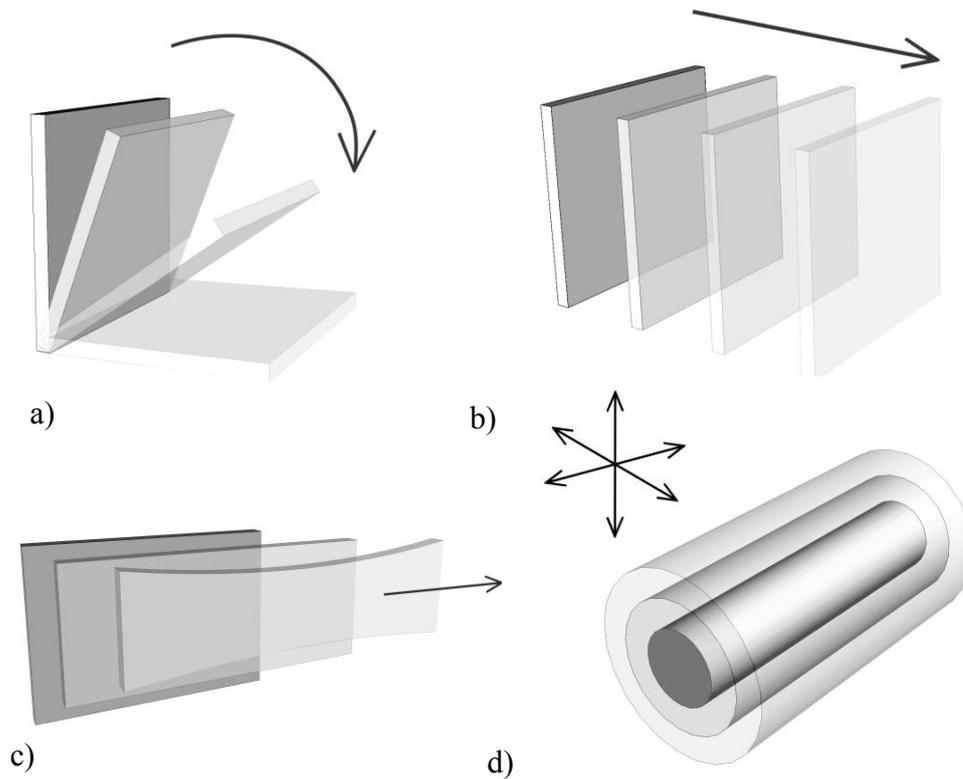
Figure 6-15: Rotation, translation, uniaxial stretching and expansion presented schematically.

Rigid body motion (RBM) tests were carried out using planar and cylindrical objects. The aim of rigid body motion test was to investigate the sources of strain uncertainty related to ShIRT and VIC-2D registration methods prior to non-zero strain measurements. After RBM tests two deformation tests were carried out:

- Elastic planar material tensile test

- Stent deployment; 3D and 2D characterisation

A summary of these tests, including the type of intensity pattern and image registration technique used, is provided in *Table 22*.

Table 22: Test undertaken to measure the strain.

Object Type	Test type	Processing method	Output
Planar Grid (regular pattern)	RBM	ShIRT	Zero strain
Planar object (speckle pattern)	RBM	ShIRT VIC-2D	Zero strain
Cylinder (speckle pattern)	RBM	ShIRT VIC-2D	Zero strain
Elastic material (speckle pattern)	Tensile test	VIC-2D	Planar strain
Analogue (stent)	Stent expansion with balloon inflation	VIC-2D	3D strain

To carry out RBM and deformation tests, the magnification of the cameras was decreased slightly (0.3), to register not only the area of the stent interacting with the analogue but also neighbouring regions. This change in magnification increased depth of field to 5.6 mm.

6.5.1.   RIGID BODY MOTION EXPERIMENTAL TESTS

It has been suggested [152, 153] that the use of translation and rotation tests can identify potential error sources of registration methods under theoretically zero-strain experimental conditions. The measured engineering strain value in RBM tests provides an indication of the measurement error. These tests allow assessment of the anticipated accuracy of the measurement of non-zero strains. Image registration with both ShIRT and VIC-2D was used to obtain 3D data at each object position and compute the strain between images as described in section 6.4.2.

6.5.1.1. METHODS

Three types of tests were carried out to explore errors related to different type of testing samples:

1.   Checkerboard grid rotation- 2D object, structured pattern;

2.   Flat surface translation- 2D object, random speckle pattern;

3.   Cylinder translation- 3D object marked, random speckle pattern.

Two desk lamps were used as light sources to decrease reflections (two lamps, specimen, and cameras) as shown in *Figure 6-16*.

Figure 6-16: Setup used to capture stent deployment in the vessel analogue.

CHECKERBOARD GRID PATTERN ROTATION

A checkerboard grid was captured in five different orientations with two Flea2 cameras separated by an angle of 45°. The field of view in the horizontal direction was approximately 15 mm due to the reduced magnification.

Image registration was undertaken as described in section 6.1, defining a region of interest (ROI) in the initial image. This ROI was divided into a grid as shown in *Figure 6-17*. The green grid shows the ROI on the left image, which was then registered to the right image. The red grid shows the position of the ROI from the left image, as registered to the right image. A grid size of 214.3 pixels and grid spacing of 10 pixels was chosen, resulting in 22 columns and 15 rows (330 points in total). 57285 measurements of distance were obtained for each orientation, as described in section 6.4.2 and these were then used for strain calculation.
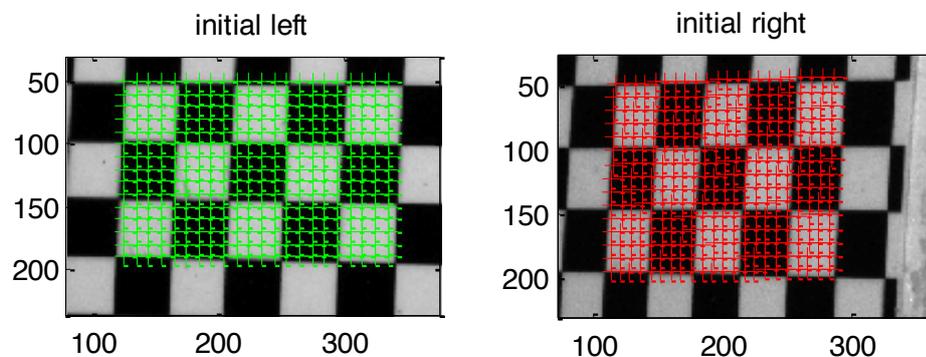
Figure 6-17: Initial left image registered to right image.

In addition the first and third grid orientations were reconstructed manually, by picking the corners of each grid square by hand, to assess the agreement between manual and image registration methods and to compute the strain from the manual approach. ShIRT was judged to have performed an acceptable registration when the nodes in the

right image (green) were observed to match the corresponding locations of the reference nodes in the left image (red).

Engineering strain was computed using the change in distance between points on the undeformed, L_0, and the deformed surface, L, as described in section 6.4.2.

VIC-2D was tested using these grid images to confirm that digital image correlation does not work with a structured pattern.

FLAT SURFACE TRANSLATION

Following the rotation test a second rigid body motion test was undertaken to directly compare results between ShIRT and VIC-2D using translation of a 2D object. A flat rigid piece of white foam board was sprayed with quick-drying enamel paint (Plasti-kote, USA) to create a random pattern.

- ***SHIRT***

For the translation test the ROI was divided into a grid as shown in *Figure 6-18* and *Figure 6-19*. The green grid shows the ROI on the left image, which was then registered to right image. The red grid shows the position of the ROI from the left image, as registered to the right image. Surface deformation was assessed using two ROI's of different size. The first grid size of 27.4 pixels and grid spacing 2 pixels was chosen (approx. 0.07 mm distance between grid points), resulting in 12 columns by 10 rows (120 points in total). 7140 measurements (combinations) of distance were obtained for each step of translation in this case. *Figure 6-18* shows this ROI defined on the images from left and right camera. A second ROI was chosen as shown in *Figure 6-19* with grid length of 91.1 pixels and grid spacing of 10 pixels

(approximately 0.38 mm distance between grid points) resulting in a grid of 90 points (10 columns by 9 rows). 4005 measurements (combinations) of distance were obtained for each step of translation in this case.
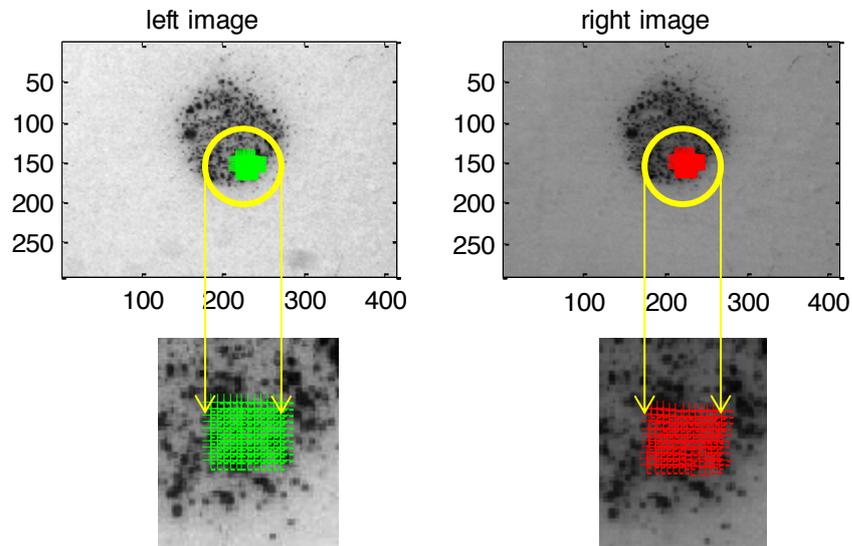
Figure 6-18: Initial left image registered to right image, good correlation.
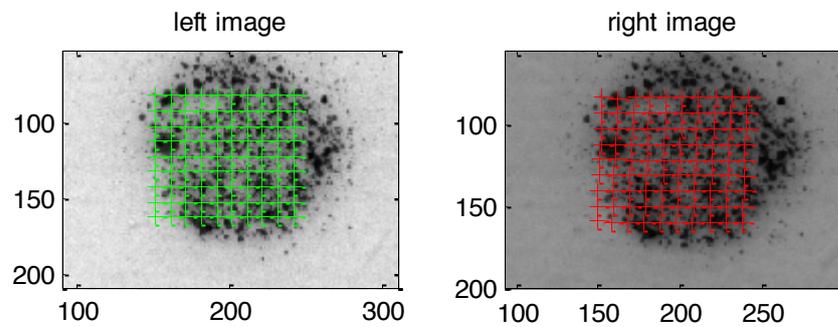
Figure 6-19: Initial left image registered to right image, good correlation.

- *VIC-2D*

The left and right initial images (L0, R0) were loaded into VIC-2D. A ROI was defined on the L0 image. A seed point location was selected and the default subset-size of 41 and step-size of 5 were used. The initial geometry was determined by

correlating the left and right images. Next all left images were correlated and all right images were correlated, the results were saved as Matlab (.mat) files. 246051 measurements (combinations) of distance were obtained at each step of translation.

For both ShIRT and VIC-2D data the engineering strain was computed using the change in distance between points on the undeformed, L_0, and the deformed surface, L, as explained in section 6.4.2.

CYLINDER TRANSLATION

The third zero strain test used a cylindrical surface to be as close as possible to the vessel shape. The cylinder was sprayed to create a random pattern and translated five times in various directions.

- *SHIRT*

The left and right images of the initial geometry were registered. A ROI was defined as a grid shown in *Figure 6-20*. The green grid shows the ROI on the left image, which was then registered to right image. The red grid shows the position of the ROI from the left image, as registered to the right image. A grid size of 115.7 pixels and grid spacing of 7 pixels (approximately 0.27 mm distance between grid points) was chosen, resulting in 15 columns and 17 rows (255 points in total). 32385 measurements (combinations) of distance were obtained at each step of translation. *Figure 6-20* presents the registration of initial 2D images from left and right camera with the presentation of the displacement vectors between left and right image.
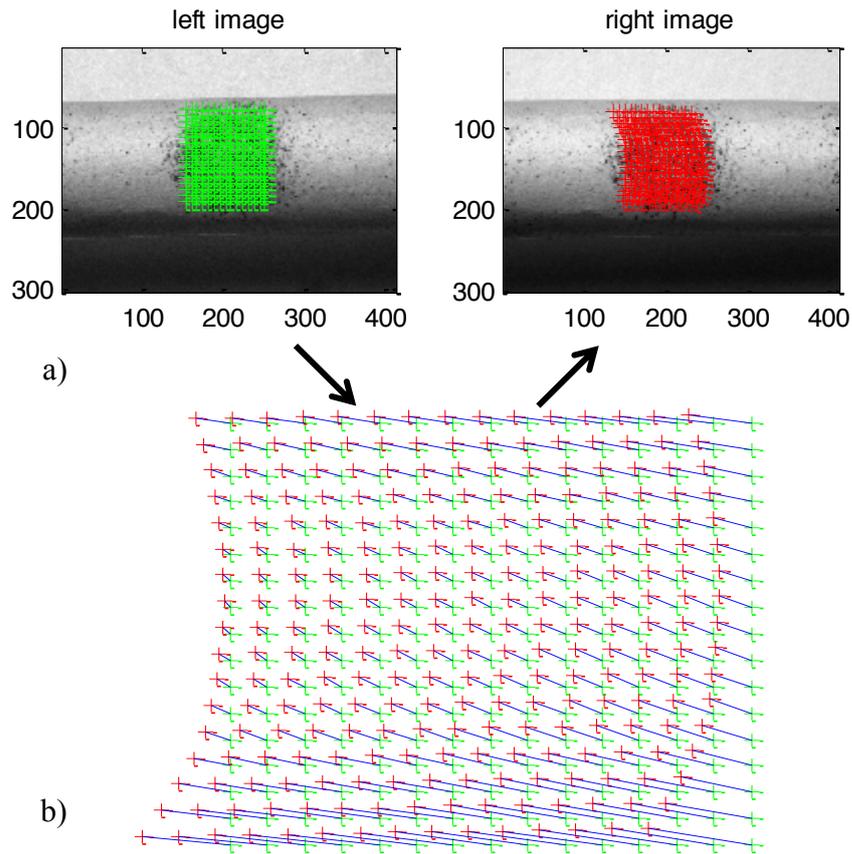
Figure 6-20: a) Initial left image registered to right image; b) the presentation of the displacement vectors between left and right image.

The displacement vectors were calculated for all steps. Registration was done in 6 steps of translation.

- *VIC-2D*

The same process was undertaken as for the flat object. The same default subset-size of 41 and step-size of 5 were used for cylinder translation. 21945 measurements (combinations) of distance were obtained for each step of translation.

For both ShIRT and VIC-2D data the engineering strain was computed using the change in distance between points on the undeformed, L_0, and the deformed surface, L, as explained in subchapter 6.4.2.

6.5.1.2. RESULTS

The strain results from the rigid body motion test of flat and cylindrical samples are presented below.

CHECKERBOARD GRID ROTATION

The registration of the left and right images was robust until the rotation was large (60° between initial and final position). This caused issues with ShIRT registration. This is clear from the 3D plot in *Figure 6-21*, where the poorly registered data is shown in black (IR5). Similar behaviour was observed in the 2D images shown in *Figure 6-22*. There was good qualitative agreement between the reconstruction obtained with ShIRT and two manual reconstructions, shown in magenta and brown in *Figure 6-21* (MR1 with IR3 and MR2 with IR1 respectively).
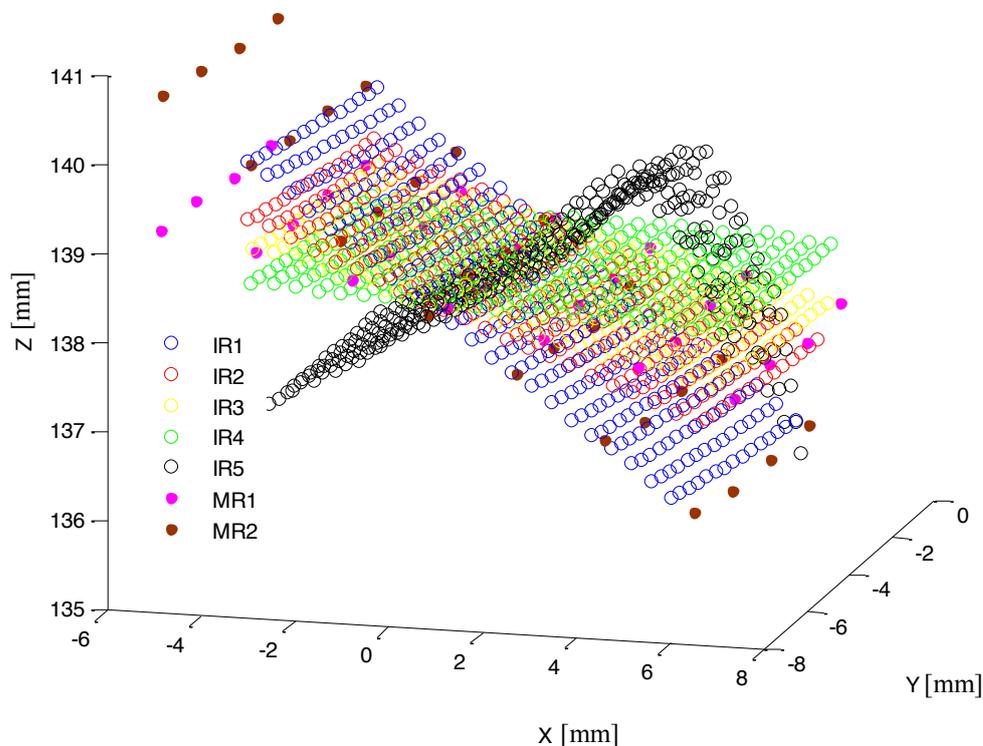
Figure 6-21: 3D plot showing grid reconstruction from data obtained using ShIRT(IR-image registration) and for two sets of rotation output data obtained from manual reconstruction (MR1 and MR2).
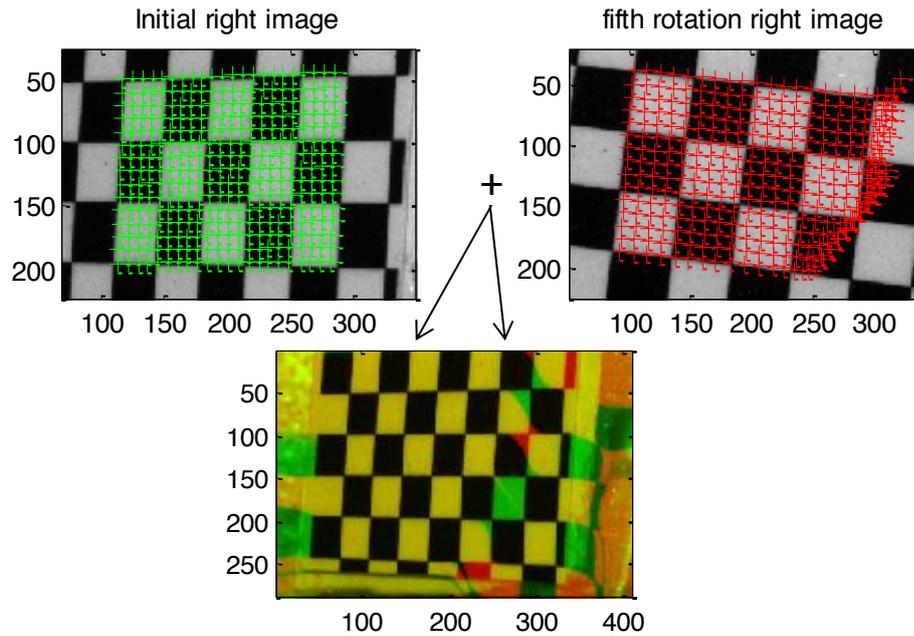
Figure 6-22: Presentation of the registration which failed in fifth step (IR5 in Figure 6-21) of rotation.

The measured strain is plotted against the distance between points used for the strain evaluation (*Figure 6-23*) as described in section 6.4.2. The measured distance varied from 0.41 mm to 11.4 mm.   The reported strain decreases as the distance between points increases.   For the 1st, 2nd and 3rd rotations, the strain error decreases to approximately 1% when the distance is larger than 2 mm. Maximum strains occurred for distances smaller than 0.5 mm ranging from 5.5% for the 3rd rotation to 3.5% for the 1st rotation. It was observed that, as the rotation angle increased, the magnitude of reported strains also increased. As it was reported previously, the registration failed for the 4th rotation (5th position), due to the large rotation angle.   In this case strains greater than 50% were reported (*Figure 6-23*, 4th rotation). In *Table 23* maximum and average strain error is reported for both ShIRT and the manual measurement (between MR1 and MR2 for a distance of 2 mm and 6 mm).
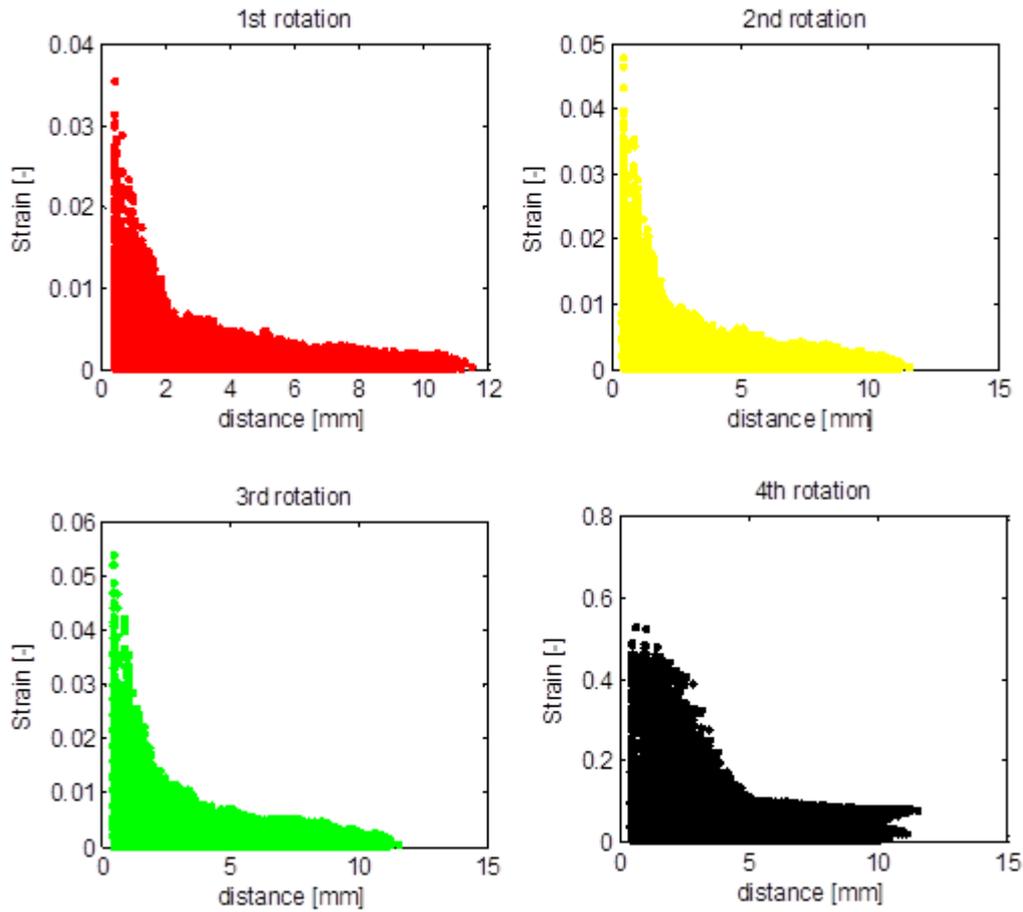
Figure 6-23: Variation in computed strain using ShIRT with distance between points from the zero strain test.

Table 23: Strain error for the registration of the grid rotation. '-' means not assessed.

Distance between points [mm]	Max Strain error [%]		Average Strain Error [%]	
	ShIRT	MR	ShIRT	MR
0.45	5	-	2	-
1.0	3	-	1.5	-
2.0	1.2	3.25	0.5	1.25
2.8	0.8	-	0.38	-
6.0	0.5	1.5	0.25	0.8

FLAT SURFACE TRANSLATION

For both registration methods, the maximum, mean and standard deviation of strain were computed as a function of the distance between nodes over a range of distances (i.e. $0.07 \rightarrow 0.09$ mm) as reported in *Table 24*.

Registration of the left and right images using ShIRT was robust for all the translation steps. Decreasing the distance between nodes to value of 0.075 mm resulted in a maximum error of 7.5%. For a distance between nodes of 0.5 mm, the error dropped to 1.8% and incrementally decreased as the distance between the points increased as reported in *Table 24*. The 3D reconstruction of the ROI for all translation steps is shown in 3D in *Figure 6-24*.

Using VIC-2D the correlation was robust for all translation steps. A maximum error of approximately 0.8% was reported (*Table 25*) for small node separations (between 0.05 and 0.07 mm). However, the mean strain error at this node separation was only 0.13%. *Figure 6-25* shows the relationship between the maximum and mean strain and the distance between nodes for both registration methods (ShIRT and VIC-2D).

Individual plots of strain for 5 translation steps for small and large ROIs using VIC-2D is shown in *Figure 6-24*.
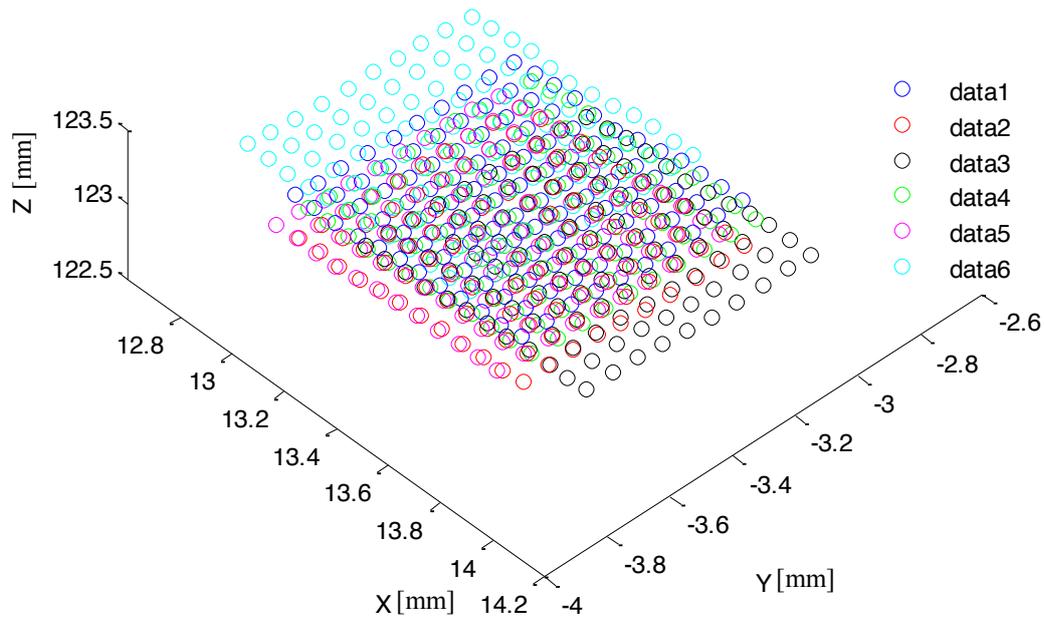
Figure 6-24: 3D plot presenting flat object translation of small area.

Table 24: Strain error for the small and large area from registration using ShIRT.

ShIRT			
distance range [mm]	max strain [%]	mean strain [%]	std [%]
0.07 → 0.09	7.5	1.70	1.4
0.25 → 0.35	3.9	0.87	1.0
0.45 → 0.55	1.8	0.45	0.6
0.65 → 0.75	1.2	0.28	0.3
0.85 → 0.95	0.7	0.25	0.2
1.30 → 1.50	0.7	0.16	0.12
1.60 → 1.80	0.55	0.13	0.11
2.00 →2.20	0.43	0.10	0.08
2.40 → 2.60	0.4	0.09	0.06
2.80 → 3.20	0.3	0.07	0.05
3.30 → 3.70	0.26	0.06	0.05
3.80→ 4.60	0.1	0.04	0.03

Table 25: Strain error for the small and large area from registration using VIC-2D.

	VIC-2D		
distance range [mm]	max strain [%]	mean strain [%]	std [%]
0.05 →0.07	0.8	0.13	0.10
0.08 → 0.12	0.75	0.12	0.10
0.14 → 0.16	0.71	0.11	0.09
0.18 → 0.30	0.55	0.092	0.07
0.40 →0.50	0.42	0.063	0.05
0.50 → 0.70	0.34	0.048	0.04
0.80 → 1.00	0.22	0.038	0.03
1.00 → 1.60	0.16	0.03	0.02
1.60 → 2.00	0.13	0.022	0.02
2.00 → 2.40	0.07	0.01	0.008
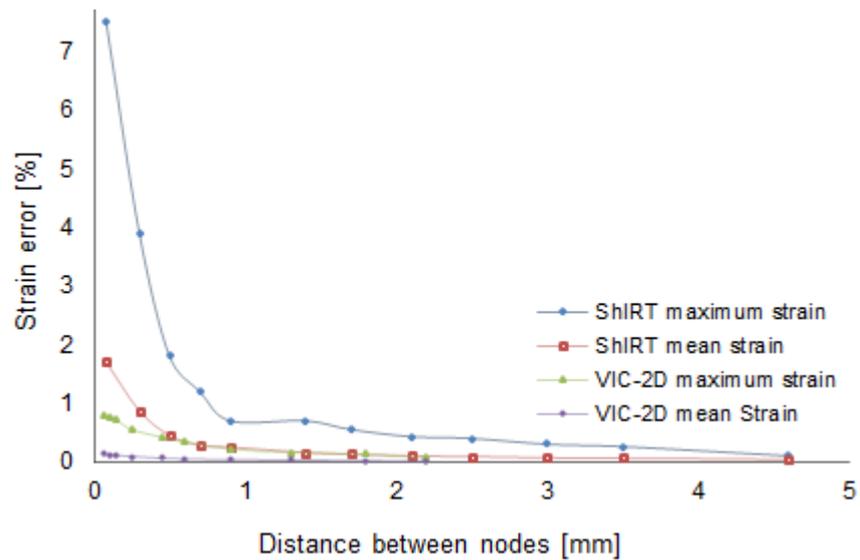
Figure 6-25: Maximum and means strain to the distance between nodes plotted for ShIRT and VIC-2D.
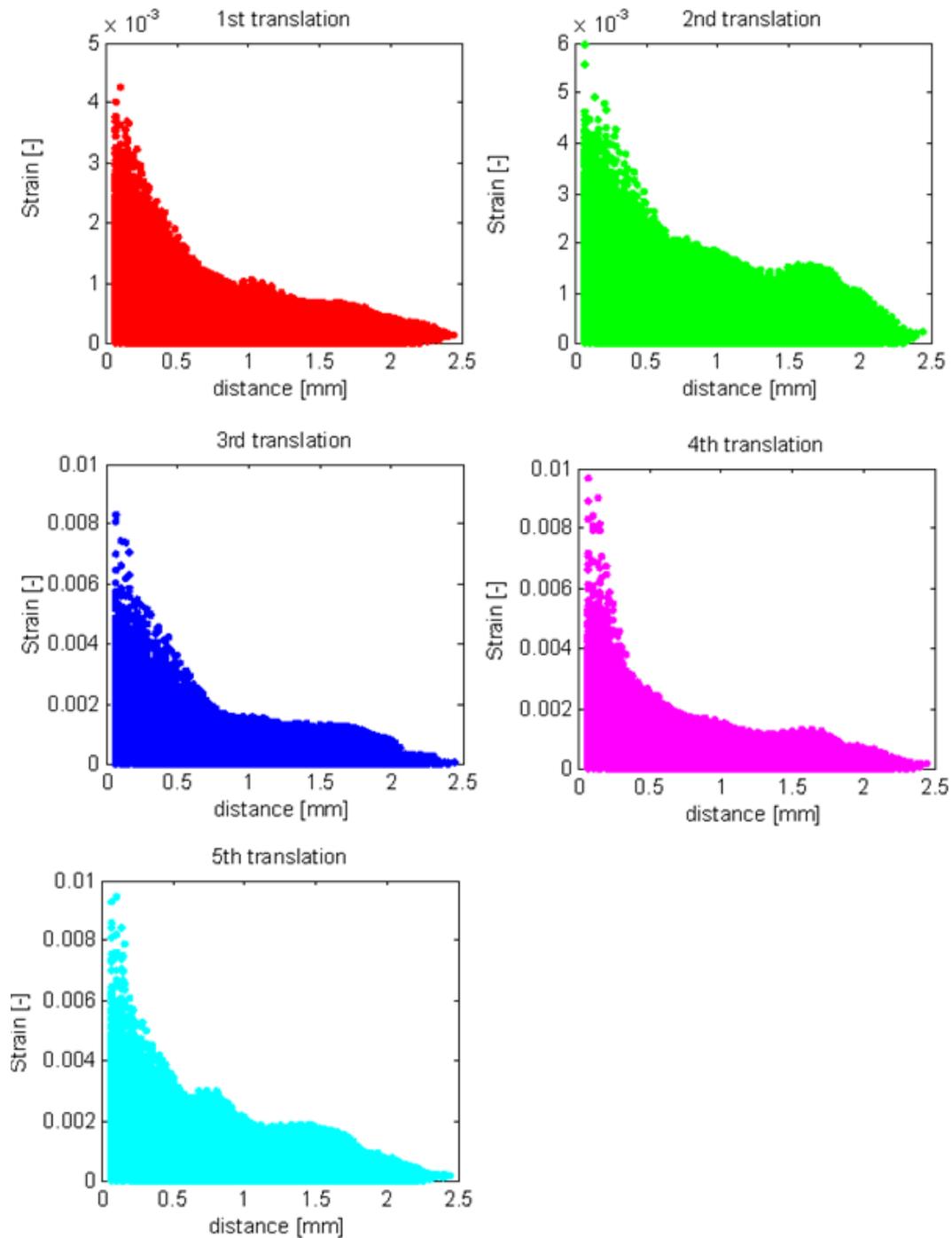
Figure 6-26: Variation in computed strain using VIC-2D with distance between points from the zero strain test.

CYLINDER TRANSLATION

Registration of the left and right images was robust for the first five translation steps using ShIRT and for all six translations using VIC-2D. To determine the translation

distance for which ShIRT failed to register the images, manual measurement between a few marker points in the initial geometry and at the sixth translation was performed, reporting a translation distance of approximately 1.15 mm (±0.025 mm). A 3D plot of the reconstruction of all translation steps using ShIRT data with the failure for the sixth translation is presented in *Figure 6-27*.
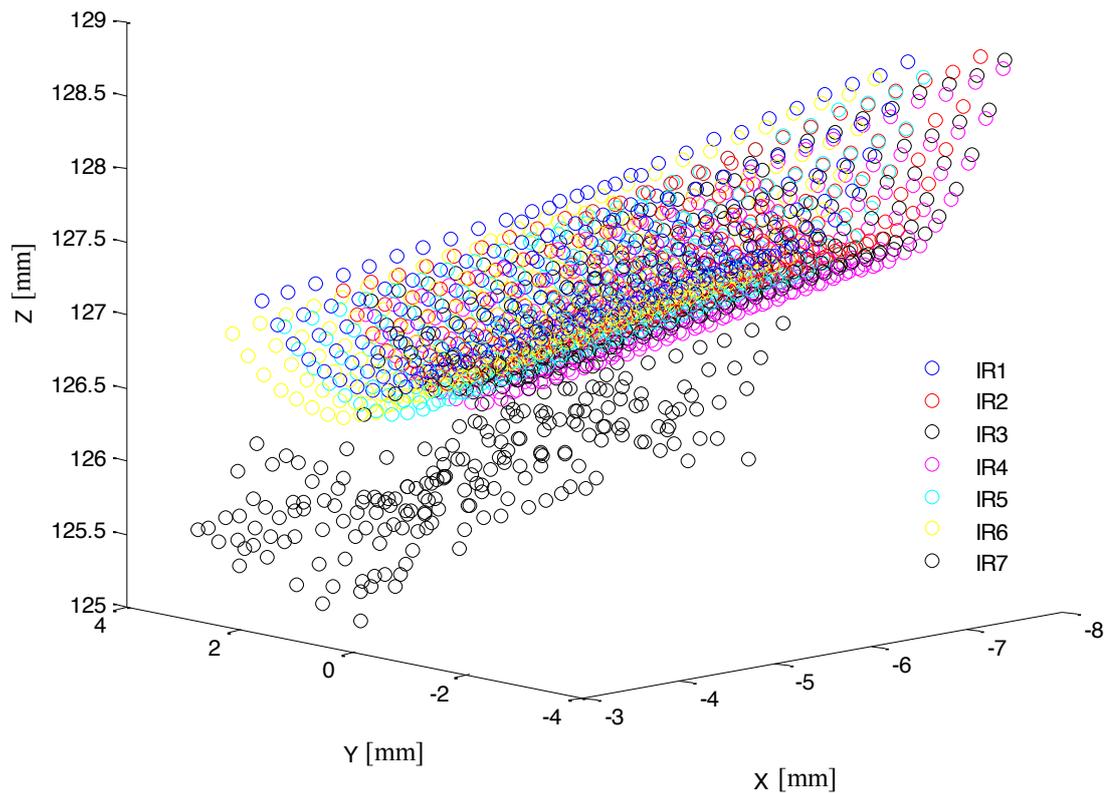
Figure 6-27: 3D plot of the cylinder translation; data form ShIRT

For both registration methods the maximum, mean and standard deviation (STDEV) of strain was computed, as a function of the distance between nodes for all points over a range of distances as presented in *Table 26*. The maximum strain obtained with ShIRT was of order of 3.3% for node separation in the distance range: 0.25 → 0.45. The values of maximum error obtained with ShIRT for the distance 1.8 → 2.1 and 2.2 →2.5 presented in the *Table 26* are with red dash lines due to single outliers shown

in *Figure 6-28.* For the VIC-2D the maximum strain was of order of 0.97% (*Table 27*) for a node separation between 0.05 and 0.07.

Table 26: Strain error for the cylindrical shape registration

ShIRT			
Distance range [mm]	max strain [%]	mean strain [%]	std [%]
0.25 → 0.45	3.3	0.6	0.5
0.5 → 0.8	2.4	0.4	0.3
0.8 → 1.2	1.5	0.23	0.2
1.3 → 1.55	1.1	0.16	0.13
1.55 → 1.8	0.73	0.14	0.11
1.8 → 2.1	1	0.13	0.11
2.2 → 2.5	0.98	0.1	0.08
2.5 → 3.0	0.6	0.09	0.07
3.0 → 3.4	0.42	0.08	0.06
3.5 → 4.0	0.39	0.08	0.06
4.0 → 4.5	0.39	0.08	0.06
4.5 → 5.5	0.29	0.08	0.05

Table 27: Strain error for the cylindrical shape registration

VIC-2D			
distance range [mm]	max strain [%]	mean strain [%]	std [%]
0.05 → 0.10	0.97	0.18	0.15
0.15 → 0.25	0.75	0.15	0.13
0.25 → 0.5	0.7	0.12	0.089
0.5 → 0.7	0.5	0.11	0.076
1.0 → 1.3	0.38	0.1	0.064
1.3 → 1.6	0.3	0.09	0.054
1.6 → 1.9	0.26	0.09	0.054
1.0 → 1.6	0.24	0.1	0.055
1.9 → 2.2	0.24	0.01	0.047
2.3 → 2.8	0.19	0.0009	0.04

Figure 6-28 shows the relationship between the maximum and mean strain and the distance between nodes for both registration methods (ShIRT and VIC-2D) for the 4th translation.
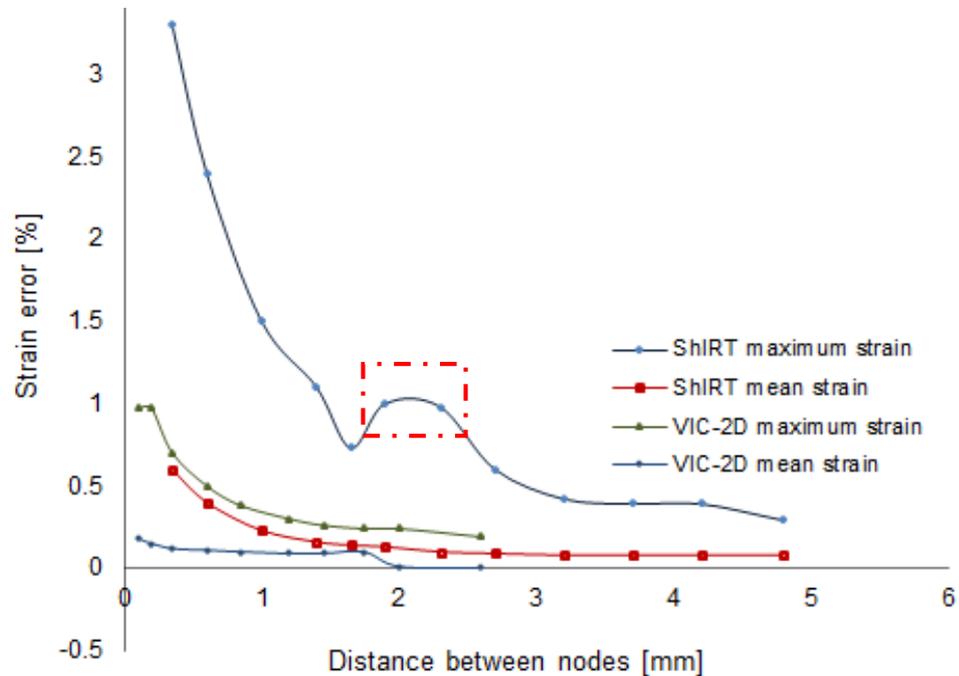
Figure 6-28: Maximum and mean strain as a function of the distance between nodes for both ShIRT and VIC-2D.

6.5.1.3. DISCUSSION

A rigid body motion (RBM) test was carried out using both ShIRT and VIC-2D image registration software to assess typical errors in strain measurement. Three control objects were examined during rotation (checkerboard grid) and translation (flat object, cylinder with applied scattered pattern) to confirm the accuracy of the registration method combined with the 3D reconstruction process. Engineering strain was computed to compare results from the RBM test.

In a previous study of Genovese *et al*. [136] one translation step of a rigid cannula was conducted to check zero strain errors. The results indicated that the error varied along

the specimen. The maximum observed error of order 6% was depicted on the results plot, but a mean error value of approximately 0.6% was reported in this paper. This value seems reasonable, given the small length scales (~0.04 mm local distance between nodes).

In the current study at least 4 steps of rotation or translation were undertaken. Even though these tests should indicate a zero-strain condition, reported strains of the order of 0.2- 5% for ShIRT and 0.07- 1% for VIC-2D, were distributed randomly across the region of interest. These errors may arise from experimental noise such as: illumination fluctuations, camera lens distortions, correlation algorithm errors and random noise present in the registration. It is important to bear in mind that the accuracy of the displacement measurements of a VIC-2D correlation algorithm is related to the type of interpolation scheme used. Higher order interpolation schemes lead to lower amounts of measurement errors. These reported RBM results were generated with the 8-tap sub-pixel interpolation scheme, which was the highest order interpolation scheme available within VIC-2D.

As a result of these tests, VIC-2D was used for all following experiments. The maximum computed error was <1% with a mean error value of approximately 0.18% (for 0.05 → 0.1 mm local distance between nodes). This value is a significant improvement and places limits on the minimum detectable strain and the confidence with any reported strain. It is small enough to support investigation of strain in the analogue artery model.

 In the next sections a tensile test of an elastic material and more complicated study of vessel analogue wall deformation during stent deployment are presented.

6.5.2. DEFORMATION TO EXAMINE STRAIN

As discussed in Chapter 1, both the angioplasty balloon and the stent deployment induce non-uniform strains in the vessel wall. Quantitative data on the local strain distribution will aid understanding of the vessel wall injury and related neointimal tissue growth and in-stent restenosis which have been reported in both numerical studies [46] and porcine models [2, 70]. This section reports experimental tests to examine the local strain distribution which occurs during stent deployment within a vessel analogue.

Following the assessment of strain uncertainty during rigid body motion (described in the previous section), image registration was applied to track deformations for non-zero strain calculation. The experimental process began with a tensile test before testing a vessel analogue mimicking the coronary artery to examine stent deployment. This approach, where the conditions of the initial tests are easy to control, was undertaken to improve confidence that final results are robust. Green-Lagrange strain was computed from the deformation of individual triangles (defined by three nodes). The deformation gradient, $\mathbf{F}$, determined at each stage of deformation was used to obtain the Green strain tensor, $\mathbf{E}$, as described in Section 6.4.2.

To examine strain variation over a range of magnitudes the objects were imaged at several stages of deformation. Stereo pairs of digital images were subsequently processed with VIC-2D to track the deformation in left and right camera, as described in Section 6.4. Stereo calibration was used for 3D stereo triangulation of the left and right camera 2D data from VIC-2D.

TENSILE TEST

Initial focus was on the simple deformation of flat silicone sheet with an applied speckle pattern. A Technic (LEGO) test rig, displayed in *Figure 6-29*, was used to apply a stretch to a 38 mm x 18 mm size silicone sample marked with a speckle pattern (using the same marking approach as for RBM translation test). The rig consisted of two rotatable rods, to which the sample was attached with double sided tape.
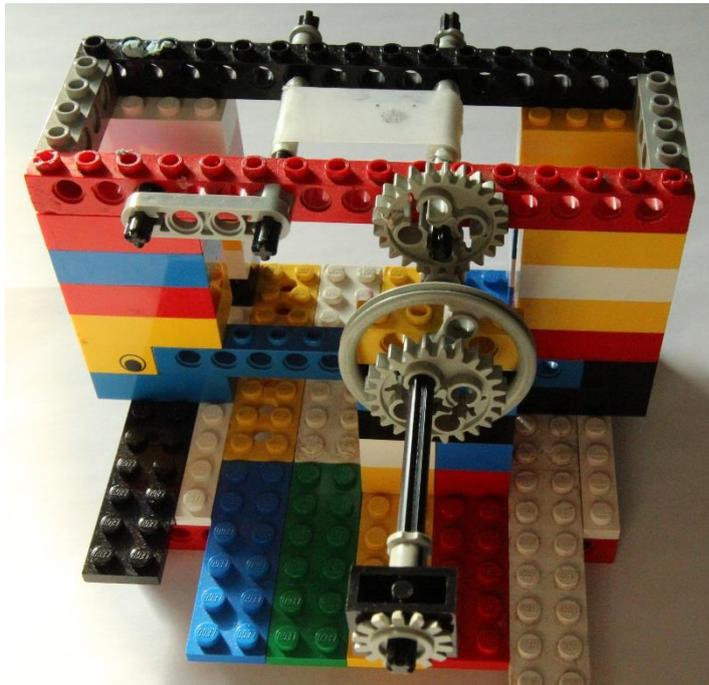
Figure 6-29: Rig used to stretch elastic material: tensile test.

One end of the sample was fixed to the left rod and the right rod was moveable (rotated) to achieve various levels of axial strain. The stereo camera rig was used to capture each deformation step.

The images were taken at the initial state and a further nine deformed states (at increasing rotation of the right rod in the test rig). The strains in the *x* direction should

be positive and in the **y** direction negative due to the inherent Poisson's ratio properties (*Figure 6-30*).
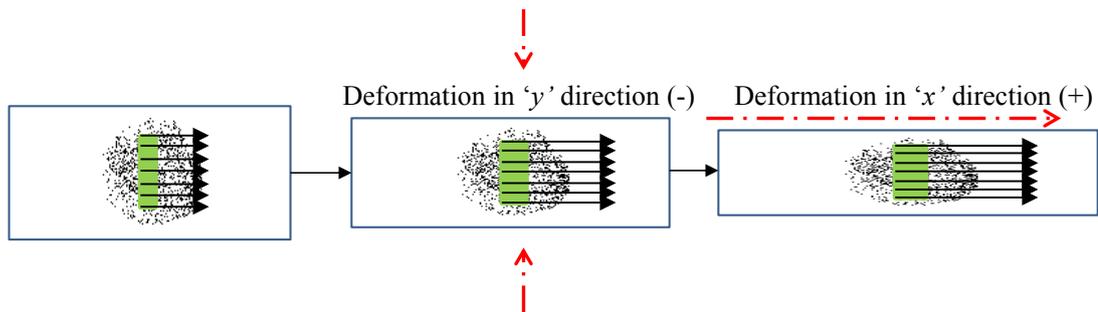
Figure 6-30: Diagram presenting tensile and compressive deformations of the elastic material during stretching.

The captured images were loaded into VIC-2D to perform image correlation. A region of interest, of approximate size 1 mm by 4 mm, (*Figure 6-31*), of the applied speckle pattern was used to track the deformation in longitudinal (**x**) and transverse (**y**) directions. A seed point location was selected in the centre of the region of interest and the default subset-size of 41 and step-size of 5 were used. Additionally two reference points, separated by a distance of approximately 6.8 mm, were used to calculate the global strain in the **x** direction using a manual method to compare with registration output, as described in Section 6.4.2.
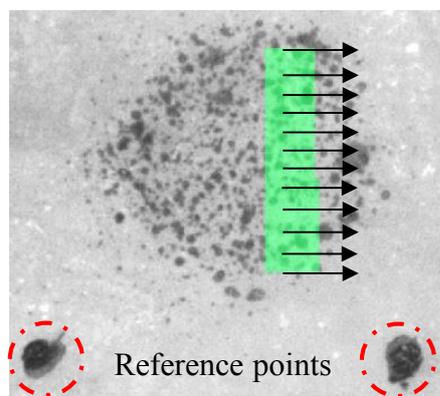
Figure 6-31: VIC-2D- Region of interest, image taken at the initial stage with left camera.

2D displacements were used to obtain the 3D coordinates of a grid of points within the region of interest, as described in section 6.4. A grid size of 0.07 mm by 0.07 mm was used for this test. Green-Lagrange strain was computed across the region of interest using the technique described by Genovese *et*. *al* [136] with a Matlab subroutine [154]. 1392 values of each component of strain were computed from the triangles defined by the X by Y grid. In addition, Pearson's correlation coefficient was calculated between the VIC-2D strain data and global strain from manual reconstruction. Green-Lagrange strain measure was used for this exercise.

STENT DEPLOYMENT

The experimental imaging of stent deployment within the vessel analogue was designed to include in the cameras field of view not only the stent, but also the balloon on which the stent was crimped and to contain regions of the vessel analogue outside the stented area. In order to achieve this, the cameras optics were modified to reduce the magnification to 0.3 (v = 41 mm, u = 135 mm).

To image the experiment a stereo rig was formed by positioning two cameras at an angle of approximately 65°. Prior to stent deployment, a checkerboard grid pattern was captured in six orientations to calibrate the cameras. Calibration accuracy was determined through reconstruction of a control checkerboard grid with internal grids of size 3 mm x 3 mm.

The silicone material (SILEX limited, Hampshire, UK) tested for suitability for coronary application (Section 6.3) was covered with white Stretchi paint (Creative Resources Distribution, Propbuilder) and sprayed with black Enamel spray (Plasti-

kote, USA) to increase image contrast and create a speckle pattern for image registration.

A vessel analogue was created by wrapping the sheet over itself and securing it between two Perspex blocks, as shown in diagram below, *Figure 6-32*.
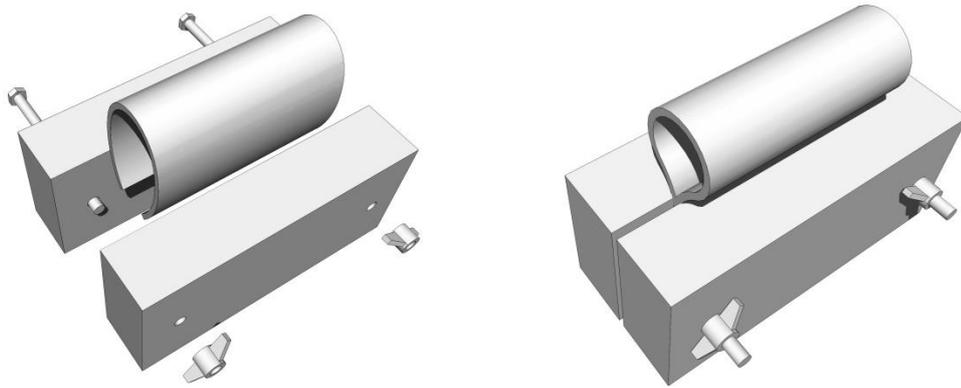
Figure 6-32: Diagram presents silicone sheet securing between two Perspex blocks to create straight vessel analogue section.

Following calibration assessment, a cobalt chromium alloy L-605 Coroflex Blue (B/Braun Medical) coronary stent (nominal deployed diameter 3.5 mm, length 10 mm), mounted on the manufacturer-supplied balloon, was attached to a clinical inflation device (Merit Medical Basix25, Ireland) and inserted into the lumen of the vessel analogue.

A stereo pair of images was obtained before balloon inflation. The pressure in the inflation device was then increased to a value of 9 atm (911.92kPa) using steps of approximately 0.6 atm ±0.2 atm. Stereo images were taken as previously using FlyCap2 (Point Grey). After each inflation step, the balloon was left for 10 seconds to stabilise before an image pair was taken to avoid creep effects. At the last step, when the pressure was increased to 9 atm (911.92kPa), the balloon was kept inflated for 30s (pressurisation), before deflation. Afterwards, the balloon was deflated and

withdrawn along with the catheter from the lumen before another image pair was captured, allowing assessment of stent recoil.

The stereo optical images of vessel analogue deformation were used to characterise vessel wall strain as for the tensile test. VIC-2D displacement data and camera calibration data were used to determine the 3D coordinates (x, y, z) of nodes within a selected region of interest. Local strains were calculated on the 3D vessel surface using the Green-Lagrange measure in longitudinal E_x and circumferential E_y directions.

The stent/vessel analogue wall interaction experiment was designed to investigate the hypothesis that the strain varies along the length and around the circumference due to behaviour of individual struts, as observed during the free stent deployment analysis described in Chapter 5.

In addition global circumferential strain was approximated by measuring the diameter of the analogue at five locations on the vessel wall as shown in *Figure 6-36* (Results Section): before the distal edge of the stent (a), at the distal edge of the stent (b), in the central part (c), at the proximal edge of the stent (d) and after the proximal edge of the stent (e). The assumption was that the analogue was cylindrical at each stage of deformation and the circumference (C_0) was calculated from the diameter as $\Pi*1/2D^2$ (Π=3.14, D- analogue internal diameter). Change in the circumference (C) was used to measure Green-Lagrange strain in the circumferential direction $(E = \frac{C^2 - C_0^2}{2C_0^2})$.

6.5.2.1. RESULTS

Strain results are presented in this section starting with the simple tensile test, followed by the more complex 3D deformation of the vessel analogue during stent deployment. The experimental tests were precisely performed and average value of calibration and reconstruction accuracy of 15 μm was found in both accuracy assessment tests, as reported in *Table 28*.

Table 28: Maximum, minimum and standard deviation (STDEV) from all 25 points reconstructed in 3 steps of translation of the control object.

Difference in computed distance [μm]			STDEV [μm]
Max	Average	Min	
18	15	6	15

TENSILE TEST

1392 local strains were computed in both x longitudinal (E_x) and y transverse (E_y) directions. *Table 29* contains the average values of E_x strain at each deformation step with VIC-2D and manual strain measurements between two reference points.

The average value of the VIC-2D strain results along with the manual measure are plotted with change in the applied strain step in *Figure 6-33a* and against each other in *Figure 6-33b*. The Pearson's correlation coefficient of 0.9925 confirms good agreement between the two methods.

Table 29: Local (image registration) and global strain (manual measurement).

Steps	Average strain VIC-2D [%]	Manual strain [%]
1	2.53	2.43
2	3.21	2.9
3	3.88	4.2
4	4.51	4.38
5	6.11	5.96
6	6.92	6.31
7	8.17	7.91
8	9.48	9.17
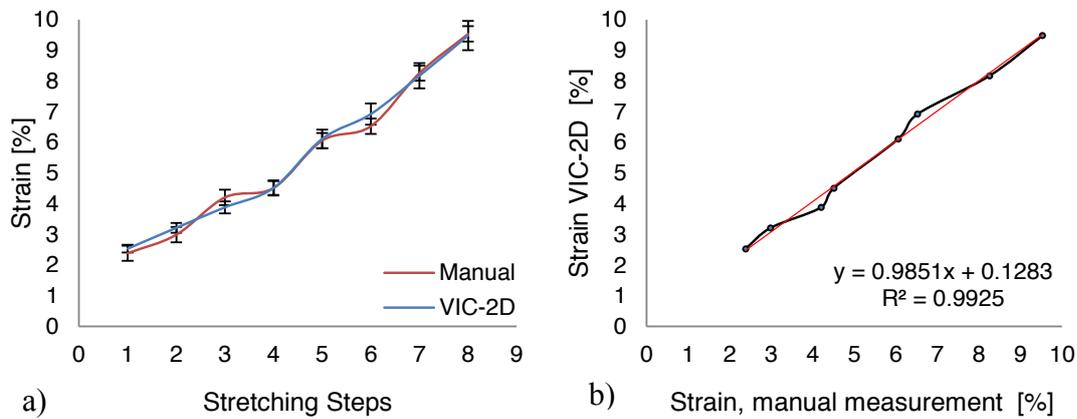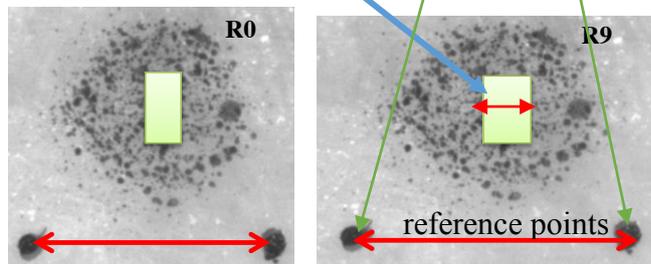
Figure 6-33: a) Variation in the average strain computed in the x direction using VIC 2D and manual method with applied strain. b) Average strain computed with VIC 2D versus strain obtained from manual reconstruction.

The strain distribution calculated in longitudinal, E_x, and transverse, E_y, directions for the 5th and 9th deformation stages are shown as a contour plot in *Figure 6-34* and the maximum, minimum and standard deviation of the strain values over the whole region

of interest are reported in *Table 30*. In *Figure 6-35* the strain data are plotted for the single line in **y** direction depicted by black markers on the *Figure 6-34* for the E_x strain and the E_y strain over three steps of deformation.
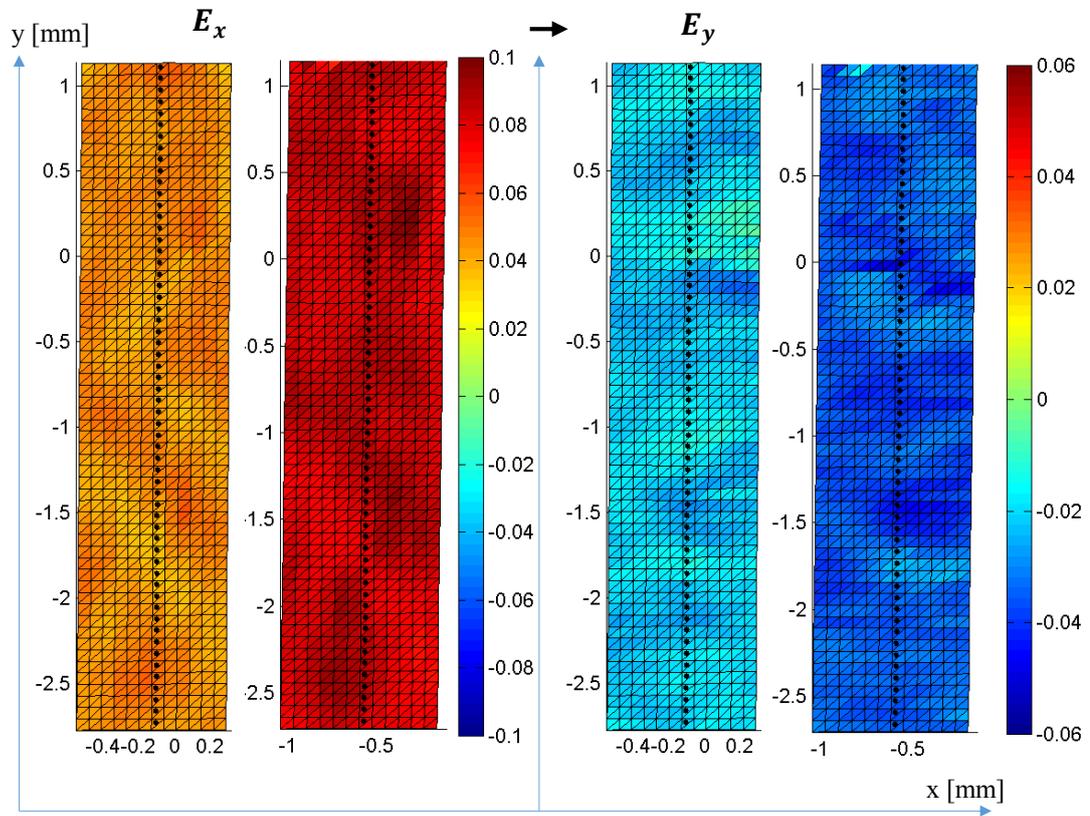
Figure 6-34: VIC-2D strain computed in longitudinal and circumferential direction for chosen region of interest: 5th and 9th deformation steps; nodes separation 0.08 mm.

Table 30: Maximum and minimum strain reported from 1392 computed local strains in longitudinal direction (Ex) and transversal direction (Ey), plus the standard deviation.

Tensile	Strain E_x [%]			Tensile	Strain E_y [%]		
Steps	MAX	MIN	STDEV	Steps	MAX	MIN	STDEV
1	2.53	-0.003	0.40	1	2.25	2.50	0.55
2	3.92	0.79	0.43	2	0.89	-2.61	0.50
3	4.33	1.17	0.42	3	0.13	-3.42	0.40
4	4.92	2.57	0.42	4	-0.47	-3.19	0.43
5	5.65	3.30	0.40	5	-0.42	-3.53	0.40
6	8.01	4.31	0.49	6	-0.84	-3.72	0.42
7	8.83	5.25	0.52	7	-0.77	-4.42	0.42
8	9.83	6.68	0.51	8	-1.61	-5.07	0.42

The maximum error (0.9% for the 0.07 mm node separation used to compute the strain values) computed during zero strain test is shown using error bars for each strain component (*Figure 6-35*).
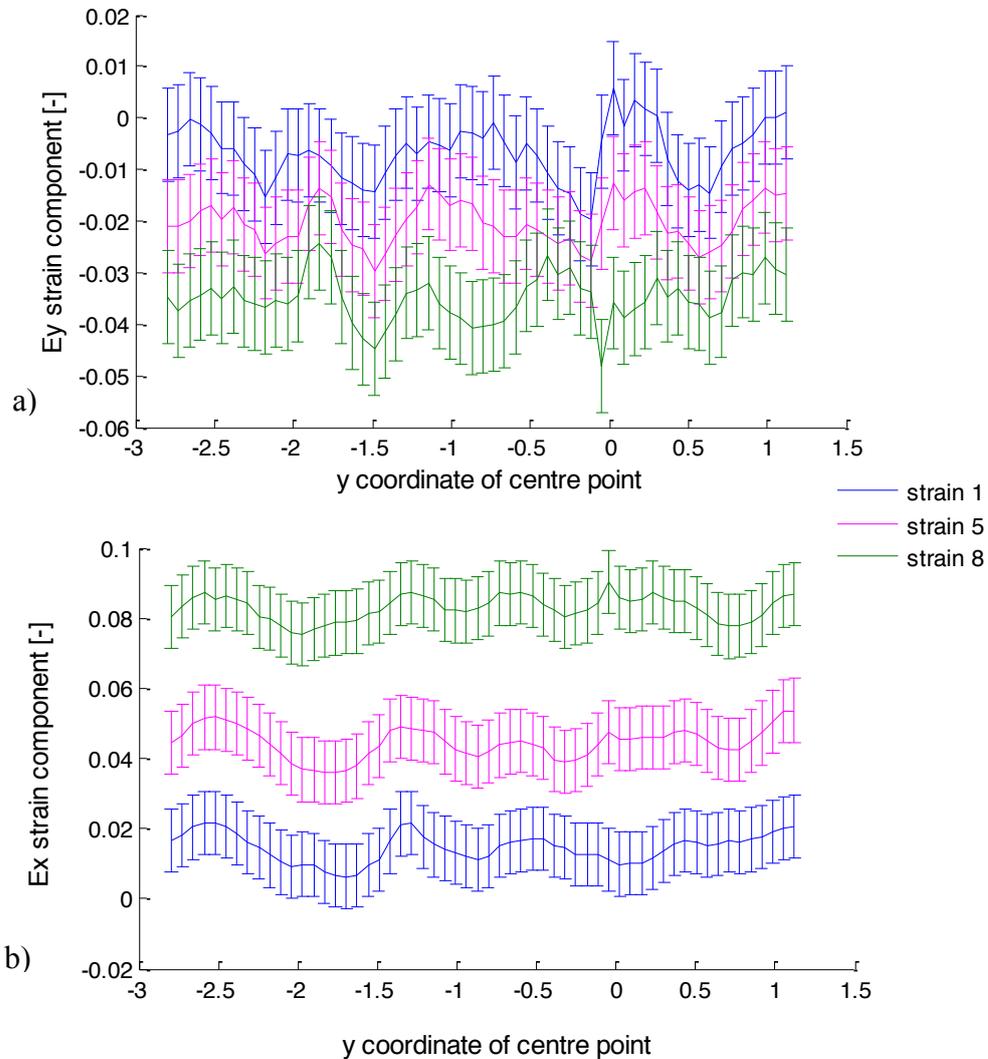
Figure 6-35: Strain variation across the length: a) E_x and b) E_y. The strain 1, strain 5 and strain 8 are the results from second, sixth and ninth tensile step respectively.

STENT DEPLOYMENT

1840, 2772 and 2058 local strains were computed in both longitudinal E_x and circumferential E_y directions for the distal, central and proximal part of the vessel

analogue respectively. During stent deployment the distal end of the stent first came into contact with the inner wall of the analogue when the inflation pressure was increased to 2.4 atm. Both the distal and proximal ends of the stent continued to expand (showing a dog-boning phase) until the pressure load increased to 6.6 atm. At a pressure load of 7.2 atm the central part of the stent deployed. The pressure in the balloon was increased to 9.0 atm to fully deploy the stent, and then held for approximately 30s (pressurisation). Afterwards, the balloon was deflated allowing stent recoil. The overall behaviour of the stent during the deployment process was observed from the image data and the displacement was computed with the VIC-2D software.

Figure 6-36 shows the vessel analogue (image taken in the initial stage, 0 atm) along with points a, b, c, d and e (yellow dashed lines) where diameter measurements were taken to approximate the strain of the analogue circumference (*Figure 6-37*) and the regions used to compute strain data from VIC-2D displacements. The variation of the circumferential strain estimate along the length of the analogue is illustrated for six balloon inflation pressures and the vessel recoil. These results illustrate high local strain due to stent deployment at both ends of the stent (position b and d) during the dog-boning phase.

0 atm
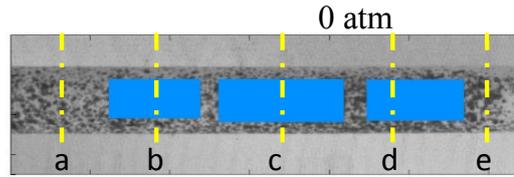
Figure 6-36: Vessel analogue before the stent deployment. Region of interest for the image registration is presented in blue.
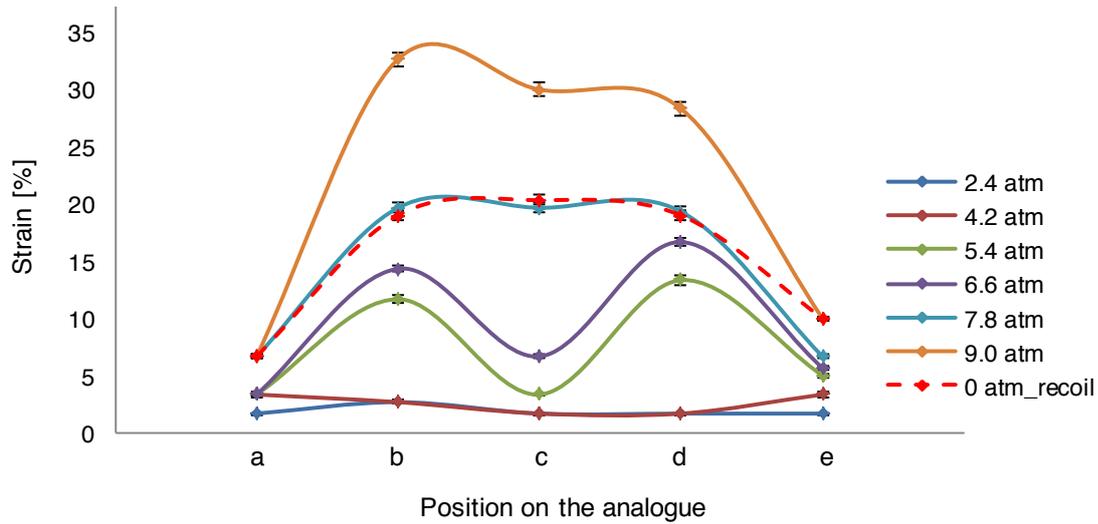
Figure 6-37: Estimated circumferential, global strain of five circumferences on the vessel analogue (a, b, c, d, e, Figure 6-36) to applied pressure (max 9 atm).
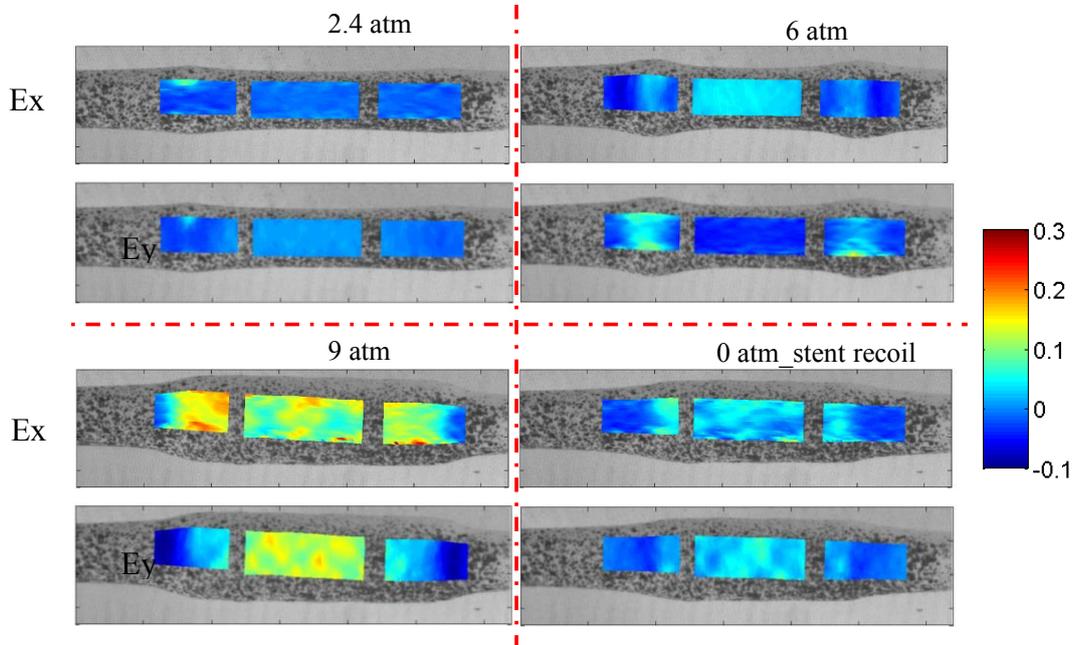
Figure 6-38: The longitudinal E_x and transversal E_y strain distribution plotted on the vessel analogue surface at the three regions of interest for balloon inflation pressures of: 2.4, 6.6, 9.0 and 0 atm.

Table 31 reports the maximum and minimum values and the standard deviation of all local strains computed from VIC-2D displacement data over the distal, central and proximal region of interest at four stages: initial contact of the stent with the vessel (2.4 atm), maximum dog-boning phase (6.6 atm), maximum stent deployment (9.0 atm) and elastic recoil (0 atm), as presented in *Figure 6-38*. Negative minimum strain represents maximum compressive strain.

Table 31: Maximum and minimum strain reported from 1840 at distal, 2772 at central and 2058 at proximal local strains measure in longitudinal direction (E_x) and transversal direction (E_y), plus the standard deviation. Data reports strain measure at four stages of stent deployment.

Pressure	Strain E_y Distal [%]			Pressure	Strain E_x Distal [%]		
[atm]	MAX	MIN	STD	[atm]	MAX	MIN	STD
2.4	9.44	-4.42	2.0	2.4	4.49	-3.66	1.0
6.6	10.58	-4.67	3.0	6.6	4.00	-7.73	3.0
9.0	22.30	-3.85	6.0	9.0	3.96	-10.68	5.0
recoil	7.65	-5.06	2.0	recoil	1.20	-4.10	1.0

Pressure	Strain E_y Central [%]			Pressure	Strain E_x Central [%]		
[atm]	MAX	MIN	STD	[atm]	MAX	MIN	STD
2.4	0.12	-2.23	0. 6	2.4	1.65	0.02	0.3
6.6	-0.40	-6.04	0. 8	6.6	4.70	1.59	0.6
9.0	19.13	3.49	3.0	9.0	16.3	7.24	0.02
recoil	9.25	-2.98	2.0	recoil	6.48	-0.72	1.4

Pressure	Strain E_y Proximal [%]			Pressure	Strain E_x Proximal [%]		
[atm]	MAX	MIN	STD	[atm]	MAX	MIN	STD
2.4	2.87	-3.09	0. 7	2.4	0.90	-1.94	0.7
6.6	17.16	-4.25	2.9	6.6	4.09	-5.41	1.7
9.0	30.95	4.16	2.8	9.0	11.35	-6.74	3.0
recoil	8.06	-3.74	3.0	recoil	10.35	-3.88	2.0

Initial contact between the stent and the analogue at the distal end (inflation pressure 2.4 atm) caused abrupt increase in the local strain, which was approximately three times greater than the strain at the proximal end and four times greater than strain in the central part (*Table 31*). Significant variation in local strain occurred on the vessel wall surface at the last stage of the dog-boning phase (6.6 atm), when the stent struts significantly deformed the vessel analogue at the proximal and distal ends. At this stage the maximum positive strain E_y was 7% greater at the proximal than distal part. The same behaviour occurred for the fully deployed stent, *Table 31*. Following balloon deflation (0 atm), the maximum strain decreased by approximately a factor of two (E_x and E_y) in the central part and factor of three E_y in distal and proximal parts.

Figure 6-39a, Figure 6-40a and Figure 6-41a illustrate the E_x and E_y strain data on a 3D contour plot of the reconstructed deformed geometry of the vessel analogue in the distal, proximal and central regions of interest at a single deformation stage. For distal and proximal part the maximum dog-boning phase (6.6 atm) is plotted with the strain variation from -6% to 15%. However, for the central part strain data from elastic recoil is presented to express local strain variation on the vessel wall after the balloon is removed.

Figure 6-39b, Figure 6-40b and *Figure 6-41b* show the E_x and E_y strain data plotted for a single circumferential line in the *y* direction (presented with black markers plotted on the 3D plots) to express strain variation around the circumference at this location at specific balloon inflation pressures. The maximum strain error (0.9% for the 0.07 mm node separation used to compute the strain values) computed during the zero strain test is shown using error bars for each strain component.
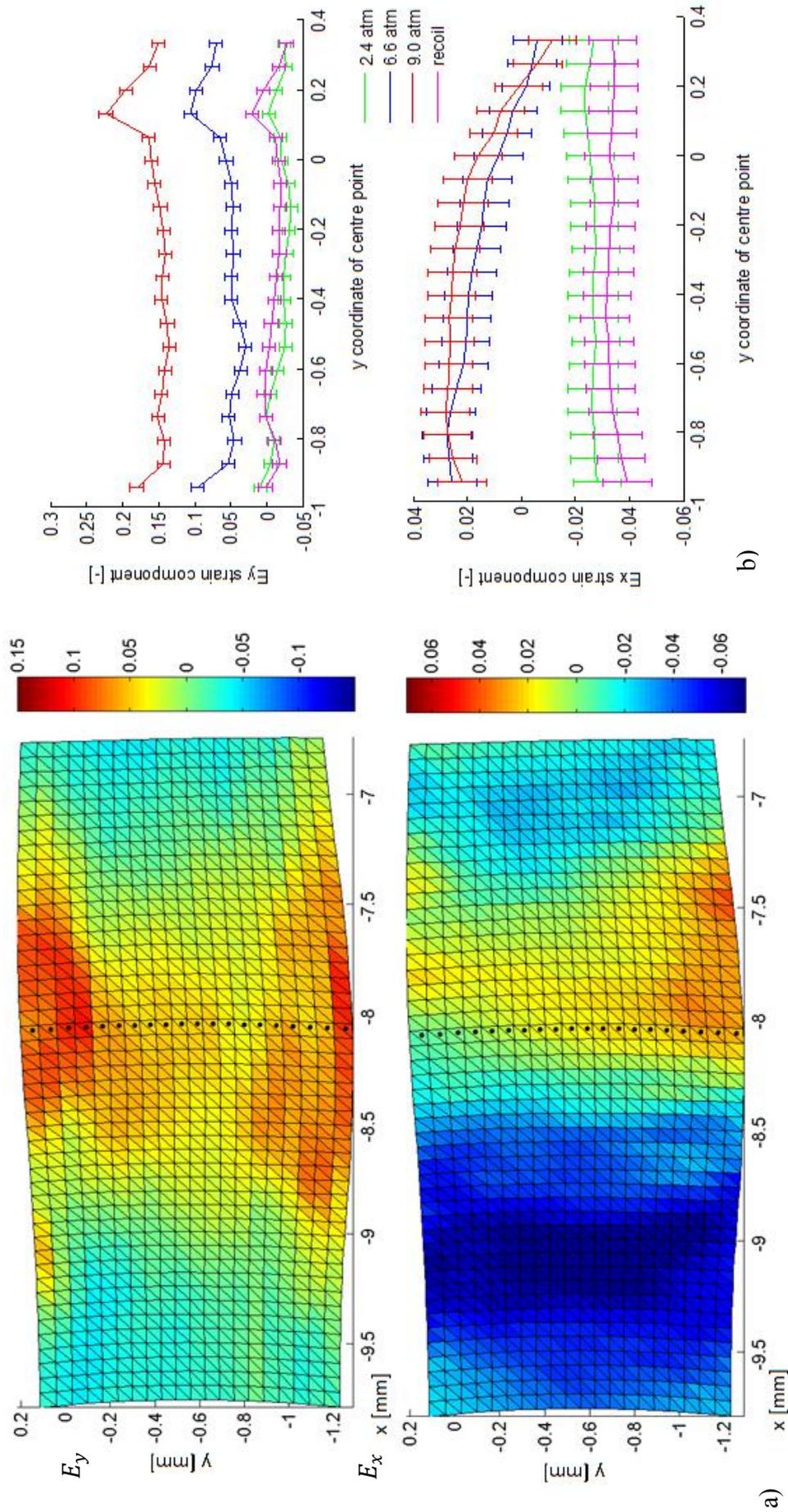
Figure 6-39: Variation of local Ex and Ey strain in the distal region of interest. a) Contour plots of Ex and Ey at balloon inflation pressure of 6.6 atm (maximum bog-boning). b) Line plots at the points shown with black markers in (a) at three balloon inflation pressures 2.4, 6.6, 9.0 atm and following elastic recoil, the error bars show the maximum error [-]computed during zero strain tests at this node separation of 0.086 mm.
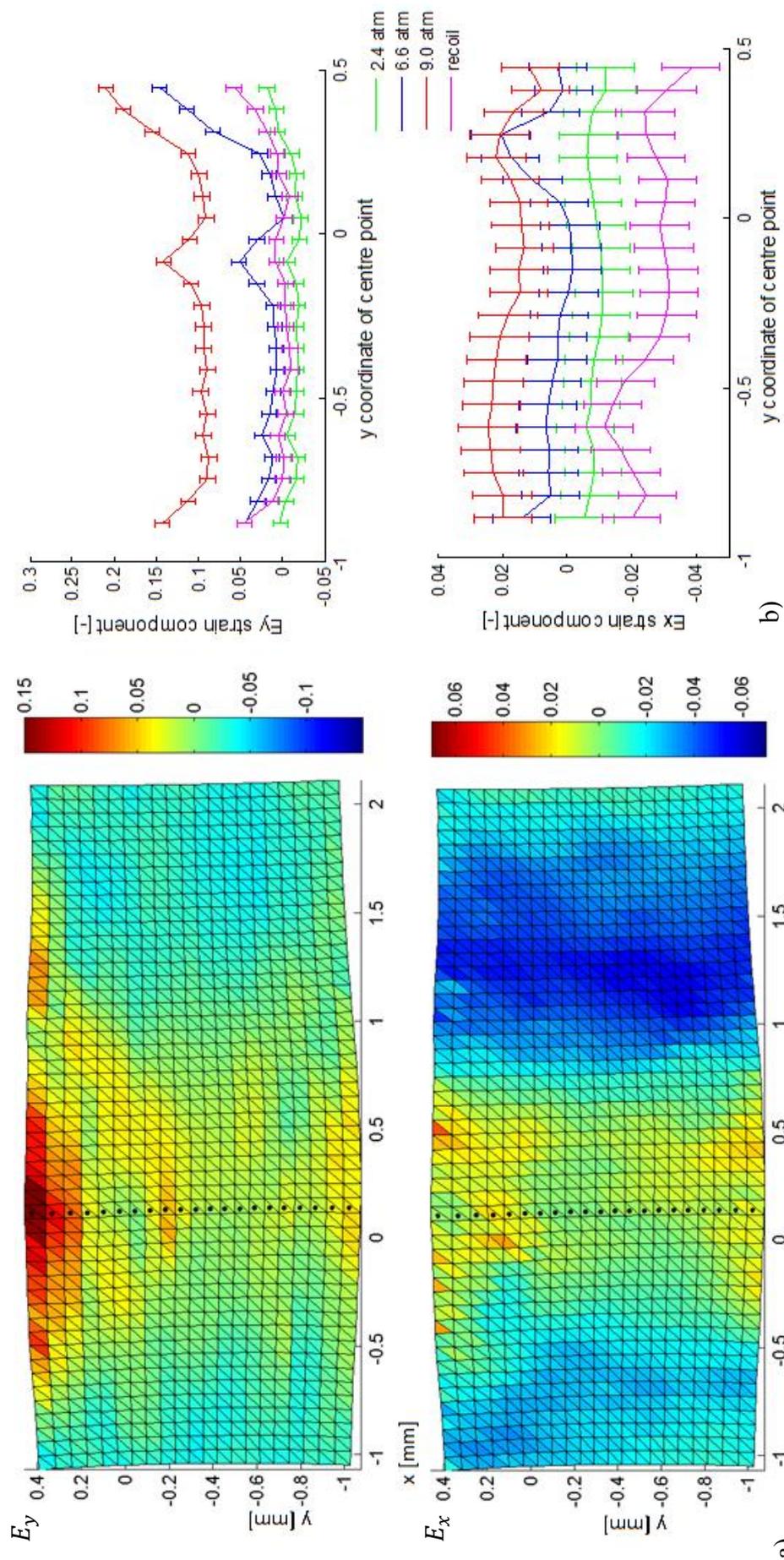
Figure 6-40: Variation of local Ex and Ey strain in the proximal region of interest. a) Contour plots of Ex and Ey at balloon inflation pressure of 6.6 atm (maximum bog-boning). b) Line plots at the points shown with black markers in (a) at three balloon inflation pressures 2.4, 6.6, 9.0 atm and following elastic recoil, the error bars show the maximum error [-]computed during zero strain tests at this node separation of 0.086 mm.
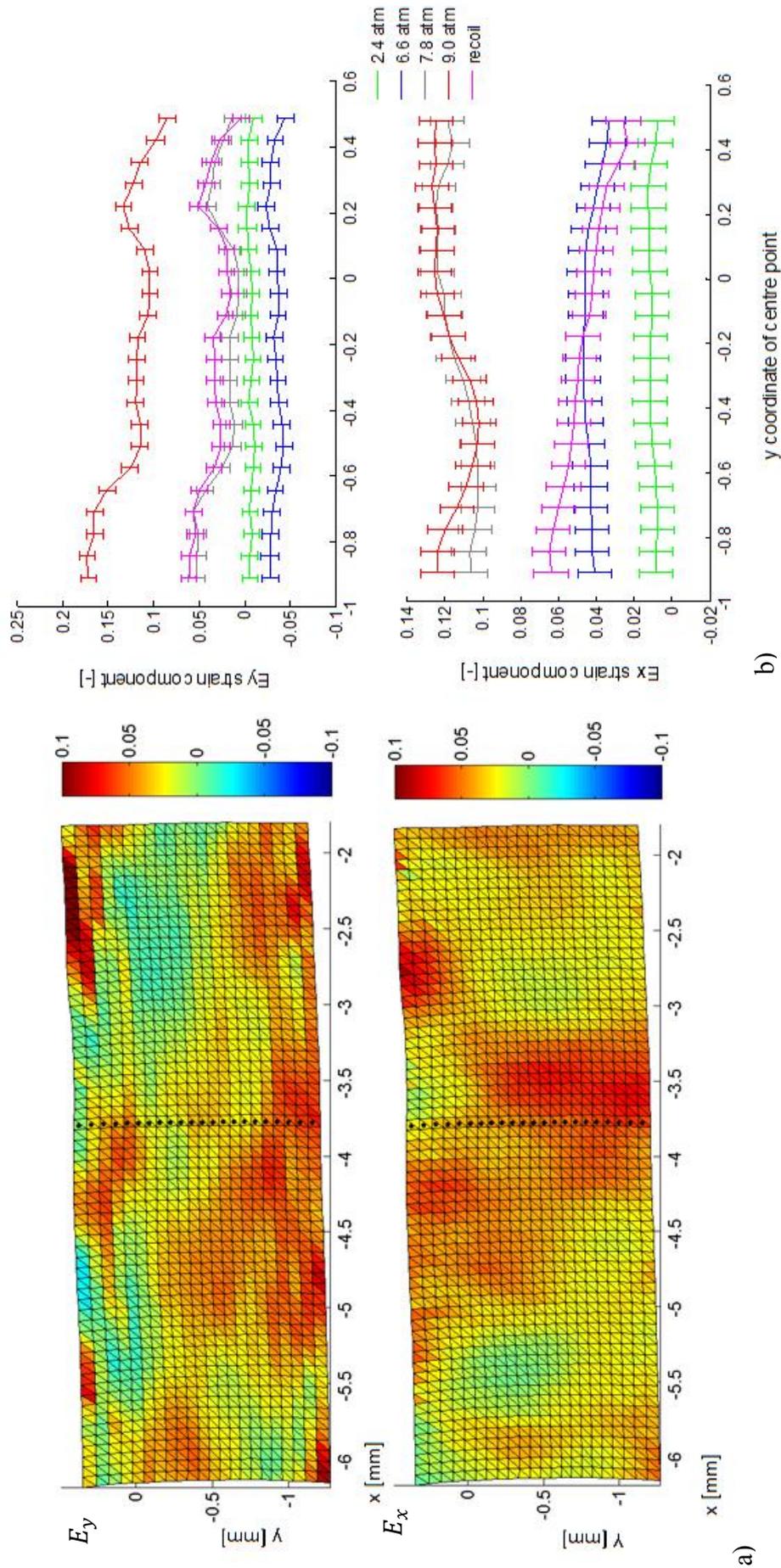
Figure 6-41: Variation of local Ex and Ey strain in the central region of interest. a) Contour plots of Ex and Ey at balloon deflation (stent recoil) b) Line plots at the points shown with black markers in (a) at four balloon inflation pressures 2.4, 6.6, 7.8 , 9.0 atm and following elastic recoil, the error bars show the maximum error [-] computed during zero strain tests at this node separation of 0.082 mm.

6.5.2.2. DISCUSSION

Section 6.5.2 describes two experimental tests to compute non-zero strain on 3D deformed surfaces: a tensile test of an elastic planar material and vessel analogue deformation due to stent deployment. For both experiments the accuracy of camera calibration was determined using reconstruction accuracy assessment, which demonstrated uncertainty in 3D position of the order 15 μm.

As expected for the tensile test output, the strains in the longitudinal, *x*, direction were positive and in the transverse, *y*, direction were negative, due to the inherent Poisson's ratio properties as shown qualitatively in *Figure 6-34* and quantitatively in *Figure 6-35* and *Table 30*.

The tensile test of the elastic material resulted in low strain variation (the maximum variation of 3.7% was found at sixth tensile step) at each deformation stage as illustrated along the central line in the *y* direction for E_x and E_y strain plotted at three steps of deformation (*Figure 6-35*) and in *Table 30*. Due to the homogeneity of the elastic material and constant uniform deformation applied across the chosen region of interest this small variation in longitudinal strain is reasonable.

A maximum standard deviation of the order 0.55 % was calculated from all localised strain outputs. Note that the variations in strain are of similar order as the maximum plotted error. It is therefore suggested that there is little variation in strain across the strip. The variations in strain may be due to uncertainty in measurement, rather than a "real" variation. Moreover, the uncertainty is less than the changes in strain between each deformation. It is important to point out that there is good agreement in terms of the average strain between the local strain and manual measurements. The correlation

coefficient of 0.9925 (y = 0.9851x + 0.1283) between manual and VIC-2D Green-Lagrange strain data confirmed this. The maximum strain error decreased from 2% to 0.2% (for 2 mm node spacing, *Table 27*) when compared to the tensile test strain results reported in Chapter 2, Section 2.4 (large length scale). In these experiments the use of image registration methods allows investigation of hundreds of nodes for local strain calculation and deformation is automatically tracked at each deformation step. This approach would be impractical using manual methods. Using the automated tracking method 1392 strains can be computed in the same time as it takes to acquire two manual strain measures, for each deformation steps. Moreover, the relative accuracy between a manual and automatic approach differs. 1392 local strain values measured manually would be poor quality, as there is likely to be a random error associated with operator's judgement. The evidence for this is presented in Chapter 4 where the reproducibility associated with manual picking introducing a significant error (sensitivity test) on the results is reported.

The limitation of this experiment was that the strain applied to the elastic sheet has been not well controlled while the tensile test was performed as the deformation applied during rotation of the rod was not directly measured. Whilst this experiment could be refined by measuring the angle of the rotation of the rod at each stretching step to compute the global strain for comparison with the derived data, the manual measurement over the region of interest provides a measure of the overall strain of the sample.

Results obtained from the confined deployment of a coronary stent within a vessel analogue confirmed the general behaviour presented in Chapter 5 for an unconstrained

stent. First the distal and proximal ends of the stent came into contact with the analogue (dog-boning phase) while the central region of the stent remained unexpanded. From the circumferential strain results (*Figure 6-37*) the dog-boning effect is most obvious at inflation pressures of 5.4 atm and 6.6 atm, but the edges of the stent were already observed to be in the contact with the analogue at a pressure load of 2.4 atm, which is confirmed by the data presented in *Figure 6-38* and *Table 31*.

The dog-boning of the stent temporarily stretched the analogue circumferentially and resulted in high local strain variation (from -4.25% to approximately 17% strain in the proximal area). Moreover, local strains increased significantly, *Table 31*, due to maximum inflation of the angioplasty balloon (9.0 atm) and decreased notably after balloon deflation. Stent recoil occurred when the pressure was decreased to 0 atm and the balloon was withdrawn from the analogue, reducing analogue strain significantly (*Figure 6-39b, Figure 6-40b, Figure 6-41a* and *b* and *Table 31*). In the proximal part maximum local E_y strain decreased from 30.9% for the fully inflated angioplasty balloon stage (9.0 atm) to 8.1% following balloon deflation.

Higher strain values are reported for the estimated global circumferential strain measure than for the local strain. This result may be related to the assumption that the vessel analogue is circular at each stage of deformation. Such estimates of global strain provide an indication of overall stent behaviour at each applied pressure load from 2D images alone, but this study confirms that full 3D reconstruction of the region of interest on the vessel surface is required to provide detailed information of the local strain distribution during contact with deploying stent struts. This knowledge is crucial

to understand strain-related vessel wall injury and possible correlations with the magnitude of neointimal tissue growth.

VIC-2D combined with 3D reconstruction methods has provided encouraging results (maximum error <1% for a 0.07 mm node spacing) of the local strain distribution on the analogue surface following stent implantation. *Figure 6-42* demonstrates the relationship between the strut geometry and the regions of high and low strains around the circumference. This behaviour was also presented in the *in silico* study of Zahedmanesh [77], where high stress occurred in the area of interaction of the stent strut with the vessel wall.
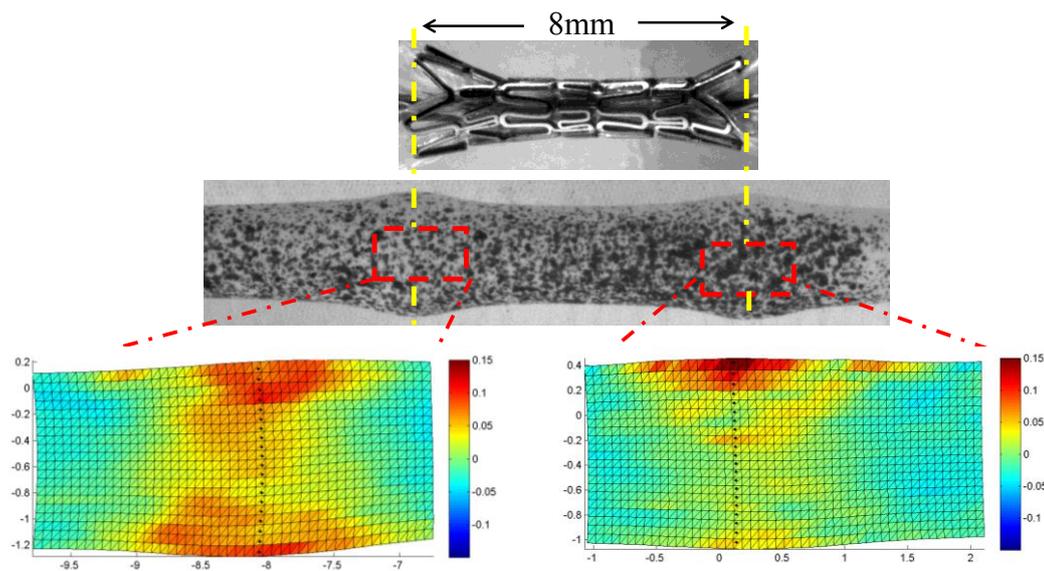
Figure 6-42: *High strains at the proximal and distal stent ends due to the dog-boning of the stent and asymmetrical struts deployment (results shown at balloon pressure 6.6 atm)*

It can be suggested that localised high strains on the vessel wall surface are due to assymetrical stent strut separation as it has been presented in Chapter 5. The magnitudes of strain variation around the circumference E_y for the maximum stent deployment (pressure load of 9 atm) alter significantly: from -3.85% to 22.3% for the

distal part and 4.16% to 30.95% for proximal part with standard deviations of 6% and 2% respectively. These differences are due to strain measured in the stented and unstented sections. Analysis of these results can be used to suggest the likely distribution of strain-related vessel wall injury caused by the stent deployment and its interaction with the vessel.

Asymmetrical behaviour of each stent unit can be determined using this experimental approach. Describing such behaviour in numerical models presents a challenge. The strain and stress on the internal surface of the artery has been studied numerically by many researchers [1, 46, 52, 71, 77] to understand the relation between arterial injury caused by the stent on the vessel wall and in-stent restenosis. Numerical models are often used to characterise stent expansion, with applications including stent interaction with a stenosed artery [155], stress/strain distributions throughout the thickness of the vessel and stent flexibility in curved vessels [74]. Detailed study of such problems can be difficult to achieve with clinical or experimental studies. Furthermore, the computational model can be used to investigate the wall shear stress, the impact on the haemodynamic environment due to stent and vessel wall deformation [156], which is not possible with optical experimental techniques. However, in many *in silico* studies the nature of the stent expansion is often idealised (using a uniform pressure to simulate balloon expansion) and often does not take into account the complex interaction between the stent and the balloon. The results of computational simulations which quantify strain on the arterial wall needs to be validated against experimental work. Experimental tests provide data on the possible variations in strain that can arise during practical expansion of stent/balloon systems. A combined numerical and experimental approach could provide optimum information about the stent/artery

interaction, resulting in the development of new stent designs to minimise vessel wall injury.

The results of this study confirmed the results obtained with porcine [2, 70] and sheep [59] models as well as with the clinical findings [157], where the greatest amount of neointimal tissue growth occurred at the proximal and distal regions. These studies confirmed the relation between stent asymmetry, vascular injury and restenosis.

Two recent publications have focused on the experimental measurement of deformation of human arteries [90] and a vessel analogue [91] following stent deployment *in vitro*, to evaluate the strain on the artery wall surface. In a preliminary study Horny *et al*. [90] applied digital image correlation (DIC) to provide information about stent/vessel interaction in the presence of atherosclerosis in a human coronary artery harvested during autopsy. The reporting of the results focussed only on a few specific locations. Moreover, Zhao [91] quantified strain on the stented latex straight tube using 3D DIC and developed computational model to recapture stenting experiment. However, the diameter and thickness of analogue investigated in this study was two times larger (6.32 mm) and five times thicker (1.55) than the typical dimensions of the coronary artery. The quantification of the strain field on the artery [90] and analogue [91] reported in these studies did not focus on local regions of stent strut deformation.

An advantage of the current study is the possibility to compare data from the local and global measures of strain distribution on the surface of the analogue with local and global measures of unconstrained stent deformation reported in Chapter 5, as shown in *Figure 6-42*. Moreover, the accuracy of the method developed in this thesis has

been assessed and validated using both micro-CT volumetric scanning (Chapter 4) and rigid body motion zero strain test. This study is the first demonstration of measurement of stent geometry using both micro-CT and optical reconstruction methods at the coronary stent length scale.

SUMMARY

Experimental data characterising the local strains on the vessel wall following stent implantation is scant. In this work considerable effort was made to check the accuracy (98%) of the stereo-photogrammetric optical method (Chapter 4) and image registration (99%) with rigid body motion tests (Chapter 6). The main calibration and reconstruction accuracy carried throughout all experimental work was of an order of 12 μm and mean repeatability error associated with manual identification of strut landmark points was of an order of 16 μm.

Stereo photogrammetry combined with image registration provided strain measurement, which allows tracking of large deformations in a non-invasive way. The VIC-2D image correlation software was used to process the images of elastic material and vessel analogue deformation obtained with high resolution Flea2 fire-wire cameras to resolve 3D strains, with focus on the interaction of the stent with a vessel analogue. The surface strain was captured at every stage of deformation to understand the local response of the analogue due to contact with the stent. A high contrast random pattern was applied to the analogue surface to track the deformation. It should be noted that Stretchi paint (Propbuilder, UK) was applied, before a black enamel spray (Plasti-kote, USA), to increase the speckle pattern contrast and reduce reflections from the surface of the analogue.

Two recent studies have investigated deformation of human arteries [90] and vessel analogues [91] *in vitro*, to evaluate the deformation after stent deployment. However, only Zhao *et al*. [91] reports strain accuracy (0.155% uncertainty in strain measurement), with no information on the spatial resolution for which this accuracy is obtained. In the current study, considerable effort was undertaken to ensure that uncertainty of the applied methods was acceptable. It was found that the error depends on the spatial resolution, for node spacing greater than 0.07 mm (0.015 mm smaller than that used in the stent test) the maximum error in measurement of strain was < 1%, allowing useful measurement of local strain with adequate accuracy.

In addition, these previous studies do not focus on the local contact of stent struts with the artery. An advantage of this study is the potential for examination of local strain distribution on the vessel wall which confirms the expected deformation of the vessel analogue based on the analysis of local stent deformation during unconstrained deployment, reported in Chapter 5.

This thesis describes a non-invasive optical technique applied to examine large deformations on the surface of a vessel analogue at sufficient depth of field (Chapter 3) for the investigated length scale. High spatial resolution was obtained (10-12 μm) due to the high magnification of the optical design. The deployment of a balloon expandable stent in a vessel analogue made of silicone was captured with two Flea2 high resolution cameras with the same method as free stent expansion (Chapter 5). The surface displacement was obtained using VIC-2D and 3D output was computed with the stereo-photogrammetry method. This approach allowed information to be

gathered along the full length of a small scale vessel analogue (15 mm) over 1/3th (120°) of its circumference.

The interpretation of these results in the context of evidence from *in vivo* studies of stent deployment provides a significant advance towards improvement of stent design through better understanding of strain-related vascular injury and the link with in-stent restenosis. Recommendations for further development of these techniques are provided in Chapter 7.

CHAPTER 7

CONCLUSION & FUTURE WORK

This chapter presents the final conclusions of the thesis and suggestions for future work. Research conducted during the PhD was an experimental work carried out during the MeDDiCA Marie Curie Initial Training Network project. Most of the output data were three dimensional (3D).

To the author's knowledge detailed quantitative measures of local stent geometry at the coronary artery length scale *in vitro* was carried for the first time; the same applies to detailed accuracy assessment of imaging modalities.

CONCLUSION

Deformations in biological soft tissue samples cannot be measured with contact methods such as strain gauges, since the attachment of the strain gauge itself will change the mechanical properties of the tissue and it will determine the strain only in localised area. Thus, optical methods are gaining popularity in biomedical science for deformation measurement (of bones, tendons, cartilage, skin and vessels *ex vivo*). Accurate quantification of the deformations taking place within these tissues may improve understanding of disease progression.

Stents are a good example of an application where measuring strain on the vessel wall following implantation would undoubtedly prove useful. Although research on stent behaviour during deployment has been undertaken experimentally for many years, a complete understanding of stent/vessel wall interaction in 3D is yet to be obtained. Optical methods are capable of producing full-field displacement, strain maps and can be used to validate the models of *in silico* studies.

This study employed 3D optical stereo-photogrammetry with image registration. An optical system to characterise stent deployment symmetry *in vitro* was developed using a stereo pair of high resolution fire-wire cameras.

A major part of this PhD was validation and error assessment of each investigated method. Camera calibration and reconstruction accuracy were assessed using different size grids and the testing of control objects to check calibration error prior to each performed test. Imaging at the coronary artery length scale involved design and testing of an optical system to obtain high magnification whilst maintaining sufficient depth

of field. Measurement of local coronary stent geometry was validated with volumetric micro-CT. Zero strain tests of different complexities were applied to check accuracy of image registration method prior to application for strain measurement. Results have shown that high accuracy (to within 12 μm of volumetric micro-CT) can be achieved during reconstruction of 3D stent geometry. Moreover, the strain error was always less than 1%, even for small distances between nodes such as 0.07 mm.

It has been shown that the extent of strain and stress imparted on the vessel wall during stent deployment is related to the level of the injury [7, 46]. Stent implantation imposes high strains on local regions of the arterial wall resulting in a higher degree of neointimal tissue growth [2]. Greater amounts of restenosis have been observed to occur at the proximal and distal regions of the stent during clinical studies [57], suggested to be related to the dog-boning effect during non-uniform stent expansion. Asymmetric stent strut deployment, examined in the current study, resulting in excessive local strains on the vessel surface may increase the risk of vascular injury leading to higher restenosis rates.

An advantage of carrying out the research for this PhD in the Medical Physics Group, Department of Cardiovascular Science was an opportunity to gain a good understanding of the in-stent restenosis problem due to collaboration with clinicians. Experience in solid mechanics and expertise of optical system design at the coronary artery length scale led to investigation of the detail of free expansion of local stent geometry in 3D (Chapter 5), and the response of the vessel analogue to stent deployment, resulting in a non-uniform strain distribution (Chapter 6).

FUTURE WORK

Opportunities for future work consist of a number of stages which include both the technical development of the experimental methods and the application of these techniques to the study of the interactions between stents and porcine coronary arteries.

A subsequent study would benefit from automated camera calibration. Automation of the calibration method will reduce errors obtained during the manual process (achieving uncertainty lower than 10-15 μm) and reducing its time (less than 10-15 min in total). The Bouguet Calibration Toolbox is currently used to calibrate cameras [115]; further integration of calibration with camera control software is possible through use of the OpenCV software libraries [111].

Due to bandwidth limitations and technical issues with dynamic synchronisation of the stereo camera pair, it was not possible to undertake high resolution imaging of stent expansion at 30fps with the current stereo rig. In this study the stent was expanded gradually and images with stereo camera rig were taken. Two fire-wire cameras were used on the same bus, but they were not fully synchronised. Synchronisation of the cameras allows assessment of full dynamic vessel wall behaviour due to loading as demonstrated using a single camera in the 2D test described in Chapter 5. Additional improvement of the code used to capture images needs to take place to run two (or more) cameras at the same time. Synchronisation allows stent expansion to be imaged in real time, as performed by clinicians. 3D data of the dynamic stent deployment would deliver detailed understanding of the influence of rate of balloon inflation on the extent of arterial strains during stent deployment. More than two, stereoscopically positioned cameras could be used to record the deformation process due to stent

deployment, as described by Narracott [88] to examine the full circumference of the vessel.

Image registration with VIC-2D results in good strain accuracy (max error < 1%) and is adequate to determine vessel analogue deformation following stent expansion as illustrated in Chapter 6. Moreover, a proper marking method for analogues was established. The deformation, and associated strain fields of *ex vivo* pig coronary arteries following stent expansion and additionally vessel analogues constructed from inhomogeneous material would determine the effects of vessel material properties on the strain distribution and stent deployment characteristics. To mimic atherosclerosis, local thickening and/or stiffening of the wall could be included. This type of complex 3D study of stent deployment would provide appropriate data to validate existing computational models and direct future model development.

The design of the optical system provided in Chapter 3, allows the technique to be used over a range of length scales, this provides the opportunity for imaging of the whole heart *ex vivo* to examine changes in vessel geometry, as described during marker evaluation in Chapter 6.

FINAL THOUGHTS

There is a great interest in improving stent design. Engineering approaches for the characterisation of the vessel wall strain caused by stents will play a role in the improved design of these implants and techniques for their deployment. Better understanding of how stent design relates to vessel wall injury and the resulting neointimal hyperplasia which causes in-stent restenosis will contribute to reduction of restenosis rates, improving patient care and quality of life. In the future this type of study will impact the economy through reduced treatment costs.

The *in vitro* 3D optical reconstruction method described in this thesis can be applied to detailed assessment of medical devices performance (over a range of length scales due to the defined protocol for lens design). In addition, the resulting data obtained from the experimental assessment of such devices has further application to provide boundary conditions or validation data for *in silico* studies.

REFERENCES

1. Gijsen, F.J., et al., *Simulation of stent deployment in a realistic human coronary artery*. Biomed Eng Online, 2008. 7: p. 23.

2. Timmins L. H, et al., *Increased artery wall stress post-stenting leads to greater intimal thickening*. Laboratory Investigation, 2011. 91(6): p. 955-967.

3. Wu, W., et al., *Stent expansion in curved vessel and their interactions: a finite element analysis*. J Biomech, 2007. 40(11): p. 2580-5.

4. Mori, F., et al., *3D Observation of Expansion of Stent and Elastic Recoil using Micro-CT*. World Congress on Medical Physics and Biomedical Engineering, Vol 25, Pt 6, 2009. 25: p. 235-238.

5. Alp, N.J., A.A. Ziad, and K.M. Channon, *Models for studying coronary artery stenting* Drug Discovery Today: Disease Models, 2006. Volume 3(Issue 3): p. 297-303

6. Perk, J., et al., *European Guidelines on cardiovascular disease prevention in clinical practice (version 2012)*. European Heart Journal, 2012. 33(13): p. 1635-U130.

7. Duraiswamy, N., et al., *Stented artery flow patterns and their effects on the artery wall*. Annual Review of Fluid Mechanics, 2007. 39: p. 357-382.

8. Schomig, A., et al., *A meta-analysis of 17 randomized trials of a percutaneous coronary intervention-based strategy in patients with stable coronary artery disease*. J Am Coll Cardiol, 2008. 52(11): p. 894-904.

9. Sechtem, U., et al., *2013 ESC guidelines on the management of stable coronary artery disease*. European Heart Journal, 2013. 34(38): p. 2949-+.

10. De Beule, M., et al., *Realistic finite element-based stent design: the impact of balloon folding*. Journal of Biomechanics, 2008. 41(2): p. 383-9.

11. Levick, J.R., *An Introduction to Cardiovascular Physiology*, ed. f. edition. 2003.

12. Wagenseil, J.E. and R.P. Mecham, *Vascular Extracellular Matrix and Arterial Mechanics*. Physiological Reviews, 2009. 89(3): p. 957-989.

13. Vito, R.P. and S.A. Dixon, *Blood vessel constitutive models-1995-2002*. Annual Review of Biomedical Engineering, 2003. 5: p. 413-439.

14. Lusis, A.J., *Atherosclerosis*. Nature, 2000. 407(6801): p. 233-241.

15. Evans, D.J.W., et al., *The application of multiscale modelling to the process of development and prevention of stenosis in a stented coronary artery*. Philosophical Transactions of the Royal Society a-Mathematical Physical and Engineering Sciences, 2008. 366(1879): p. 3343-3360.

16. Wang, J.H.C. and B.P. Thampatty, *An introductory review of cell mechanobiology*. Biomechanics and Modeling in Mechanobiology, 2006. 5(1): p. 1-16.

17. Canfield, T.R. and P.B. Dobrin, *Mechanics of Blood Vessels*. The Biomedical Engineering Handbook, ed. J.D. Bronzino. 1999.

18. Lehoux, S. and A. Tedgui, *Cellular mechanics and gene expression in blood vessels*. Journal of Biomechanics, 2003. 36(5): p. 631-643.

19. Prado, C.M., S.G. Ramos, and M.A. Rossi, *Turbulent Blood Flow Plays an Essential Localizing Role in the Development of Atherosclerotic Plaques in Experimentally-Induced Hypercholesterolemia in Rats*. Atherosclerosis Supplements, 2008. 9(1): p. 217-217.

20. Libby, P., M. DiCarli, and R. Weissleder, *The Vascular Biology of Atherosclerosis and Imaging Targets*. Journal of Nuclear Medicine, 2010. 51: p. 33s-37s.

21. Plutzky, J., *The vascular biology of atherosclerosis*. American Journal of Medicine, 2003. 115: p. 55-61.

22. Barakat, A.I. and D.K. Lieu, *Differential responsiveness of vascular endothelial cells to different types of fluid mechanical shear stress*. Cell Biochemistry and Biophysics, 2003. 38(3): p. 323-343.

23. Debakey, M.E., G.M. Lawrie, and D.H. Glaeser, *Patterns of Atherosclerosis and Their Surgical Significance*. Annals of Surgery, 1985. 201(2): p. 115-131.

24. Shaaban, A.M. and A.J. Duerinckx, *Wall shear stress and early atherosclerosis: A review*. American Journal of Roentgenology, 2000. 174(6): p. 1657-1665.

25. Falk, E., P.K. Shah, and V. Fuster, *Coronary Plaque Disruption*. Circulation, 1995. 92(3): p. 657-671.

26. Penz, S., et al., *Human atheromatous plaques stimulate thrombus formation by activating platelet glycoprotein VI*. Faseb Journal, 2005. 19(8): p. 898-909.

27. Zaman, A.G., et al., *The role of plaque rupture and thrombosis in coronary artery disease*. Atherosclerosis, 2000. 149(2): p. 251-66.

28. Kiousis, D.E., T.C. Gasser, and G.A. Holzapfel, *A numerical model to study the interaction of vascular stents with human atherosclerotic lesions*. Ann Biomed Eng, 2007. 35(11): p. 1857-69.

29. Garcia-Moll, X., et al., *Serum neopterin and complex stenosis morphology in patients with unstable angina*. Journal of the American College of Cardiology, 2000. 35(4): p. 956-962.

30. Michaels, A.D. and K. Chatterjee, *Angioplasty versus bypass surgery for coronary artery disease*. Circulation, 2002. 106(23): p. E187-E190.

31. Athanasiou, T., et al., *Radial artery versus saphenous vein conduits for coronary artery bypass surgery: forty years of competition - which conduit offers better patency? A systematic review and meta-analysis*. European Journal of Cardio-Thoracic Surgery, 2011. 40(1): p. 208-220.

32. Rihal, C.S., et al., *Indications for coronary artery bypass surgery and percutaneous coronary intervention in chronic stable angina - Review of the evidence and methodological considerations*. Circulation, 2003. 108(20): p. 2439-2445.

33. Hall, R.J., et al., *Percutaneous Trans-Luminal Coronary Angioplasty Update*. Texas Heart Institute Journal, 1984. 11(1): p. 10-16.

34. http://www.vascular.co.nz.

35. Dangas, G. and F. Kuepper, *Cardiology patient page. Restenosis: repeat narrowing of a coronary artery: prevention and treatment*. Circulation, 2002. 105(22): p. 2586-7.

36. Lange, R.A., E.D. Flores, and L.D. Hillis, *Restenosis after Coronary Balloon Angioplasty*. Annual Review of Medicine, 1991. 42: p. 127-132.

37. Nakatani, M., et al., *Mechanisms of restenosis after coronary intervention: difference between plain old balloon angioplasty and stenting*. Cardiovasc Pathol, 2003. 12(1): p. 40-8.

38. Mintz, G.S., et al., *Arterial remodeling after coronary angioplasty - A serial intravascular ultrasound study*. Circulation, 1996. 94(1): p. 35-43.

39. Post, M.J., et al., *Arterial remodeling after balloon angioplasty or stenting in an atherosclerotic experimental model*. Circulation, 1997. 96(3): p. 996-1003.

40. Kakuta, T., et al., *Differences in Compensatory Vessel Enlargement, Not Intimal Formation, Account for Restenosis after Angioplasty in the Hypercholesterolemic Rabbit Model*. Circulation, 1994. 89(6): p. 2809-2815.

41. Levine, G.N., et al., *2011 ACCF/AHA/SCAI Guideline for Percutaneous Coronary Intervention A Report of the American College of Cardiology Foundation/American Heart Association Task Force on Practice Guidelines and the Society for Cardiovascular Angiography and Interventions*. Circulation, 2011. 124(23): p. E574-E651.

42. *http://www.bccresearch.com/market-research/healthcare/coronary-stent-devices-global-market-hlc111a.html*.

43. Atherton, M.A. and R.A. Bates, *Robust optimization of cardiovascular stents: A comparison of methods*. Engineering Optimization, 2004. 36(2): p. 207-217.

44. Palmaz, J.C., et al., *Expandable Intraluminal Graft - a Preliminary-Study - Work in Progress*. Radiology, 1985. 156(1): p. 73-77.

45. Lau, K.W., et al., *A stent is not just a stent: Stent construction and design do matter in its clinical performance*. Singapore Med J, 2004. 45(7): p. 305-11; quiz 312.

46.	Gu, L.X., et al., *The Relation Between the Arterial Stress and Restenosis Rate After Coronary Stenting*. Journal of Medical Devices-Transactions of the Asme, 2010. 4(3): p. -.

47.	Marx, S.O., H. Totary-Jain, and A.R. Marks, *Vascular smooth muscle cell proliferation in restenosis*. Circ Cardiovasc Interv. 4(1): p. 104-11.

48.	Migliavacca, F., et al., *Stainless and shape memory alloy coronary stents: a computational study on the interaction with the vascular wall*. Biomech Model Mechanobiol, 2004. 2(4): p. 205-17.

49.	Butany, J., et al., *Coronary artery stents: identification and evaluation*. J Clin Pathol, 2005. 58(8): p. 795-804.

50.	Lau, K.W., et al., *Clinical impact of stent construction and design in percutaneous coronary intervention*. American Heart Journal, 2004. 147(5): p. 764-773.

51.	Levesque, J., et al., *Materials and properties for coronary stents*. Advanced Materials & Processes, 2004. 162(9): p. 45-48.

52.	Zahedmanesh, H. and C. Lally, *Determination of the influence of stent strut thickness using the finite element method: implications for vascular injury and in-stent restenosis*. Medical & Biological Engineering & Computing, 2009. 47(4): p. 385-393.

53.	Grech, E.D., *ABC of interventional cardiology - Percutaneous coronary intervention. II: The procedure*. British Medical Journal, 2003. 326(7399): p. 1137-1140.

54.	Edelman, E.R. and C. Rogers, *Pathobiologic responses to stenting*. American Journal of Cardiology, 1998. 81(7A): p. 4E-6E.

55.	Farb, A., et al., *Pathology of acute and chronic coronary stenting in humans*. Circulation, 1999. 99(1): p. 44-52.

56.	L. H Timmins, et al., *Increased artery wall stress post-stenting leads to greater intimal thickening*. Laboratory Investigation, 2011. 91(6): p. 955-967.

57.	Kastrati, A., et al., *Restenosis after coronary placement of various stent types*. Am J Cardiol, 2001. 87(1): p. 34-9.

58. Castellanos, E. and J. Almendral, *Acute Right Coronary artery Occlusion During Cooled-Tip Radiofrequency Ablation of the Cavotricuspid Isthmus*. Indian Pacing Electrophysiol J. 13(2): p. 76-9.

59. Schulz, C., et al., *Coronary stent symmetry and vascular injury determine experimental restenosis*. Heart, 2000. 83(4): p. 462-7.

60. Harnek, J., et al., *Differences in endothelial injury after balloon angioplasty, insertion of balloon-expanded stents or release of self-expanding stents: An electron microscopic experimental study*. Cardiovascular and Interventional Radiology, 1999. 22(1): p. 56-61.

61. Otsuka, F., et al., *The importance of the endothelium in atherothrombosis and coronary stenting*. Nature Reviews Cardiology, 2012. 9(8): p. 439-453.

62. Bennett, M.R., *In-stent stenosis: pathology and implications for the development of drug eluting stents*. Heart, 2003. 89(2): p. 218-224.

63. Sullivan, T.M., et al., *Effect of endovascular stent strut geometry on vascular injury, myointimal hyperplasia, and restenosis*. Journal of Vascular Surgery, 2002. 36(1): p. 143-149.

64. Hoffmann, R., et al., *Patterns and mechanisms of in-stent restenosis. A serial intravascular ultrasound study*. Circulation, 1996. 94(6): p. 1247-54.

65. Zwierzak, I., J.W. Fenner, and A.J. Narracott, *3D Optical Reconstruction Technique for Balloon Expandable Stent Characterisation*, in *The 10th International Symposium on Biomechanics and Biomedical Engineering (CMBBE2012)*. 2012: Berlin, Germany.

66. Moore, J.E., *Biomechanical Issues in Endovascular Device Design*. Journal of Endovascular Therapy, 2009. 16: p. 1-11.

67. Ito, S., et al., *Intracoronary Imaging and Histopathology of Late Phase In-Stent Restenosis after Coronary Stent Implantation*. ISRN Vascular Medicine, 2012.

68. Park, S.J., et al., *In-Stent Neoatherosclerosis A Final Common Pathway of Late Stent Failure*. Journal of the American College of Cardiology, 2012. 59(23): p. 2051-2057.

69. Kastrati, A., et al., *Time course of restenosis during the first year after emergency coronary stenting*. Circulation, 1993. 87(5): p. 1498-505.

70. Gunn, J., et al., *Coronary artery stretch versus deep injury in the development of in-stent neointima*. Heart, 2002. 88(4): p. 401-405.

71. Lally, C., F. Dolan, and P.J. Prendergast, *Cardiovascular stent design and vessel stresses: a finite element analysis*. J Biomech, 2005. 38(8): p. 1574-81.

72. Wang, W.Q., et al., *Analysis of the transient expansion behavior and design optimization of coronary stents by finite element method*. Journal of Biomechanics, 2006. 39(1): p. 21-32.

73. Takashima, K., et al., *Simulation and experimental observation of contact conditions between stents and artery models*. Med Eng Phys, 2007. 29(3): p. 326-35.

74. Petrini, L., et al., *Numerical investigation of the intravascular coronary stent flexibility*. J Biomech, 2004. 37(4): p. 495-501.

75. Seo, T., L.G. Schachter, and A.I. Barakat, *Computational study of fluid mechanical disturbance induced by endovascular stents*. Annals of Biomedical Engineering, 2005. 33(4): p. 444-456.

76. Pache, J., et al., *Intracoronary stenting and angiographic results: Strut thickness effect on restenosis outcome (ISAR-STEREO-2) trial*. Journal of the American College of Cardiology, 2003. 41(8): p. 1283-1288.

77. Zahedmanesh, H., H. Van Oosterwyck, and C. Lally, *A multi-scale mechanobiological model of in-stent restenosis: deciphering the role of matrix metalloproteinase and extracellular matrix changes*. Comput Methods Biomech Biomed Engin, 2014. 17(8): p. 813-28.

78. De Beule, M., et al., *Finite element analysis and stent design: Reduction of dogboning*. Technol Health Care, 2006. 14(4-5): p. 233-41.

79. Pericevic, I., et al., *The influence of plaque composition on underlying arterial wall stress during stent expansion: The case for lesion-specific stents*. Medical Engineering & Physics, 2009. 31(4): p. 428-433.

80.	Wang, Y., Yi, H. and Ni, Z., *Experimental Research on Balloon-expandable Endovascular Stent Expansion*. Conf Proc IEEE Eng Med Biol Soc, 2005. 3: p. 2272-5.

81.	Squire, J.C., C. Rogers, and E.R. Edelman, *Measuring arterial strain induced by endovascular stents*. Med Biol Eng Comput, 1999. 37(6): p. 692-8.

82.	Sutton, M.A., et al., *Strain field measurements on mouse carotid arteries using microscopic three-dimensional digital image correlation*. J Biomed Mater Res A, 2008. 84(1): p. 178-90.

83.	Hoeks, A.P.G., et al., *Non-invasive measurement of mechanical properties of arteries in health and disease*. Proceedings of the Institution of Mechanical Engineers Part H-Journal of Engineering in Medicine, 1999. 213(H3): p. 195-202.

84.	Rogers, C., et al., *Balloon-artery interactions during stent placement - A finite element analysis approach to pressure, compliance, and stent design as contributors to vascular injury*. Circulation Research, 1999. 84(4): p. 378-383.

85.	Walke, W., Z. Paszenda, and J. Filipiak, *Experimental and numerical biomechanical analysis of vascular stent*. Journal of Materials Processing Technology, 2005. 164: p. 1263-1268.

86.	Kiousis, D.E., Wulff, A. R. and Holzapfel, G. A., *Experimental studies and numerical analysis of the inflation and interaction of vascular balloon catheter-stent systems*. Ann Biomed Eng, 2009. 37(2): p. 315-30.

87.	Horny, L., et al., *In vitro Coronary Stent Implantation: Vessel Wall-Stent Interaction*. 5th European Conference of the International Federation for Medical and Biological Engineering, Pts 1 and 2, 2012. 37: p. 795-798.

88.	Narracott, A.J., et al., *Measurement of the symmetry of in vitro stent expansion: a stereo-photogrammetric approach*. J Med Eng Technol, 2003. 27(2): p. 59-70.

89.	Connolley, T., et al., *X-ray micro-tomography of a coronary stent deployed in a model artery*. Medical engineering & physics, 2007. 29(10): p. 1132-41.

90.   Horny, L., et al., *Ex Vivo Coronary Stent Implantation Evaluated with Digital Image Correlation*. Experimental Mechanics, 2012. 52(9): p. 1555-1558.

91.   Zhao, S., L. Gu, and S.R. Froemming, *Experimental investigation of the stent-artery interaction*. J Med Eng Technol, 2013. 37(7): p. 463-9.

92.   Walker, R.D., et al., *Latex vessels with customized compliance for use in arterial flow models*. Physiological measurement, 1999. 20(3): p. 277-86.

93.   Conti, J.C. and E.R. Strope, *Radial compliance of natural and mock arteries: how this property defines the cyclic loading of deployed vascular stents*. Biomed Sci Instrum, 2002. 38: p. 163-72.

94.   Rajesh, R., et al., *Frequency dependent hysteresis of silicone and latex mock arteries used in stent testing*. Biomedical sciences instrumentation, 2005. 41: p. 163-8.

95.   Toner, D., *An Investigation into Stent Expansion using Numerical and Experimental Techniques*. 2009, DUBLIN CITY UNIVERSITY, School of Mechanical & Manufacturing Engineering.

96.   Colombo, A., *The role of altered cyclic strain patterns on proliferation and apoptosis of vascular smooth muscle cells - Implications for in-stent restenosis*. 2009, DUBLIN CITY UNIVERSITY, School of Mechanical & Manufacturing Engineering.

97.   Gu, L.X., S.J. Zhao, and S.R. Froemming, *Arterial Wall Mechanics and Clinical Implications after Coronary Stenting: Comparisons of Three Stent Designs*. International Journal of Applied Mechanics, 2012. 4(2).

98.   Schmidt, T., J. Tyson, and K. Galanulis, *Full-field dynamic displacement and strain measurement using advanced 3D image correlation photogrammetry: Part I*. Experimental Techniques, 2003. 27(3): p. 47-50.

99.   Morton, R.A., *Photography for the Scientist*. Second ed. 1984: ACADEMIC PRESS INC.

100.   Grediac, M., *The use of full-field measurement methods in composite material characterization: interest and limitations*. Composites Part a-Applied Science and Manufacturing, 2004. 35(7-8): p. 751-761.

101. Dulieu-Barton, J.M., et al., *Thermoelastic stress analysis of vascular devices*. Strain, 2008. 44(1): p. 102-118.

102. Gao, Z.B., et al., *Bioprosthetic heart valve leaflet motion monitored by dual camera stereo photogrammetry*. Journal of Biomechanics, 2000. 33(2): p. 199-207.

103. Schenk, T., *Introduction to Photogrammetry*. 2005.

104. Memon, Q. and S. Khan, *Camera calibration and three-dimensional world reconstruction of stereo-vision using neural networks*. International Journal of Systems Science, 2001. 32(9): p. 1155-1159.

105. Zwierzak, I., J.W. Fenner, and A.J. Narracott, *Strain Measurement in an Elastic Material under Large Deformation Using Optical Reconstruction Methods* in *International Conference on Advancements of Medicine and Health Care through Technology IFMBE Proceedings*. 2011. p. 120-123.

106. Zwierzak, I., J. W.Fenner, and A.J. Narracott, *Three dimensional optical reconstruction method for stent geometry characterisation; data validation using micro CT technique*, in *VPH2012*. 2012: London, UK.

107. Mikulenka, V., R. Kapica, and D. Sladkova, *The Potential of Photogrammetry for Object Monitoring in Undermined Areas*. Acta Montanistica Slovaca, 2011. 16(4): p. 262-269.

108. Liu P., W.A., Sui Y., *Stereoscopic 3D Reconstruction using Motorized Zoom Lenses within an Embedded System*. Image Processing: Machine Vision Applications II, 2009. SPIE-IS&T/ Vol. 7251 72510W-1.

109. Stancik, P. and V. Ricny, *Software for Camera Calibration and 3d Points Reconstruction in Stereophotogrammetry*. Eurocon 2009: International Ieee Conference Devoted to the 150 Anniversary of Alexander S. Popov, Vols 1- 4, Proceedings, 2009: p. 1169-1175.

110. Bradski G., K.A., *OpenCV*. 2008: O'Reilly Media, Inc.

111. Bradski, G. and A.Kaehler, *Learning OpenCV*. 2008: O'Reilly Media, Inc., 1005 Gravenstein Highway North, Sebastopol, CA 95472.

112. Tsai, R.Y., *A Versatile Camera Calibration Technique for High-Accuracy 3d Machine Vision Metrology Using Off-the-Shelf Tv Cameras and Lenses*. Ieee Journal of Robotics and Automation, 1987. 3(4): p. 323-344.

113. Sutton, M.A., J. Orteu, and H.W. Schreiner, *Image Correlation for Shape, Motion and Deformation Measurements*. Basic Concepts, Theory and Applications. 2009: Springer.

114. Fryer, J.G. and D.C. Brown, *Lens Distortion for Close-Range Photogrammetry*. Photogrammetric Engineering and Remote Sensing, 1986. 52(1): p. 51-58.

115. Bouguet, *Camera Calibration Toolbox for Matlab*, *Retrieved* 2008, http://www.vision.caltech.edu/bouguetj/calib_doc/. Retrieved September , 2010.

116. Zhang, Z., *A flexibile new technique for camera calibration*. IEEE Trans. Pattern Anal. Mach. Intell., 2000. 11: p. 1330-1334.

117. Heikkila, J., Silven, O., *Calibration procedure for short focal length off-the-shelf CCD cameras*, in *IEEE Proceedings of the 13th International Conference on Pattern Recognition*. 1996. p. 166-170.

118. House, B. and K. Nickels, *Increased automation in stereo camera calibration techniques*. 3rd International Conference on Computing, Communications and Control Technologies, Vol 2, Proceedings, 2005: p. 112-115

119. Peer, P. and F. Solina, *Where physically is the optical center?* Pattern Recognition Letters, 2006. 27(10): p. 1117-1121.

120. Randall, D., *Stereoscopic Optical Reconstruction Technique Applied to Strain Measurement* in *ESB 2010*. 2010: Edinburgh.

121. Lujan, T.J., et al., *Simultaneous measurement of three-dimensional joint kinematics and ligament strains with optical methods*. Journal of Biomechanical Engineering-Transactions of the Asme, 2005. 127(1): p. 193-197.

122. Hartley, R.I. and P. Sturm, *Triangulation*. Computer Vision and Image Understanding, 1997. 68(2): p. 146-157.

123. Hughes, J., *Are static strains measured in phantom aneurysms in 3TMRI comparable to those measured optically?* 2007.

124. Bornert, M., et al., *Assessment of Digital Image Correlation Measurement Errors: Methodology and Results*. Experimental Mechanics, 2009. 49(3): p. 353-370.

125. Ning, J.F., et al., *Speckle Patterning of Soft Tissues for Strain Field Measurement Using Digital Image Correlation: Preliminary Quality Assessment of Patterns*. Microscopy and Microanalysis, 2011. 17(1): p. 81-90.

126. Han, S.S., et al., *Contrast and resolution in direct Fresnel diffraction phase-contrast imaging with partially coherent x-ray source*. Review of Scientific Instruments, 2004. 75(10): p. 3146-3151.

127. Fowels, G.R., *Introduction to Modern Optics*, ed. Second. 1975.

128. Malacara, D. and Z. Malacara, *Handbook of Optical Design*. © 2004 by Marcel Dekker, Inc. ed. OPTICAL ENGINEERING, ed. B.J. Thompson. 2004, New York.

129. Shamsi, T., *Development of Physical Model of the Coronary Artery Circulation*. 2nd International Conference on Asia Agriculture and Animal (Icaaa 2012), 2012. 4: p. 188-195.

130. Cosentino, D., et al., *Uncertainty assessment of imaging techniques for the 3D reconstruction of stent geometry*. Med Eng Phys, 2014.

131. Kiousis, D.E., Wulff, A. R. and Holzapfel, G. A., *Experimental studies and numerical analysis of the inflation and interaction of vascular balloon catheter-stent systems*. Ann Biomed Eng, 2008. 37(2): p. 315-30.

132. Pochrzast, M., W. Walke, and M. Kaczmarek, *Biomechanical characterization of the balloon-expandable slotted tube stents*. Journal of Achievements in Materials and Manufacturing Engineering, 2009. 37(2).

133. *http://www.bbraun.co.uk/cps/rde/xchg/cw-bbraun-en-gb/hs.xsl/products.html?prid=PRID00002589*.

134. Migliavacca, F., et al., *Mechanical behavior of coronary stents investigated through the finite element method*. Journal of Biomechanics, 2002. 35(6): p. 803-811.

135. Evison, F. and D. Silva Soto, *VIEW* 2011, University of Sheffield, Cardiovascular Science Dept.: Sheffield. p. Graphical measurements software tool.

136. Genovese, K., Y.U. Lee, and J.D. Humphrey, *Novel optical system for in vitro quantification of full surface strain fields in small arteries: I. Theory and design*. Computer Methods in Biomechanics and Biomedical Engineering, 2011. 14(3): p. 213-225.

137. Sztefek, P., et al., *Using digital image correlation to determine bone surface strains during loading and after adaptation of the mouse tibia*. Journal of Biomechanics, 2010. 43(4): p. 599-605.

138. Zitova, B. and J. Flusser, *Image registration methods: a survey*. Image and Vision Computing, 2003. 21(11): p. 977-1000.

139. Hand, A.J., et al., *Automated tracking of migrating cells in phase-contrast video microscopy sequences using image registration*. Journal of Microscopy-Oxford, 2009. 234(1): p. 62-79.

140. Hua, T., et al., *A new mark shearing technique for strain measurement using digital image correlation method*. Review of Scientific Instruments, 2008. 79(10): p. -.

141. Khennouf, D., et al., *Assessing the Feasibility of Monitoring Strain in Historical Tapestries Using Digital Image Correlation*. Strain, 2010. 46(1): p. 19-32.

142. Verhulp, E., B. van Rietbergen, and R. Huiskes, *A three-dimensional digital image correlation technique for strain measurements in microstructures*. Journal of Biomechanics, 2004. 37(9): p. 1313-1320.

143. Pan, B., et al., *Two-dimensional digital image correlation for in-plane displacement and strain measurement: a review*. Measurement Science & Technology, 2009. 20(6).

144. Genovese, K., Y.U. Lee, and J.D. Humphrey, *Novel optical system for in vitro quantification of full surface strain fields in small arteries: II. Correction for refraction and illustrative results*. Computer Methods in Biomechanics and Biomedical Engineering, 2011. 14(3): p. 227-237.

145. Barber, D.C., *Sheffield Image Registration Toolkit (ShIRT) report*. University of Sheffield.

146. Lecompte, D., et al., *Quality assessment of speckle patterns for digital image correlation*. Optics and Lasers in Engineering, 2006. 44(11): p. 1132-1145.

147. Solutions, C., *VIC-2D Reference Manual*. 2009.

148. Helm, J.D., *Digital Image Correlation for Specimens with Multiple Growing Cracks*. Experimental Mechanics, 2008. 48(6): p. 753-762.

149. Meunier, L., et al., *Mechanical experimental characterisation and numerical modelling of an unfilled silicone rubber*. Polymer Testing, 2008. 27(6): p. 765-777.

150. Ozolanta, I., et al., *Changes in the mechanical properties, biochemical contents and wall structure of the human coronary arteries with age and sex*. Medical Engineering & Physics, 1998. 20(7): p. 523-533.

151. Karimi, A., et al., *Measurement of the uniaxial mechanical properties of healthy and atherosclerotic human coronary arteries*. Materials Science & Engineering C-Materials for Biological Applications, 2013. 33(5): p. 2550-2554.

152. Smith, B.W., X. Li, and W. Tong, *Error assessment for strain mapping by digital image correlation*. Experimental Techniques, 1998. 22(4): p. 19-21.

153. Wattrisse, B., et al., *Analysis of strain localization during tensile tests by digital image correlation*. Experimental Mechanics, 2001. 41(1): p. 29-39.

154. Colombo, F. and S. Buzago, *Evaluation of Stereo-photogrammetry to assess full-field vessel strain measurements following stent implantation*, in *Facoltà di Ingegneria dei Sistemi*. 2013, POLITECNICO DI MILANO: Italy.

155.	Chua, S.N.D., B.J. Mac Donald, and M.S.J. Hashmi, *Finite-element simulation of stent expansion*. Journal of Materials Processing Technology, 2002. 120(1-3): p. 335-340.

156.	Martin, D.M., E.A. Murphy, and F.J. Boyle, *Computational fluid dynamics analysis of balloon-expandable coronary stents: Influence of stent and vessel deformation*. Med Eng Phys, 2014. 36(8): p. 1047-56.

157.	Hoffmann, R., et al., *Stent design related neointimal tissue proliferation in human coronary arteries; an intravascular ultrasound study*. Eur Heart J, 2001. 22(21): p. 2007-14.

158.	Moore, J.E. and J.L. Berry, *Fluid and solid mechanical implications of vascular stenting*. Annals of Biomedical Engineering, 2002. 30(4): p. 498-508.

159.	Zwierzak I, Cosentino D, *Measurement of in vitro and in vivo stent geometry and deformation by means of 3D imaging and stereo-photogrammetry*. Int J Artif Organs. 2014 Dec;37(12):918-27. doi: 10.5301/ijao.5000362. Epub 2014 Nov 25

APPENDIX

PUBLICATIONS

Journal Articles

1. *Measurement of in vitro and in vivo stent geometry and deformation by means of 3D imaging and stereo-photogrammetry.*
   Zwierzak I*, Cosentino D*, Narracott AJ, Bonhoeffer P, Diaz V, Fenner JW, Schievano S.Int J Artif Organs. 2014 Dec;37(12):918-27. doi: 10.5301/ijao.5000362. Epub 2014 Nov 25. PMID: 25450318

2. *Uncertainty assessment of imaging techniques for the 3D reconstruction of stent geometry.*

   Cosentino D*, Zwierzak* I, Schievano S, Díaz-Zuccarini V, Fenner JW, Narracott AJ. Med Eng Phys. 2014 Aug;36(8):1062-8. doi: 10.1016/j.medengphy.2014.04.008. Epub 2014 Jun 2. PMID: 24894028

   *Both authors contributed equally to this study.

Conference Proceedings

1. Zwierzak, I. & Narracott, A., *In vitro characterization of stent deployment and vessel deformation* "SCIENCE – Passion, Mission, Responsibilities" Warsaw Marie Curie Symposium, 2011

2. I. Zwierzak, J. W. Fenner, A. J. Narracott, *Strain Measurement in an Elastic Material under Large Deformation Using Optical Reconstruction Methods,* International Conference on Advancements of Medicine and Health Care through Technology IFMBE Proceedings Volume 36, 2011, pp 120-123

3. I.Zwierzak, J.W.Fenner, A.J.Narracott, *3D Optical Reconstruction Technique for Balloon Expandable Stent Characterisation,* The 10th International Symposium on Biomechanics and Biomedical Engineering (CMBBE2012).

4. Iwona Zwierzak, John Fenner, Andrew Narracott, *Experimental Characterisation of an Optical System at Coronary Artery Length Scales, Journal of Biomechanics, Volume 45, Supplement 1, July 2012, Page S23*

5. <u>Iwona Zwierzak</u>, John Fenner, Andrew Narracott, *Three dimensional optical reconstruction method for stent geometry characterisation; data validation using micro CT technique*, VPH2012

6. Daria Cosentino[1,2], <u>Iwona Zwierzak</u>[3], Vanessa Diaz-Zuccarini[2], John W.Fenner[3], Silvia Schievano[1] and Andrew J.Narracott[3], Characterization Of Stent Deformed Shape Using Medical Images, Proceedings of the ASME/FDA 2013 1st Annual Frontiers in Medical Devices: Applications of Computer Modeling and Simulation, FMD2013September 11-13, 2013, Washington, DC, USA

Book Chapter

1. <u>Iwona Zwierzak</u>[1], John W. Fenner[1], Andrew J.Narracott[1], Development and assessment of a three dimensional optical reconstruction technique for experimental analysis of coronary stent deployment, 2013.

Conference Presentations

1. 29th Aug – 1st Sep, 2011: MediTech International Conference on Advancements of Medicine and Health Care through Technology, Cluj-Napoca, Romania; oral presentation.

2. 25th Sep – 27th Sep, 2011: Marie Curie Researchers Symposium, Warsaw, Poland; poster presentation.

3. 11th-14th April, 2012: 10th International Symposium: Computer Methods in Biomechanics and Biomedical Engineering 2012. Berlin, Germany; poster presentation.

4. 1st -4th July, 2012: 18th Congress of the European Society of Biomechanics - ESB 2012, Lisbon, Portugal; oral presentation.

5. 18th-20th September, 2012: The Virtual Physiological Human Network of Excellence Conference; oral presentation;

NATURE PUBLISHING GROUP LICENSE
TERMS AND CONDITIONS

Mar 31, 2015

This is a License Agreement between Iwona Zwierzak ("You") and Nature Publishing Group ("Nature Publishing Group") provided by Copyright Clearance Center ("CCC"). The license consists of your order details, the terms and conditions provided by Nature Publishing Group, and the payment terms and conditions.

All payments must be made in full to CCC. For payment instructions, please see information listed at the bottom of this form.

License Number	3439350910158
License date	Jul 31, 2014
Licensed content publisher	Nature Publishing Group
Licensed content publication	Nature
Licensed content title	Atherosclerosis
Licensed content author	Aldons J. Lusis
Licensed content date	Sep 14, 2000
Volume number	407
Issue number	6801
Type of Use	post on a website
Requestor type	academic/university or research institute
Format	electronic
Portion	figures/tables/illustrations
Number of figures/tables/illustrations	1
Figures	Figure 1
Author of this NPG article	no
Your reference number	None
Homepage URL for posting content	http://etheses.whiterose.ac.uk/
Name of internet owner	White Rose Universities (Leeds, Sheffield & York)
Expected posting date	Sep 2014
Total	0.00 GBP
Terms and Conditions	

Terms and Conditions for Permissions

Nature Publishing Group hereby grants you a non-exclusive license to reproduce this material for this purpose, and for no other use,subject to the conditions below:

1. NPG warrants that it has, to the best of its knowledge, the rights to license reuse of this material. However, you should ensure that the material you are requesting is original to Nature Publishing Group and does not carry the copyright of another entity (as credited in the published version). If the credit line on any part of the material you have requested

indicates that it was reprinted or adapted by NPG with permission from another source, then you should also seek permission from that source to reuse the material.

2. Permission granted free of charge for material in print is also usually granted for any electronic version of that work, provided that the material is incidental to the work as a whole and that the electronic version is essentially equivalent to, or substitutes for, the print version.Where print permission has been granted for a fee, separate permission must be obtained for any additional, electronic re-use (unless, as in the case of a full paper, this has already been accounted for during your initial request in the calculation of a print run).NB: In all cases, web-based use of full-text articles must be authorized separately through the 'Use on a Web Site' option when requesting permission.

3. Permission granted for a first edition does not apply to second and subsequent editions and for editions in other languages (except for signatories to the STM Permissions Guidelines, or where the first edition permission was granted for free).

4. Nature Publishing Group's permission must be acknowledged next to the figure, table or abstract in print. In electronic form, this acknowledgement must be visible at the same time as the figure/table/abstract, and must be hyperlinked to the journal's homepage.

5. The credit line should read:
Reprinted by permission from Macmillan Publishers Ltd: [JOURNAL NAME] (reference citation), copyright (year of publication)
For AOP papers, the credit line should read:
Reprinted by permission from Macmillan Publishers Ltd: [JOURNAL NAME], advance online publication, day month year (doi: 10.1038/sj.[JOURNAL ACRONYM].XXXXX)

Note: For republication from the _British Journal of Cancer,_ the following credit lines apply.
Reprinted by permission from Macmillan Publishers Ltd on behalf of Cancer Research UK: [JOURNAL NAME] (reference citation), copyright (year of publication)For AOP papers, the credit line should read:
Reprinted by permission from Macmillan Publishers Ltd on behalf of Cancer Research UK: [JOURNAL NAME], advance online publication, day month year (doi: 10.1038/sj.[JOURNAL ACRONYM].XXXXX)

6. Adaptations of single figures do not require NPG approval. However, the adaptation should be credited as follows:

Adapted by permission from Macmillan Publishers Ltd: [JOURNAL NAME] (reference citation), copyright (year of publication)

Note: For adaptation from the _British Journal of Cancer,_ the following credit line applies.
Adapted by permission from Macmillan Publishers Ltd on behalf of Cancer Research UK: [JOURNAL NAME] (reference citation), copyright (year of publication)

7. Translations of 401 words up to a whole article require NPG approval. Please visit http://www.macmillanmedicalcommunications.com for more information.Translations of up to a 400 words do not require NPG approval. The translation should be credited as follows:

Translated by permission from Macmillan Publishers Ltd: [JOURNAL NAME] (reference citation), copyright (year of publication).

Note: For translation from the _British Journal of Cancer,_ the following credit line applies.
Translated by permission from Macmillan Publishers Ltd on behalf of Cancer Research UK: [JOURNAL NAME] (reference citation), copyright (year of publication)

We are certain that all parties will benefit from this agreement and wish you the best in the use of this material. Thank you.

Special Terms:

v1.1

Questions? customercare@copyright.com or +1-855-239-3415 (toll free in the US) or +1-978-646-2777.

Gratis licenses (referencing $0 in the Total field) are free. Please retain this printable license for your reference. No payment is required.

WOLTERS KLUWER HEALTH, INC. LICENSE
TERMS AND CONDITIONS

Mar 31, 2015

This Agreement between Iwona Zwierzak ("You") and Wolters Kluwer Health, Inc. ("Wolters Kluwer Health, Inc.") consists of your license details and the terms and conditions provided by Wolters Kluwer Health, Inc. and Copyright Clearance Center.

License Number	3439411213643
License date	Jul 31, 2014
Licensed Content Publisher	Wolters Kluwer Health
Licensed Content Publication	Annals of Surgery
Licensed Content Title	Patterns of Atherosclerosis and their Surgical Significance.
Licensed Content Author	MICHAEL DEBAKEY, GERALD LAWRIE, and DONALD GLAESER
Licensed Content Date	Jan 1, 1985
Licensed Content Volume Number	201
Licensed Content Issue Number	2
Type of Use	Dissertation/Thesis
Requestor type	Individual
Portion	Figures/table/illustration
Number of figures/tables/illustrations	1
Figures/tables/illustrations used	Fig.1
Author of this Wolters Kluwer article	No
Title of your thesis / dissertation	In vitro characterisation of stent deployment and local arterial strains
Expected completion date	Aug 2014
Estimated size(pages)	240
Billing Type	Invoice
Billing Address	66 Upper Allen Street Apartment 16
	Sheffield, United Kingdom S37GW Attn:
Total	0.00 GBP
Total	
Terms and Conditions	

Terms and Conditions

1. A credit line will be prominently placed and include the author(s), title of article, title of journal, volume number, issue number and inclusive pages.
2. The requestor warrants that the material shall not be used in any manner which may be considered derogatory to the title, content, or authors of the material, or to Wolters Kluwer.
3. Permission granted is non-exclusive, and is valid throughout the world in the English language and the languages specified in your original request.
4. Wolters Kluwer cannot supply the requestor with the original artwork or a "clean copy."
5. Permission is valid if the borrowed material is original to a Wolters Kluwer imprint (Lippincott-Raven Publishers, Williams & Wilkins, Lea & Febiger, Harwal, Rapid Science, Little Brown & Company, Harper & Row Medical, American Journal of Nursing Co, and Urban & Schwarzenberg - English Language).
6. If you opt not to use the material requested above, please notify RightsLink or Wolters Kluwer Health/Lippincott Williams & Wilkins within 90 days of the original invoice date.
7. This permission does not apply to images that are credited to publications other than Wolters Kluwer journals. For images credited to non-Wolters Kluwer journal publications, you will need to obtain permission from the journal referenced in the figure or table legend or credit line before making any use of the image(s) or table(s).
8. Adaptations are protected by copyright, so if you would like to reuse material that we have adapted from another source, you will need not only our permission, but the permission of the rights holder of the original material. Similarly, if you want to reuse an adaptation of original LWW content that appears in another publisher's work, you will need our permission and that of the next publisher. The adaptation should be credited as follows: Adapted with permission from Lippincott Williams and Wilkins/Wolters Kluwer Health: Book author, title, year of publication or Journal name, article author, title, reference citation, year of publication.
9. **Please note that modification of text within figures or full-text article is strictly forbidden.**
10. Please note that articles in the ahead-of-print stage of publication can be cited and the content may be re-used by including the date of access and the unique DOI number. Any final changes in manuscripts will be made at the time of print publication and will be reflected in the final electronic version of the issue. Disclaimer: Articles appearing in the Published Ahead-of-Print section have been peer-reviewed and accepted for publication in the relevant journal and posted online before print publication. Articles appearing as publish ahead-of-print may contain statements, opinions, and information that have errors in facts, figures, or interpretation. Accordingly, Lippincott Williams & Wilkins, the editors and authors and their respective employees are not responsible or liable for the use of any such inaccurate or misleading data, opinion or information contained in the articles in this section.
11. Permission is granted for a one time use only within 12 months from the date of this invoice. Rights herein do not apply to future reproductions, editions, revisions, or other derivative works. Once the 12-month term has expired, permission to renew must be submitted in writing.
12. The following statement needs to be added when reprinting the material in Open Access journals only: 'promotional and commercial use of the material in print, digital or mobile device format is prohibited without the permission from the publisher Lippincott Williams & Wilkins. Please contact journalpermissions@lww.com for further information'.
13. In case of *Disease Colon Rectum, Plastic Reconstructive Surgery, The Green Journal, Critical Care Medicine, Pediatric Critical Care Medicine, the American Heart Publications, the American Academy of Neurology* the following guideline applies: no drug brand/trade name or logo can be included in the same page as the material re-used
14. When requesting a permission to translate a full text article, Wolters Kluwer/Lippincott Williams & Wilkins requests to receive the pdf of the translated document
15. Other Terms and Conditions:

v1.9

Questions? customercare@copyright.com or +1-855-239-3415 (toll free in the US) or +1-978-646-2777.

Gratis licenses (referencing $0 in the Total field) are free. Please retain this printable license for your reference. No payment is required.

ANNUAL REVIEWS

Title: Stented Artery Flow Patterns and Their Effects on the Artery Wall

Author: Nandini Duraiswamy, Richard T. Schoephoerster, Michael R. Moreno, et al

Publication: Annual Review of Fluid Mechanics

Publisher: Annual Reviews

Date: Jan 1, 2007

Copyright © 2007, Annual Reviews

Permission Not Required

Material may be republished in a thesis / dissertation without obtaining additional permission from Annual Reviews, providing that the author and the original source of publication are fully acknowledged.

BACK   CLOSE WINDOW

Taylor & Francis
Taylor & Francis Group

Title: A multi-scale mechanobiological model of in-stent restenosis: deciphering the role of matrix metalloproteinase and extracellular matrix changes

Author: Houman Zahedmanesh, Hans Van Oosterwyck, Caitríona Lally

Publication: Computer Methods in Biomechanics & Bio Engineering

Publisher: Taylor & Francis

Date: Jun 11, 2014

Copyright © 2014 Taylor & Francis

Thesis/Dissertation Reuse Request

Taylor & Francis is pleased to offer reuses of its content for a thesis or dissertation free of charge contingent on resubmission of permission request if work is published.

BACK | CLOSE WINDOW

ELSEVIER LICENSE
TERMS AND CONDITIONS

Mar 31, 2015

This is a License Agreement between Iwona Zwierzak ("You") and Elsevier ("Elsevier") provided by Copyright Clearance Center ("CCC"). The license consists of your order details, the terms and conditions provided by Elsevier, and the payment terms and conditions.

All payments must be made in full to CCC. For payment instructions, please see information listed at the bottom of this form.

Supplier	Elsevier Limited The Boulevard,Langford Lane Kidlington,Oxford,OX5 1GB,UK
Registered Company Number	1982084
Customer name	Iwona Zwierzak
Customer address	66 Upper Allen Street
	Sheffield, S37GW
License number	3440150383542
License date	Aug 01, 2014
Licensed content publisher	Elsevier
Licensed content publication	Medical Engineering & Physics
Licensed content title	Uncertainty assessment of imaging techniques for the 3D reconstruction of stent geometry
Licensed content author	Daria Cosentino,Iwona Zwierzak,Silvia Schievano,Vanessa Díaz-Zuccarini,John W. Fenner,Andrew J. Narracott
Licensed content date	August 2014
Licensed content volume number	36
Licensed content issue number	8
Number of pages	7
Start Page	1062
End Page	1068
Type of Use	reuse in a thesis/dissertation
Intended publisher of new work	other
Portion	figures/tables/illustrations
Number of figures/tables/illustrations	3
Format	both print and electronic
Are you the author of this Elsevier article?	Yes
Will you be translating?	No
Title of your	In vitro characterisation of stent deployment and local arterial strains

thesis/dissertation

Expected completion date	Aug 2014
Estimated size (number of pages)	240
Elsevier VAT number	GB 494 6272 12
Permissions price	0.00 GBP
VAT/Local Sales Tax	0.00 GBP / 0.00 GBP
Total	0.00 GBP

Terms and Conditions

INTRODUCTION

1. The publisher for this copyrighted material is Elsevier. By clicking "accept" in connection with completing this licensing transaction, you agree that the following terms and conditions apply to this transaction (along with the Billing and Payment terms and conditions established by Copyright Clearance Center, Inc. ("CCC"), at the time that you opened your Rightslink account and that are available at any time at http://myaccount.copyright.com).

GENERAL TERMS

2. Elsevier hereby grants you permission to reproduce the aforementioned material subject to the terms and conditions indicated.

3. Acknowledgement: If any part of the material to be used (for example, figures) has appeared in our publication with credit or acknowledgement to another source, permission must also be sought from that source. If such permission is not obtained then that material may not be included in your publication/copies. Suitable acknowledgement to the source must be made, either as a footnote or in a reference list at the end of your publication, as follows:

"Reprinted from Publication title, Vol /edition number, Author(s), Title of article / title of chapter, Pages No., Copyright (Year), with permission from Elsevier [OR APPLICABLE SOCIETY COPYRIGHT OWNER]." Also Lancet special credit - "Reprinted from The Lancet, Vol. number, Author(s), Title of article, Pages No., Copyright (Year), with permission from Elsevier."

4. Reproduction of this material is confined to the purpose and/or media for which permission is hereby given.

5. Altering/Modifying Material: Not Permitted. However figures and illustrations may be altered/adapted minimally to serve your work. Any other abbreviations, additions, deletions and/or any other alterations shall be made only with prior written authorization of Elsevier Ltd. (Please contact Elsevier at permissions@elsevier.com)

6. If the permission fee for the requested use of our material is waived in this instance, please be advised that your future requests for Elsevier materials may attract a fee.

7. Reservation of Rights: Publisher reserves all rights not specifically granted in the combination of (i) the license details provided by you and accepted in the course of this licensing transaction, (ii) these terms and conditions and (iii) CCC's Billing and Payment terms and conditions.

8. License Contingent Upon Payment: While you may exercise the rights licensed

immediately upon issuance of the license at the end of the licensing process for the transaction, provided that you have disclosed complete and accurate details of your proposed use, no license is finally effective unless and until full payment is received from you (either by publisher or by CCC) as provided in CCC's Billing and Payment terms and conditions. If full payment is not received on a timely basis, then any license preliminarily granted shall be deemed automatically revoked and shall be void as if never granted. Further, in the event that you breach any of these terms and conditions or any of CCC's Billing and Payment terms and conditions, the license is automatically revoked and shall be void as if never granted. Use of materials as described in a revoked license, as well as any use of the materials beyond the scope of an unrevoked license, may constitute copyright infringement and publisher reserves the right to take any and all action to protect its copyright in the materials.

9. Warranties: Publisher makes no representations or warranties with respect to the licensed material.

10. Indemnity: You hereby indemnify and agree to hold harmless publisher and CCC, and their respective officers, directors, employees and agents, from and against any and all claims arising out of your use of the licensed material other than as specifically authorized pursuant to this license.

11. No Transfer of License: This license is personal to you and may not be sublicensed, assigned, or transferred by you to any other person without publisher's written permission.

12. No Amendment Except in Writing: This license may not be amended except in a writing signed by both parties (or, in the case of publisher, by CCC on publisher's behalf).

13. Objection to Contrary Terms: Publisher hereby objects to any terms contained in any purchase order, acknowledgment, check endorsement or other writing prepared by you, which terms are inconsistent with these terms and conditions or CCC's Billing and Payment terms and conditions. These terms and conditions, together with CCC's Billing and Payment terms and conditions (which are incorporated herein), comprise the entire agreement between you and publisher (and CCC) concerning this licensing transaction. In the event of any conflict between your obligations established by these terms and conditions and those established by CCC's Billing and Payment terms and conditions, these terms and conditions shall control.

14. Revocation: Elsevier or Copyright Clearance Center may deny the permissions described in this License at their sole discretion, for any reason or no reason, with a full refund payable to you. Notice of such denial will be made using the contact information provided by you. Failure to receive such notice will not alter or invalidate the denial. In no event will Elsevier or Copyright Clearance Center be responsible or liable for any costs, expenses or damage incurred by you as a result of a denial of your permission request, other than a refund of the amount(s) paid by you to Elsevier and/or Copyright Clearance Center for denied permissions.

LIMITED LICENSE

The following terms and conditions apply only to specific license types:

15. **Translation**: This permission is granted for non-exclusive world **English** rights only unless your license was granted for translation rights. If you licensed translation rights you may only translate this content into the languages you requested. A professional translator must perform all translations and reproduce the content word for word preserving the integrity of the article. If this license is to re-use 1 or 2 figures then permission is granted for

non-exclusive world rights in all languages.

16. **Posting licensed content on any Website**: The following terms and conditions apply as follows: Licensing material from an Elsevier journal: All content posted to the web site must maintain the copyright information line on the bottom of each image; A hyper-text must be included to the Homepage of the journal from which you are licensing at http://www.sciencedirect.com/science/journal/xxxxx or the Elsevier homepage for books at http://www.elsevier.com; Central Storage: This license does not include permission for a scanned version of the material to be stored in a central repository such as that provided by Heron/XanEdu.

Licensing material from an Elsevier book: A hyper-text link must be included to the Elsevier homepage at http://www.elsevier.com . All content posted to the web site must maintain the copyright information line on the bottom of each image.

Posting licensed content on Electronic reserve: In addition to the above the following clauses are applicable: The web site must be password-protected and made available only to bona fide students registered on a relevant course. This permission is granted for 1 year only. You may obtain a new license for future website posting.

17. **For journal authors:** the following clauses are applicable in addition to the above:

Preprints:

A preprint is an author's own write-up of research results and analysis, it has not been peer-reviewed, nor has it had any other value added to it by a publisher (such as formatting, copyright, technical enhancement etc.).

Authors can share their preprints anywhere at any time. Preprints should not be added to or enhanced in any way in order to appear more like, or to substitute for, the final versions of articles however authors can update their preprints on arXiv or RePEc with their Accepted Author Manuscript (see below).

If accepted for publication, we encourage authors to link from the preprint to their formal publication via its DOI. Millions of researchers have access to the formal publications on ScienceDirect, and so links will help users to find, access, cite and use the best available version. Please note that Cell Press, The Lancet and some society-owned have different preprint policies. Information on these policies is available on the journal homepage.

Accepted Author Manuscripts: An accepted author manuscript is the manuscript of an article that has been accepted for publication and which typically includes author-incorporated changes suggested during submission, peer review and editor-author communications.

Authors can share their accepted author manuscript:

- – immediately
    - ○ via their non-commercial person homepage or blog
    - ○ by updating a preprint in arXiv or RePEc with the accepted manuscript
    - ○ via their research institute or institutional repository for internal institutional uses or as part of an invitation-only research collaboration work-group

- directly by providing copies to their students or to research collaborators for their personal use

- for private scholarly sharing as part of an invitation-only work group on commercial sites with which Elsevier has an agreement

  - after the embargo period

    - via non-commercial hosting platforms such as their institutional repository

    - via commercial sites with which Elsevier has an agreement

In all cases accepted manuscripts should:

- link to the formal publication via its DOI

- bear a CC-BY-NC-ND license - this is easy to do

- if aggregated with other manuscripts, for example in a repository or other site, be shared in alignment with our hosting policy not be added to or enhanced in any way to appear more like, or to substitute for, the published journal article.

Published journal article (JPA): A published journal article (PJA) is the definitive final record of published research that appears or will appear in the journal and embodies all value-adding publishing activities including peer review co-ordination, copy-editing, formatting, (if relevant) pagination and online enrichment.

Policies for sharing publishing journal articles differ for subscription and gold open access articles:

<u>**Subscription Articles:**</u> If you are an author, please share a link to your article rather than the full-text. Millions of researchers have access to the formal publications on ScienceDirect, and so links will help your users to find, access, cite, and use the best available version.

Theses and dissertations which contain embedded PJAs as part of the formal submission can be posted publicly by the awarding institution with DOI links back to the formal publications on ScienceDirect.

If you are affiliated with a library that subscribes to ScienceDirect you have additional private sharing rights for others' research accessed under that agreement. This includes use for classroom teaching and internal training at the institution (including use in course packs and courseware programs), and inclusion of the article for grant funding purposes.

<u>**Gold Open Access Articles:**</u> May be shared according to the author-selected end-user license and should contain a [CrossMark logo](#), the end user license, and a DOI link to the formal publication on ScienceDirect.

Please refer to Elsevier's [posting policy](#) for further information.

18. **For book authors** the following clauses are applicable in addition to the above: Authors are permitted to place a brief summary of their work online only. You are not allowed to download and post the published electronic version of your chapter, nor may you scan the printed edition to create an electronic version. **Posting to a repository:** Authors are permitted to post a summary of their chapter only in their institution's repository.

19. **Thesis/Dissertation**: If your license is for use in a thesis/dissertation your thesis may be submitted to your institution in either print or electronic form. Should your thesis be published commercially, please reapply for permission. These requirements include permission for the Library and Archives of Canada to supply single copies, on demand, of the complete thesis and include permission for Proquest/UMI to supply single copies, on demand, of the complete thesis. Should your thesis be published commercially, please reapply for permission. Theses and dissertations which contain embedded PJAs as part of the formal submission can be posted publicly by the awarding institution with DOI links back to the formal publications on ScienceDirect.

Elsevier Open Access Terms and Conditions

You can publish open access with Elsevier in hundreds of open access journals or in nearly 2000 established subscription journals that support open access publishing. Permitted third party re-use of these open access articles is defined by the author's choice of Creative Commons user license. See our open access license policy for more information.

Terms & Conditions applicable to all Open Access articles published with Elsevier:

Any reuse of the article must not represent the author as endorsing the adaptation of the article nor should the article be modified in such a way as to damage the author's honour or reputation. If any changes have been made, such changes must be clearly indicated.

The author(s) must be appropriately credited and we ask that you include the end user license and a DOI link to the formal publication on ScienceDirect.

If any part of the material to be used (for example, figures) has appeared in our publication with credit or acknowledgement to another source it is the responsibility of the user to ensure their reuse complies with the terms and conditions determined by the rights holder.

Additional Terms & Conditions applicable to each Creative Commons user license:

CC BY: The CC-BY license allows users to copy, to create extracts, abstracts and new works from the Article, to alter and revise the Article and to make commercial use of the Article (including reuse and/or resale of the Article by commercial entities), provided the user gives appropriate credit (with a link to the formal publication through the relevant DOI), provides a link to the license, indicates if changes were made and the licensor is not represented as endorsing the use made of the work. The full details of the license are available at http://creativecommons.org/licenses/by/4.0.

CC BY NC SA: The CC BY-NC-SA license allows users to copy, to create extracts, abstracts and new works from the Article, to alter and revise the Article, provided this is not done for commercial purposes, and that the user gives appropriate credit (with a link to the formal publication through the relevant DOI), provides a link to the license, indicates if changes were made and the licensor is not represented as endorsing the use made of the work. Further, any new works must be made available on the same conditions. The full details of the license are available at http://creativecommons.org/licenses/by-nc-sa/4.0.

CC BY NC ND: The CC BY-NC-ND license allows users to copy and distribute the Article, provided this is not done for commercial purposes and further does not permit distribution of the Article if it is changed or edited in any way, and provided the user gives appropriate credit (with a link to the formal publication through the relevant DOI), provides a link to the license, and that the licensor is not represented as endorsing the use made of the work. The

full details of the license are available at http://creativecommons.org/licenses/by-nc-nd/4.0.
Any commercial reuse of Open Access articles published with a CC BY NC SA or CC BY
NC ND license requires permission from Elsevier and will be subject to a fee.

Commercial reuse includes:

- Associating advertising with the full text of the Article

- Charging fees for document delivery or access

- Article aggregation

- Systematic distribution via e-mail lists or share buttons

Posting or linking by commercial companies for use by customers of those companies.

20. **Other Conditions**:

**Questions? customercare@copyright.com or +1-855-239-3415 (toll free in the US) or
+1-978-646-2777.**

**Gratis licenses (referencing $0 in the Total field) are free. Please retain this printable
license for your reference. No payment is required.**

ELSEVIER LICENSE
TERMS AND CONDITIONS

Mar 31, 2015

This is a License Agreement between Iwona Zwierzak ("You") and Elsevier ("Elsevier") provided by Copyright Clearance Center ("CCC"). The license consists of your order details, the terms and conditions provided by Elsevier, and the payment terms and conditions.

All payments must be made in full to CCC. For payment instructions, please see information listed at the bottom of this form.

Supplier	Elsevier Limited The Boulevard,Langford Lane Kidlington,Oxford,OX5 1GB,UK
Registered Company Number	1982084
Customer name	Iwona Zwierzak
Customer address	66 Upper Allen Street
	Sheffield, S37GW
License number	3440150072906
License date	Aug 01, 2014
Licensed content publisher	Elsevier
Licensed content publication	Journal of Biomechanics
Licensed content title	Realistic finite element-based stent design: The impact of balloon folding
Licensed content author	Matthieu De Beule,Peter Mortier,Stéphane G. Carlier,Benedict Verhegghe,Rudy Van Impe,Pascal Verdonck
Licensed content date	2008
Licensed content volume number	41
Licensed content issue number	2
Number of pages	7
Start Page	383
End Page	389
Type of Use	reuse in a thesis/dissertation
Intended publisher of new work	other
Portion	figures/tables/illustrations
Number of figures/tables/illustrations	1
Format	both print and electronic
Are you the author of this Elsevier article?	No
Will you be translating?	No
Title of your	In vitro characterisation of stent deployment and local arterial strains

thesis/dissertation

Expected completion date	Aug 2014
Estimated size (number of pages)	240
Elsevier VAT number	GB 494 6272 12
Permissions price	0.00 GBP
VAT/Local Sales Tax	0.00 GBP / 0.00 GBP
Total	0.00 GBP

Terms and Conditions

INTRODUCTION

1. The publisher for this copyrighted material is Elsevier. By clicking "accept" in connection with completing this licensing transaction, you agree that the following terms and conditions apply to this transaction (along with the Billing and Payment terms and conditions established by Copyright Clearance Center, Inc. ("CCC"), at the time that you opened your Rightslink account and that are available at any time at http://myaccount.copyright.com).

GENERAL TERMS

2. Elsevier hereby grants you permission to reproduce the aforementioned material subject to the terms and conditions indicated.

3. Acknowledgement: If any part of the material to be used (for example, figures) has appeared in our publication with credit or acknowledgement to another source, permission must also be sought from that source. If such permission is not obtained then that material may not be included in your publication/copies. Suitable acknowledgement to the source must be made, either as a footnote or in a reference list at the end of your publication, as follows:

"Reprinted from Publication title, Vol /edition number, Author(s), Title of article / title of chapter, Pages No., Copyright (Year), with permission from Elsevier [OR APPLICABLE SOCIETY COPYRIGHT OWNER]." Also Lancet special credit - "Reprinted from The Lancet, Vol. number, Author(s), Title of article, Pages No., Copyright (Year), with permission from Elsevier."

4. Reproduction of this material is confined to the purpose and/or media for which permission is hereby given.

5. Altering/Modifying Material: Not Permitted. However figures and illustrations may be altered/adapted minimally to serve your work. Any other abbreviations, additions, deletions and/or any other alterations shall be made only with prior written authorization of Elsevier Ltd. (Please contact Elsevier at permissions@elsevier.com)

6. If the permission fee for the requested use of our material is waived in this instance, please be advised that your future requests for Elsevier materials may attract a fee.

7. Reservation of Rights: Publisher reserves all rights not specifically granted in the combination of (i) the license details provided by you and accepted in the course of this licensing transaction, (ii) these terms and conditions and (iii) CCC's Billing and Payment terms and conditions.

8. License Contingent Upon Payment: While you may exercise the rights licensed

immediately upon issuance of the license at the end of the licensing process for the transaction, provided that you have disclosed complete and accurate details of your proposed use, no license is finally effective unless and until full payment is received from you (either by publisher or by CCC) as provided in CCC's Billing and Payment terms and conditions. If full payment is not received on a timely basis, then any license preliminarily granted shall be deemed automatically revoked and shall be void as if never granted. Further, in the event that you breach any of these terms and conditions or any of CCC's Billing and Payment terms and conditions, the license is automatically revoked and shall be void as if never granted. Use of materials as described in a revoked license, as well as any use of the materials beyond the scope of an unrevoked license, may constitute copyright infringement and publisher reserves the right to take any and all action to protect its copyright in the materials.

9. Warranties: Publisher makes no representations or warranties with respect to the licensed material.

10. Indemnity: You hereby indemnify and agree to hold harmless publisher and CCC, and their respective officers, directors, employees and agents, from and against any and all claims arising out of your use of the licensed material other than as specifically authorized pursuant to this license.

11. No Transfer of License: This license is personal to you and may not be sublicensed, assigned, or transferred by you to any other person without publisher's written permission.

12. No Amendment Except in Writing: This license may not be amended except in a writing signed by both parties (or, in the case of publisher, by CCC on publisher's behalf).

13. Objection to Contrary Terms: Publisher hereby objects to any terms contained in any purchase order, acknowledgment, check endorsement or other writing prepared by you, which terms are inconsistent with these terms and conditions or CCC's Billing and Payment terms and conditions. These terms and conditions, together with CCC's Billing and Payment terms and conditions (which are incorporated herein), comprise the entire agreement between you and publisher (and CCC) concerning this licensing transaction. In the event of any conflict between your obligations established by these terms and conditions and those established by CCC's Billing and Payment terms and conditions, these terms and conditions shall control.

14. Revocation: Elsevier or Copyright Clearance Center may deny the permissions described in this License at their sole discretion, for any reason or no reason, with a full refund payable to you. Notice of such denial will be made using the contact information provided by you. Failure to receive such notice will not alter or invalidate the denial. In no event will Elsevier or Copyright Clearance Center be responsible or liable for any costs, expenses or damage incurred by you as a result of a denial of your permission request, other than a refund of the amount(s) paid by you to Elsevier and/or Copyright Clearance Center for denied permissions.

LIMITED LICENSE

The following terms and conditions apply only to specific license types:

15. **Translation**: This permission is granted for non-exclusive world **English** rights only unless your license was granted for translation rights. If you licensed translation rights you may only translate this content into the languages you requested. A professional translator must perform all translations and reproduce the content word for word preserving the integrity of the article. If this license is to re-use 1 or 2 figures then permission is granted for

non-exclusive world rights in all languages.

16. **Posting licensed content on any Website**: The following terms and conditions apply as follows: Licensing material from an Elsevier journal: All content posted to the web site must maintain the copyright information line on the bottom of each image; A hyper-text must be included to the Homepage of the journal from which you are licensing at http://www.sciencedirect.com/science/journal/xxxxx or the Elsevier homepage for books at http://www.elsevier.com; Central Storage: This license does not include permission for a scanned version of the material to be stored in a central repository such as that provided by Heron/XanEdu.

Licensing material from an Elsevier book: A hyper-text link must be included to the Elsevier homepage at http://www.elsevier.com . All content posted to the web site must maintain the copyright information line on the bottom of each image.

Posting licensed content on Electronic reserve: In addition to the above the following clauses are applicable: The web site must be password-protected and made available only to bona fide students registered on a relevant course. This permission is granted for 1 year only. You may obtain a new license for future website posting.

17. **For journal authors:** the following clauses are applicable in addition to the above:

Preprints:

A preprint is an author's own write-up of research results and analysis, it has not been peer-reviewed, nor has it had any other value added to it by a publisher (such as formatting, copyright, technical enhancement etc.).

Authors can share their preprints anywhere at any time. Preprints should not be added to or enhanced in any way in order to appear more like, or to substitute for, the final versions of articles however authors can update their preprints on arXiv or RePEc with their Accepted Author Manuscript (see below).

If accepted for publication, we encourage authors to link from the preprint to their formal publication via its DOI. Millions of researchers have access to the formal publications on ScienceDirect, and so links will help users to find, access, cite and use the best available version. Please note that Cell Press, The Lancet and some society-owned have different preprint policies. Information on these policies is available on the journal homepage.

Accepted Author Manuscripts: An accepted author manuscript is the manuscript of an article that has been accepted for publication and which typically includes author-incorporated changes suggested during submission, peer review and editor-author communications.

Authors can share their accepted author manuscript:

- immediately

  - via their non-commercial person homepage or blog

  - by updating a preprint in arXiv or RePEc with the accepted manuscript

  - via their research institute or institutional repository for internal institutional uses or as part of an invitation-only research collaboration work-group

- directly by providing copies to their students or to research collaborators for their personal use

- for private scholarly sharing as part of an invitation-only work group on commercial sites with which Elsevier has an agreement

- after the embargo period

  - via non-commercial hosting platforms such as their institutional repository

  - via commercial sites with which Elsevier has an agreement

In all cases accepted manuscripts should:

- link to the formal publication via its DOI

- bear a CC-BY-NC-ND license - this is easy to do

- if aggregated with other manuscripts, for example in a repository or other site, be shared in alignment with our hosting policy not be added to or enhanced in any way to appear more like, or to substitute for, the published journal article.

Published journal article (JPA): A published journal article (PJA) is the definitive final record of published research that appears or will appear in the journal and embodies all value-adding publishing activities including peer review co-ordination, copy-editing, formatting, (if relevant) pagination and online enrichment.

Policies for sharing publishing journal articles differ for subscription and gold open access articles:

Subscription Articles: If you are an author, please share a link to your article rather than the full-text. Millions of researchers have access to the formal publications on ScienceDirect, and so links will help your users to find, access, cite, and use the best available version.

Theses and dissertations which contain embedded PJAs as part of the formal submission can be posted publicly by the awarding institution with DOI links back to the formal publications on ScienceDirect.

If you are affiliated with a library that subscribes to ScienceDirect you have additional private sharing rights for others' research accessed under that agreement. This includes use for classroom teaching and internal training at the institution (including use in course packs and courseware programs), and inclusion of the article for grant funding purposes.

Gold Open Access Articles: May be shared according to the author-selected end-user license and should contain a CrossMark logo, the end user license, and a DOI link to the formal publication on ScienceDirect.

Please refer to Elsevier's posting policy for further information.

18. **For book authors** the following clauses are applicable in addition to the above: Authors are permitted to place a brief summary of their work online only. You are not allowed to download and post the published electronic version of your chapter, nor may you scan the printed edition to create an electronic version. **Posting to a repository:** Authors are permitted to post a summary of their chapter only in their institution's repository.

19. **Thesis/Dissertation**: If your license is for use in a thesis/dissertation your thesis may be submitted to your institution in either print or electronic form. Should your thesis be published commercially, please reapply for permission. These requirements include permission for the Library and Archives of Canada to supply single copies, on demand, of the complete thesis and include permission for Proquest/UMI to supply single copies, on demand, of the complete thesis. Should your thesis be published commercially, please reapply for permission. Theses and dissertations which contain embedded PJAs as part of the formal submission can be posted publicly by the awarding institution with DOI links back to the formal publications on ScienceDirect.

Elsevier Open Access Terms and Conditions

You can publish open access with Elsevier in hundreds of open access journals or in nearly 2000 established subscription journals that support open access publishing. Permitted third party re-use of these open access articles is defined by the author's choice of Creative Commons user license. See our open access license policy for more information.

Terms & Conditions applicable to all Open Access articles published with Elsevier:

Any reuse of the article must not represent the author as endorsing the adaptation of the article nor should the article be modified in such a way as to damage the author's honour or reputation. If any changes have been made, such changes must be clearly indicated.

The author(s) must be appropriately credited and we ask that you include the end user license and a DOI link to the formal publication on ScienceDirect.

If any part of the material to be used (for example, figures) has appeared in our publication with credit or acknowledgement to another source it is the responsibility of the user to ensure their reuse complies with the terms and conditions determined by the rights holder.

Additional Terms & Conditions applicable to each Creative Commons user license:

CC BY: The CC-BY license allows users to copy, to create extracts, abstracts and new works from the Article, to alter and revise the Article and to make commercial use of the Article (including reuse and/or resale of the Article by commercial entities), provided the user gives appropriate credit (with a link to the formal publication through the relevant DOI), provides a link to the license, indicates if changes were made and the licensor is not represented as endorsing the use made of the work. The full details of the license are available at http://creativecommons.org/licenses/by/4.0.

CC BY NC SA: The CC BY-NC-SA license allows users to copy, to create extracts, abstracts and new works from the Article, to alter and revise the Article, provided this is not done for commercial purposes, and that the user gives appropriate credit (with a link to the formal publication through the relevant DOI), provides a link to the license, indicates if changes were made and the licensor is not represented as endorsing the use made of the work. Further, any new works must be made available on the same conditions. The full details of the license are available at http://creativecommons.org/licenses/by-nc-sa/4.0.

CC BY NC ND: The CC BY-NC-ND license allows users to copy and distribute the Article, provided this is not done for commercial purposes and further does not permit distribution of the Article if it is changed or edited in any way, and provided the user gives appropriate credit (with a link to the formal publication through the relevant DOI), provides a link to the license, and that the licensor is not represented as endorsing the use made of the work. The

full details of the license are available at http://creativecommons.org/licenses/by-nc-nd/4.0. Any commercial reuse of Open Access articles published with a CC BY NC SA or CC BY NC ND license requires permission from Elsevier and will be subject to a fee.

Commercial reuse includes:

- Associating advertising with the full text of the Article

- Charging fees for document delivery or access

- Article aggregation

- Systematic distribution via e-mail lists or share buttons

Posting or linking by commercial companies for use by customers of those companies.

20. **Other Conditions**:

Questions? customercare@copyright.com or +1-855-239-3415 (toll free in the US) or +1-978-646-2777.

Gratis licenses (referencing $0 in the Total field) are free. Please retain this printable license for your reference. No payment is required.